universität wien

DISSERTATION / DOCTORAL THESIS

Titel der Dissertation /Title of the Doctoral Thesis

„Atmospheres of evolved C-rich stars - from observations to models, and back“

verfasst von / submitted by

Dott.ssa mag. Gioia Rau

angestrebter akademischer Grad / in partial fulfilment of the requirements for the degree of

Doktorin der Naturwissenschaften (Dr.rer.nat.)

Wien, 2016

Studienkennzahl lt. Studienblatt / degree programme code as it appears on the student record sheet:	A 796 605 413
Dissertationsgebiet lt. Studienblatt / field of study as it appears on the student record sheet:	Astronomie
Betreut von / Supervisor:	ao. Univ.-Prof. Mag. Dr. Franz Kerschbaum Ass.Prof. Dr. Josef Hron

Acknowledgments

Doing a PhD is a school of Science, and of life. Hereafter I would like to thank all the people who made the accomplishment of this thesis possible in those years.

First of all, I would like to express my deep gratitude to my supervisor Josef Hron, who, welcoming me in the AGB research group, gave me the possibility to grow so much professionally and personally. I learn a lot from you, thank you to be always available in explaining me the physics of the AGB stars and of interferometry, for our discussions, and for all the support and flexibility you gave me over the last year. I think that I gained a little bit of your trust, and this is very important to me! And of course thanks for sharing the passion for volleyball... and sweets! :) Thanks to my second supervisor Franz Kerschbaum, who has always been supportive and gave me very helpful inputs for my research.

Thanks to Claudia Paladini, our talks and confrontations helped me to grow and develop many skills. Thanks for your availability for email and Skype discussions. And for pushing me to go beyond my limits. A special thought goes to Thomas Posch, who always gave me his trust, encouraged me, was available for discussion, helpful comments and answered my questions in a very detailed way. Your broad and deep knowledge and culture are very inspiring to me! Not to mention the shared passion for public outreach and philosophy. Thank you Thomas!

I would like to thank also the many great scientists and collaborators I met during those years of PhD, below listed in alphabetical order, who gave me very useful inputs for my research. Kjell Eriksson, Susanne Höfner, Maria Lugaro, Paola Marigo, and all the people from our Vienna research group: Bernard Aringer, Magdalena Brunner, Thomas Lebzelter, Claire Lykou, Andreas Mayer, Marco Mecina, Christine Nicholls, Walter Nowotny. Thanks to the PhD students and postdocs from the Institute, who made these times full of happy shared moments: Carla Baldovin, Ines Brott, Oliver Czoske, Odysseas Dionatos, Lucas Ellmeier, Josefa Großschedl, Alvaro Hacar Gonzalez, Jan Forbich, Daniela Klotz, Rainer Koehler, Karolina Kubiak, Ulrike Kuchner, Theresa Lüftinger, Stefan Meingast, Paula Teixeira, Miguel Verdugo. The secretary and other members of the institute contributed to made my days always nice and productive. A big thanks goes also to all my friends throughout Europe - especially those closest to me in the last period. Your warmness, talks, support and all the fun helped me to relax from the hard work, and to reach one of my dreams which is this thesis. You are too many to be written all here, but if you are reading this, I am sure that you know the special place you have for

me. Though, I cannot avoid to mention some of my Viennese friends: Julia, who helped me in translating the abstract in german, and was my very first friend in Vienna: thanks for our talks, skiing, dinners, shared moments: you are a great friend to me Julietta! Mari your caring is something I will never forget, "Anita"! And Claudia: sharing is caring, and our deep conversations sustained me everyday.

And, last but not least, my biggest gratitude goes to my brightest inspiring star: my dad. You always believed in me, giving me support, trust, teachings. Thanks for providing me the opportunity to study, grow, experience a greater reality, and for having nurtured in me the intellectual curiosity for Science and the Universe, since the young age. Thank you for making my education always your priority, and for teaching me, through your example, what it means the hard work, the sense of responsibility, of justice, and of duty. Your unconditional love will last forever, because I can feel your daily support. Thank you for having always reminded me how strong I am: today I am who I am because of you. I will be forever grateful for all that you are to me. Thank you mum for always listening and understanding, our chats are a precious treasure to me. I love you both up to the stars and beyond. Thanks to my brothers for all your love: you as well teached me how to grow, and you are two high reference points to me. Thanks to my nice, which is as my little sister, to be exactly as you are; and to my nephews, who inspire me to discover what is the magic of wonder.

The work presented in this thesis was supported by the Austrian Science Fund FWF under project number AP23006, and by the Abschlussstipendium der Universität Wien.

Astronomy and Astrophysics
Editor in Chief: T. Forveille

T. Forveille
Astronomy & Astrophysics
Observatoire de Paris
61, avenue de l'Observatoire
75014 Paris, France

Tel.: 33 0(1) 43 29 05 41
Fax: 33 0(1) 43 29 05 57
e-mail: aanda.paris@obspm.fr
Web: http://www.aanda.org

merging
Annales d'Astrophysique
Arkiv for Astronomi
Bulletin of the Astronomical Institutes of the Netherlands
Bulletin Astronomique
Journal des Observateurs
Zeitschrift fur Astrophysik
Bulletin of the Astronomical Institutes of Czechoslovakia

Paris, August 23, 2016

Reprint Permission

Material:
Article by Rau et al. 2015, A&A, 583, A106

To be used in:
PhD thesis, University of Vienna

Permission granted to:
Gioia Rau
Institut für Astrophysik
Department of Astrophysics, University of Vienna
Tuerkenschanzstr. 17
A-1180 Vienna / Austria
mail to: gioia.rau@univie.ac.at

I hold copyright on the material referred to above, and hereby grant permission for its use as requested herewith. The credit should be given as follows:
Credit: Author, A&A, vol, page, year, reproduced with permission © ESO.

Thierry Forveille
A&A Editor-in-Chief

Sponsored by Argentina, Austria, Belgium, Brazil, Chile, Czech Republic, Denmark, Estonia, Finland, France, Germany, Greece, Hungary, Italy, Netherlands, Poland, Portugal, Slovak Republic, Spain, Sweden, and Switzerland.
Produced and distributed by EDP Sciences for ESO.

A mio padre, la mia Stella preferita, e a mia madre.

"Fatti non foste per viver come bruti,
ma per seguire virtute e canoscenza."
Dante Alighieri - Inferno, Canto XXVI

Abstract

A short but intriguing stage in the evolution of low to intermediate ($\sim$ 0.8 to $\sim$ 8 $\odot$) mass stars, the Asymptotic Giant Branch (AGB) is populated by stars with extended, complex, shell-like structured atmospheres.

Modelling giant star atmospheres remains a challenging task in contemporary astronomy. Carbon-rich AGB star atmospheres have been widely studied by several authors, who compared observations with hydrostatic and dynamic atmospheric models but rarely in a systematic way with multi-facility observations. The methodical testing of models with multi-technique observations has in fact emerged as the only adequate way to provide strong constraints on models.

The study of C-enriched AGB stars atmospheres, is the main purpose of this thesis. Advanced state-of-the-art dynamic and hydrostatic model atmospheres have been compared with new and archive mid-infrared interferometric MIDI observations and literature spectro-photometric data. In total eight C-rich stars have been investigated: RU Vir, R Lep, R Vol, Y Pav, AQ Sgr, U Hya, X TrA and R For.

The first part of this monograph consists of three introductory chapters, which present general background on AGB stars, on the types of models used to interpret the data, and on the main observational technique used in this work: optical interferometry.

Chapter 4 focuses on the study of the atmosphere of RU Vir. Hydrostatic, geometric and dynamic models have been fit to the observations. The dynamic model Spectral Energy Distributions (SED) were first fitted to the literature data, obtaining one best-fitting model; then, for all the stellar pulsational phases of this specific model, the interferometric intensity profiles and visibilities were computed. This method was adopted for the whole thesis. Showing an SED which agrees well with the models only betwee 2 and 14 μm, this star turned out to be a peculiar, puzzling Mira.

This research was extended to a set of carbon-enriched Mira, Semi-regular and Irregular variables, in Chapter 5. Characteristics of the atmospheres of these stars, such as their extension, dust properties and mass loss, together with further constraints on

the models, are given. Stellar parameters are derived and the stars are located in in Hertzsprung-Russell diagram, with results showing a good accord between the main parameters obtained from the modelling and evolutionary computations of the thermally pulsating AGB.

A substantial amount of effort was devoted to the data-reduction, quality checks, and analysis of Very Large Telescope Interferometer/MIDI data, part of a ESO Large Program of observations. The scientific results of this program are given in Chapter 6.

Even though encouraging results regarding the dynamic models are obtained in this thesis, some differences between SEDs and interferometric studies persist. Chapter 7 investigates, from an observational standpoint, if removing the assumption of the small particle limit (SPL) could improve the agreement between models and observations. A test-case star, R Lep, is used, and its measurements are compared to the newly produced non-SPL model from the Uppsala group. Achieved improvements and remaining differences are described.

In Chapter 8 the preliminary dynamic modelling of the spectro-photometric and interferometric MIDI data of R For is presented. Finally, Chapter 9 summarizes conclusions and future prospects on this study.

Zusammenfassung

Das AGB (Asymptotic Giant Branch) Stadium ist eine kurze aber faszinierende Phase in der Entwicklung von Sternen mit niedriger bis mittlerer Masse (0.8 bis 8 Sonnenmassen). AGB Sterne sind durch eine ausgedehnte Atmosphäre mit einer schalenartigen Struktur gekennzeichnet. Das Modellieren solcher Atmosphären stellt nach wie vor eine Herausforderung in der gegenwärtigen Astronomie dar. Kohlenstoffreiche AGB-Stern Atmosphären wurden bereits in verschiedenen Arbeiten erforscht, welche hydrostatische und dynamische Modelle von Atmosphären mit Beobachtungsdaten verglichen haben, jedoch kaum auf systematische Art und Weise und durch Verwendung von Messungen mit verschiedensten Beobachtungstechniken. Ein derartiges methodisches Testen erweist sich tatsächlich als beste Möglichkeit, zur Einschränkung und Verbesserung der Modelle. Ziel dieser Doktorarbeit ist die Analyse von C-angereicherten Atmosphären von AGB-Sternen. Hochmoderne dynamische und hydrostatische Modellatmosphären wurden mit neuen und vorhandenen interferometrischen Beobachtungen im mittleren Infrarot (MIDI Instrument) sowie spektroskopischen und photometrischen Daten verglichen.

Insgesamt wurden acht kohlenstoffreiche Sterne erforscht: RU Vir, R Lep, R Vol, Y Pav, AQ Sgr, U Hya, X TrA und R For. Der erste Teil dieser Arbeit besteht aus drei einleitenden Kapiteln, welche sich im Allgemeinen mit AGB Sterne befassen und die verschiedenen Atmosphärenmodelle sowie die wichtigste Beobachtungstechnik die in dieser Arbeit angewendet wurde, nämlich die optische Interferometrie, beschreiben.

In Kapitel vier wird die Atmosphäre des Sternes RU Vir studiert, welche mit Hilfe von hydrostatischen, geometrischen und dynamischen Modellen analysiert wurde. Die spektralen Energieverteilungen (SED, Spectral Energy Distributions) der dynamischen Modelle wurden erstmals mit Literaturdaten angeglichen, sodass ein optimales Modell gefunden werden konnte. Danach wurden die interferometrischen Messgrößen für alle Pulsationsphasen dieses spezifischen Modells berechnet. Diese Methode wurde für die gesamte Doktorarbeit angewendet. RU Vir zeigte eine SED welche nur zwischen 2 und 14 μm gut mit dem Modell übereinstimmt und auch die MIDI Daten konnten nicht gut

reproduziert werden. Der Stern erwies sich somit als etwas rätselhafter Mira.

Die Untersuchungen wurden in Kapitel fünf auf eine Reihe von kohlestoffreichen veränderlichen Sternen (Mira, Semi-reguläre und Irreguläre Variable) ausgeweitet. Die Eigenschaften der Atmosphären dieser Sterne wie etwa die Ausdehnung, die Staubeigenschaften und der Masseverlust sowie weitere Modellgrößen werden hier beschrieben. Stellare Parameter werden hergeleitet und die Sterne werden im Hertzsprung-Russell Diagramm lokalisiert. Die Resultate zeigen eine gute Übereinstimmung zwischen den Fundamentalparametern, welche durch das Erstellen des Modells erzielt wurden, und Entwicklungsrechnungen für thermisch pulsierende AGB Sterne. Die Datenreduktion, Qualitäts-Überprüfung und Analyse von „Very Large Telescope“ Interferometer/ MIDI Daten, die als Teil eines „ESO Large Programs“ erhalten wurden, machten einen beträchtlichen Teil des Arbeitsaufwandes der vorliegenden Doktorarbeit aus. Die wissenschaftlichen Ergebnisse des oben genannten Programmes werden im Kapitel sechs dargelegt. Trotz der ermutigenden Ergebnisse bezüglich dynamischer Modelle, die durch diese Forschungsarbeit erzielt werden konnten, bleiben Unterschiede zwischen Beobachtungen und Modellen bestehen. Diese betreffen sowohl die SEDs als auch die interferometrischen Observablen. In Kapitel sieben wird an Hand eines ersten Testfalls untersucht, ob die in den dynamischen Modellen verwendete Näherung kleiner Staubteilchen (SPL, small particle limit) die Übereinstimmung zwischen Modellen und Beobachtungen beeinflusst und ob durch das Weglassen dieser Annahme eine bessere Übereinstimmung erzielt werden könnte. Die Messwerte des Teststerns, R Lep werden mit einem neu gerechneten „non-SPL model“ der Uppsala Guppe verglichen. Verbesserungen sowie bestehende Unterschiede werden infolge beschrieben. Der ebenfalls im Rahmen der Dissertation durchgeführte Vergleich von dynamischen Modellen mit den der spektro-photometrischen und interferometrischen MIDI Daten des Sternes R For wird in Kapitel acht vorgestellt. Schlussfolgerungen und Zukunftsprospektiven zu dieser Arbeit finden sich in den Kapitel neun.

Contents

List of Figures

List of Tables

Symbols

Table 1: Symbol description.

Symbol	Meaning	Unit
Variables		
AM	Airmass	dimensionless
B_p	Projected baseline	m
C/O	Carbon-oxygen ratio	dimensionless
d	Distance	pc
I	Intensity	$\mathrm{W \cdot m^{-2} \cdot ster^{-1}}$
L	Luminosity	$\mathrm{L_\odot}$
M	Mass	$\mathrm{M_\odot}$
$\dot{\mathrm{M}}$	Mass loss rate	$\mathrm{M_\odot \cdot yr^{-1}}$
P	Period	days
PA	Position angle	degree
R	Radius	$\mathrm{R_\odot}$
R_{Ross}	Rosseland radius	$\mathrm{R_\odot}$
T_{eff}	Effective temperature	K
u, v	Spatial frequencies	$\mathrm{arcsec^{-1}}$
V	Visibility	dimensionless
α, δ	Sky coordinates	degree, mas
ϕ	Phase	radians
λ	Wavelength	cm, μm
θ	Diameter	mas
χ^2_{red}	Reduced chi-square	dimensionless
Units		
AU	Astronomical units	1.496×10^{11} m
Jy	Flux density	$10^{-26}\ \mathrm{W \cdot m^{-2} \cdot Hz^{-1}}$
$L_\odot$	Solar luminosity	$3.846 \times 10^{26}\,\mathrm{W}$
$M_\odot$	Solar mass	$1.989 \times 10^{30}\,\mathrm{kg}$

...

Table 1: Symbol description.

Symbol	Meaning	Unit
pc	Parsec	$3.086 \times 10^{16}\,\mathrm{m}$
$R_\odot$	Solar radius	$6.963 \times 10^{8}\,\mathrm{m}$
Constants		
c	Speed of light	$2.998 \times 10^{8}\ \mathrm{m \cdot s^{-1}}$
k	Stefan-Boltzmann constant	$5.670 \times 10^{-8}\ \mathrm{W \cdot m^{-2} \cdot K^{-4}}$

Abbreviations

AGB - Asymptotic giant branch
ALMA - Atacama Large Millimiter/submillimiter Array
amC - amorphous carbon
AT - Auxiliary telescope
CSE - Circumstellar envelope
C-rich - Carbon-rich
COMA - Copenhagen Opacities for Model Atmospheres
DARWIN - Dynamic Atmosphere & Radiation-driven Wind models based on Implicit Numerics
DOF - Degree of freedom
DMA - Dynamic Model Atmospheres
E-ELT - European Extremely Large Telescope
ESO - European Southern observatory
EWS - Expert work station
FOV - Field of view
FWHM - Full width half maximum
H-R - Hertzsprung-Russell
IR - Infrared
IRAS - InfraRed Astronomical Satellite
ISM - Interstellar medium
ISO - Infrared Space Observatory
Lb - Irregular variable
LP - Large Program
LTE - Local Thermal Equilibrium
MIA - MIDI Interactive Analysis
MIDI - Mid-infrared interferometric instrument
MOD - More Of Dusty

OPD - Optical Path Difference
OS - Opacity Sampling
O-rich - Oxygen-rich
PA - Position angle
RT - Radiative Transfer
SED - Spectral energy distribution
SiC - Silicon Carbide
SPL - Small Particle Limit
SRb - Semiregular variable
TP - Thermal Pulse
TDU - Third Dredge-Up
UD - Uniform Disk
UT - Unit telescope
VLT - Very large telescope
VLTI - Very Large Telescope Interferometer

List of Publications

This thesis is based on the following papers:

- **Refereed journal papers:**
  I
  Title: *Modelling the atmosphere of the carbon-rich Mira RU Vir*
  Authors: **G. Rau**, C. Paladini, J. Hron, B. Aringer, M. A. T. Groenewegen, and W. Nowotny
  Year: 2015
  Journal: A&A, 583, A106

  III
  Title: *The carbon stars adventure - Observations and modelling of a set of C-rich AGB stars*
  Authors: **G. Rau**, J. Hron, C. Paladini, B. Aringer, K. Eriksson, P. Marigo, W. Nowotny and R. Grellmann
  Year: 2016
  Journal: submitted to A&A on the 18^{th} of July 2016

  II
  Title: *The VLTI/MIDI view on the inner mass loss of evolved stars from the Herschel MESS sample*
  Authors: C. Paladini, D. Klotz, S. Sacuto, E. Lagadec, M. Wittkowski, J. Hron, A. Jorissen, A. Richichi, M. A. T. Groenewegen, F. Kerschbaum, T. Verhoelst, **G. Rau**, H. Olofsson, and R. Zhao-Geisler
  Year: 2015
  Journal: submitted to A&A on the 19^{th} of August 2015

IV

Title: *Comparison of spectro- photometric- and interferometric-observations with dynamic model atmospheres, with and without the small particle limit approximation - The observational test case of R Lep*

Authors: **G. Rau**, K. Eriksson, B. Aringer, J. Hron, and C. Paladini

Year: 2016

Journal: A&A, in prep.

V

Title: *MIDI Observations of R For compared with dynamic model atmospheres*

Authors: C. Paladini, **G. Rau** et al.

Year: 2016

Journal: A&A, in prep.

- **Conference Proceedings:**

I

Title: *Into the Modelling of RU Vir*

Authors: **G. Rau**; J. Hron, C. Paladini, K. Eriksson, B. Aringer, M. A. T. Groenewegen, and M. Mecina

Year: 2014

Journal: 2015 ASPC, 497, 137

II

Title: *Modelling a set of C-rich AGB stars: the case of RU Vir and more*

Authors: **G. Rau**, C. Paladini, J. Hron, B. Aringer, K. Eriksson, and M. A. T. Groenewegen

Year: 2015

Journal: MemSAIt, 87, 260

III

Title: *VLTI/MIDI Large Program: AGB Stars at Different Spatial Scales*

Authors: C. Paladini, D. Klotz, S. Sacuto, E. Lagadec, M. Wittkowski, J. Hron, A. Jorissen, A. Richichi, M. A. T. Groenewegen, F. Kerschbaum, T. Verhoelst, **G. Rau**, H. Olofsson, and R. Zhao-Geisler

Year: 2014
Journal: 2015 ASPC, 497, 97

IV
Title: *The carbon star adventure: modelling atmospheres of a set of C-rich AGB stars*
Authors: **G. Rau**, C. Paladini, J. Hron, B. Aringer, K. Eriksson and M. A. T. Groenewegen
Year: 2015
Journal: IAU General Assembly, 22:2254798.

Chapter 1

Introduction to the AGB stars

Our life, human life, is the gift wherewith all the scientific discoveries in the human history were made, until now. And, one of the most fascinating facts is that the human beings are made of matter coming from the stars. Indeed, the production of the heaviest elements of our body, as oxygen, carbon or iron, was possible only inside the stars. Among these, the Asymptotic Giant Branch (AGB) stars represent one of the most important producers of those elements. Furthermore, an AGB star's atmosphere is the crucial interface between the interior and the Inter Stellar Medium (ISM). This thesis is devoted to this: the study of carbon-rich AGB stars atmospheres.

1.1 What is an AGB star?

Stars with initial masses ranging from ~ 0.8 to ~ 8.0 $M_{\odot}$ (Habing and Olofsson, 2003) will undergo, late in their evolution, the AGB phase. This part of the stellar evolution is characterized by luminous, very cool extended objects, being gigantic stars. Figure 1.1 shows how stars with different initial masses will experience different evolutionary paths in the Hertzsprung–Russell diagram. These giants will end their life as white dwarfs, shrouded by planetary nebulae, after having ejected all the mass around the dense carbon-oxygen core.

1.1.1 AGB star structure

Four main parts can be recognized in the structure of an AGB star, from the center outward:

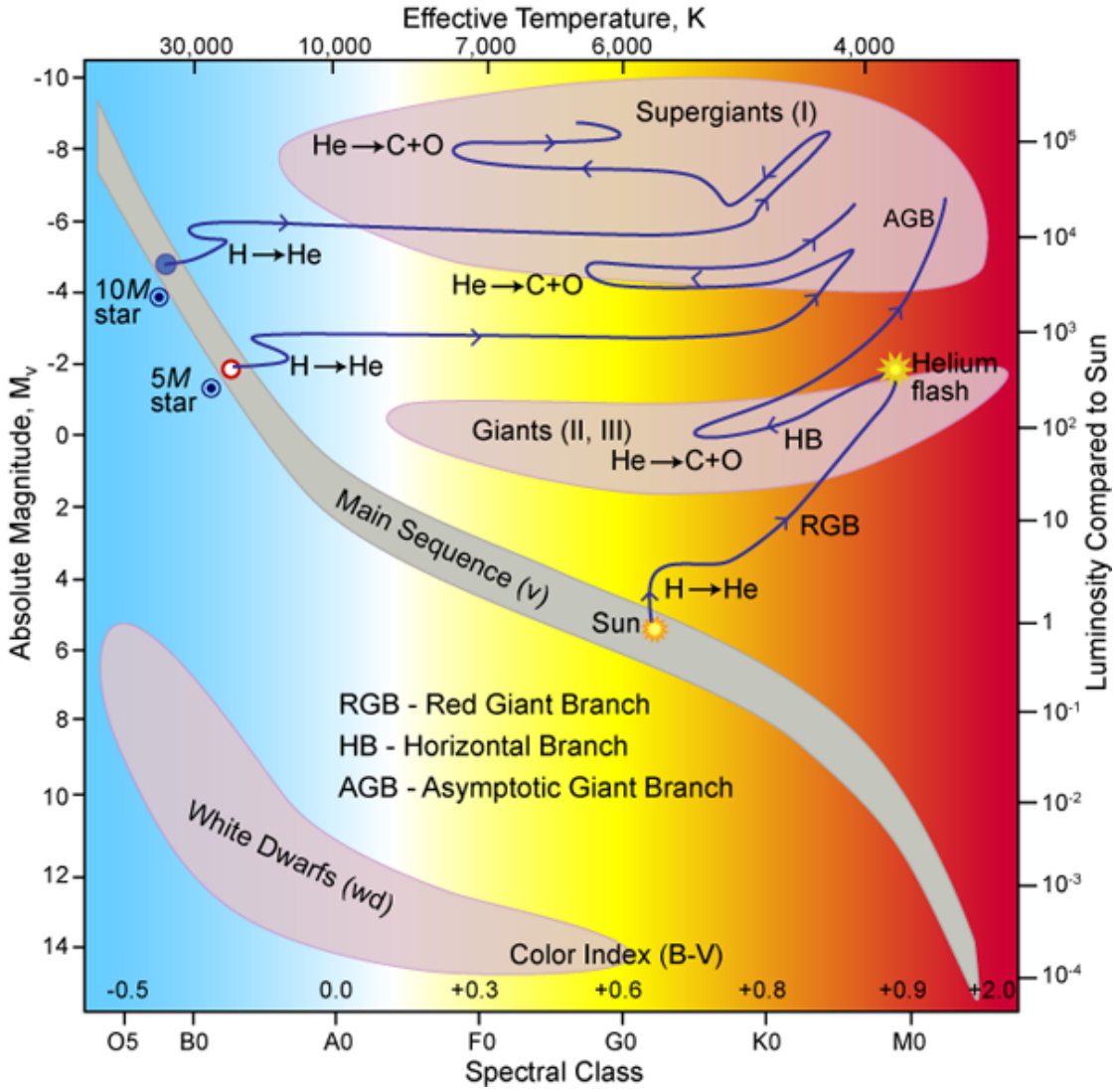

Figure 1.1: The Hertzsprung-Russell diagram, organizes stars in terms of their luminosity and surface temperature (effective temperature). Three different evolutionary tracks are represented by the three blue lines, for stars of 1, 5 and 10 $M_{\odot}$ as they go through H-burning, He-burning, and beyond. Figure credit: Robert Hollow `http://www.atnf.csiro.au/outreach/education/senior/astrophysics/stellarevolution_hrintro.html`.

1. *Dense core*: small and very hot (up to $\sim 10^8$ K), in which heavy elements are produced by nucleosynthesis.

2. *Stellar envelope*: less dense, hot, large convective stellar envelope, where nucleosynthesis products are brought to the surface.

3. *Atmosphere*: tenuous and warm stellar atmosphere, where molecules can form.

4. *Circumstellar envelope*: large, extended and cool circumstellar envelope where dust forms and where the dust-driven stellar wind will moves outwards at a typical speed of a few km/s.

This structure is schematically drawn in Fig. 1.2.

1.1.2 AGB star evolution

When the star is located at the horizontal branch in the HR diagram, is a giant, has finished the H in its core, and started to burn He into C and O via the 3α process. When this process has finished, the He-burning zone moves outward, and the core of C+O contracts until it has a very high density, approximately the same of a white dwarf. The contraction of the core and the expansion of the envelope lead to a rapid increase in luminosity. This is the start of the **Early-AGB**: the stage at which He burns in a shell, producing most of the energy. At some point, the envelope gets pulsationally unstable, with a time-scale in the order of ~ 100 days.

Then, when the star reaches luminosity $\sim$ 3000 $L_\odot$, it becomes able to burn both He and H in shells. Periodically, the He produced by H burning is accreted onto the He shell, and "helium shell flashes" occur. In this way the mass of the central core is increased by the "flashes" of the thin He-layer around the core into C, and a convective intershell develops. These short moments (timescales of $\sim$ several tens of years) are called "thermal pulses", and the object undergoes a luminosity modulation.

The **Thermally Pulsing-AGB** therefore, is the stage of the AGB life, at which He and H are intermittently burning. At the end of the early-AGB phase, the H-burning and He-burning shells are thin and close together, which combined with the high temperature dependence of the He-burning reactions, makes the environment thermally unstable. As the star ascends the AGB, the burning of H and He will turn into a process called *thermal pulse cycle*. However, in very massive stars (those with $M > 8\ M_\odot$) the temperature in the core will be high enough for C to ignite before the thermal pulses, so they do not undergo this phase. The thermal instability grows in strength during the AGB evolution and the

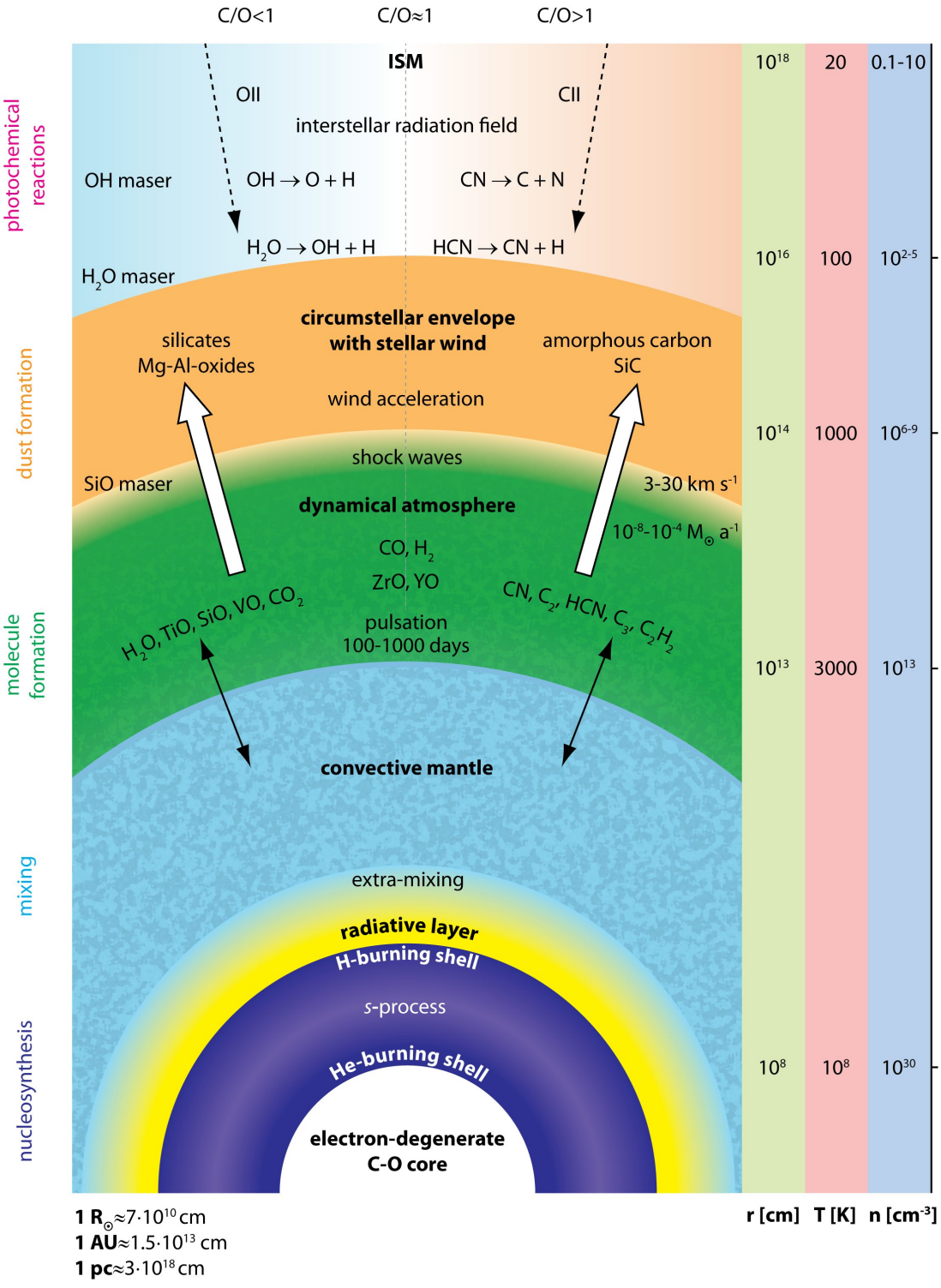

Figure 1.2: Simplified view of an AGB star structure. Some processes are underlined, at different scales in the star. Figure credit: Lederer (2009).

He-shell luminosity becomes larger after each successive pulse. The luminosity generated by the He shell grows after each pulse, reaching up to 10^8 $L_\odot$. A star undergoing the AGB can experience many thermal pulses. The consequences of the pulses are relevant to both the chemistry and the structure of the stars, as explained in the following section.

1.1.3 The origin of Carbon-rich stars: the Third Dredge-up

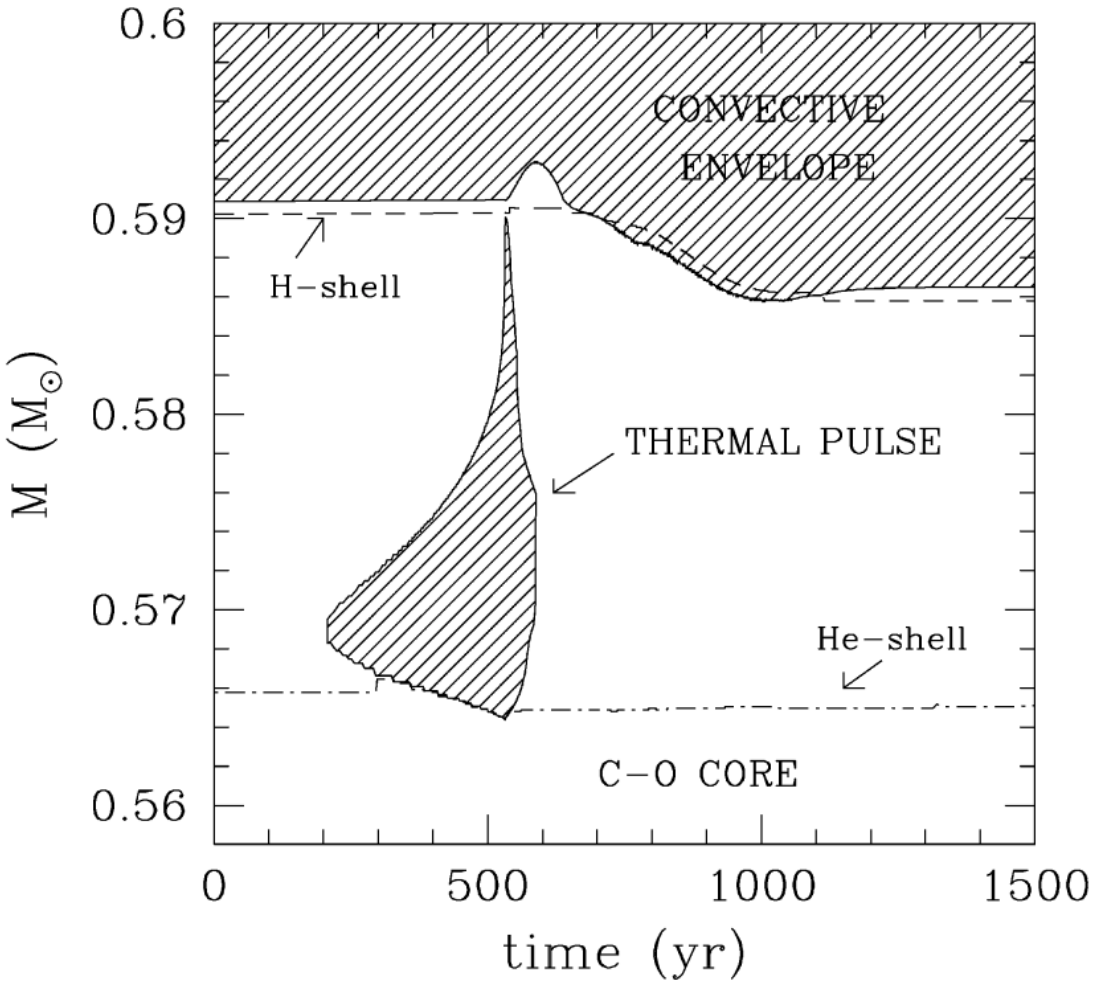

Figure 1.3: Schematic view of the process of the third dredge-up. The dashed area shows a convective episode, in a model of mass $M = 2\ M_\odot$, $Z = 0.015$ (metallicity) and $Y = 0.275$ (fraction of the mass that is composed of helium), during and after the tenth thermal pulse. In about 200 years, the external convection penetrates inward generating the so-called third dredge-up. Figure credit: Straniero et al. (2006).

An important process, fundamental for the creation of C-rich stars, happening during

a thermal pulse is the dredge-up: when convection reaches the layers where nuclear processes occured, it can bring material to the stellar surface. This matter is enriched by products of nuclear-burning, especially "new" carbon. If this process can last long enough, the abundance of C in the atmosphere will exceed the one of O. This is also called **third dredge-up** (TDU), because it is the third important dredge-up process for an intermediate-mass star[1]. This process produces the stars to which this thesis is dedicated: the carbon-rich AGB stars (see Sect. 1.2). Also, knowing that the molecule CO is the most strongly bound one in the atmosphere of cool stars, if $C/O > 1$, then all the oxygen is locked in CO, and surplus C-atoms are available to form molecules such as C_2 and CN. The spectral appearance of C-stars is in fact dominated by bands of CN, HCN, CO, C_2H_2, C_2, C_3 and other molecules and dust species.

The process of the TDU was discovered at the same time by Iben (1975) and Sugimoto and Nomoto (1975). Figure 1.3 illustrates a schematic view of this process, and will be described below. Following Iben and Renzini (1981), 4 phases can be detected in a thermal-pulse cycle. An *on-phase*, when the He-shell is burning brightly, producing up to ~ 100 million $L_\odot$ and an energy that can not be transported just by radiation alone, leading to the development of a convection zone in the He-rich intershell, exactly above the He-burning region called "intershell convective zone" driven by the thermal pulse. The composition of this intershell convective zone is mostly ^{4}He ($\sim 80-75\%$) and ^{12}C ($\sim 20-25\%$), and it will survive for ~ 100 years, depending on the core-mass size. Then, the He-shell burning dies down, and the energy released by the flash drives the expansion of the intershell region, which extinguishes the H-shell that is now pushed to very low temperatures and densities (*"power-down"* phase). Afterwards, the *third dredge-up* phase comes: the energy released by the He-shell flash escapes from the stellar core into the convective envelope, causing the convection to penetrate inward in response to the increasing luminosity coming out of the core. Then, the convective envelope reaches across the extinct H-shell and into what was the intershell convective zone. Thus the convection, named "third dredge-up", succeeds in mixing material to the surface that is thus enriched in ^{12}C, ^{4}He, ^{22}Ne and other products (s-process elements), and this phase lasts for ~ 100 years. One last phase called *interpulse* can be identified: the star contracts and the H-shell is re-ignited, providing most of the surface luminosity for the next 10^4-10^5 years.

The efficiency of the TDU process can be estimated by the so-called "dredge-up parameter" λ, defined as follows:

[1]The second for low-mass stars.

$$\lambda = \Delta M_{DU}/\Delta M_c, \tag{1.1}$$

where ΔM_{DU} is the total mass dredged-up by the convective envelope during one thermal-pulse and ΔM_c is the mass through which the H-shell has moved during the interpulse-phase. The biggest difficulty encountered in estimating λ is due to the uncertainties in calculating the amount of convective overshoot occurring at the convective boundaries. E.g. Karakas et al. (2002) shown that the parameter λ reaches values close to one (0.9) for stars of intermediate mass. A value of $\lambda = 1$ would mean that the core is not growing.

In more massive stars there is another process competing with the just described process of the TDU: C will burn into N before the stellar surface is reached, leading to the so called **hot bottom burning**. The bottom of the convective envelope reaches temperatures high enough for nuclear processing via the CNO cycle, i.e the convective envelope reaches into the top of the H-burning shell.

1.2 The Carbon-rich AGB stars

In addition to be interesting celestial objects by themselves, AGB stars are prominent as member of stellar populations. This is the reason for their importance in population synthesis and models, where photometric properties from those high-luminosity stars are needed (Aringer et al., 2009; Marigo and Girardi, 2007; Marigo et al., 2008). Thus, they are an important tool for extragalactic studies.

In particular, carbon-rich AGB stars are the most important contributors to the total flux emitted by galaxies containing populations of (young/)intermediate ages. This Section is inspired by the reviews on carbon stars by Wallerstein and Knapp (1998) and Lloyd Evans (2010).

1.2.1 A bit of history

Father Angelo Secchi, in 1868, was the first astronomer ever to recognize carbon stars as a new spectral type, introducing them as type IV in his pioneering stellar spectra classification. The fourth class contains red stars that show, in their spectra, bands and lines of carbon. The prototype of carbon stars that he found was 19 Psc.

In the middle of the last century, only $\sim$ 60 years ago, the carbon stars were considered still an "enigma" (see e.g. Bidelman, 1956). Around that time studies on C-rich

objects focused on their spectral type, radial velocities, proper motion and spectra. Key molecules such as CH, CN, C_2 were recognized, together with enhanced lines of light element as Li (McKellar, 1940, on WZ Cassiopeiae), or heavy elements such as Tc (Merrill, 1952). The identification of the latter two, Li and Tc, was essential to stellar nucleosynthesis, showing that there is nucleosynthetic activity inside C-stars [2]. ^{13}C was also identified, giving in this way the first chance to obtain an isotopic ratio outside the Solar System.

Stars are classified as: *Semi-regular*, showing noticeable periodicity in their light changes, accompanied or sometimes interrupted by various irregularities, with periods ranging from 20 to more than 2000 days; *irregular* with no defined periodicity; *Mira* variables, with periods P$\sim$ $300 - 500$ days and large amplitude of variability in the visual, and pulsation in the fundamental mode (Samus et al., 2009b).

Only with the advent of IR instruments, in the 1970s, it was possible to reveal that many carbon stars were extremely bright in the near-IR. Of fundamental importance was the low resolution spectrometer on board the *IRAS* satellite (Olnon et al., 1986), able to observe for the first time bright and unsuspected C-stars by the presence of the emission feature of silicon carbide (from now on: SiC) at $\sim$ 11.3 μm, arising in circumstellar material (Lloyd Evans, 2010). Furthermore, with IR and millimeter instruments the investigation of mass loss from cool stars began. It was finally possible to investigate the infrared emission from circumstellar dust, the vibrational-rotational and rotational-vibrational lines of diverse molecular species and the scattering of optical and near-IR light from the circumstellar dust.

In the last decades, interferometric measurements of C-stars have caught the attention of the stellar astrophysics community. This powerful technique is undergoing recently many developments: in the optical with the Very Large Telescope Interferometer (VLTI), and in the millimeter/sub-millimeter with ALMA (Atacama Large Millimiter/sub-millimeter Array). Although being largely studied, many AGB stars are still under investigation to properly understand processes as the mass-loss or dust formation, and precious opportunities to observe them will be developed in the near future, with the second generation instruments at VLTI, as MATISSE (Lopez et al., 2006) and GRAVITY (Eisenhauer et al., 2008). Also, spectroscopic measurements with instruments at the future largest telescope in the world E-ELT (European Extremely Large Telescope), like METIS (e.g. Hron et al., 2015a), will open exciting perspectives to enrich

[2]Proton capture can destroy ^{6}Li and ^{7}Li at T$\approx 2 \cdot 10^6$ K, so they can not survive in stars that later become C-stars, such as stars on the main sequence or red giants. Also ^{99}Tc is the isotope that can be most synthesized in stars; its half-life is $\approx 2 \cdot 10^5$ yr. Both those species are essential to explain how nucleosynthesis is active inside C-stars (Wallerstein and Knapp, 1998).

and enlarge the knowledge on the AGB stars field and galactic evolution.

1.2.2 Dust in carbon-rich AGB stars

Carbon-enriched AGB stars are surrounded by a carbon-rich dusty envelope made of amorphous carbon (amC), featureless in the spectra, and SiC dust which can be identified by its typical SED emission feature at $\sim$ 11.3 μm (Hackwell, 1972; Treffers and Cohen, 1974; Goebel et al., 1980).

The study of the formation process of SiC grains is important to reveal the structure, size and chemical composition of the dust grains formed in circumstellar envelopes of C-rich stars. Historically, SiC has been predicted to exists in the atmosphere of C-rich stars based on chemical equilibrium calculations by Gilman (1969) and Friedman (1969). Hackwell (1972) discovered the characteristic 11.3 μm feature and Goebel et al. (1980) identified the observed feature with that of SiC grains comparing the laboratory spectra of powder samples measured by Dorschner et al. (1977).

Cosmic dust, after its ejection by stellar winds into the interstellar medium, can be trapped in meteorites that are now recovered in the Solar System (Hedrosa et al., 2013). The first presolar grains, diamond and SiC, were physically and chemically isolated from meteorites by Ed Anders and co-workers at the University of Chicago in the 1980s (Hoppe et al., 2010; Bernatowicz et al., 1987; Lewis et al., 1987). Isotopic anomalies of presolar SiC grains discovered in carbonaceous meteorites strongly support the formation of SiC grains in the envelope of C-rich AGB stars (Virag et al., 1992; Lewis et al., 1994). However, as Kozasa et al. (1996) pointed out, the origin of the large presolar SiC grains in the meteorites still remains unexplained. Common sizes of presolar grains vary from 0.3 to 3 μm (Amari et al., 1994), but also very large grains up to 26 μm are present (e.g. Ávila et al., 2013). Such large grains can probably only be formed during extreme mass-loss phases or in clumps of high density (Bernatowicz et al., 1996).[3]

Is was suspected by Kozasa et al. (1996) that the nucleation of SiC grains always precedes the one of carbon grains. One first attempt of formulation of the SiC grains' formation process around carbon-rich stars was done by Gauger et al. (1990). Recently Yasuda and Kozasa (2012) included a theory on the formation process of SiC in hydrodynamic models, but their predictions on the amount and size distribution of SiC dust grains around C-rich AGB stars are very model dependent and need to be observationally verified.

[3]It is interesting to note that SiC on Earth can have several practical optical ground/space applications. E.g. the Herschel primary mirror is composed by segments formed by isostatic pressing and sintering of SiC (Bougoin and Deny, 2004; Pilbratt et al., 2010).

In particular, questions like where in the star does the SiC form, how it is spatially distributed, and how the SiC abundance changes in the different layers, need to be investigated in greater details. It is necessary to cover a wide range of stellar and dust parameters in order to reveal the grain-size distribution and the amount of SiC dust around C-rich AGB stars, that could heavily depend on C/O ratio as well as on other stellar parameters (Yasuda and Kozasa, 2012). Moreover, so far, there is no spectroscopic evidence for SiC grains in the diffuse interstellar medium. This fact is not yet satisfactorily explained, although core-mantle, inhomogeneous, or very large grains may offer a solution (Ossenkopf et al., 1992; Kozasa et al., 1996; Andersen, 2007).

There are two main ways to tackle the above mentioned unresolved questions: (i) investigating the distinctive 11.3 μm feature in astronomical spectra and (ii) examining the presolar grains found in meteorites.

In the first case, we know that the emission feature around 11.3 μm is due to SiC grains condensed in the circumstellar envelopes of carbon stars. This emission feature can be used as a diagnostic tool of the dust grains' formation process. The strength of the 11.3 μm feature indeed well reflects the difference in the mass-loss rate and the evolutionary stage. However, the behavior of the emission feature, due to SiC's infrared vibrational modes, heavily depends on the size distribution and the structure of dust grains. Thus, the 11.3 μm emission feature strength does not only reflect the abundance of SiC condensed in the envelopes. Furthermore, the emission feature is very weak or absent in the spectra of extreme carbon stars, probably due to self-absorption, within optically very thick circumstellar envelope (Kozasa et al., 1996).

In the second case, isotopic analysis of meteoritic SiC makes use of the information that may be recorded in the grains, offering a tool to explore the structure and evolution of our galaxy. Analysis of SiC grains found in the Murchison meteorite (Hoppe et al., 1994; Swan et al., 1989) revealed that isotopic ratios of carbon and silicon are non-solar.

Thompson et al. (2006) underline how, being the dust parameters closely linked to each other and to stellar parameters, there exists a large free parameter space. This implies that it is not possible to determine the parameters using exclusively optical/IR spectra. Interferometric studies provide the possibility to examine the properties of SiC from the stars' upper photosphere up to the envelope, resolving different atmospheric layers (see also Chap. 3). High-angular resolution techniques give access to to access the layers where the dust is forming, allowing to validate and improve the theory and, hopefully, constrain the scenario for SiC formation. The strong and broad dust feature at 11.3 μm of SiC can be studied in the N-band with spectrally-dispersed interferometry.

1.2.3 Stellar parameters

- **Luminosities** of C-rich stars vary from $\sim 10^3$ to $\sim 10^4$ $L_\odot$. The major factor of uncertainty is the distance of the targets. The biggest database source of distances is the Hipparcos catalogue (Perryman et al., 1997), which shows increasing uncertainties with the increase of the angular size of the star. This is because stars are often resolved and may indicate surface brightness spatial/temporal variations (Feast, 1999). This affects of course also C-rich AGB stars, as Sacuto et al. (2011a); Cruzalèbes et al. (2013a) demonstrate, and studies to find a solution to this problem are still going on. Also, the survey of the Gaia satellite (soon to be released, Perryman et al., 2001), will furnish the possibility to estimate more accurately the distances.

- **Masses:** The usual procedure to derive definitive masses of stars takes into account the binaries orbit with measured parallaxes. Unfortunately, there are no such systems with a carbon-star member (Wallerstein and Knapp, 1998). Also, no eclipsed carbon-giant was ever seen in a binary system (Kenyon, 1986). Therefore, other procedures are used to estimate progenitor C-stars masses, and these could come from stellar evolution and from the galactic distribution of stellar population. Both of them show that a likely range of progenitor masses is ~ 1 to ~ 3 $M_\odot$ – with uncertain lower and upper limits.

- **Effective temperatures:** Usually, in models of carbon-stars the effective temperatures vary from ~ 2400 to ~ 3400 K. The fundamental equation that links the effective temperature $T_{\rm eff}$ of a star to its luminosity L is:

$$L = 4\pi R^2 \sigma T_{eff}^4 \tag{1.2}$$

  with σ the Stefan-Boltzmann constant, and R the radius, that can be derived from lunar occultations or interferometric methods[4]. For C-rich AGB stars the angular diameter varies strongly with the wavelength, so the temperature that can be derived is actually an "effective temperature", and is therefore very uncertain. Also, the optical depth profile can be very shallow and not monotonic, which adds another uncertainty in the effective temperature determination.

- **Radii:** The definition of the stellar radius is widely discussed, and a complete

[4]What one actually can derive, is the angular diameter θ [mas]. But since both flux and angular size depend on D^2, then the effective temperature can be derived without knowing the distance.

review on that can be found in Scholz (2003). Measurements from interferometry or lunar occultation estimate values of few 100 $R_{\odot}$, for C-rich AGB stars (van Belle et al., 1997; Dyck et al., 1996; van Belle et al., 2013). Stellar radii are of particular importance in order to derive an escape velocity, which is essentially related to the mass-loss. Also, the intensity profiles of models with mass loss, are very different from UD (Uniform Disk) profiles (Paladini et al., 2009).

- **C/O ratio and abundances:** the C/O ratio is the parameter that distinguishes the nature of the object, i.e. C-rich if the C/O ratio is higher than 1, O-rich otherwise. In AGB stars with thin CSEs the elemental composition can be estimated via visual and near-IR high-resolution spectra (e.g. Lebzelter et al., 2010), and detailed models describing the atmosphere. For the more extreme stars, with more opaque CSEs, one needs to use circumstellar mm-data (e.g. Groenewegen et al., 2002). These are also suitable for low mass loss stars, and important comparisons are possible (e.g. Olofsson et al., 1993).

1.3 Outline

The focus of this thesis lies in the study of C-rich AGB stars' atmospheres, and comparing state-of-the-art models with observations. This is done in order to constrain the models for future generations of models, and to derive stellar parameters, that are essential in the broader context of stellar and galactic evolution studies. The main parts of this thesis can be summarized as follows (see also Fig. 1.4).

1. **Introductions.** In the present Chapter 1, an overview on the main processes occurring inside AGB stars has been given. The next Chapters 2 and 3 will furnish introductions respectively on the models used in this thesis and on the fundamental principles of optical interferometry.

2. **Modelling the atmosphere of the C-rich Mira RU Vir.** In Chapter 4 the atmosphere of a C-rich AGB star is investigated, combining different types of observations, and comparing them with the state-of-the-art dynamic model atmospheres.

3. **Modelling of a set of C-rich AGB stars atmospheres.** In Chapter 5 the same methodology as before is applied to a larger group of C-rich AGB stars.

4. **Large Program.** A large portion of time and efforts dedicated to this thesis was devoted to the reduction and quality check of interferometric MIDI/VLTI data. Those are part of the observations described in Chapters 4, 5 and of a large program, whose results are described in Chapter 6.

5. **New model without the SPL assumption.** Last but not least, the results derived in point 3 and 4 above, are compared to one model which drops the assumption of SPL. This is described in Chapter 7.

6. **Preliminary comparison of the VLTI/MIDI observations of the C-rich Mira R For, with dynamic model atmospheres.** A preliminary analysis of the MIDI interferometric data of the carbon-rich star R For is presented in Chapter 8.

7. **Conclusions and outlook.** Finally, in Chapter 9 an overview on the findings of this thesis and on the possible follow-ups of this work are provided.

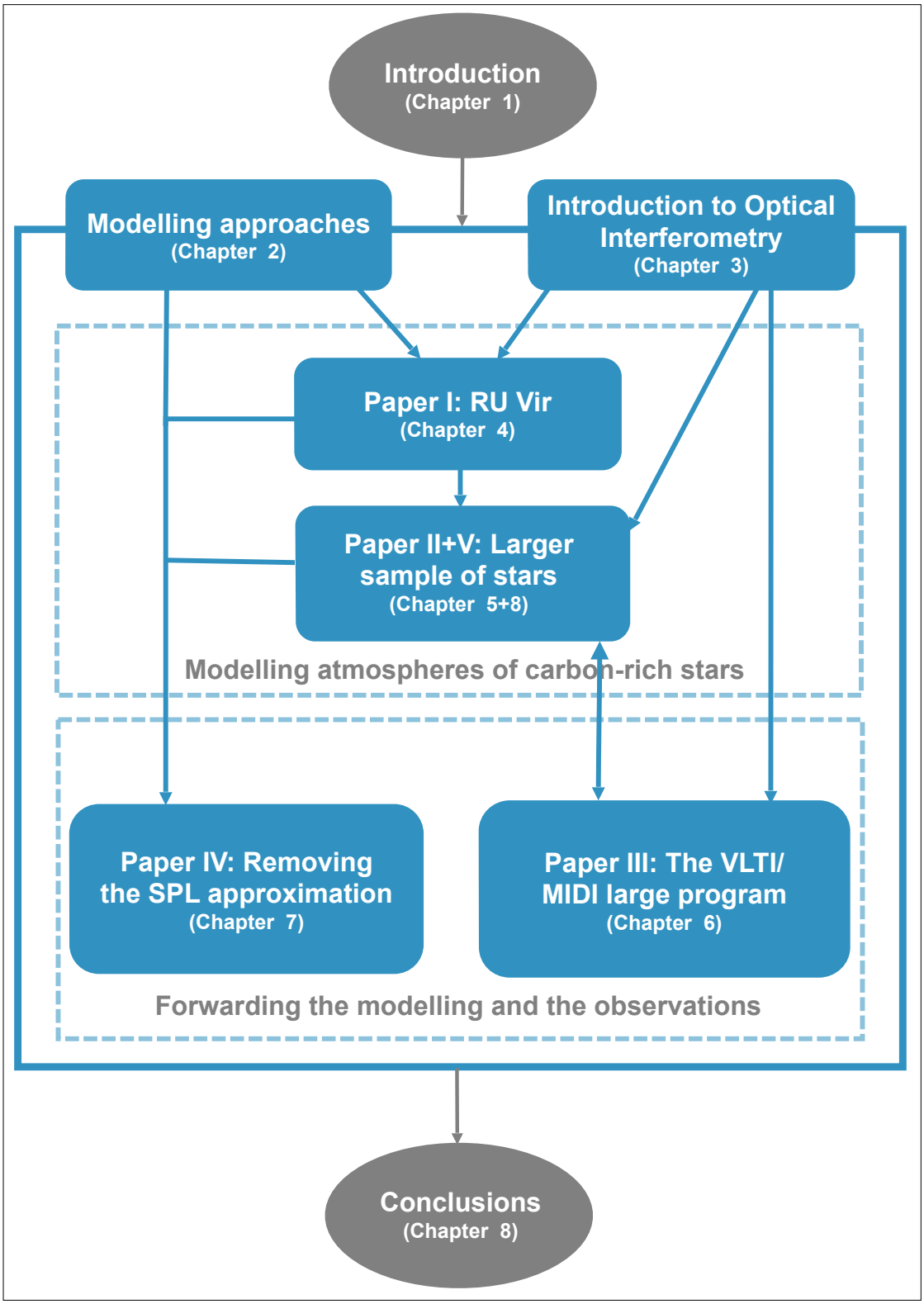

Figure 1.4: Schematic view of the outline of this thesis.

Chapter 2

Modelling approaches

This chapter provides an overview on the different types of models used to analyze the atmospheres of the sample of targets of this thesis. Those models are: the radiative transfer code More Of Dusty (Sect. 2.1), the hydrostatic MARCS models (Sect. 2.2) and the dynamic model atmospheres (Sect. 2.3). This chapter is thus based on the following papers: Groenewegen (2012); Aringer et al. (2009); Höfner et al. (2003); Eriksson et al. (2014); Gautschy-Loidl et al. (2004) and Nowotny et al. (2005a).

2.1 "More Of Dusty"

"More Of Dusty" (from now on: MOD, see Groenewegen, 2012) is an extension of the Dusty code (Ivezić and Elitzur, 1995; Ivezić et al., 1999). DUSTY is a 1D publicly available radiative transfer (RT) code that solves the problem of radiation transport in a dusty environment, and was designed to solve the issues that many astrophysical environments encounter: how the radiation coming from a source is seen after being processed by a dusty region. Its mathematical formulation is explained in detail in Ivezic and Elitzur (1997).

For the study of the AGB stars, useful informations on e.g. the mass-loss processes and dust formation, are coded in several quantities. Those are: the spectral energy distribution (SED), the density distribution of the dust in the CSE; the dust optical depth τ that, together with the spectra, contains informations on the type of dust present in the environment; intensity profiles, that are responsive to the density distribution, and high-angular resolution data that can investigate the inner part of the dust shells. RT models may offer a tool to infer properties on the dust, dust formation processes, and mass-loss rates, but usually the solutions are not unique.

In DUSTY, the properties of the radiation source and dusty envelope can be specified, and with them, the code can compute the dust temperature distribution and the radiation field. This is done via solving the radiative energy density equation, i.e. taking into account the scattering, the absorption and the emission of dust, providing in the end an exact solution. Following Rowan-Robinson and Harris (1982), we can consider a basic model consisting of a black body of radius r_s and temperature T_s, at the center of a spherical cavity of radius r_1 in a spherically symmetric dust cloud of radius r_2. Given $Q_{\nu,abs}$ the absorption efficiency of the grains, and assuming that the grain condensation temperature T_1 determines r_1, and that $r_s << r_1$, if the heating by other grains could be neglected, the temperature of the grains at the radius r_1 would then be given by:

$$\int_0^\infty Q_{\nu,abs} B_\nu(T_1) d\nu = \frac{r_s^2}{4r_1^2} \int_0^\infty Q_{\nu,abs} B_\nu(T_s) d\nu. \tag{2.1}$$

The number density of the grains is expected to satisfy the relation $n(r) \propto r^{-\beta}$, with $\beta = 2$ for a continuous steady mass-loss at a constant (terminal) velocity.

The optical depth to the center of the shell, at frequency ν is given by:

$$\tau_\nu = (Q_{\nu,abs} + Q_{\nu,sc})\, \pi a^2 n_2 r_2 \int_{r_1/r_2}^1 [n(r)/n_2]\, d(r/r_2) \tag{2.2}$$

with $n_2 = n(r_2)$ and $Q_{\nu,sc}$ the scattering efficiency.

Qualitatively MOD can judge the fit, separately for the four types of observables: spectroscopy, photometry, interferometry and intensity profiles. This is done by the χ^2 analysis:

$$\chi^2 = \sum_{i=1}^{i=n} (x_{obs}(i) - x_{pred}(i))^2 / \sigma^2_{x_{obs}(i)} \tag{2.3}$$

where x is the observed or predicted magnitude (for photometry), flux (for spectroscopy), visibility at a given spatial frequency (for interferometry), or normalized intensity at a radial offset (for intensity curves). $\sigma_{x_{obs}}$ are the error bars on the observations, and n is the total number of observations.
Given f the number of free parameter, the reduced χ^2 is given by:

$$\chi^2_{red} = \chi^2/(n - f). \tag{2.4}$$

Optical properties of several types of dust are taken in consideration in DUSTY, and a library with properties of many different grains is included. The density distribution can

be added in different analytical forms. A stationary dust-driven wind around AGB stars can be calculated, and its structure is controlled by radiation pressure on dust grains, therefore the density distribution does not need to be prescribed in advance (Ivezic and Elitzur, 1997), but it is instead determined from the coupling of hydrodynamics and radiative transfer. The solution requires only the optical depth.

The SED of the central sources might be defined by the user to be a broken power-law, or a Planckian. DUSTY also supports the reading of external files in which one can specify arbitrary dust optical properties, density distributions and external radiation.

MOD was introduced basically for this reason: the growing number of datasets available and of parameters involved in the radiative transfer modelling lead to the need of having a minimization procedure to derive a best fit and to estimate quantitatively the goodness of a fit. MOD can perform the minimization of the χ^2 for a set of parameters: luminosity L, dust optical depth τ, temperature at the inner radius T_c, slope of the density law p. The observables that can be used as constraints are: photometric-, spectroscopic- and interferometric-data, plus intensity profiles. In theory, every combination of parameters that appears in a standard DUSTY input file may be minimized. To the purpose of this thesis a one-shell structure was assumed, and the parameters L, τ, T_c, p were fitted, with the possibility of keeping some of them fixed to a value, or fitting them (see Sect. 4.4.2 and Rau et al., 2015c).

Input of MOD is a file containing the following informations: the distance d of the target, the interstellar reddening A_V, the effective temperature $T_{\rm eff}$, the parameter of the density law p, the number of shells, the outer radius of these shells, the link to a file containing the dust absorption and scattering coefficients and the spectrum of the central star. Other inputs of MOD are files containing the observed data.

Fig. 2.1 shows the variation of the SED depending on different optical thickness, for two different type of dust: amorphous carbon and silicates. The shape of the SED possess some general characteristics that are common to all solutions. Given λ_p the wavelength around which the distribution peaks and $\rm T_{sub}$ the sublimation temperature, that can not be exceeded by the dust, then dust emission is negligible for $\lambda < \lambda_p(T_{\rm sub})$, and the scattered light dominates the diffuse component at these wavelengths. Instead as τ_ν goes beyond 10 the external radiation and light are completely absorbed, and then the dust emission dominates.

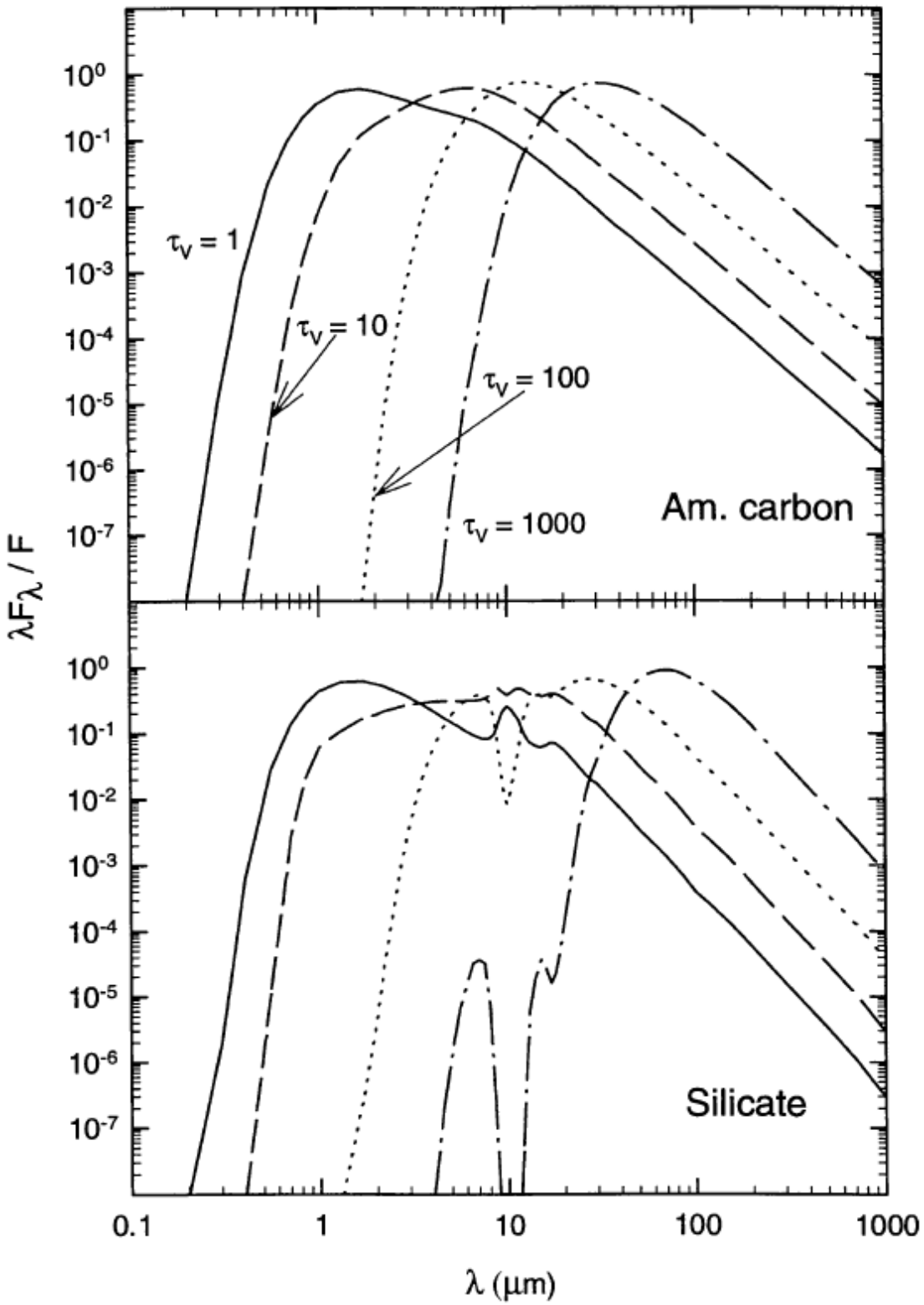

Figure 2.1: SEDs variation at different optical depth values. The dust contribution is: amorphous carbon, in the upper panel, and silicates in the lower panel. Figure from Ivezic and Elitzur (1997).

2.2 COMARCS

Synthetic spectra from COMARCS hydrostatic models are used in this thesis. Those are described in Aringer et al. (2009), for comparison with the observations of C-rich AGB stars. Hydrostatic models do not take into account the effects of time-dependent processes happening inside the stars, such as pulsation and dust formation. Those effects will become instead essential as the star evolves. The COMARCS code, based on the MARCS code (Gustafsson et al., 1975, Gustafsson et al., 2008), was used for the calculations. One of the major differences with its predecessor is that COMARCS works with external and more accurate opacity tables. For the opacity sampling (OS), the grid from Aringer et al. (1997) was used. The OS technique is based on picking the value of the monochromatic absorption coefficient in a sufficiently large number of frequency points, such that the statistical character of the variation of a complex absorption coefficient is well represented inside regions where the source function does not vary too much (Jørgensen, 1992).

For each combination of microturbulence and chemical abundances, the opacities are approximated by a spline fit. This was possible using the COMA code (Copenhagen Opacities for Model Atmospheres, Aringer, 2000). Through COMA, the following molecules contributing to the total absorption were covered: CO, CH, C_2, SiO, CN, TiO, H_2O, C_2H_2, HCN, C_3, OH, VO, CO_2, SO_2, HF, HCl, FeH, CrH, ZrO, YO. An example of the spectra of the most important molecular species spectra is given in Fig. 2.2.

2.2.1 Parameters of the hydrostatic models

The model spectral grid used includes spectra for 746 spherically symmetric hydrostatic model atmospheres, each described by a set of parameters of the related model atmosphere. Those are: effective temperature $T_{\rm eff}$, surface gravity g, mass in solar masses $M/M_\odot$, metallicity relative to the solar one $Z/Z_\odot$, carbon-to-oxygen ratio C/O and microturbulent velocity ξ [km/s]. The parameter range of $T_{\rm eff}$, C/O and g was chosen considering typical ranges expected for C-rich stars, from synthetic evolution calculations presented by Marigo and Girardi (2007) and Marigo et al. (2008). Sub-grids of models were calculated for metallicities $\rm Z/Z_\odot = 1.0$, $\rm Z/Z_\odot = 0.33$, $\rm Z/Z_\odot = 0.1$, and masses M= 2.0 $\rm M_\odot$, M= 1.0 $\rm M_\odot$. C/O ranges from 1.05 to 2.00 and effective temperatures from 2400 to 4000 K in steps of 100 K, even if the AGB phase extends typically only up to $\sim$ 3500 K. $\log((g)[cm/s^2])$ varies from 0.0 to -1.0, $\xi = 2.5$ [km/s].

Fig. 2.3 shows the influence of the change in parameters on the overall spectral appearance of the models.

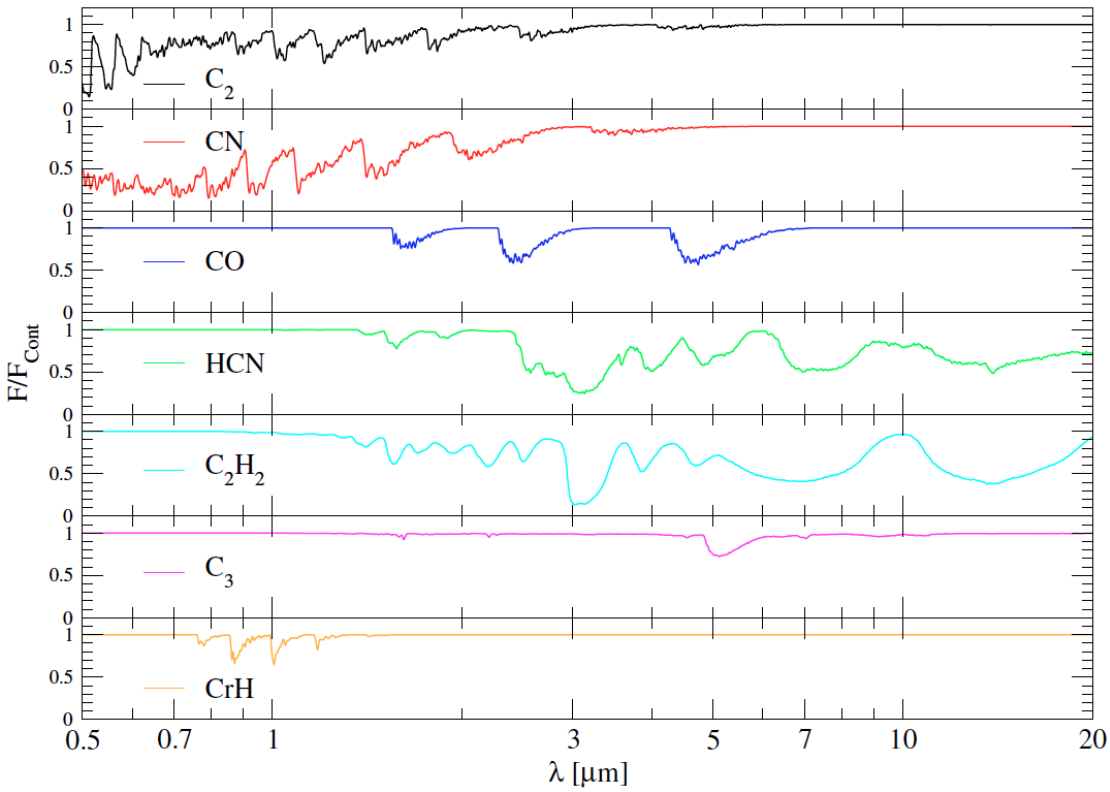

Figure 2.2: Continuum normalized spectra for the most important molecular species. The spectra are based on a COMARCS model, with T_{eff} = 2600 K, log(g)= −0.2, C/O= 1.10 and solar mass and metallicity. From Aringer et al. (2009).

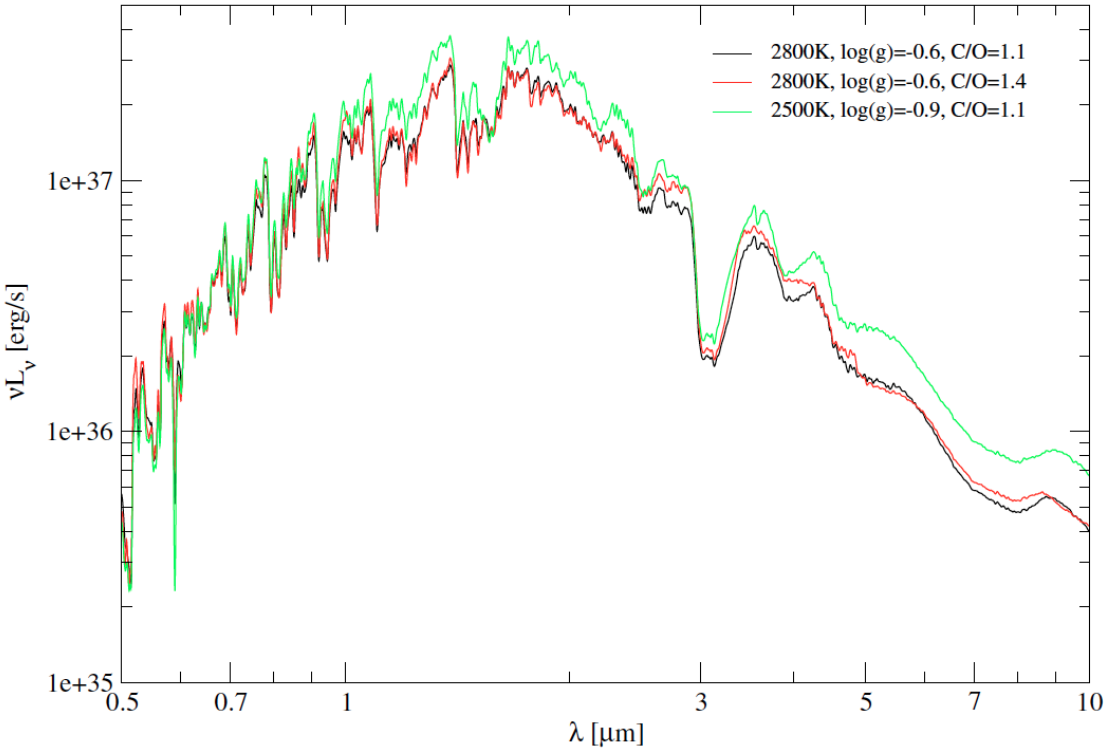

Figure 2.3: Three spectra based on COMARCS models, with different values of T_{eff}, log(g), C/O, and constant solar mass and metallicity. The resolution is 200. (Aringer et al., 2009).

2.2.2 Synthetic spectra

Spectra have been calculated with the COMA07/SPHREAD03 spectral synthesis code from COMARCS04 hydrostatic models, assuming local hydrostatic thermal and chemical equilibrium. They extend from 0.4448 to 25.0 μm, and the molecular and atomic opacities are treated in OS approximation. Circumstellar dust reddening is not taken into account. Aringer et al. (2009) explain the details of the computations, the input physics and the application of these spectra. The original resolution of those spectra is R= 10000, but considering the statistical nature of the OS approach, only the average over a larger number of wavelength points ($\sim 20 - 100$) gives a realistic view of the observed stellar SEDs. This is why the spectra have been reduced to a resolution $R = 200$.

As Aringer et al. (2009) demonstrate, the hydrostatic dust-free atmospheres fail to reproduce the cooler, redder C-rich AGB stars, since most of the time-dependent phenomena, as pulsation or dust formation, can not be included in hydrostatic models. Therefore, as previously mentioned, this thesis extends the comparison models-observations to the dynamic model atmospheres, as the following Section will describes.

2.3 Dynamic Model Atmospheres

AGB stars atmospheres are strongly affected by dynamical processes on local and global scales. Hydrostatic atmospheres models are not able to reproduce those effects (pulsation, shock-waves, winds), and the inclusion of time-dependent dynamics in the model is not only necessary, but also essential, since they are the only consistent way to analysze the strongly pulsating atmosphere of C-rich AGB stars.

This Section is dedicated to the description of the dynamic model atmospheres (DMA[1]) used in this thesis, for C-rich AGB stars, and is based on the works of Höfner et al. (2003), Mattsson et al. (2010), Gautschy-Loidl et al. (2004), Nowotny et al. (2005a) and Eriksson et al. (2014).

2.3.1 Overview

Fleischer et al. (1992) and Höfner and Dorfi (1997) presented dynamic models with time-dependent dust formation in a self-consistent way. Later, a new generation of model atmospheres for AGB stars was presented in Höfner et al. (2003), including, in contrast to the earlier model, also the treatment of the radiation field in a frequency-dependent

[1]DARWIN is the new acronym for these models. It stands for Dynamic Atmosphere & Radiation-driven Wind models based on Implicit Numerics

way. A series of hydrodynamic equations describe the atmospheric structure: equation of continuity, equation of motion, and energy equation. The models are spherically symmetric, and combine time-dependent dynamics (dust component: formation, growth, evaporation of dust grains, Sect. 2.3.3), and frequency-dependent (non-grey) radiative transfer (gas component, Sect. 2.3.2) that take into account the energy and momentum balance of the radiative field. In this way the effect of pulsation, such as stellar winds and shock waves, together with the influence of molecular opacities on the models, are self-consistently considered. The models have an inner boundary below the stellar photosphere, but above the driving zone of the pulsation. The effects of the pulsation are simulated by a "piston" through time dependent variations at the inner boundary.

2.3.2 Radiation

The gas component, the three conservation laws for momentum, mass and energy, together with the description of the net energy and momentum exchange between gas and the radiation field. The radiation field is determined from the zeroth and first order moment of the radiative transfer equation:

$$\frac{1}{c}\frac{\partial}{\partial t}J + \frac{1}{c}\nabla\cdot(Ju) = -\nabla\cdot H - \frac{1}{c}K\nabla\cdot u + \frac{u}{c}\frac{3K-J}{r} - \rho(\kappa_J J - \kappa_s S_g) \tag{2.5}$$

$$\frac{1}{c}\frac{\partial}{\partial t}H + \frac{1}{c}\nabla\cdot(Hu) = -\nabla K - \frac{3K-J}{r} - \frac{1}{c}H\nabla u - (\kappa_H\rho + \chi_H)H. \tag{2.6}$$

ρ is the density and c speed of light constant. κ_s is the frequency-integrated absorption coefficient of the gas, S_g the source function of the gas, r the radius coordinate, t the time, u the matter velocity, J the zeroth frequency-integrated moment of the radiation intensity (being J_ν the frequency-dependent moment of the radiative intensity), H the first and K the second. κ_X (with X corresponding to J, H or S) is the frequency-integrated opacities of gas and dust, e.g. $\kappa_J = \int_\nu \kappa_\nu J_\nu d\nu/J$ and $\chi_J = \int_\nu \chi_\nu J_\nu d\nu/J$. κ_ν is the mass absorption coefficient of the gas, and χ_ν the absorption coefficient of the dust.

To close the system (composed by Eq. (2.5) and (2.6)), the Eddington factor $f_{edd} = K/J$ and a closing condition, i.e. the equation of state for perfect gas, are needed. This system will define the gas temperature stratification, and in principle will allow for deviations from radiative equilibrium, e.g., in strong shocks. These models are based on OS data, meaning that the RT equation is solved at typically ~ 50 frequency points which are roughly equidistant in wavenumber but randomly distributed concerning opacity fea-

tures of molecular opacities for: CO, CH, C_2, CN, C_2H_2, HCN, C_3, TiO, H_2O, SiO (Jørgensen, 1992; Aringer et al., 2009).

2.3.3 Dust formation

When a dense gas cools down (expanding envelope), it will reach a temperature allowing large molecule aggregation (few tens to hundreds of atoms). This is the seed of the nucleation process. Then, an accretion process may cause dust growing on seeds by addition of other molecules or atoms. The dust chemistry is dictated mainly by the C/O ratio parameter.

The dust grains growth and evaporation is included in the C-rich models via the "method of moments" approach (Gail and Sedlmayr, 1988; Gauger et al., 1990). The dust component is described in terms of moments K_j of the grain size distribution function, where j is a power of the grain radius used to weigh the function.

Given the assumption of spherical amC grains, the equations that determine the evolution of the dust component can be formulated as follows:

$$\frac{\partial}{\partial t}K_0 + \nabla \cdot (K_0 u) = J \tag{2.7}$$

$$\frac{\partial}{\partial t}K_j + \nabla \cdot (K_j u) = \frac{j}{3}\frac{1}{\tau}K_{j-1} + N_l^{j/3}J \tag{2.8}$$

with J the net grain formation rate per volume, N_l the lower size limit of grains contributing to K_j, and $1 \leq j \leq 3$.

The grain temperature is derived by assuming the condition of radiative equilibrium: the internal energy transferred between gas and dust is minor compared to the interaction of the single component with the radiative field (Gauger et al., 1990). The optical properties of the dust grains are calculated using amC data from Rouleau and Martin (1991).

In the SPL approximation, dust opacities are fully determined by the amount and dielectric function of condensed material, irrespective of grain sizes, which greatly simplifies the modelling, because an explicit knowledge of the actual grain size distribution in each layer is not required (Mattsson and Höfner, 2011). Without the SPL assumption the condensation degrees are lower, which likely implies less dust extinction in the visual region; investigations on that are described in Chap. 7.

2.3.4 Models structure

Starting with an hydrostatic initial model described by luminosity, mass, effective temperature and elemental abundances, the equations of hydrodynamics, frequency-dependent radiative transfer and time-dependent dust formation are solved. This is done in order to get an adequate description of the highly dynamic AGB atmospheres. This is certainly a more realistic description, with respect to the hydrostatic case, of a dust-free pulsating atmosphere and dust-driven stellar wind.

The stellar pulsation is simulated by a variable inner boundary $R_{\rm in}(t)$ below the stellar photosphere (piston), and a velocity amplitude δu_p that changes sinusoidally with period P. Across the inner boundary there can not be any mass flow, in this way forcing the gas close to the inner boundary to move together with the boundary. $L_{\rm in}$, the luminosity at the inner boundary, together with $R_{\rm in}(t)$, define the boundary conditions and simulate a mass-shell in the stellar interior. During the pulsation cycle the mass-shell moves outwards if the luminosity increases, and inwards when the luminosity decreases.

Contrary to O-rich objects, for C-rich stars the formation of polyatomic molecules and dust happens within similar temperature regimes (Loidl et al., 1999). Therefore, opacities of molecules and dust must be simultaneously treated in the computations of the model atmospheres, in order to get realistic atmospheric structures and near-IR spectra.

In Fig. 2.4 the radial density structure of a DMA for several phases (colors) of one pulsation cycle is shown. While the hydrostatic initial model (black line) is relatively compact, the atmosphere becomes much more extended as pulsation leads to a periodic levitation of the outer layers (see also Fig. $1, 2$ of Nowotny et al., 2005a, and Fig. $2a$ of Höfner et al., 2003).

A shock wave triggered by pulsation emerges during every pulsation cycle and propagates outwards through the atmosphere, causing a levitation of the outer layers. At this point, two kinds of behaviour can form: without or with wind. In the first case, the mechanical energy input coming from the pulsation is too small: no wind will form, and therefore no dust-driven mass loss can develop. In this case the models will undergo an initial transition phase of adjusting from the initial hydrostatic structure, and then will settle into a periodic dynamical behaviour. Models that do not develop winds have the outer boundary located close to the photosphere, moving along with the upper atmospheric layers during the computations. In the second case, if the mechanical energy input by the pulsation and the levitation of the cool outer layers of the atmosphere are strong enough, i.e. the densities will be high enough and the temperatures cool

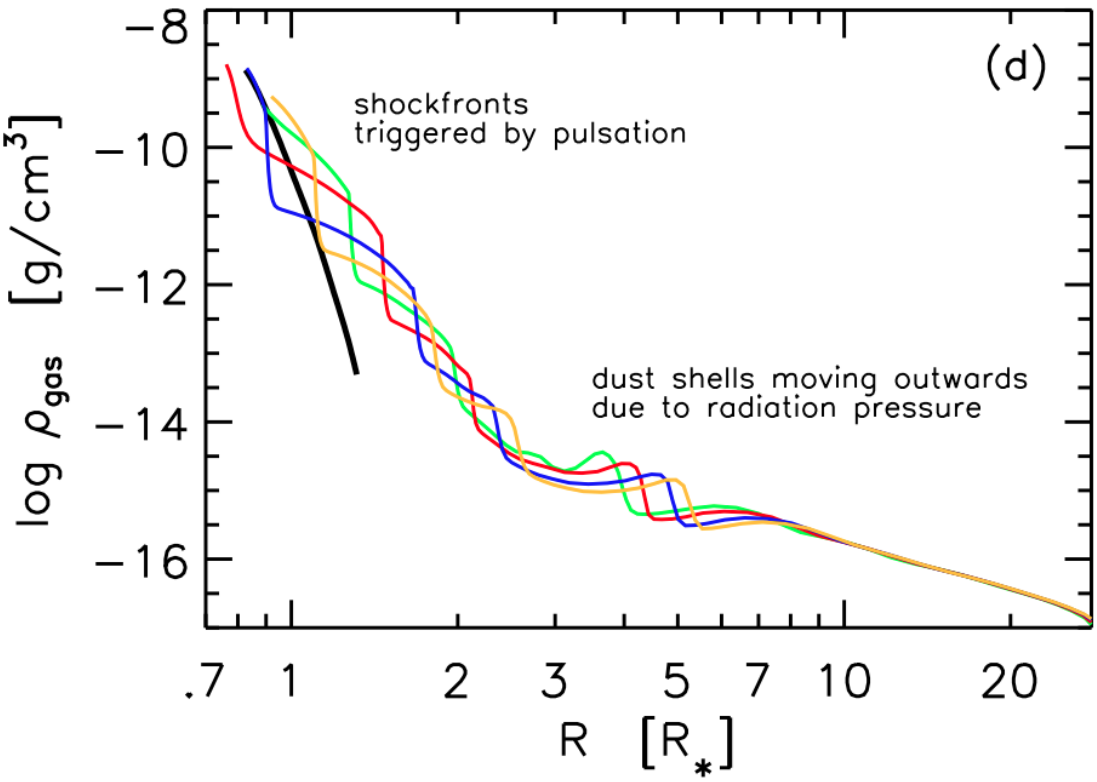

Figure 2.4: Atmospheric DMA structure. The hydrostatic initial model (black line) is relatively compact, the DMA become much more extended, and with a more shallow density profile than the hydrostatic models, as pulsation leads to a periodic levitation of the outer layers. Local density variation in the density structure are noticeable for DMAs. Also, in the inner regions are present shock fronts due to pulsation, while further out the reader can distinguish dust shells propagating outwards. Figure from Nowotny et al. (2011).

enough in the cool outer layers, dust condensation can happen, e.g. amC grain formation. Afterwards, the radiation pressure acting upon the formed dust particles results in an outwards directed acceleration. Subsequently, momentum transfer between the grains and surrounding gas via direct collisions leads to the development of a stellar wind (outflow driven by radiation pressure on dust). Models that form stellar winds have the outer boundary located at $20-30$ stellar radii, where the boundary is fixed and allows outflows (mass-loss). An example of the difference in the structure for models with or without wind is given in Fig. 2.5, where we show how the dust formation strongly influences the atmospheric extension. In fact, the model without mass loss stays rather compact compared to the hydrostatic initial model, and the model which develops a wind is inflated thereby and becomes much more extended than the corresponding initial model (Nowotny, 2005).

A schematic view of the occurrence or not of a wind in the DMAs, and their parameters, is given in Fig. 2.6. In Fig. 2.7 the density structure, wind velocity and wind speed vs. stellar radii of one DMA, with T_{eff} = 2600K, log(L)= 4 L$\odot$, M = 1.5 M$\odot$, C/O = 1.69, $f_L = 1$ are shown.

The temporally varying radial structure of the DMAs is significantly different from the hydrostatic case. The atmospheric structure of the fully developed mass-losing model changes much with respect to the initial hydrostatic model at any point in time, and it becomes extremely extended in comparison, with strong local variations superposed on the shallow density gradient (see Fig. 2.4).

2.3.5 Parameters

The parameters that define the models are the following: mass M, luminosity L_*, effective temperature $T_{\rm eff}$, C/O ratio, and they refer to the initial hydrostatic structure used as an input for the calculations. From L_* and $T_{\rm eff}$, a stellar radius R_* can be derived (see Eq. (1.2). Other input parameters controlling the pulsation are the piston velocity amplitude δu_p and the period P. Results of the hydrodynamical computations are the mean degree of condensation $\langle f_c \rangle$ and the rate of mass-loss $\dot{M}$. The luminosity at the inner boundary varies as $L_{\rm in} \propto f_L \cdot R_{\rm in}^2(t)$ (Gautschy-Loidl et al., 2004) , where f_L is the parameter introduced to vary the amplitude of this luminosity.

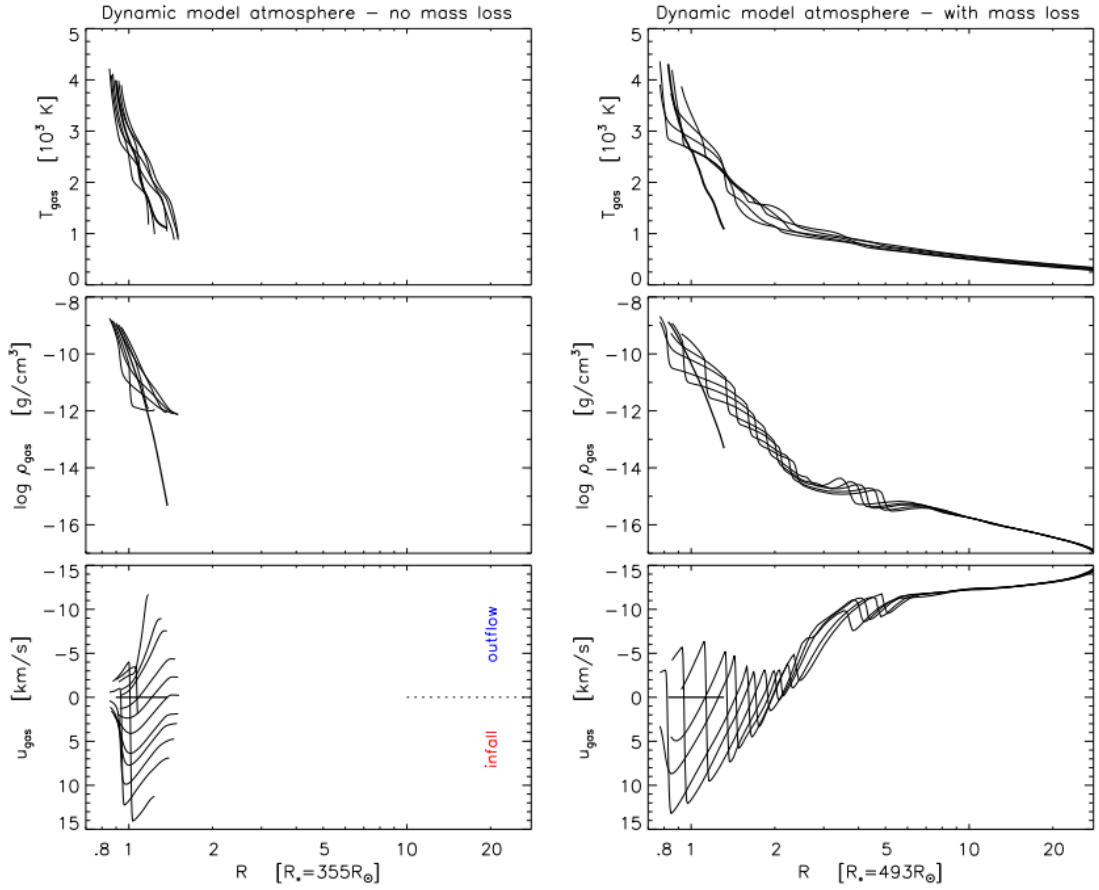

Figure 2.5: Comparison of temperature density and velocity for a dust-free model without mass loss (left panels) and for a dusty model which develops a stellar wind (right panels), on the same scale in stellar radii. To be noted are the different extensions, that are evident in the structures for several illustrative phases during one pulsation cycle. Figure from Nowotny (2005).

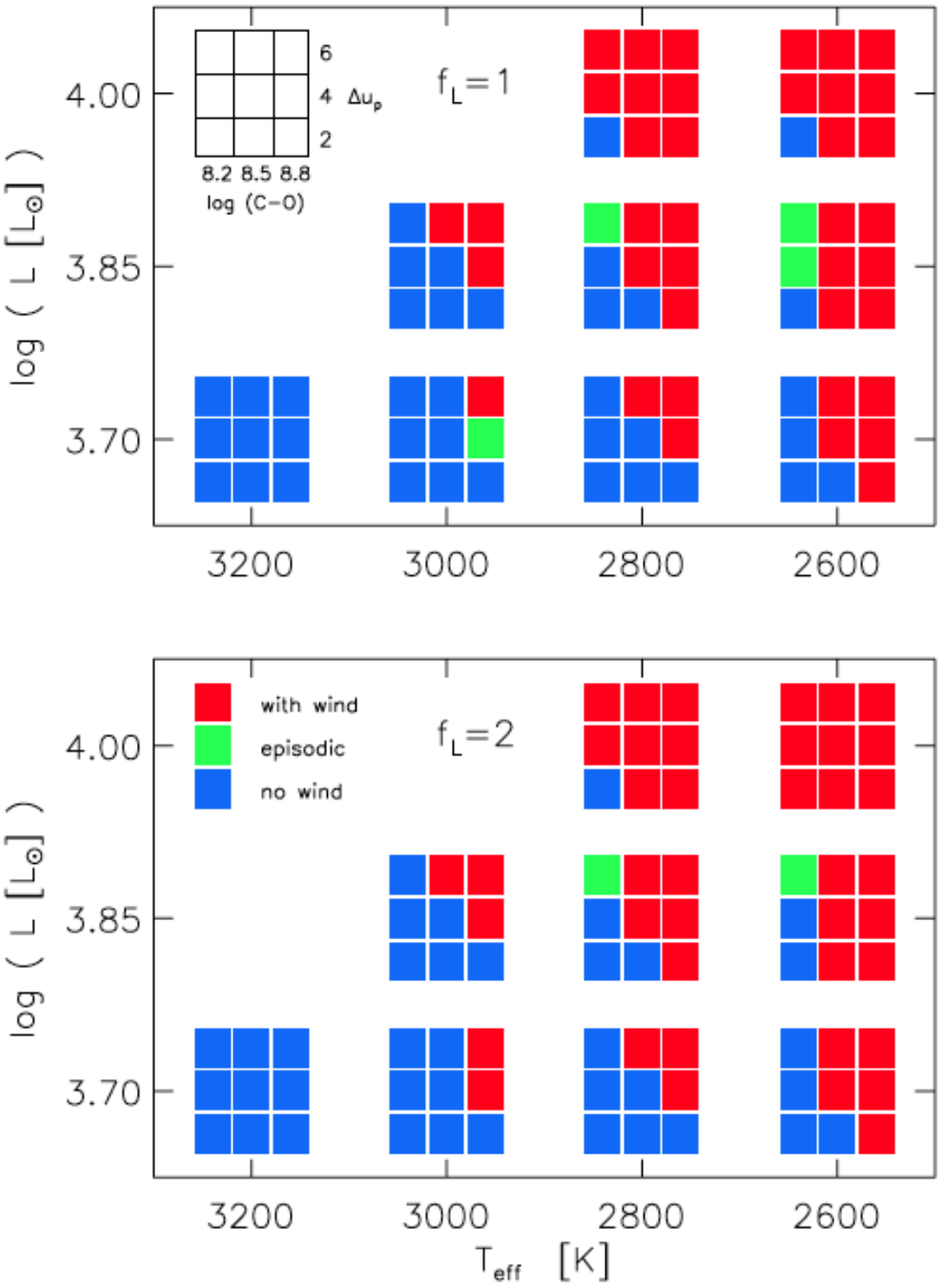

Figure 2.6: Schematic view of the parameter space of the DMAs (with one solar mass), in a diagram resembling the HR. The distinction between models with wind or without is given by the colors of the squares. Episodic models are the ones that show an intermittent outflow. From Eriksson et al. (2014).

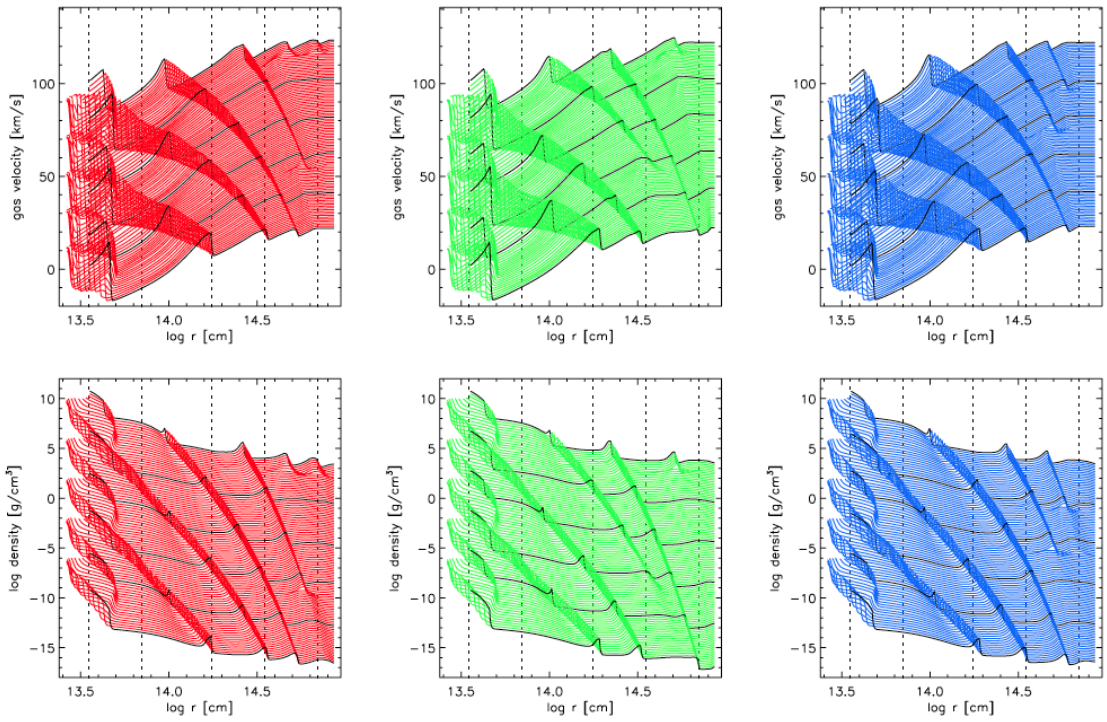

Figure 2.7: Wind speed and density structure of the DMA vs. stellar radii are shown for a representative DMA.. Each curve corresponds to a snapshot in time, which decreases downwards. The distance between the curves is ~ 0.5 in phase. From Eriksson et al. (2014).

2.3.6 Synthetic DMA spectra

In the Chap. 4 of this thesis, the models described in Eriksson et al. (2014) (that is a sub-grid of Mattsson et al., 2010) are used. The grid contains 540 models, spanning a wide range of fundamental stellar parameters, taken from C-star models in synthetic stellar evolution calculations for solar metal abundances (e.g. Marigo et al., 2008; Bertelli et al., 2008). Those models cover the two major dynamical aspects that influence the observables of AGB stars: the dust-driven wind and the shock-waves resulting from the pulsation. Each DMA provides a series of snapshots of radial structures, that covers ~ 100 pulsation periods. Models are classified in "classes": windless models, models with steady wind, models with periodic, irregular, or episodic variation of the wind properties.

The parameter $f_L = 2$ was introduced by Nowotny et al. (2010) to the aim of doubling the luminosity amplitude, with respect to the original grid. The interval of time was extended with respect to previous models in order to cover the long-term behaviour of the models. The wind was considered existing when the outer boundary reached 25 stellar radii, and the mass-loss was calculated from the mean value over several hundred cycles.

COMA was used a posteriori to calculate the detailed opacities (atomic, molecular and dust – amC), for each wavelength point and atmospheric layer, assuming LTE (local thermal equilibrium) and SPL (small particle limits). The calculations with COMA result in a grid of synthetic spectra from 0.35 to 25 μm. From the spectra, mean photometric magnitudes and their variation in different filters were also calculated.

Chapter 3

Introduction to optical interferometry

Obtaining observations at high angular resolution is possible by using optical long baseline interferometry. This term is used to refer to not only visible light, but also to infrared light. This thesis focuses on using data acquired trough this technique, at mid-infrared wavelengths.

The following Sections summarize the basic principles of optical interferometry, and introduce the VLTI/MIDI instrument used for observations as part of the PhD thesis. The present chapter is based on the text books by Glindemann (2011) and Labeyrie et al. (2006).

3.1 Optical interferometry

In the case of single-dish observations, a telescope of diameter D would produce a resolved image of a source if:

$$\theta > \lambda/D, \tag{3.1}$$

where θ is the angular diameter of the observed source and λ the wavelength of observations.

AGB stars have a luminosity distribution that peaks in the infrared. Indeed, the large amount of dust surrounding them absorbs the light coming from the star and re-emits at infrared wavelengths. A common size of the dusty shell is $\sim$ 50 mas at 11 μm, and therefore to resolve the source an aperture of $\sim$ 45 m would be needed. The same

can be applied to other astronomical sources, which would need even bigger apertures! Building such huge single-aperture telescopes would be very expensive, and would only partially solve the problem. In fact, if big apertures would on the one hand increase the sensitivity, on the other hand increasing the dish size would lead to a resolution limit which is defined by the Earth's atmosphere or any adaptive optics system. This problem could be solved by space missions, carrying telescopes out of the Earth's atmosphere. Again this is an expensive solution, and would have the disadvantage of making the observations less flexible to the various observational needs of the astronomers. The use of a ground-based technique would therefore be the best way to solve those problems.

Ground-based interferometry is the optimal way to allow observations at high-angular resolution. Combining light from two or more telescopes, interferometry makes the resolution depend not on the single dish aperture, but on the distance between the telescopes, which is called *baseline* B, and thus the relation (3.1) becomes:

$$\theta > \lambda/B. \tag{3.2}$$

The light coming from the astronomical object is collected by the two (or more) telescopes. For Michelson interferometers, in the case of observing not at the Zenith, the photons will arrive first at one aperture and then at the other, and a delay line will be needed at this wavelength to recombine the light. Fringes will be collected in the interferometric laboratory. The fringes contrast is called "*visibility*", which depends on the size of the observed source, i.e. its brightness distribution. The visibility is 1 when an unresolved source is observed – i.e. a point source. The lower the visibility, the more resolved the object is.

Another important quantity that can be measured by an interferometer is the fringes phase of the source. This gives information on the (a)symmetries of the target in the case of an extended source, otherwise on the object position on the sky. Fringes phase and amplitude describe respectively the real and complex part of the Fourier transform of the source's brightness distribution (Monnier, 2007). A two-telescope interferometer, such as MIDI, which is the main instrument used in this thesis, can not provide an absolute phase, because of the phase-shift caused by the instrumental setup and the atmosphere. This shift can be removed by combining three or more telescopes (closure phase). However, a differential phase is measurable with the correlation, in each spectral channel, of the contribution of the atmospheric phase. Moreover, holding a large number of observations, some methods as the image reconstruction can provide the image of the object by an inverse Fourier transformation.

3.2 Main principles

3.2.1 Monochromatic point source

The aim of this section is to describe the basic principles of optical interferometry in the case of two-telescopes following Ratzka (2005). The two-pinhole experiment that Young performed in 1804 is what inspired the current optical astronomical interferometers. Given $\vec{x}_A$, $\vec{x}_B$ the position vectors of the two telescopes, the baseline $\vec{B}$ is given by:

$$\vec{B} = \vec{x}_B - \vec{x}_A. \tag{3.3}$$

Indicating with $k = 2\pi/\lambda$ the wave vector, with $\omega = kc$ the angular frequency and with the unit vector $\vec{l}$ the pointing direction of the collectors, the electric field vector of a plane wave describes the monochromatic light coming from a celestial object at an infinite distance:

$$\vec{E}_A = \vec{E}_{A_0} e^{-i(k\vec{l}\vec{x}_A + \omega t)} \qquad \text{and} \tag{3.4}$$

$$\vec{E}_B = \vec{E}_{B_0} e^{-i(k\vec{l}\vec{x}_A + k\vec{l}\vec{B} + \omega t)}. \tag{3.5}$$

The intensity measured by the optical interferometers is averaged over time, and is given by:

$$I = |\vec{E}_A + \vec{E}_A|^2 \tag{3.6}$$

$$= I_A + I_B + 2\sqrt{I_A I_B}\cos(k\vec{l}\vec{B}) \tag{3.7}$$

$$= 2I_{tel}\left[1 + \cos(k\vec{l}\vec{B})\right], \tag{3.8}$$

where in the last equation it is assumed that the intensities at each telescope equal each other: $I_{tel} = I_A = I_B$, and $I_A = |\vec{E}_A|^2$. If a phase shift is introduced, as $k\alpha$, one can modulate the signal:

$$I = 2I_{tel}\left(1 + \cos(k\vec{l}\vec{B} + k\alpha)\right) \tag{3.9}$$

$$= 2I_{tel}\left(1 + \cos(k\delta)\right) \tag{3.10}$$

with $\delta = \left(\vec{l}\vec{B} + \alpha\right)$ the optical path difference (OPD). $\vec{l}\vec{B}$ describes the external

OPD, while α the internal one.

There exist two types of interferometers, depending on how the beams are interferometrically combined. The Fizeau (or image-plane), and the Michelson (or pupil-plane) type. The latter one is described in the following, as it is a type of interferometer similar to MIDI.

In a Michelson interferometer the beam combiner merges the light in the pupil-plane, and a half-coated mirror is used to transmit only 50 % of the beam, while the rest is reflected. The reflected beam of one telescope is combined with the transmitted beam of the other aperture, and viceversa, leading in this way to a phase shift of $\pm\pi/2$ between the transmitted and reflected beams. Indicating the telescopes with indexes A and B, and the beams with 1 and 2, it can be written:

$$I_1 = |\vec{E}_1|^2 = |\vec{E}_{A,1} + \vec{E}_{B,1}e^{i\pi/2}|^2 \tag{3.11}$$

$$= I_{A,1} + I_{B,1} - 2E_{A,1}E_{B,1}\sin(k\vec{\delta}) \qquad \text{and} \tag{3.12}$$

$$I_2 = |\vec{E}_2|^2 = |\vec{E}_{A,2} + \vec{E}_{B,2}e^{-i\pi/2}|^2 \tag{3.13}$$

$$= I_{A,2} + I_{B,2} + 2E_{A,2}E_{B,2}\sin(k\vec{\delta}). \tag{3.14}$$

Given $I_{tel} = I_A = I_B$ (equal intensities as input), $I_{A,1} = I_{A,2} = I_A/2$ and $I_{B,1} = I_{B,2} = I_B/2$, when adding together the beams in a Michelson interferometer Eq. (3.11) results:

$$I_1 + I_2 = I_A + I_B = 2I_{tel}. \tag{3.15}$$

The interferometric flux I_{int}, for a source which is monochromatic, is given by the difference in flux of the two beams:

$$I_{int} = I_2 - I_1 = I_A - I_B + 2I_{tel}\sin(k\delta) = 2I_{tel}\sin(k\delta), \tag{3.16}$$

where δ is the OPD between the two incoming beams can be tuned by moving the internal delay-line.

3.2.2 Polychromatic point source

The case of a non-monochromatic light coming from the source (polychromatic light), is the case of a real celestial object. Considering the limitation in the signal due to instrumentation and the Earth's atmosphere, which can be formalized by the spectral

filter function $\eta(\lambda)$, the interferometric flux becomes:

$$I_{int} = 2 \int I(\lambda)\eta(\lambda)\sin(k\delta)d\lambda, \tag{3.17}$$

where $I(\lambda)$ is the wavelength dependent intensity, and the spectral filter function is $\eta(\lambda) = \eta_0$ if $\lambda_0 - \Delta\lambda/2 < \lambda < \lambda_0 + \Delta\lambda/2$, and $\eta(\lambda) = 0$ otherwise. Integrating the interferometric flux one can obtain:

$$I_{int} = 2I(\lambda_0)\Delta\lambda\eta_0\sin(k_0\delta)\mathrm{sinc}(\pi\delta/\Lambda), \tag{3.18}$$

where the sinc function $\mathrm{sinc}(\pi\delta/\Lambda) = (\sin(\pi\delta/\Lambda)) \,/\, (\pi\delta/\Lambda)$ is the Fourier transform of the spectral filter function. Λ is a parameter that describes the length of coherence:

$$\Lambda \equiv \lambda_0^2/\Delta\lambda, \tag{3.19}$$

because if Λ is small compared to $|\pi\delta|$, then also the sinc function is small. This implies that, to perform observations with high signal, interferometric fringes should be detected at $\sim$ 0 OPD and high Λ.

MIDI wavelength-dispersed signal is recorded in the wavelength range from 8 to 13 μm. Different wavelengths result thus in different interferometric fluxes; in other words the fringe signal depends on the observational wavelength.

3.2.3 Polychromatic extended source

In order to perform science on our astronomical objects, we want to resolve them. They need thus to be considered not as point sources but as extended objects. This can be defined as a superposition of different coherent point objects located at $\vec{l}$ with $I = I(\vec{l})$. Contrary to the case of point sources, the telescopes A and B measure now two fractions of light: f_A and f_B:

$$f_A = \frac{I_A}{I_A + I_B}; \tag{3.20}$$

$$f_B = \frac{I_B}{I_A + I_B}. \tag{3.21}$$

The interferometric flux of an extended polychromatic source thus becomes:

$$I_{int} = 2\sqrt{f_A f_B} \int I(\vec{l}) sin\left[k(\delta + \vec{l}\vec{B})\right] d\vec{l} \tag{3.22}$$

$$= 2\sqrt{f_A f_B}|I(B_\lambda)|sin\left[k\delta + \phi(B_\lambda)\right], \tag{3.23}$$

being $\phi(B_\lambda)$ the phase term, $I(B_\lambda)$ the Fourier transform of the intensity of the source, and $B_\lambda = \vec{l}\vec{B}/\lambda$ the projected baseline (see Ratzka, 2005 for a detailed derivation of Eq. (3.22)).

3.2.4 Visibilities

From the amplitude of the fringes, one can derive the normalized visibility of a source. This is described by the vanCittert-Zernike theorem:

$$V(B_\lambda) = \frac{|I(B_\lambda)|}{I(0)} = \frac{|I_{int}|}{2\sqrt{f_A f_B}(I_A + I_B)} = \frac{|I_{int}|}{2\sqrt{I_A I_B}}, \tag{3.24}$$

where I_A and I_B are the interferometric fluxes.

In two-dimensional planes, using coordinate vectors, $\vec{\theta}$ in the source plane and $\vec{B}$ in the plane of the difference coordinates, the vanCittert-Zernike theorem states that the visibility of an astronomical object is the Fourier transform of its brightness distribution:

$$V(\vec{B}) = \frac{\int I(\vec{\theta}) e^{-ik\vec{\theta}\cdot\vec{B}} d\vec{\theta}}{I_0} \tag{3.25}$$

with $I(\vec{\theta})$ the source intensity distribution, and I_0 the integral over the source intensity: $I_0 = \int I(\vec{\theta}) d\vec{\theta}$.

Thus, the visibility of a given astronomical object is highly dependent on the projected baseline chosen and on the morphology of the source itself. Few examples of sources morphologies are given in the next Sect. 3.2.5.

This thesis deals with 1-D sources, and in the special case of a circular symmetric intensity distribution, which is produced by spherical symmetric models, the visibility is given by the Hankel transform of the intensity profile:

$$V(q) = \int_0^{\phi_{max}} I(\phi)\phi J_0(2\pi\phi q) d\phi, \tag{3.26}$$

where $q = \sqrt{u^2 + v^2}$, given u and v the spatial frequencies in arcsec^{-1}, $\phi = r/d$, and J_0 Zeroth-order Bessel function.

3.2.5 Examples of the sources morphologies

Interferometry is a powerful tool to retrieve informations on the morphology of celestial objects. As mentioned above the visibility is proportional to the Fourier transform (in modulus) of the brightness distribution of the object, projected into the plane that contains the telescopes interferometers and the astronomical object. Considering (x, y) the coordinates of the source in the sky, with y normal to the baselines and x parallel to it, the brightness distribution can be written as:

$$I(x) = \int I(x, y)dy. \tag{3.27}$$

The intensity distribution can assume different shapes, depending on the morphologies of the astronomical object observed. Some examples are given below. More complex structures can be portrayed by two or more simple intensity distribution added together. The visibilities can be then derived by multiplication of the simple structures visibilities (Convolution Theorem).

1. **Point Source**: the δ-function can describe a point source placed in p and whose intensity is I_0 as following:

   $$I(x) = I_0\delta(p - x). \tag{3.28}$$

   Its Fourier transform results in a constant, and therefore the normalized visibility is:

   $$V(B_\lambda) \equiv 1, \tag{3.29}$$

   where B_λ is still the projected baseline length, in units of wavelength.

2. **Binary**: two δ-functions can describe a binary star. Considering the two components located at $\pm p/2$, and the flux ratio of the components $f = I_1/I_2$, the brightness distribution is:

   $$I(\vec{x}) = I_1\delta\left(x - p/2\right) + I_2\delta\left(x - p/2\right), \tag{3.30}$$

   and the visibility:

$$V(B_\lambda) = \sqrt{\frac{1 + f^2 + 2f\cos(2\pi p B_\lambda)}{(1+f)^2}}, \tag{3.31}$$

for a derivation please refer to Ratzka (2005).

3. **Uniform disk**: this can be considered the simplest model to describe a star which is resolved. If the uniform circular disk has a diameter d, then $I(x)$ is a semicircle. Assuming that the disk is placed at the origin of the coordinates system, then the intensity is constant if $-d/2 < x < +d/2$; otherwise is 0. Then the visibility, given by the Fourier transform, is:

$$V(B_\lambda) = \left| \frac{2J_1(\pi d B_\lambda)}{\pi d B_\lambda} \right|, \tag{3.32}$$

with J_1 is the Bessel function of the first order.

4. **Gaussian disk**: it can be used in the case of objects which have extended structures (e.g. circumstellar disks). The FWHM (full-width-half-maximum) σ defines the gaussian disks, and it is described as the disk's width when one measures the values of the intensity which is the half of the maximum. This means that at a distance from the center of $\sigma/2$, the intensity becomes half of the peak value. The intensity distribution and the visibility are thus given by:

$$I(x) = I_0 e^{-\left(\frac{2\sqrt{ln(2)}}{\sigma} x\right)^2}, \tag{3.33}$$

$$V(B_\lambda) = e^{-\left(\frac{\pi\sigma}{2\sqrt{ln(2)}} B_\lambda\right)^2}. \tag{3.34}$$

3.3 The MIDI instrument at the ESO/VLTI

The MID-infrared interferometric Instrument (MIDI) was located at the Very Large Telescope Interferometer (VLTI) of the European Southern Observatory (ESO) in Paranal (Atacama desert, Chile). This location has also been chosen for its dryness, which allow excellent observing conditions in the infrared.

A total of eight telescopes compose the VLTI: four Unit Telescopes (UTs, 8.2 m of aperture) and four Auxiliary Telescopes (ATs, 1.8 m of aperture), the latter used only for interferometric observations. Indeed, while the UTs are anchored, the ATs can move

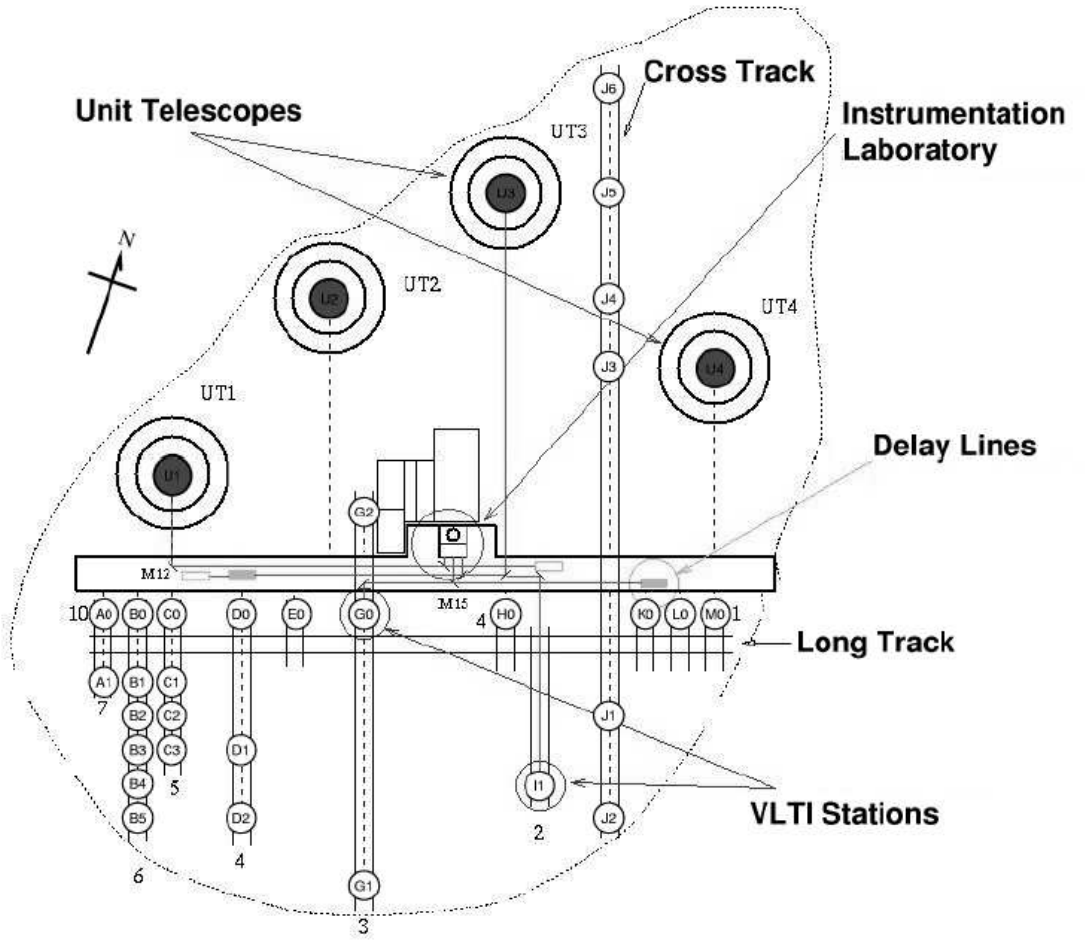

Figure 3.1: Schematic view of the VLTI stations. Figure courtesy of ESO.

along some fixed slits on the ground. The possible baselines range from 8 to 200 m, allowing an angular resolution up to milli-arcsec, which makes the VLTI widely used among several astrophysical topics: from AGB stars to YSO (Young Stellar Objects) and AGN (Active Galactic Nuclei). Depending on the observational period, different baselines configurations are available. Figure 3.1 shows schematically the eight telescopes configuration at VLTI, and the available ATs positions.

3.3.1 MIDI layout

The first ideation of MIDI, and its construction proposal to ESO, were made in 1997 at the MPIA (Max Planck Institut für Astronomie; Heidelberg, Germany). Subsequently, other institutions joined the project. After several years of tests and work, MIDI was delivered

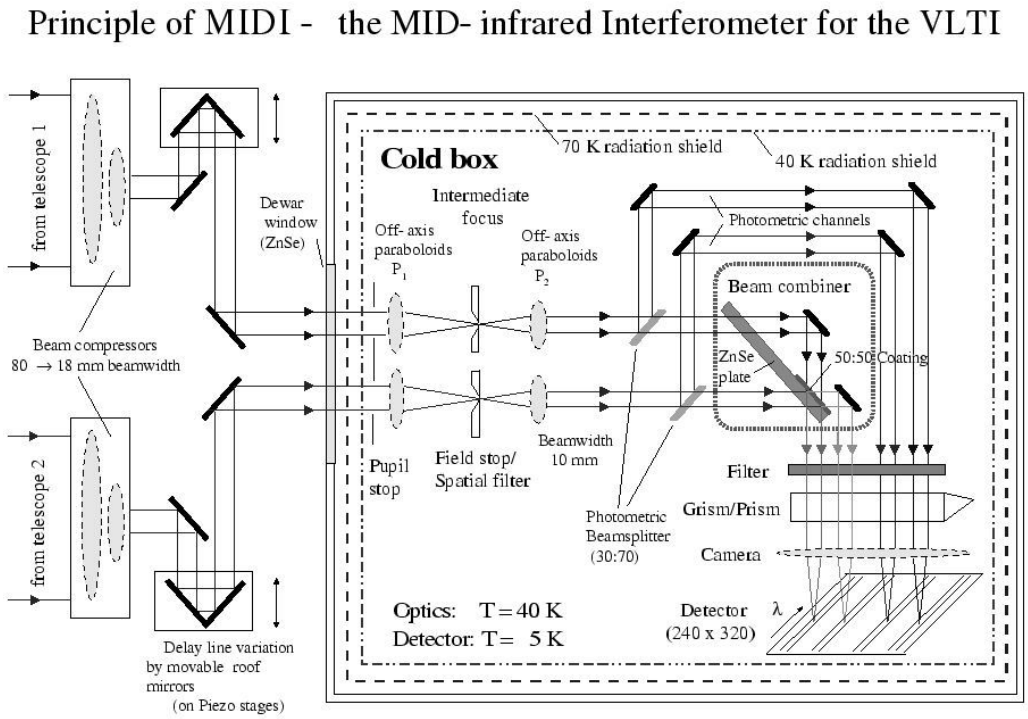

Figure 3.2: Schematic view of MIDI instrument. Figure courtesy of ESO.

to Chile in September 2002. MIDI's first fringes are dated 2002, while the following year the proposals for observations were opened to the international community. MIDI has been decommissioned at the end of P94 (March 2015).

The MIDI instrument can combine the light coming from two telescopes. The instrument itself is located in the instrumentation laboratory, at the center of the station map, below the ground (see Fig. 3.1). In this place the optical benches that host the various interferometric instruments are located. The light coming from the observed stars reaches the telescopes, and after being corrected from the differences in optical path length by the delay lines, arrives in the laboratory.

MIDI is composed by two main parts: the warm and the cold optics. First, the two light beams receive the delay compensation, which is needed in order to generate the interferograms. Up to 200 μm of optical path delay can be compensated by piezo-driven mirrors. Afterwards, the light goes through the cold optical bench, which is cooled down to 40 $\pm$ 5 K, in order to be able to avoid the dominating thermal background at 10 μm. The cooling is made with helium and liquid nitrogen. The light then passes the pupil stop, which cut the edge of the beams, further reducing the thermal background

radiation, and then goes through the field stop.

Depending on the mode chosen to be used, the light is now able to enter either a beam-splitter or the beam-combiner. In the first case, $\sim$ 30 % of the light is extracted in order to record at the same time the photometry of the observed object and the interferometry (other $\sim$ 70 %). In the pupil plane, the light is combined by the beam combiner: $\sim$ 50% of the light coming from beam A is transmitted and combined with $\sim$ 50 % of light of beam B , and vice versa. The beams now have reversed phase. They are spectrally filtered, and with a prism or grism they are spectrally dispersed, with a resolution of R = 30 or R = 230, respectively. With dispersion, the detector integration time can be increased[1]. Indeed, the diffusion of the light over a larger area of the detector prevents its saturation. Also, the dispersion permits the determination of visibilities at various spectral channels within the N band. Lastly, the dispersed beams can be focused, with a camera, onto the detector. The detector cooling temperature is even lower ($\sim$ 4 K) and its frame readout very fast ($\sim$ 6 ms).

MIDI can observe in two modes: *HIGH-SENS* and *SCI-PHOT*.

In the first case (high-sensitivity mode), the beam splitter is not inserted to derive photometry at the same time. Thus, the whole beam of light interfers, making this mode ideal to ensure high sensitivity even for faint targets. Photometry needs to be acquired afterwards, or before, closing and opening alternatively shutters A and B. This could cause extra errors, due to possible atmosphere's transmission changes between the two observations, leading to visibility errors in the order of $\sim$ 10 %.

In the second case (science-photometry mode), the acquisition of photometry and interferometry is simultaneous, which reduces the thermal background noise, thus the error on the visibilities is decreased to $\sim$ 7 %. However, the use of the SCI-PHOT mode reduces the sensitivity, because of the introduced light splitting. Also it requires further photometry recording, in order to derive the precise instrumental light split ratio between the interferometric and photometric channels (cross-coupling coefficients).

3.3.2 Observing strategy and data reduction

A considerable amount of time devoted to this thesis was dedicated to reduction of MIDI data used in several publications (e.g. the papers described in Chap. 4, 5, 6). Thus, in the following, a brief summary of the strategies to observe with MIDI and a general description of the data reduction procedure will be given. For an extensive description, see Klotz (2013), Ratzka (2005) and the MIDI user manual.

[1] Another limitation is the time of integration: should be below the atmospheric coherence time, which is $\sim$ 100 ms in the mid-IR.

To carry out the observations, scientists prepare a series of observing blocks (OB), which contain necessary informations, e.g. on the target, mode, filter, coordinates, seeing and baselines. Each OB is composed by a succession of calibrators and target. Each block of observation (cal-sci) of photometry and interferometry lasts about 50 min.

Given the coordinates, the night astronomer at VLTI points the telescopes to the chosen target. The position of the object in the sky is tracked by a guide star. The delay line searches for the expected position of the zero-OPD. When the images from the beams are perfectly aligned, they are acquired through the chopping-technique, which subtracts the sky background from the target's image to remove the background. Now the piezo-driven mirrors scan a length of a few microns, on the warm optical bench, to search for the fringes, which are then recorded. Afterwards, or at the same time (depending on the observing mode chosen), the photometry is recorded. With the photometric measures one can obtain the integrated flux. Later one records also the ratio of the correlated flux and the integrated one, which will give the normalized visibilities.

The data used in this thesis have been reduced with the IDL and C software packages MIDI Interactive Data Analysis (MIA) and Expert Work Station (EWS) (Jaffe, 2004; Leinert et al., 2004; Ratzka, 2005). MIA extracts visibilities through a power spectrum analysis, while EWS uses an off-line fringe tracking algorithm, which first aligns the interferograms and then adds them. This is the reason why the visibility amplitude signal-to-noise ratio is better in EWS than in MIA.

MIA uses a mask to extract the light of the target from the detector, excluding in this way the contamination from the thermal background. The mask decides therefore which pixel is used, giving each pixel a weight. In MIA the mask is not fixed, but adaptable, i.e. it is new for each single observation. Its dimension, in low resolution, is 40 pixels (spatial direction) x 100 pixels (spectral direction). In order to detect the exact position of the interferometric and photometric channels, 1-D Gaussian fits are performed. The two interferometric channels are then multiplied with the generated mask. At this point, in case of observations performed in the SCI-PHOT mode, the cross-coupling-coefficients are calculated. The OPD is then defined, and the compression of the frames ($\sim$ 8000) in 1-D arrays along the y-direction, is performed. Once the correlated flux modulation is calculated, the frames can be sorted into OPD scans ($\sim$ 200), and the scans are binned in wavelengths. To derive the raw photometry, one needs to subtract the sky photometric flux from the target photometric flux. Then, the raw visibility can be calculated by dividing the interferometric flux of the scans with a factor calculated through the square root of the photometric measures of each beam. It is important to remark that the raw visibility should be always below one. If this is not the case, this could be an indicator

either that something in the data reduction went wrong (in particular in the photometry extraction because of e.g. N-band background fluctuations) or that the data are of poor quality because of e.g. bad weather conditions.

Afterwards, from the theoretical and raw visibilities of the calibrator, the transfer function (instrumental visibility V_{ins}) can be calculated:

$$V_{ins} = \frac{V_{raw,cal}}{V_{theor,cal}}, \tag{3.35}$$

where $V_{theor,cal} = \frac{2J_1(\pi\theta_{cal}r)}{\pi\theta_{cal}r}$. The more a calibrator is resolved, the larger is its diameter θ_{cal}, the more it needs to be measured with high accuracy, in order to diminish its error. In this thesis most of the calibrator measurements come from Verhoelst (2005). Then, the calibrated visibility can be estimated as follows:

$$V_{sci} = \frac{V_{raw,sci}}{V_{ins}}, \tag{3.36}$$

and this means that the raw science visibility is corrected from instrumental and atmospheric effects. The raw MIDI spectra need to be calibrated in flux, using calibrator objects of spectral type earlier than M3, and close in airmass to the science one (Chesneau, 2007).

EWS instead has a fixed mask, which has the disadvantage not to be reactive to changes in the beam properties. The steps in the data reduction are the same as the ones described for MIA. In addition, to further reduce the noise signal in the data, a high-pass filter can be used, but only if the noise varies on time-scales longer than the fringes (i.e. at lower frequencies). The instrumental delay (d_{ins}), contained in the intensities together with the atmospheric delay, must be removed from the data. This is done by multiplying the intensity for $e^{-ikd_{ins}}$. On the other hand, the atmospheric delay also needs to be removed, and this can be done via estimating the group-delay, which is the maximum value of the delay function. The delay function is calculated by a Fourier transform of the intensity distribution. The group delay is also removed from the data. Then, to derive the complex visibility, the frames are averaged. But first, the offset of the phase has to be removed, i.e. the phase shift caused by the water vapor in the delay tunnels has to be corrected. Then, the calibration of the visibilities and flux is performed as for MIA.

Once several measurements of the visibility with different calibrators have been obtained, one can calculate the final calibrated visibility by averaging them. The errors are derived as the standard deviation of the visibility, but when the error is < 10 %, a

conservative 10 % multiplicative error is assumed.

As stated in Chesneau (2007), the differences in the data reduction with MIA and EWS should lie within 5 % and 10 %. When this divergence was higher, a quality check has been performed. The MIA data were reduced with the EWS mask, and vice versa, checking in this way if the results depend on the mask used. In fact, a small shift of the spectra on the detector could produce such differences. Instead, if the results depend on the routines MIA or EWS, one needs to check if differences in the photometric or interferometric measurements are present, if some fringe signal is contained in the MIA noise scans, or if one of the two routines excludes a high number of frame. Additional details on the data quality check analysis can be found in Klotz et al. (2012a).

Chapter 4

Modelling of AGB stars atmospheres: the case of RU Vir (Paper I)

This chapter is based on the paper Rau et al. (2015c)

Title: *Modelling the atmosphere of the carbon-rich Mira RU Vir*
Authors: G. Rau, C. Paladini, J. Hron, B. Aringer, M.A.T. Groenewegen and W. Nowotny
Year: 2015
Journal: Astronomy and Astrophysics, DOI: http://dx.doi.org/10.1051/0004-6361/201526418

We study the atmosphere of the carbon-rich Mira RU Vir using the mid-infrared high spatial resolution interferometric observations from VLTI/MIDI. The aim of this work is to analyse the atmosphere of the carbon-rich Mira RU Vir with hydrostatic and dynamic models, in this way deepening the knowledge of the dynamic processes at work in carbon-rich Miras. We compare spectro-photometric and interferometric measurements of RU Vir with the predictions of different types of modelling approaches (hydrostatic model atmospheres plus MOD-More Of Dusty, self-consistent dynamic model atmospheres). A geometric model fitting tool is used for a first interpretation of the interferometric data. The results show that a joint use of different kinds of observations (photometry, spectroscopy, interferometry) is essential for shedding light on the structure of a carbon-rich Mira atmosphere. The dynamic model atmospheres fit the ISO spectrum well in the wavelength range $\lambda = [2.9, 25.0]$ μm. Nevertheless, a discrepancy is noticeable both in the SED (visible) and in the interferometric visibilities (shape and level). A possible explanation are intra-/inter-cycle variations in the dynamic model atmospheres, as well as in the observations. The presence of a companion star and/or a disk or a decrease in mass loss within

the past few hundred years cannot be excluded, but these interpretations are considered unlikely.

4.1 Introduction

The asymptotic giant branch (AGB) is the late evolutionary stage of low-to-intermediate mass stars (typically $\sim$ 0.8 to $\sim$ 8$M_{\odot}$). These objects are characterized by a C-O core and He/H-burning shells, surrounded by a convective envelope, while the atmosphere consists of atomic and molecular gas, including dust grains. Stellar pulsation can generate shock waves that run through the atmosphere. These shocks can propagate outwards, causing a levitation of the outer atmosphere layers and improving the conditions for the formation of dust, which may then lead to a dust-driven wind.

At the early stages of their life, AGB stars have a carbon-to-oxygen-ratio below one. The third dredge-up can turn the chemistry of these objects from oxygen- into carbon-rich (Iben and Renzini, 1983). Carbon-rich AGB stars are important contributors to the enrichment of the interstellar medium, and in their spectra there are signs of carbon-bearing molecules such as C_2, C_3, C_2H_2, CN, or HCN, while the dust is mainly dominated by amorphous carbon dust grains and SiC (Loidl et al., 2001; Yamamura and de Jong, 2000).

By studying the stellar atmospheres of AGB stars, we hope to better understand many processes that can occur, such as the dust formation and mass loss via strong stellar winds or the connection between pulsation and atmospheric structure. In the case of C-rich AGB stars with no pronounced pulsation, most of the observables derived from hydrostatic models agree fairly well with the observations (Aringer et al., 2009). However, as the star evolves, time-dependent processes become more important, and the atmosphere expands, causing a decrease in the effective temperature. As a result, model atmospheres that take those dynamic processes into account (pulsation, dust formation, mass loss) are necessary (e.g. Bowen, 1988; Fleischer et al., 1992; Höfner and Dorfi, 1997; Höfner et al., 2003; see also the excellent reviews from Woitke, 2003 and Höfner, 2007).

In recent years there has been an increase in the number of works that investigate the atmosphere of AGB stars by combining various techniques (Wittkowski et al., 2001, 2008, 2011a; Neilson and Lester, 2008; Martí-Vidal et al., 2011). On the other hand, to date only a few interferometric observations of carbon stars have been compared with model atmospheres (Sacuto et al., 2011a; Paladini et al., 2011; Cruzalèbes et al., 2013a; Klotz et al., 2013a; van Belle et al., 2013).

In this paper we intend to study the atmosphere of the carbon-rich Mira RU Vir, by means of photometry, spectroscopy, interferometry, and model atmospheres (Mattsson et al., 2010; Aringer et al., 2009), using the most recent grid of dynamic atmosphere models and synthetic spectra (Eriksson et al., 2014). RU Vir is a C-rich AGB Variable Star of Mira type. It has a period of 433.2 days in the V band (Samus et al., 2009b). Its distance is 910 pc (based on the period-luminosity relation from Whitelock et al., 2006), the amplitude of the variability in the V band is 5.2 mag, and the average value of the magnitude in V is $< V >= 11.6$ mag. RU Vir is

surrounded by a carbon-rich dusty shell made of amorphous carbon (AmC) and silicon carbide (SiC). The latter shows its presence through the strong emission feature around ~ 11 μm.

We present new MIDI (MID-infrared Interferometric instrument) observations (P.I. G. Rau: ID 093.D-0708(A)) that probe regions of dust formation in the circumstellar envelope (Nowotny et al., 2011; Danchi et al., 1994). In a forthcoming paper, we will also consider a larger sample of carbon-rich AGB stars.

In Sect. 4.2 we present the photometry, the spectroscopy, and the interferometric observations of RU Vir and describe the data reduction performed. Section 4.3 explores the geometry of the environment and the fit of the geometrical models to the interferometric visibilities to constrain the morphology and the brightness distribution of the object. In general, the visibility V as a function of spatial frequencies u and v, as described, for example, in Winters et al. (1995), is the two-dimensional Fourier transform of the intensity distribution $I(\eta, \zeta)$, where η and ζ are the corresponding coordinates on the celestial sphere. In the special case of a circular symmetric intensity distribution, which is produced by spherical symmetric models, the visibility is given by the Hankel transform of the intensity profile:

$$V(q) = \int_0^{\phi_{max}} I(\phi)\ \phi J_0(2\pi\phi q)\ d\phi\ ,$$

where $q = \sqrt{u^2 + v^2}$ is the spatial frequency, ϕ the angular separation from the center of the star ($\phi = r/d$) with d the distance of the star, r the radius, and J_0 the zeroth-order Bessel function. Therefore, the term interferometric visibilities will from now on be referred to as visibilities V, used to denote the normalized quantity $V(q)/V(0)$. In Sects. 4.4 and 4.5 we investigate the modelling of the atmosphere of RU Vir from the hydrostatic and hydrodynamic point of view. In Sect. 4.6 we propose some of the possible scenarios that could justify the optical excess (Sect. 4.6.2) and the discrepancy in the visibilities (Sect. 4.6.3). Moreover, a discussion of the stellar parameters can be found in Sect. 4.6.1. Finally, we present the conclusions and perspectives for future works in Sect. 4.6.5.

4.2 Observational data for RU Vir

4.2.1 Spectroscopy

RU Vir was observed with the Short Wavelength Spectrometer on board the ISO satellite (SWS, de Graauw et al., 1996) once on 20 July 1996 (Sloan et al., 2003). This ISO/SWS spectrum covers the wavelengths range from 2.36 to 45.35 μm with a spectral resolution of R $\approx$ 200. For the purpose of our investigations, an error of $\pm$ 10% is assumed for wavelengths < 4.05 μm and $\pm$ 5% towards red wavelengths (Sloan et al., 2003). The ISO spectrum can be seen in black in Fig. 4.4.

B	V	R	I	J	H	K
15.95 ± 0.90	11.75 ± 0.70	8.50 ± 0.50	6.90 ± 0.50	5.50 ± 0.20	3.75 ± 0.15	2.30 ± 0.20

Table 4.1: RU Vir photometry in different filters adopted from Nowotny et al. (2011), in units of mag. The photometry is interpolated to the phase of the ISO/SWS spectrum (see Sect. 4.2.2).

4.2.2 Photometry

RU Vir photometry in the filters B, V, R, I, J, H, and K is given in Table 4.1. For our study, following Nowotny et al. (2011), we picked the B, V, R, I observations from Eggen (1975) and J, H, K observations from Whitelock et al. (2006). The photometry is taken at the same phase ϕ as the ISO/SWS spectrum, which can be calculated in the following way:

$$\phi_{\rm ISO}^{RU\ Vir} = \frac{(t - T_0)|P|}{P} = 0.65 \pm 0.1 \tag{4.1}$$

where t is the time of the observation in Julian date, T_0 the selected phase-zero point, corresponding to the nearest visual light maximum of the star. The light curves were interpolated to this phase (Nowotny et al., 2011, Fig. 8 there). The uncertainties of the different photometric measurements are estimated from the uncertainty in the phase and the scatter of the phased light curve data.

The visual light curve of RU Vir from AAVSO observations is shown in Fig. 4.1. The time of the observation of the ISO spectrum and the time interval of Eggen (1975) photometry (that covers more than one pulsation cycle) are shown. The light curves favor the presence of a secondary period on a timescale of $\sim$ 30yr (Percy and Bagby, 1999).

4.2.3 Interferometry

RU Vir was observed in 2010 (ID: 085.D-0756(C)) and 2014 (ID: 093.D-0708(A)) with the 1.8 m Auxiliary Telescopes (ATs) of the Very Large Telescope Interferometer MIDI (Leinert et al., 2003b). MIDI provides wavelength-dependent visibilities, photometry, and differential phases in the N band ($\lambda_{\rm range} = [8, 13]$ μm).

The journal of the observations is available in Table A.1 of the appendix. The calibrators used are listed below the corresponding science, and the second-to-last column identifies whether the observations are carried out in SCI-PHOT or HIGH-SENS mode. All the observations are in low spectral resolution ($R = 30$). The uv-coverage is shown in Fig. 4.2. The main characteristics of the calibrators are listed in Table 4.2. The choice of the calibrators follows the selection criteria described in Klotz et al. (2012a).

Data were reduced with the latest data reduction software package MIA+EWS (Jaffe, 2004). The calibrated visibilities at different baselines are plotted in Fig. 4.3. The wavelength-dependent visibility exhibits the typical shape of the visibilities for carbon stars with dust shells containing SiC grains (Paladini et al. in prep.). There is a drop between $8 - 9$ μm caused by C_2 H_2 + HCN opacities and another decline in the visibility shape at $\sim$ 11.3 μm due to SiC.

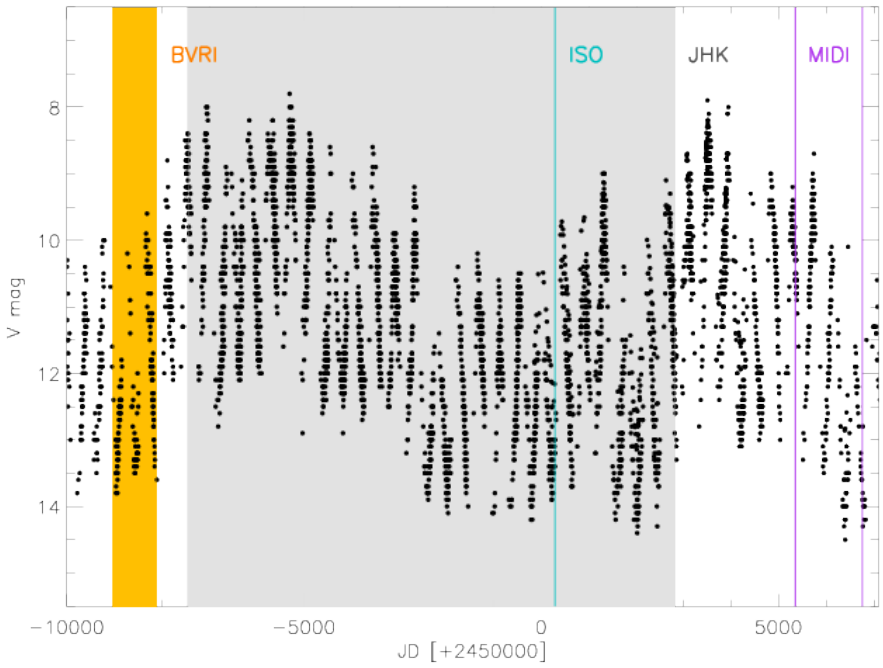

Figure 4.1: AAVSO light curve of RU Vir in black. The grey shadow shows the time range of the $BVRI$ photometry observed by Eggen (1975). The vertical green, blue, and violet lines denote the epoch of the ISO spectrum, JHK photometry, MIDI observation, respectively.

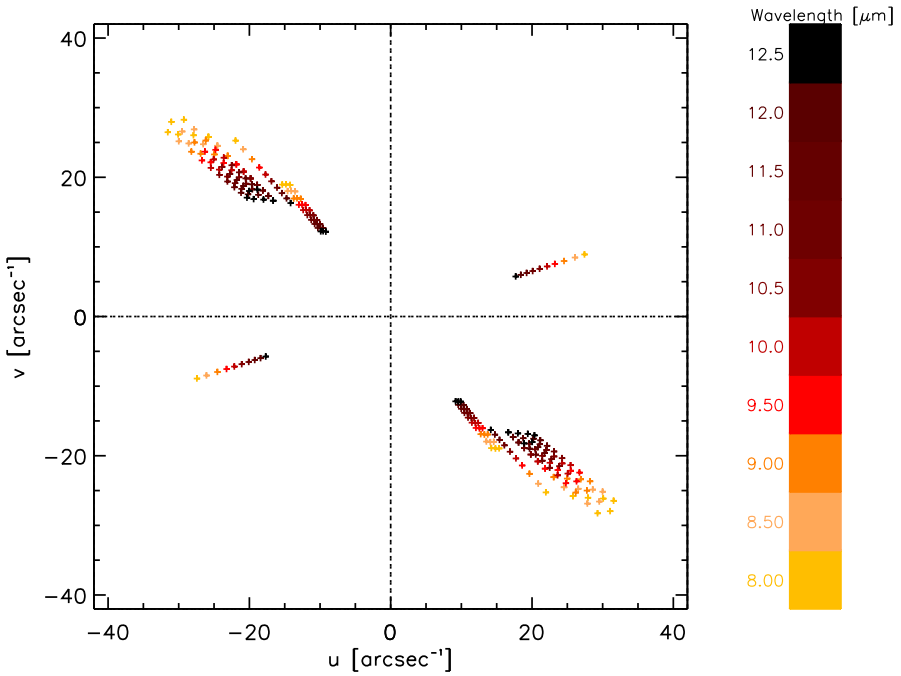

Figure 4.2: *uv*-coverage of the MIDI RU Vir observations listed in Table A.1, dispersed in wavelengths.

.

The difference in position angle between the two sets of the observations (in 2010 and 2014) does not allow us to perform a check for interferometric variability because they do not probe the same spatial frequencies. So far, interferometric variability was observed only for one star (V Oph, Ohnaka et al., 2007); therefore, we decided to analyze the data all at the same time. When it comes to studying the geometry below (Sect. 4.3) we keep in mind that if these two points push for an asymmetric solution, then variability could still be an explanation.

The MIDI differential phase is zero, and the MIDI spectra are shown in Fig. 4.4. The shape of the MIDI spectra agree within the errors with the ISO spectrum. The difference in flux level between the two sets of MIDI observations is typical for C-rich Miras (Hron et al., 1997).

4.3 Geometrical models

Before comparing the model atmospheres and the data, we studied the morphology of the circumstellar environment, interpreting the MIDI interferometric data with geometric models. This has been done by using the geometrical model-fitting tool GEM-FIND (GEometrical Model Fitting for INterferometric Data) of Klotz et al., 2012b. The program fits geometrical models to wavelength-dependent visibilities in the N band, to constrain the morphology and brightness distribution of an object. A detailed description of the fitting strategy and of the χ^2 minimization procedure can be found in Klotz et al. (2012a).

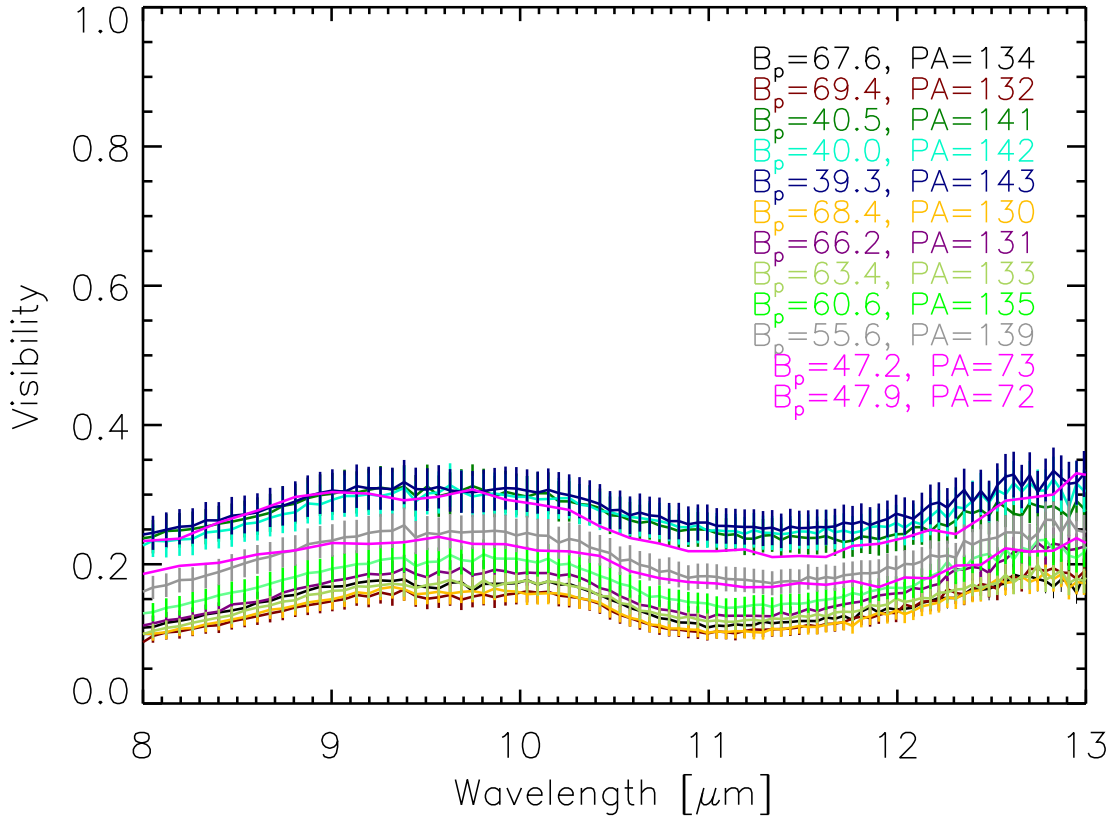

Figure 4.3: RU Vir calibrated visibilities at different baselines and projected angles.

Table 4.2: Parameters of the calibrator targets.

Target	Spectral type	F_{12} [a] [Jy]	Diameter [b] [mas]
HD120323	M4.5III	255.4	13.25 ± 0.060
HD133216	M3/M4III	200.7	11.154 ± 0.046
HD81797	K3II-III	157.6	9.142 ± 0.045

(a)IRAS Point Source Catalog.
(b)`http://www.ster.kuleuven.ac.be/~tijl/MIDI_calibration`

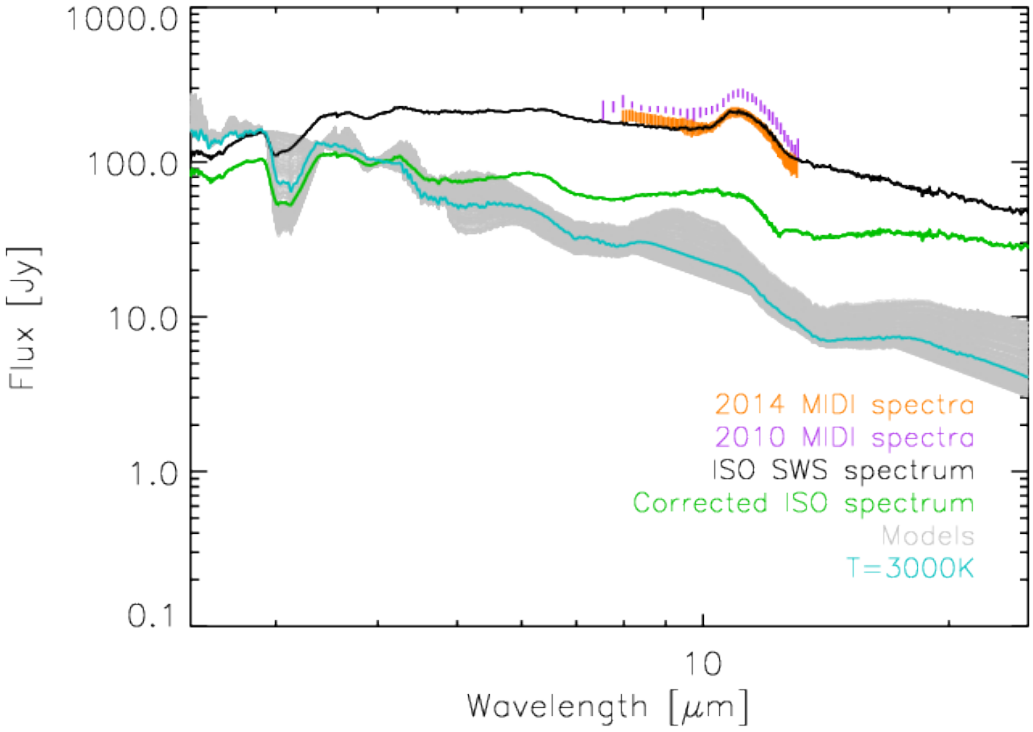

Figure 4.4: Comparison of observational data with modelling results. The black line shows the ISO/SWS spectrum of RU Vir, the green line the SED corrected from dust emission. The orange and violet shadows indicate the MIDI spectra, while the grey one denotes the hydrostatic models grid. The best-fitting hydrostatic model is shown in cyan.

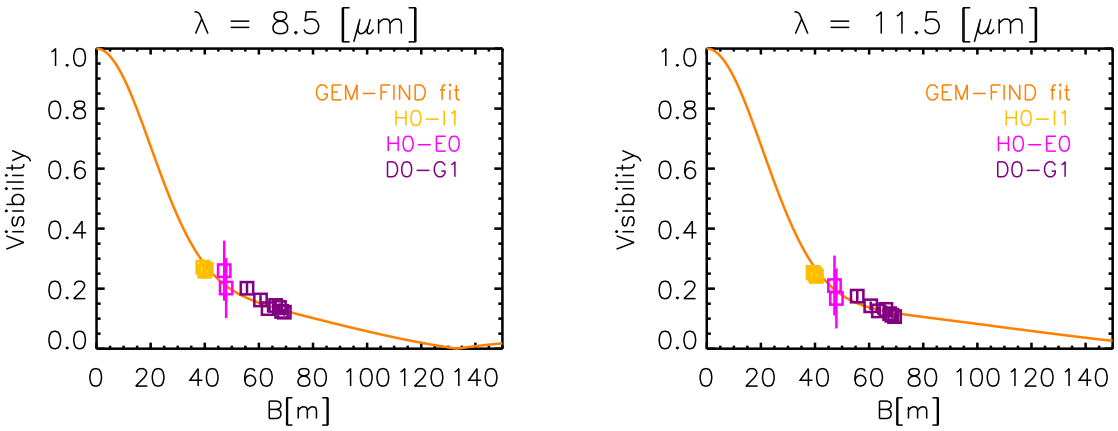

Figure 4.5: Comparison of observational data with the best-fitting geometrical model. The calibrated visibilities are shown versus baseline length for two different wavelengths (left: 8.5 μm; right: 11.5 μm). The symbols represent MIDI observations at three different baseline configurations. The lines show the best-fitting model that consists of a circular UD and a circular Gaussian.

Different models with optically thick (models with one component) or thin (models with two components) circumstellar envelopes were tested. In Table 4.3 we list the corresponding reduced χ^2 values and the parameters fitting best. In the case of elliptic models, the ratio of major and minor axes is shown. The brightness ratio is indicated for the two-component models with a circular uniform disc (UD) and a circular Gaussian. In the latter case, the fit was performed with a fixed value of the angular diameter, to avoid having too many free parameters in the fit. We started the fit of the composite model by imposing that the diameter is equal to the one derived from the $\theta/(V-K)$ relation of van Belle et al. (2013): $\theta = 2.18$ mas. Then we increased the diameter by steps of 2 mas until a $\theta_{\rm max} = 20$ mas.

One-component spherically symmetric and elliptical models have large reduced χ^2 and are not able to reproduce the data. A better fit to the data is obtained by a two-component model, including a circular UD plus a Gaussian distribution of the circular dusty envelope. This yields a reduced $\chi^2_{\rm min}$ of 0.96 for a central star simulated by a UD with angular diameter at 11 μm of 18 mas (see Table 4.3), probably because of molecular opacities. In Fig. 4.3 we show the the visibilities vs. wavelength and in Fig. 4.5 the fit of the visibility vs. baseline at different wavelengths.

In general, the geometric models show that, for the u-v covered by our RU Vir observations, there is no major asymmetry detected.

Table 4.3: GEM-FIND results. For each fit (one or two components), the full width at half maximum and angular diameter at 11 μm are given. When applicable also the ratio of minor and major axis and the brightness ratio are given. The best fitting model is shown in bold face.

Geometric model	$\chi^2_{\mathbf{red}}$	$FWHM_{11}$ [mas]	θ_{11} [mas]	a/b	B_{ratio}
One component					
Circular UD	40.10	···	38.10 ± 0.17	···	···
Circular Gauss	15.42	28.44 ± 0.24	···	···	···
Elliptic UD	12.31	···	177.34 ± 0.77	0.2	···
Elliptic Gauss	5.41	···	56.62 ± 0.44	0.3	···
Two components					
Circ UD+Circ Gauss	1.59	37.88 ± 0.99	2.81 [a]	···	0.12 ± 0.01
Circ UD+Circ Gauss	1.57	38.02 ± 1.01	6.00 [a]	···	0.12 ± 0.01
Circ UD+Circ Gauss	1.53	38.18 ± 1.02	8.00 [a]	···	0.13 ± 0.01
Circ UD+Circ Gauss	1.49	38.38 ± 1.05	10.00 [a]	···	0.13 ± 0.01
Circ UD+Circ Gauss	1.43	38.65 ± 1.08	12.00 [a]	···	0.15 ± 0.01
Circ UD+Circ Gauss	1.35	39.01 ± 1.12	14.00 [a]	···	0.15 ± 0.01
Circ UD+Circ Gauss	1.27	39.47 ± 1.18	16.00 [a]	···	0.17 ± 0.01
Circ UD+Circ Gauss	1.15	40.08 ± 1.12	18.00 [a]	···	0.19 ± 0.01
Circ UD+Circ Gauss	1.01	40.90 ± 1.38	20.00 [a]	···	0.21 ± 0.01

Notes. (a): Models with central star diameter fixed at the values indicated above during the fit.

4.4 Hydrostatic model atmospheres

4.4.1 COMARCS models

Following Sacuto et al. (2011a), we perform the first step of our study first by fitting the ISO spectrum with hydrostatic model atmospheres (COMARCS models, Aringer et al., 2009). Each hydrostatic model is identified by the following initial parameters: mass, effective temperature, C/O, log(g), metallicity. Details about these model atmospheres and the computed spectra are described in Aringer et al. (2009). The resolution of each synthetic spectrum[1] is R = 200 to match the resolution of ISO in the spectral range: $[0.4, 45.0]$ μm.

4.4.2 MOD: More Of Dusty

Since RU Vir is a dust-enshrouded carbon-Mira, we included dust by using the radiative transfer code MOD-More Of Dusty(Groenewegen, 2012). This code is based on DUSTY, which is a publicly available 1 D dust radiative transfer code (Ivezić and Elitzur, 1995), whose mathematical formulation is described in detail in Ivezić et al. (1997). MOD tries to optimize a set of parameters (e.g. luminosity, dust optical depth, dust condensation temperature, and slope of the density law) with some constraints as spectro- photometric-data, 1D intensity profiles and visibility curves. A quantitative measure of the quality of the fit is obtained through performing a χ^2 minimization, where the χ^2 are computed separately for all the four types of observations (see Table 4.4). We note at this point that the dust condensation temperature in this context actually is the dust temperature at the inner boundary of the dust shell. Following previous work (e.g. Groenewegen, 2012) we call it the dust condensation temperature.

Following Sacuto et al. (2011a), we use a mixture of 90 % AmC and 10 % SiC for the dust composition. This ratio gave the best results for the ISO/SWS spectrum of the carbon star R Scl. Fits for RU Vir with a lower SiC fraction were not as good. The optical constants for the opacities of silicon carbide are taken from Pitman et al. (2008) and of amorphous carbon from Rouleau and Martin (1991). Since the standard grain size distribution of DUSTY produced SiC features that were much too peaked, we used the distribution of hollow spheres (DHS, Groenewegen, 2012 and references therein) with a mean grain size of the dust mixture of 0.2 μm. This grain size is similar to the typical sizes found from models for dust-driven mass loss (Mattsson and Höfner, 2011). However, we note that these models only include amorphous carbon grains. On the other hand, the SiC grains found in presolar meteorites have sizes of the order of 1 μm (e.g. Gail and Sedlmayr, 2013), indicating that our mean size falls in the range of laboratory data. The chosen grain size distribution then gave a good fit of the SiC feature.

4.4.3 The fitting procedure

The hydrostatic models alone are not able to reproduce the ISO spectrum. This is because the hydrostatic models do not include dust, while the dust content in the atmosphere of RU Vir is

[1] Available at `http://stev.oapd.inaf.it/synphot/Cstars/`

Table 4.4: Output values of MOD fitting for three different cases. The parameters are luminosity L, optical depth τ, dust condensation temperature T_c, and parameter of the slope of the density law p. The last four lines show the reduced χ^2 for the fit of: photometry, spectroscopy, interferometric visibilities, and then the total one.

	$T_c^* = 1000$ K	$T_c^* = 1300$ K	all free
L $[L_\odot]$	6118.05 ± 32.54	5770 ± 28.02	6322.66 ± 51.07
τ	7.96 ± 0.10	12.52 ± 0.15	7.11 ± 0.24
T_c [K]	1000	1300	1008.68 ± 12.27
p	2.54 ± 0.01	2.19 ± 0.01	2.28 ± 0.01
χ^2_{red}[pho]	22.41	63.31	9.86
χ^2_{red}[spe]	3.35	3.66	5.63
χ^2_{red}[int]	60.13	161.77	65.88
χ^2_{red}[TOT]	6.12	11.56	7.90

Notes. Parameters without errors were fixed (not fitted) in MOD. See Sect 4.4 for details.

quite prominent, as the spectral energy distribution from ISO/SWS shows (see Fig. 4.4, black line). In the following, we use the hydrostatic model atmosphere as the inner radiation source for MOD. The model parameters are selected as described below. Considering that RU Vir is located in the vicinity of the Sun, a first selection of the hydrostatic models was made by choosing only those models with solar metallicity. With the aim of being independent of the distance, each hydrostatic model spectrum was normalized to the ISO flux at 2.9 μm. We chose this wavelength because the local minimum of the molecular absorption resides here (Aringer et al., 2009).

We constrained the effective temperature of RU Vir by fitting the ISO spectrum with the synthetic spectra and by performing a χ^2 minimization in the range $[2.9, 3.6]$ μm. The molecular features in this wavelength range are good temperature indicators for hydrostatic C stars (Jørgensen et al., 2000), and they provide a first approximation for our case. The result obtained in this way is $T = 3100 \pm 100$ K. The C/O is set to C/O= 2.0, because this value is the one corresponding to the lowest χ^2 in the wavelength region above. Figure 4.6 illustrates the χ^2 vs. $T_{\rm eff}$ in the wavelength range chosen as the best for the parameter determination; the best-fitting value is located at the minimum of the χ^2.

We proceed by including the dust component with MOD a posteriori, as described below. With MOD we fit the photometry (see Sect. 4.2.2), spectroscopy (see Sect. 4.2.1), and interferometry (see Sect. 4.2.3) of the star. The input parameters of MOD are effective temperature (determined with the hydrostatic model atmosphere fit), distance, and the dust properties. The optical depth τ, the parameter that governs the shape of the density law p, and the dust condensation temperature T_c can be fitted or set to a fixed value.

An iterative procedure was used to assess how much the spectrum used for the inner radiation source is affected by dust emission. We determined a "corrected" ISO spectrum by performing a MOD fit using the 3100 K spectrum (see Fig. 4.4) derived above. We then subtracted the contribution of the dust emission at each wavelength from the total flux, in this way obtaining

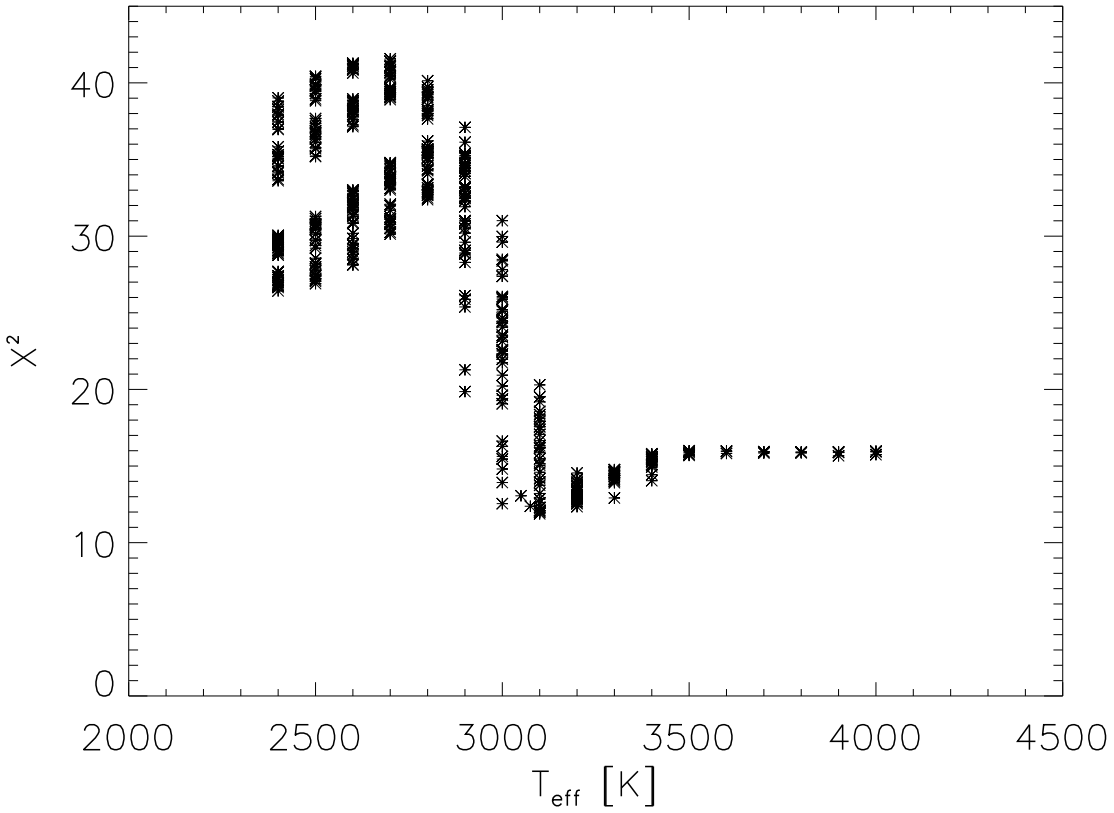

Figure 4.6: Results of the χ^2 fitting for the effective temperature and of the synthetic spectra based on COMARCS models with the ISO spectrum. The fit is done in the range of $[2.9, 3.6]$ μm.

a stellar photospheric contribution. Repeating the effective temperature determination results in a best-fit model atmosphere with an effective temperature of 3000 K, i.e. only slightly cooler than the first estimate. This model spectrum was then used for the remaining calculations. We note that the corrected ISO spectrum has its maximum flux at a longer wavelength than the hydrostatic model, but the depth of the 3 μm feature is very similar to the model. This indicates that any difference between the corrected and the original ISO spectrum is caused by residual dust emission and not by an incorrect model temperature.

As there is no generally agreed value of the dust condensation temperature in the literature, we performed the fit using three different T_c values: (i) $T_c = 1000\ K$, based on the theoretical equilibrium condensation temperature from Gail and Sedlmayr (2013); (ii) $T_c = 1300\ K$, an average of the dust condensation temperature values from Nowotny et al., 2011 and from Lobel et al., 1999; (iii) finally we allowed all the input parameters to vary freely in order to verify the behaviour of the models. The results are shown in Table 4.4.

To check the relevance of the ISO spectrum for the final result of the MOD fit, we made some experiments using a coarser sampled ISO spectrum and artificially increasing the error associated with the ISO spectrum. These tests show that the full ISO spectrum is essential for constraining the parameters of the dust envelope. Nevertheless, the real uncertainties of the dust parameters are considerably higher than their formal errors.

In Fig. 4.7 we present the comparison between the photometry (violet circles), the spectroscopy (blue line), and the SED of the best-fitting model. We note that the photometry shortwards of 1 μm cannot be well reproduced even if a maximum of free parameters is allowed. A hotter effective temperature cannot solve this discrepancy because it would be incompatible with the strength of the molecular features in the ISO spectrum. Figure 4.8 shows the comparison between MOD visibilities (lines) and observed visibilities (circles). Since RU Vir observed visibilities do not depend strongly on the wavelength, we selected only the two wavelengths corresponding to the maximum and minimum visibility (Fig. 4.3).

Comparing the spatial frequencies at a given visibility level, one can conclude that the model is roughly a factor 2 too small. The visibilities could be brought to agreement by assuming a distance of $\sim$ 300 pc, but this is unrealistically small. Therefore we have to conclude that the model is not extended enough or is missing a component. Another possibility is a difference between the observed and synthetic brightness contrast of multiple shells.

In the following we compare the observations with the dynamic model atmospheres (DMAs), which in principle would provide a more complete and physically consistent description of RU Vir.

4.5 Dynamic model atmospheres

In this section we present the analysis made by using the DMAs from Mattsson et al. (2010) and model spectra from Eriksson et al. (2014). For a detailed description of the modelling approach see Höfner and Dorfi (1997), Höfner (1999), Höfner et al. (2003), Mattsson et al. (2010), and Eriksson et al. (2014)). For applications to observations we refer the reader to Loidl

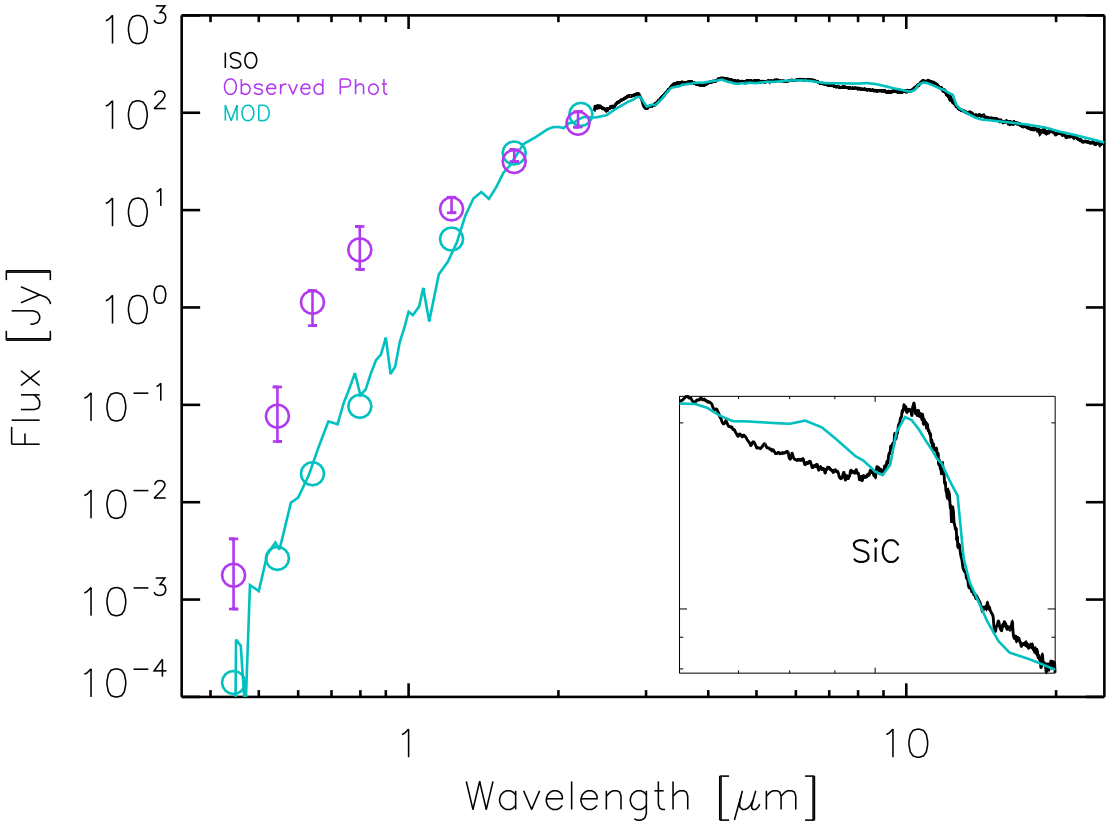

Figure 4.7: Comparison of observed photometry (Table 4.2.2) and spectroscopy with the best-fitting synthetic spectrum based on hydrostatic model atmospheres and a dusty envelope (see Table 4.4 + Sect. 4.5.1).

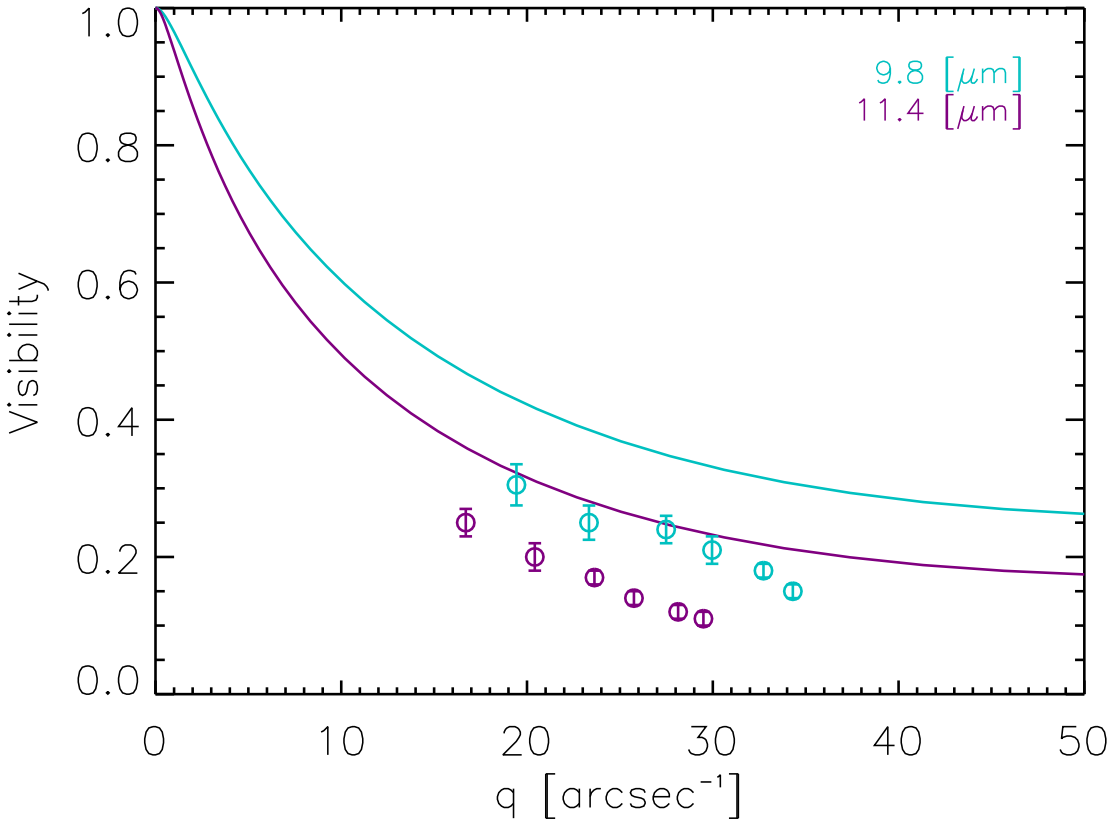

Figure 4.8: Comparison of MOD visibilities (lines) compared with the VLTI/MIDI observations of RU Vir (circles) at 9.8 μm (blue) and 11.4 μm (violet).

et al. (1999), Gautschy-Loidl et al. (2004), Nowotny et al. (2010), and Nowotny et al. (2011). Those models are the result of solving the system of equations for hydrodynamics, frequency-dependent, and spherically symmetric radiative transfer, plus a set of equations that describe the time-dependent dust grains formation, growth, and evaporation. The dynamic model starts from an initial hydrostatic structure. The stellar pulsation is introduced by a "piston", i.e. a variable inner boundary below the stellar photosphere, while the dust formation (only amorphous carbon) is evaluated by the "method of moments" (Gauger et al., 1990; Gail and Sedlmayr, 1988).

The main parameters that characterize the DMA are luminosity L, effective temperature $T_{\rm eff}$ (corresponding Rosseland radius, defined by the distance from the center of the star to the layer at which the Rosseland optical depth equals unity), [Fe/H], C/O, as well as for the dynamical aspects period P, piston velocity amplitude $\Delta_{\rm u}$, and the parameter f_L used to adjust the luminosity amplitude of the model. The resulting proprieties of the hydrodynamic calculations are the mean degree of condensation, wind velocity, and the mass-loss rate. Each model provides a set of "time steps", representing the different phases of the stellar pulsation.

We computed synthetic spectra using the COMA code and the associated radiative transfer (Aringer, 2000; Aringer et al., 2009). The abundances of all the relevant atomic, molecular, and dust species were computed, starting from temperature-density structure and considering the equilibrium for ionization and molecule formation. Both the continuous gas opacity and the intensities of atomic and molecular spectral lines are subsequently calculated assuming LTE. The corresponding data are consistent with the ones used for constructing the models and are listed in Cristallo et al. (2007) and Aringer et al. (2009). SiC is added a posteriori with COMA by dividing the condensed material from the model into 90 % amorphous carbon using data from (Rouleau and Martin, 1991) and 10 % silicon carbide based on (Pegourie, 1988).

To be consistent with the model spectra from Eriksson et al. (2014), we have treated all grain opacities in small particle limit[2] (SPL). The temperature of the SiC particles was assumed to be equal to the one of amorphous carbon. This is justified, since the overall distribution of the absorption is quite similar for both species, except for the SiC feature around 11.4 μm. As a consequence, the addition of SiC would also not cause significant changes in the thermal model structure. It should be noted that the effects of scattering are not included, since the SPL is adopted.

4.5.1 The fitting procedure

Given the difficulties of MOD to reproduce the photometry, and the fact that the ISO/SWS spectrum provides the strongest constraints for gas *and* dust, we decided to first base the comparison with DMA only on the ISO/SWS spectrum. Thus we performed a χ^2 minimization in the wavelength range: $2.9 - 25$ μm between spectroscopic observation (ISO/SWS spectrum) and each of the 540 models of the grid (with a total of $\sim$ 140 000 time steps). Based on the χ^2 we obtain a best-fitting time step for each model.

[2] An inconsistent treatment of grain opacities causes larger errors in the results than does neglecting the grain sizes.

Table 4.5: The table shows the parameters values for the selected models from the grid of Mattsson et al. (2010).

$T_{eff}[K]$	$lg\ L_\star[L_\odot]$	$M[M_\odot]$	$log\ g$	C/O	Δu_p	f_L	$\dot{M}[M_\odot/yr]$	$\chi^2_{[2.9-25.0]}$
2600	3.85	1	-0.81	2.38	6	1	5.74E-06	17.5
2600	4.00	1.5	-0.79	1.69	6	1	6.75E-06	37.4
2600	4.00	1.5	-0.79	2.38	6	1	1.05E-05	10.2
2600	4.00	1	-0.96	1.69	6	1	7.32E-06	15.5
2600	4.00	1	-0.96	2.38	4	1	9.13E-06	10.9
2600	4.00	1	-0.96	2.38	6	1	1.07E-05	9.8
2600	3.85	1.5	-0.64	1.69	6	1	2.60E-06	69.3
2600	3.85	1.0	-0.81	1.69	6	1	3.34E-06	74.2
2800	3.85	1.0	-0.51	1.69	6	1	2.25E-06	82.9
2800	4.00	1.5	-0.66	1.69	6	1	2.02E-06	115.2
2800	4.00	1.0	-0.84	1.69	4	1	3.25E-06	113.2
2800	4.00	1.0	-0.84	1.69	6	1	4.77E-06	82.8
2600	3.85	1.0	-0.81	1.69	4	2	2.43E-06	92.7
2600	3.85	1.0	-0.81	1.69	4	2	2.43E-06	76.9
2600	3.85	1.5	-0.64	1.69	4	2	3.11E-06	94.5
2600	3.85	1.5	-0.64	1.69	4	2	3.11E-06	93.7
2800	4.00	1.0	-0.84	1.69	4	2	2.98E-06	78.3
2800	4.00	1.0	-0.84	1.69	4	2	2.98E-06	69.4
3000	3.85	1.0	-0.57	2.38	6	1	3.85E-06	96.7

First, based on the parameters determined in the previous analysis, a subgrid from the grid of models (Eriksson et al., 2014; Mattsson et al., 2010) was selected. We also consider only models with solar metallicity. We present in Table 4.5 the results of this fit in the wavelengths region $[2.9 - 25.0\ \mu\text{m}]$.

Since the choose of the subgrid, i.e. the range of the parameters, was not correct, we perform as a second approach the analysis over the whole grid of models.
In Fig. 4.9, the χ^2 vs. average outflow velocity at the outer boundary and vs. mass loss are shown. In Table 4.6 we list the parameters of the best three time steps of the whole grid and the corresponding χ^2. These time steps cover the 68% confidence region of χ^2. The relevant SEDs, without SiC added, are shown in the left-hand panel of Fig. 4.10. The right-hand panel shows in grey all the time steps of the model that belong to the best-fitting time step ($\chi^2 = 9.79$). This best fitting time-step is marked in pink, now with the artificial inclusion of SiC (see also inset in Fig. 4.10).

There is good agreement between models and observations in the spectral range of the ISO spectrum. Even based on this broad range of $\sim$ 140 000 time steps, it is not possible to reproduce the photometry shortwards of 1μm. Possible explanations for this disagreement are discussed in Sect. 4.6.

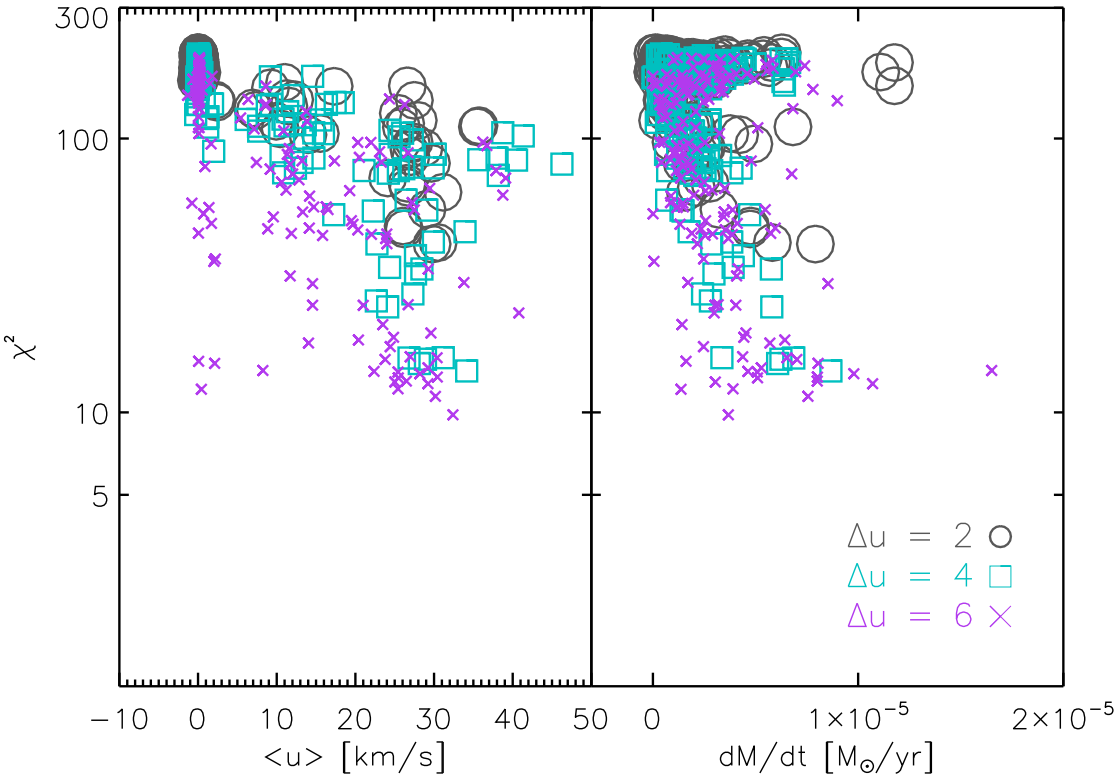

Figure 4.9: Reduced $\chi^2_{\rm red}$ vs. average outflow velocity at the outer boundary and vs. mass loss. Different symbols and colours are used for different piston velocities: 2, 4, 6.

Table 4.6: Three best-fitting time-step dynamic models from the whole grid from Eriksson et al. (2014) resulting from comparison in Sect. 4.5.2. Listed are the corresponding values of the χ^2 for the best-fitting time steps, the parameters, and the phase ϕ.

$T_{\rm eff}$ [K]	$lg\ L_\star$ [$L_\odot$]	M [$M_\odot$]	$log\ g$	C/O	Δu_p	f_L	$\dot{M}$ [$M_\odot/yr$]	ϕ	$\chi^2{}_{\rm red[0.4-25]}$
2800	4.00	1.5	-0.66	2.38	6	2	3.68E-06	6.50	9.79
2800	4.00	1	-0.84	2.38	6	2	7.56E-06	0.53	11.44
2600	4.00	1	-0.96	2.38	6	2	1.44E-05	3.40	12.72

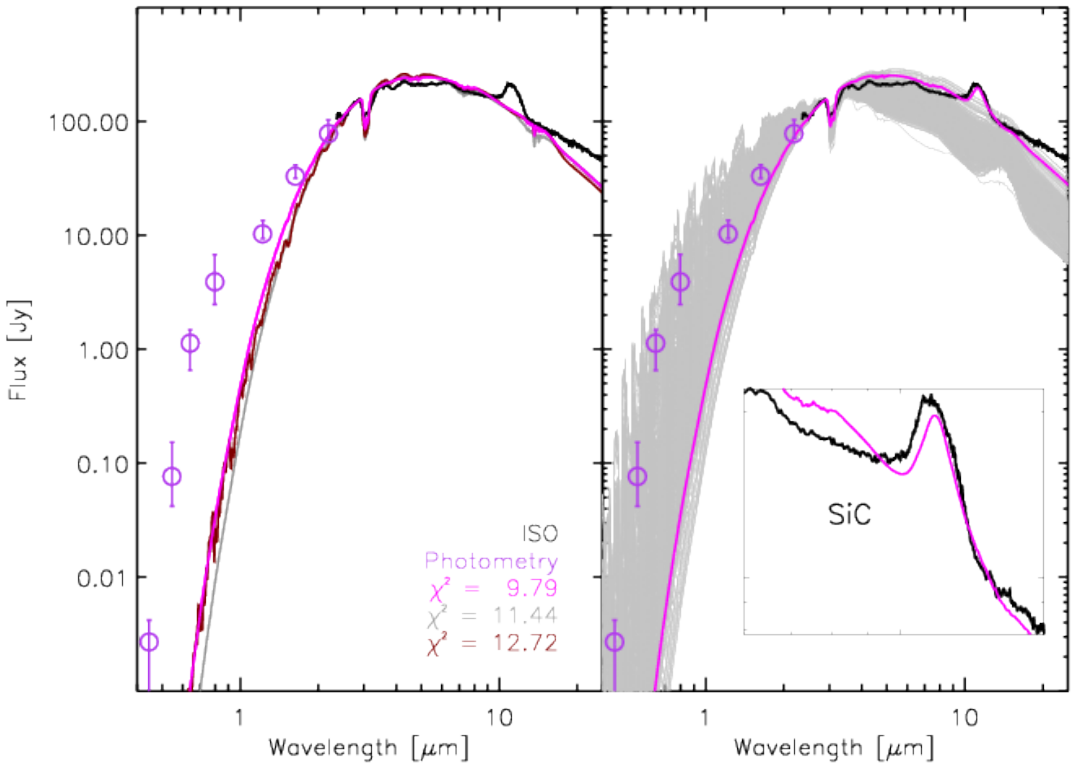

Figure 4.10: Left: Observational data (ISO spectrum in black line and photometry in violet circles) compared with synthetic spectra of the three best-fitting time steps (belonging to different DMA). Right: Best-fitting time step (pink) compared with ISO (black). The grey lines are the various other phases (time steps) of the same model.

4.5.2 MIDI data vs. DMA

Following Paladini et al. (2009), we calculated the intensity and visibility profiles for all the time steps of the best-fitting DMA derived in Sect. 4.5.1.We combined all the interferometric data (even though they are taken at different epochs, see Sect. 4.2.3), and we performed a χ^2 test to obtain the best-fitting visibility profile. We obtained a new best-fitting time step for the visibilities observations of RU Vir, different from the one fitting the ISO spectrum best.

The time step best fitting the visibility is shown in Fig. 4.11. The upper panels illustrate the behaviour of the intensity profiles at two wavelengths (8.5 and 11.4 μm), while the lower panels show the visibility vs. spatial frequencies. The phase of the best-fitting time step is 0.24, i.e. slightly different from that one best fitting the SED (see Sect. 4.6). The best-fitting time step has a Rosseland radius of 2.561 mas (500.9 $R_\odot$) and a luminosity of 3982.8 $L_\odot$.

The intensities are characterized by a first lobe (the photosphere with the hotter molecular gas) followed by two shells. The first shell is brighter at 11.4 μm, where SiC contributes. While at short wavelengths (lower left panel) the visibility can reproduce the data, at long wavelengths (lower right panel) the model is off. The size of the model stays the same ($\sim$ 20 AU), but the flux ratio between the different components is changing.

The discrepancy between the model and the data is also observed when plotting the wavelength dependent visibility for the three baseline configurations (Fig. 4.12). While at short wavelengths ($8 - 9$ μm), the synthetic visibilities match the level of the observations, at longer wavelengths there is a slope in the model that is not observed in the data. The differences between model and observations are more pronounced when the baselines are shorter.

4.6 Discussion of the results and outlook

While all our attempts to reproduce the SED (ISO spectrum + photometry) and interferometric MIDI data by different models showed some agreement, three major discrepancies remain: (1) No model can describe both the optical part and the infrared part of the SED. This may be interpreted either as an excess in the optical or beyond 2 μm. (2) The model visibilities show higher values and/or a different behaviour as a function of wavelength than the MIDI data. (3) The DMA predict fluxes that are too low beyond 14 μm.

Since (1) and (2) apply to all model approaches, we believe that this is mostly caused by properties of the object that can be described neither by the rather flexible MOD approach nor by the physically consistent DMA (see Sects. 4.6.2 and 4.6.3). In the following, we compare our results with previous work and discuss possible reasons for the discrepancies.

4.6.1 Stellar parameters

As described in Sects. 4.4 and 4.5, stellar parameters were derived from the fit of synthetic spectra based on COMARCS hydrostatic models + MOD to the observations (see Fig. 4.7) and from the study of the SED and MIDI data with the DMAs. The best-fitting **optical depth**

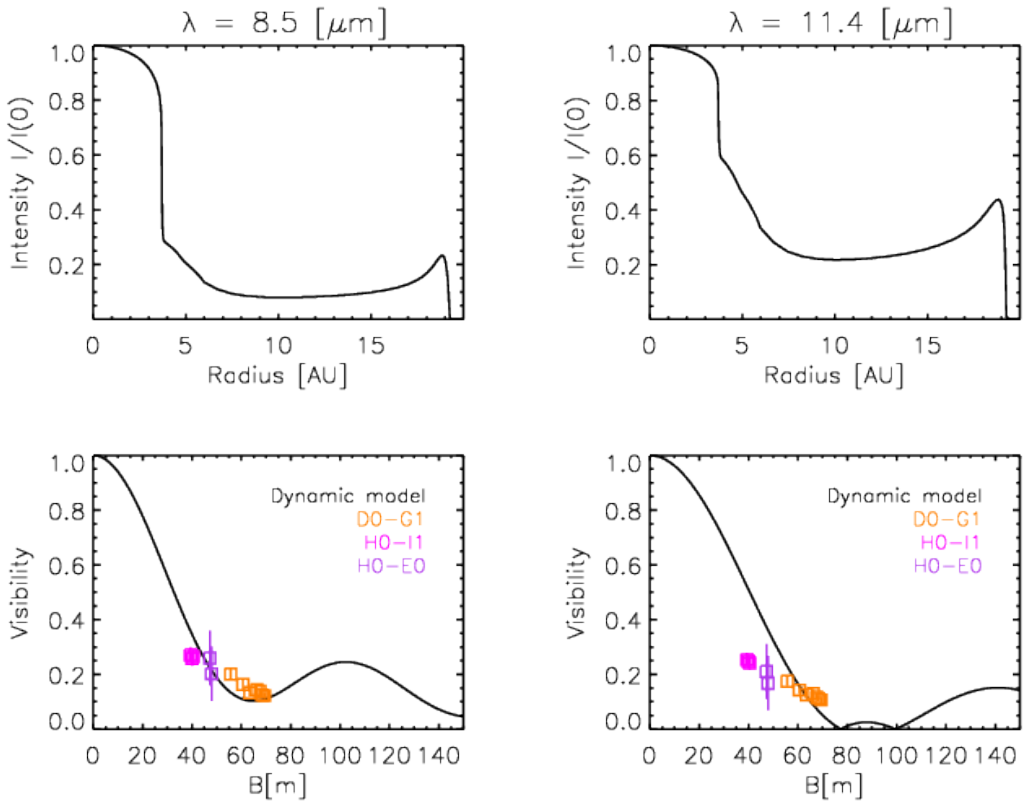

Figure 4.11: Comparison of interferometric observational data for RU Vir with the modelling results based on the DMA that best-fit the visibilities. **Up**: intensity profile at two different wavelengths: 8.5 μm and 11.4 μm. **Down**: visibility vs. baseline; the black line shows the dynamic model, and the coloured symbols illustrate the MIDI measurements at different baselines configurations.

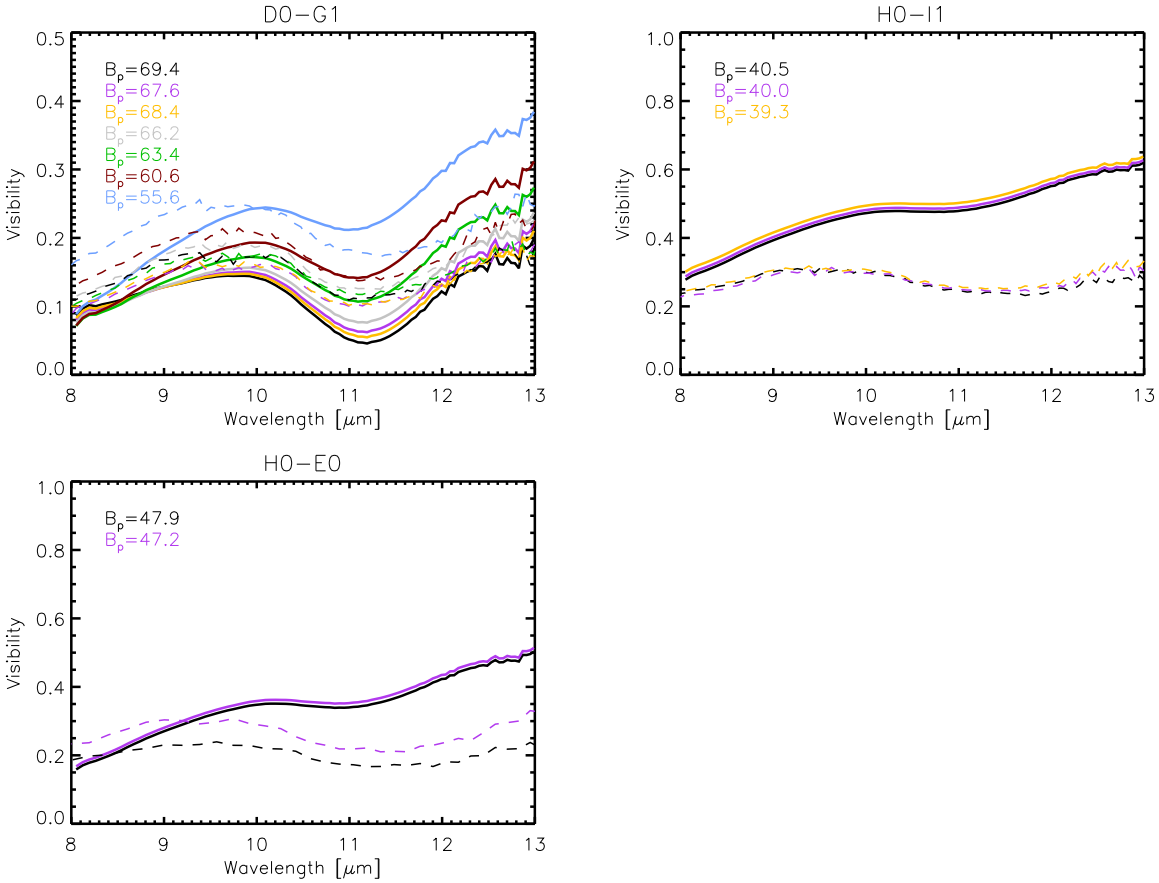

Figure 4.12: Wavelength-dependent visibilities in the MIDI range. The different panels show the three different baseline configurations of our observations. Models are plotted in full line and observations in dashed lines at different projected baselines (see colour legend).

value resulting from this work is $\tau_{0.55} = 7.96 \pm 0.10$ at $\lambda = 0.55$ μm. Lorenz-Martins et al. (2001) find $\tau = 2.5$ at 1 μm. Ivezić and Elitzur (1995) indicate an optical depth value at the wavelength $\lambda = 2.2$ μm of $\tau_{2.2} = 0.47$. Assuming $\tau_\lambda \propto 1/\lambda$ and scaling the above literature results to 0.55 μ, we arrive at 4.5 and 1.9, respectively. Our value is significantly higher, but our result is based on a broader and much better sampled SED, which should explain the differences.

The **Rosseland radius** of the best-fitting time step(s) of $\sim$ 2.6 mas is close to the ones derived from the diameter $(V - K)$ relations of van Belle (1999) and van Belle et al. (2013): 2.7 mas and 2.81 mas, respectively. The intensity distribution of the DMA (Fig. 4.11) has a radius of $\sim$20 mas, which is comparable to the **half width half maximum (HWHM)** resulting from the GEM-FIND fit. If we adopt these numbers for the photospheric (stellar) and outer envelope radius, we can conclude that we are observing the stratification of the star out to $\sim 6 - 7$ $R_\star$. Moreover, the agreement of the GEM-FIND radius with the DMA radius supports the fact that the discrepancy between the MIDI data and the DMA are due to different flux ratios between the various shells in the photosphere and envelope, rather than a global difference in size.

The **effective temperature** is a parameter that distinguishes the different DMAs. Literature values for RU Vir are in the range: $[1945 - 2200]$ K (Bergeat and Chevallier, 2005; Lorenz-Martins et al., 2001). These values agree with the one derived from the Rosseland radius of the time step that fits the SED ($T_{\rm eff} = 2050$ K), while the value obtained for the MIDI fit is slightly higher ($T_{\rm eff} = 2545$ K). Both temperatures are lower than the ones derived from fitting a static model to the C_2H_2 feature in the $[2.9, 3.6]$ μm region (3000 K) and than the static initial model of the best-fitting DMAs (2800 K). As elaborated in Nowotny et al. (2005b), dynamic effects can cause the atmospheric structure of DMAs to be fundamentally different from any static model, including the static initial model of the DMAs. Therefore, a $T_{\rm eff}$ derived from fitting a static model atmosphere to observations is only very indirectly linked to the T_{eff} of the static initial model of the best-fitting DMA, so a comparison between the two is somewhat misleading in general. In the case of the strongly pulsating atmosphere of RU Vir and especially for the $[2.9, 3.6]$ μm region that we are fitting, this is particularly relevant (Loidl et al., 1999). We also note that DMAs with $T_{eff} = 3000$ K often do not yield the outflow required to reproduce the SED of RU Vir (e.g. Eriksson et al., 2014). Given the highly non-static atmospheric structure of the DMA, there is no straightforward relation between these different temperatures, but the results indicate that the $[2.9, 3.6]$ μm region is a reasonable indicator for the (static) effective temperature.

Finally, the **mass** of the best-fitting dynamic model is 1.5 $M_\odot$. This value agrees with the 1.48 $M_\odot$ obtained from the period-mass-radius relation of Vassiliadis and Wood (1993).

4.6.2 Shape of the SED

Given the success of both models in reproducing the IR part of the SED, we consider an optical excess flux to be more likely than an IR excess and will discuss this option first. The flux difference between observed photometry and the models (spectroscopy) in the V band is at least a factor of $\sim$ 10 in the SED. The quality of those used $BVRI$ data appears to be high as judged

from later measurements, such as Alfonso-Garzón et al. (2012). This author shows a light curve that, at the phase of the ISO spectrum, has $V \approx 11.6$. This value is even brighter than the one used in the SED (see Table 4.1); moreover, the amplitude in the same band is $\sim$ 2 mag, and this can still not justify our excess in V.

A much hotter temperature of the Mira photosphere can be ruled out as the origin of the excess on the basis of the strength of the molecular features around 3 μm. Assuming a contribution from a companion would thus be the most obvious possibility. However, the optical spectrum (e.g. Barnbaum, 1992) shows no signatures from another star and no emission lines as is typical of a symbiotic system (Welty and Wade, 1995). RU Vir has a GALEX NUV-flux but no FUV-flux (Bianchi et al., 2014). Based on this flux and the predictions for white dwarf models (Bianchi et al., 2011), one can exclude the presence of a white dwarf. One may also use the V and I magnitudes to assess the properties of a possible companion. However, after correcting V and I for the contribution from the dusty envelope as fitted with MOD, the resulting $(V - I)$ and M_V cannot be reconciled with any main sequence companion. Therefore a stellar companion cannot explain the SED shape.

The presence of a sub-stellar companion that is not seen in the optical spectrum may, however, imply the presence of a dusty disk that would produce excess emission in the IR. A star like V Hya would be a possible template (Sahai et al., 2008). The above-mentioned GALEX flux is, however, a few orders of magnitude lower than what is expected for such an evolved star with an accretion disk. As is evident from the MOD fit, the optical and near-IR parts of the SED do not show the amount of reddening as expected from the dust emission seen at longer wavelengths. Therefore any disk must not obscure the stellar photosphere, meaning it should be seen almost face on. This would also be the only disk orientation compatible with the lack of evidence for asymmetries from the MIDI data. We thus consider a disk as a very unlikely explanation.

One aspect that has not been discussed so far is that the optical photometry and the ISO spectrum were obtained many different pulsation cycles apart. While we have interpolated the optical and IR photometry to the pulsation phase of the ISO spectrum, this cannot correct for any cycle-to-cycle differences. As mentioned in Sect. 4.2.2, RU Vir has a long secondary period in the optical, which could be an indication for such inter-cycle variations. Interestingly, our best-fitting DMA also has notable inter-cycle variations. However, the optical and ISO data were obtained at similar phases of the long-term optical changes. Therefore, to explain the full SED with our best-fitting DMA model, inter-cycle variations and a rather large phase uncertainty within a cycle have to be combined.

It is known that there are differences between visual phases and DMA model phases and that these differences, as well as the effects of cycle-to-cycle variations, increase towards shorter wavelengths (Nowotny et al., 2011). Therefore intra-cycle variations, together with phase assignment uncertainties, might improve the agreement between the observed and the DMA SEDs but are probably not enough. Obtaining a broad SED within one pulsation cycle would be the only way to verify this.

4.6.3 The visibilities

While the shape of the MOD visibilities are similar to the observations, the systematically lower observed level cannot be achieved by assuming a reasonable smaller distance (Sect. 4.4). Reducing the dust condensation temperature can lower the visibilities but produces the wrong shape. Therefore we believe that a simple two-component MOD model (star plus envelope with a single power law for the density) cannot reproduce the visibilities.

With regard to the slope of the DMA visibilities, we identify two possible explanations for the discrepancies observed.

(i) The first one is related to the model. The models with high mass-loss rates produce a shell-like gas (and dust) component that is not observed in the data, i.e. the actual density distribution is smoother. This explanation is supported by the fact that models that do not produce a wind also do not exhibit the kind of slope seen in the best-fit DMA. An example of the visibility of this kind of model is shown in Sacuto et al. (2011a). A comprehensive comparison of the dynamic model grid with interferometric observations of dusty and dust-free objects will be able to exclude or confirm this hypothesis.

(ii) Besides this explanation, another possibility is that the environment around the star is clumpy. This might also explain the lack of reddening mentioned in Sect. 4.6.2. Because of the presence of clumps, the shells appear fainter than what is predicted by the model. On the other hand, we do not observe any signal of clumps (i.e. departure from asymmetries) in the MIDI differential phases. Future observations with the second-generation VLTI instrument MATISSE will provide differential phases but also closure phases that will be more sensitive to small asymmetries. This kind of observation will be able to confirm the presence of clumps.

The differences between synthetic visibilities based on the DMA and MIDI visibilities around the SiC feature are most pronounced for the longest baselines, i.e. closest to the star. Since the formation process of SiC is not really known, the calculations assume that the SiC abundance scales with the amorphous carbon abundance as provided by the DMA. The above differences indicate that SiC could form farther in and/or in a smaller amount, but this has to be confirmed by comparisons based on a larger sample of stars.

That the model phases best fitting the SED and the visibilities are different is probably caused by the above-mentioned cycle-to-cycle variations of the best DMA model. In the MIDI-range these variations are comparable to the intra-cycle variations, meaning that a certain pulsation phase within one cycle may give similar visibility profiles as a different phase in another cycle. To investigate on those cycle-to-cycle and intra-cycle variations, we perform an analysis of the synthetic visibilities grouping them by phases and epoques. This is shown in Appendix A.1.1.

4.6.4 The flux beyond 14 μm

The long-wavelength region of the SED can be reproduced well with MOD, while the DMA always predicts too steep a decline in flux towards the longest wavelengths. Tests have shown that an extension of the DMA farther out cannot account for this difference. Assuming a smoother

density distribution of the DMA, as already argued from the visibilities and as present in the MOD model, should increase the dust emission at longer wavelengths. A more extensive comparison between DMA and a larger sample of C-rich Miras (Rau et al., in prep.) is needed to check whether the difference beyond 14 μm is found only in RU Vir or is a general characteristic of DMAs.

A higher mass loss in the past might be an explanation for this, although the shell parameters from MOD are close to a stationary wind solution. If the mass loss has even stopped in the recent past, this might also account for the overall differences in the shape of the SED because a very small mass loss now should shift the emission from circumstellar dust to longer wavelengths. However, besides the good fit with a stationary wind, a higher mass loss in the past would affect the visual light curve. But the average visual magnitude and the period have been stable over the past $\sim$ 100 years, and therefore such a scenario is also not very likely.

4.6.5 Conclusions and outlook

As demonstrated in this study, the joint use of photometry, spectroscopy, and interferometry and a comparison with models is essential to achieve a full understanding of the atmospheres of AGB stars. In this work we presented a study of the atmosphere of the Mira C-rich star RU Vir. We combined spectroscopic photometric and interferometric observations and hydrostatic and dynamic model atmospheres, as well as simple geometrical models. Until now, the only studies with a similar approach to the one in the present study are those by Sacuto et al. (2011a) on R Scl and RT Vir Sacuto et al. (2013) on RT Vir. While R Scl is a semi-regular pulsating star and RT Vir an M-type star, RU Vir is the first carbon-rich Mira variable for which photometry, spectroscopy, and interferometry are compared to DMAs. Studying C-rich stars is particularly important since DMAs are more advanced for the C-rich stars than for the O-rich stars, because the dust formation process is considered to be simpler and better understood in the C-rich case (Nowotny et al., 2010, 2011).

The HWHM derived by the GEM-FIND fitting shows overall agreement with the DMA size in the N band (see Sect. 4.6.1). Furthermore, the Rosseland radius corresponding to the time step that best fits the interferometric data is in agreement with the diameter derived via the $(V-K)$ relation by van Belle (1999) and van Belle et al. (2013). The fitted effective temperature of the best-fitting DMA time steps is in the range of previous observational estimates but much lower than the temperature of the hydrostatic model of Sect. 4.4.3 and of the initial model of the best-fitting DMA.

The shape of the SED in the ISO range can be reproduced well with both MOD and DMA, and some discrepancies remain shortwards of 2 μm and longwards of 14 μm. A similar situation exists with regard to the interferometric data, both in the shape and in the visibility level. Some of the discrepancies might be explained by a combination of intra- and inter-cycle differences since the observations are spread over many pulsation cycles and both the star and the best-fitting DMA show inter-cycle variations. Other possible reasons could be a decrease in mass loss over the last few hundred years or a sub-stellar companion associated with a dusty disk. However,

these scenarios are not considered to be very likely, and to check them, further observations and modelling are both necessary. Based on the current work, we suspect that RU Vir is a somewhat peculiar object. Extending the comparison between models and observations to a larger sample of C-rich Mira variables (Rau et al., in prep.) will be necessary to clarify this, and will provide the general characteristics of the atmospheres of these stars and further constraints for the models.

Chapter 5

Dynamic atmospheres and C-rich AGB stars: comparison of models with spectro-interferometric observations (Paper II)

This chapter is based on the paper Rau et al. (2016b) (see also Rau et al., 2015a,b)

Title: *The adventure of carbon stars - Observations and modelling of a set of C-rich AGB stars*
Authors: G. Rau, J. Hron, C. Paladini, B. Aringer, K. Eriksson, P. Marigo, W. Nowotny, and R. Grellmann
Year: 2016
Journal: Astronomy and Astrophysics, submitted on the 18$^{\text{th}}$ of July 2016

Modelling stellar atmospheres is a complex, intriguing task in modern astronomy. A systematic comparison of models with multi-technique observations is the only efficient way to constrain the models.

We intend to perform self-consistent modelling of the atmospheres of six carbon-rich AGB stars: R Lep, R Vol, Y Pav, AQ Sgr, U Hya and X TrA, with the aim of enlarging the knowledge on the dynamic processes occurring in their atmospheres. We used VLTI/MIDI interferometric observations, in combination with spectro-photometric data, and compared them with self-consistent dynamic models atmospheres.

We found that the models can reproduce SED data well at wavelengths longward of 1 μm, and the interferometric observations between 8 μm and 10 μm. Discrepancies observed at wavelengths

shorter than 1 μm in the SED, and longwards of 10 μm in the visibilities, could be due to a combination of data- and model-related effects. The models best fitting the Miras are significantly extended, and have a prominent shell-like structure. On the contrary, the models best fitting the non-Miras are more compact, showing lower average mass-loss rate.

The SiC feature in the models is narrower and sharper. We adopted the general 10% of SiC dust, and increasing this percentage does not lead to major changes in the fit. We found a satisfying fit in the wavelength-dependent visibilities for all the stars but X TrA, which appear to be compact but with an higher mass loss, configuration that can not be reproduced by any of the models and is discussed in the text.

A number of stellar parameters were derived from the model fitting: $T_{\rm eff}$, $L_{\rm eff}$, M, C/O, $\dot{M}$. Our findings agree well with literature values within the uncertainties. $T_{\rm eff}$ and $L_{\rm eff}$ are also in good agreement with the temperature derived from the angular diameter $\theta_{\rm (V\text{-}K)}$ and the bolometric luminosity from the SED fitting $L_{\rm bol}$, except for AQ Sgr. The possible reasons are discussed in the text. Finally, $\theta_{\rm Ross}$ and $\theta_{\rm (V\text{-}K)}$ agree with each other, better for the Miras targets than for the non-Miras, which is probably connected to the episodic nature of the latter models.

We also located the stars in the H-R diagram, comparing them with evolutionary tracks. We found that the main derived properties (L, $T_{\rm eff}$, C/O ratios and stellar masses) from the model fitting are in good agreement with TP-AGB evolutionary calculations for carbon stars carried out with the COLIBRI code.

5.1 Introduction

Stars less massive than $\sim$ 8 $M_\odot$ and more massive than $\sim$ 0.8 $M_\odot$, after moving from the Main Sequence through the Red Giant Phase and past the Horizontal Branch, will spend part of their life on the Asymptotic Giant Branch.

At the beginning of the AGB, the stars are characterized by a C-O core, surrounded by two nuclear burning layers: the inner one consisting of He, and the outer one of H. Those layers are in turn wrapped by a convective mantle and, further, by an atmosphere consisting of atomic and molecular gas, which is surrounded by a circumstellar envelope of gas and dust.

The third dredge-up is the mechanism responsible for turning the abundance of AGB stars from O-rich into C-enriched (Iben and Renzini, 1983). Carbon-rich AGB stars are one of the most influential contributors to the enrichment of the interstellar medium, with dust made of amorphous carbon (amC) and silicon carbide (SiC). In their atmospheres carbon-bearing molecules, such as C_2, C_3, C_2H_2, CN, HCN, can be found.

The evolution of the stars on the AGB is characterized by cooling, expansion and growing in brightness, burning the nuclear fuel faster and faster, and the star eventually begins to pulsate. The pulsation generates shock waves running through star's atmosphere, creating conditions of pressure and temperature suitable for dust formation. The sequence of pulsation and dust formation may drive a wind off the surface of the star into the interstellar space: when the opacity of amorphous carbon dust is high enough, the radiative pressure can provide enough

momentum to the grains to accelerate them and to drag along the gas by collisions, causing an outflow from the star (e.g. Fleischer et al., 1992; Höfner and Dorfi, 1997).

Höfner et al. (2003) describes this scenario with the solution of the coupled equations of hydrodynamics, together with frequency-dependent radiative transfer, including as well the time-dependent formation, growth, and evaporation of dust grains. The Dynamic Atmosphere & Radiation-driven Wind models based on Implicit Numerics (from here on: DARWIN models, Höfner et al., 2016) that come from this code have successfully reproduced observations, e.g. line profile variations (Nowotny et al., 2010) and time-dependent spectroscopic data (Gautschy-Loidl et al., 2004; Nowotny et al., 2013) of carbon-rich stars.

In our previous work (Rau et al., 2015c) we studied the atmosphere of the C-rich AGB star RU Vir, comparing in a systematic way spectroscopic-, photometric- and interferometric-data with the grid of DARWIN models from Mattsson et al. (2010) and Eriksson et al. (2014) .

The investigation of AGB stars using a combination of different techniques has been increasing over the last few years, while to date only a few interferometric observations of carbon stars have been directly compared with model atmospheres (Ohnaka et al., 2007; Paladini et al., 2011; Cruzalèbes et al., 2013a; Klotz et al., 2013a; van Belle et al., 2013). From those, only very few have made use of time-dependent self-consistent dynamic models (Sacuto et al., 2011a; Rau et al., 2015c). As suggested by Höfner et al. (2003), this is the only way to acquire knowledge about the influence of the dynamic processes on the atmospheric structure, at different spatial scales.

The purpose of this paper, is to extend our previous one on RU Vir, investigating the dynamic processes happening in the atmospheres of a set of C-rich AGB stars. To pursue this goal, we will compare predictions of DARWIN models with observations, by meaning of photometry, spectroscopy, interferometry. Indeed, long-baseline optical interferometry is an essential tool to study the stratification of the atmosphere, allowing to scan the regions of molecules and dust formation.

The targets object of this study are the C-rich AGB stars: R Lep, R Vol, Y Pav, AQ Sgr, U Hya, X TrA, whose observations and parameters are described in Sect. 5.2.
Section 5.3 explores the geometry of the targets. Sect. 5.4 introduces the self-consistent dynamic model atmospheres used, and presents their comparison with the different types of observables. In Sect. 5.5 we present our results. Sect. 5.6 is a discussion of our results, including a comparison with the evolutionary tracks, and we conclude in Sect. 5.7 with perspectives for future work.

5.2 Observational data

5.2.1 The sample of targets

Our sample consists of stars observed with the Very Large Telescope Interferometer (VLTI) of ESO's Paranal Observatory with the mid-infrared interferometric recombiner (MIDI, Leinert et al., 2003b) instrument, showing (1) an SiC feature in the visibility spectrum and (2) no evidence of asymmetry from differential phase. The stars can be grouped into: Mira variables

Table 5.1: Main parameters of our target sample, adopted from the literature.
... indicates that no literature value is given.

Name	Variability Type[a]	P [a] $[d]$	d [b] $[pc]$	L_{bol} $[L_\odot]$	$\dot{M}$ [c] $10^{-6}[M_\odot/yr]$	$\dot{M}$ [d] $10^{-6}[M_\odot/yr]$	$\dot{M}$ $10^{-6}[M_\odot/yr]$	ΔV [a]
R Lep	M	427	470^{+301}_{-122}	8514	2.0 ± 0.68	0.70 ± 0.35	0.93 ± 0.19 [e]	6.2
R Vol	M	454	880^{+149}_{-176}	8252	2.9 ± 0.68	1.80 ± 0.90	1.99 ± 0.34 [e]	5.2
Y Pav	SRb	233	400^{+125}_{-77}	5076	2.8 ± 0.96	0.16 ± 0.08	$0.23 \pm \ldots$ [f]	1.7
AQ Sgr	SRb	200	330^{+95}_{-60}	2490	$2.5 \pm \cdots$	0.25 ± 0.12	$0.77 \pm \ldots$ [f]	2.3
U Hya	SRb	450	208^{+35}_{-41}	3476	0.5 ± 0.05	0.14 ± 0.07	$0.21 \pm \ldots$ [f]	2.4
X TrA	Lb	385	360^{+67}_{-49}	8599	0.5 ± 1.05	0.13 ± 0.06	$0.18 \pm \ldots$ [f]	1.4

Notes. (a): Samus et al. (2009b) (b): the distances measurements come from van Leeuwen (2007), except from R Vol and U Hya, which distances come from Whitelock et al. (2006). (c): Loup et al. (1993) (d) Schöier and Olofsson (2001) (e) Whitelock et al. (2006) (f): Bergeat and Chevallier (2005).

(R Lep, R Vol), Semiregular (Y Pav, AQ Sgr, U Hya) and Irregular (X TrA) stars (Samus et al., 2009b).

The main parameters of the stars, namely variability class, period, amplitude of variability, distance, and mass-loss rates, are presented in Table 5.1. For two stars, namely R Vol and U Hya, we are presenting new VLTI/MIDI data observed within the programs 090.D-0410(A), 086.D-0899(K). For the remaining stars, our data come from archive observations (Paladini et al. submitted).

5.2.2 Photometry

We collected light curves for the V-band (Pojmanski, 2002; Henden et al., 2016), and the bands J, H, K, L (Whitelock et al., 2006; Smith et al., 2004; Le Bertre, 1992). A mean value was derived for each filter, with amplitudes taken from the variability (see Table A.5 for details). For the filters where no light curves are available (mainly B, R, and I), we averaged data collected from the literature. The errors were calculated as the standard deviation from those values. For the filters with only one value without any literature associated error, an error of 20 % was assumed.

5.2.3 Spectroscopy

Ideally, one would like to constrain the DARWIN models spectroscopically at least from 0.4 to 25 μm. Only few visible spectra are available in the literature. For R Lep we collected a NASA/IRTF spectrum presented in Rayner et al. (2009). The star was observed on 18 January 2007. The IRTF spectrum extends from 0.8 to 2.5 μm with a resolution R $\sim$ 2000 until 2.5 μm and R $\sim$ 2500 afterwards (see Fig 5.5).

We also considered R Lep spectra from Lançon and Mouhcine (2002). But the observations

Table 5.2: Calibrator list.

HD	Spectral type[a]	F_{12}^{a} [Jy]	θ^{b} [mas]
32887	K4III	56.82	5.90 ± 0.06
81797	K3II-III	157.6	9.14 ± 0.04
82668	K4/5III	73.10	6.95 ± 0.05

(a)IRAS Point Source Catalog: `http://simbad.u-strasbg.fr/simbad/`.
(b)`www.eso.org/observing/dfo/quality/MIDI/qc/calibrators`

are poorly flux calibrated, moreover they were obtained during a dust obscuration event Whitelock et al. (1997). For both these reasons this Lançon and Mouhcine (2002) spectrum was not used.

5.2.4 Interferometry: MIDI data

All the targets of this study have been observed with the Auxiliary Telescopes (ATs) at VLTI. The observations were carried out with MIDI, which provides wavelength-dependent visibilities, photometry, and differential phases in the N band ($\lambda_{\rm range} = [8, 13]$ μm).

Details on R Lep, Y Pav, AQ Sgr, X Tra can be found in Paladini et al. (submitted). In the latter the reader will also find the *uv*-coverage and the journal of the observations.

The journal of observations of R Vol and U Hya is available in Appendix (Table A.3 and A.4), together with the *uv*-coverages (Fig. A.3). The calibrators used are listed below the corresponding science observation. The selection criteria for calibrators stars described in Klotz et al. (2012a) were applied. The list of calibrators and their main characteristics are in Table 5.2.

The data reduction was made with software package MIA+EWS (V2.0 Jaffe, 2004; Ratzka et al., 2007; Leinert et al., 2003b). The size of the error bars is based on the calculated error in the visibilities. A conservative error of 10% on the visibilities is assumed in the case of a calculated error < 10 %. The wavelength-dependent visibilities, shown in Figs. 5.3 and 5.4, exhibits the typical shape of carbon stars with dust shells containing SiC grains, which manifests its presence in the visibility minimum around ~ 11.3 μm. The typical drop in the visibility shape between $8 - 9$ μm is caused by C_2 H_2 and HCN molecular opacities.

5.3 Geometry of the environment

As a first step, the MIDI interferometric data are interpreted with geometric models. To this purpose we used the GEM-FIND tool (GEometrical Model Fitting for INterferometric Data of Klotz et al., 2012b) to fit geometrical models to wavelength-dependent visibilities in the N band, allowing the constraint of the morphology and brightness distribution of an object. The detailed description of the fitting strategy and of the χ^2 minimization procedure can be found in Klotz et al. (2012a).

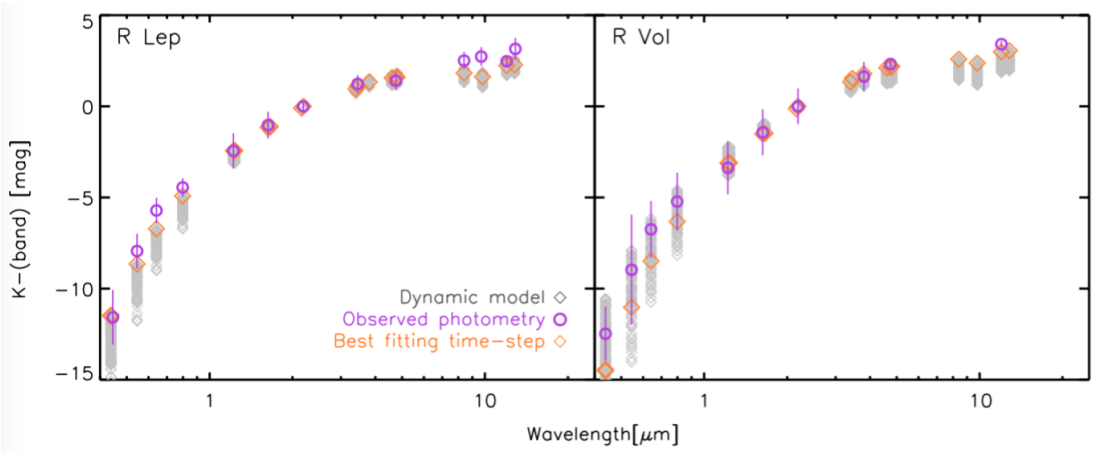

Figure 5.1: Photometric observations of **Mira** stars: R Lep (left) and R Vol (right). Observations (violet circles), compared to the DARWIN models synthetic photometry (grey diamonds). Orange diamonds show the best fitting time-steps of the two stars.

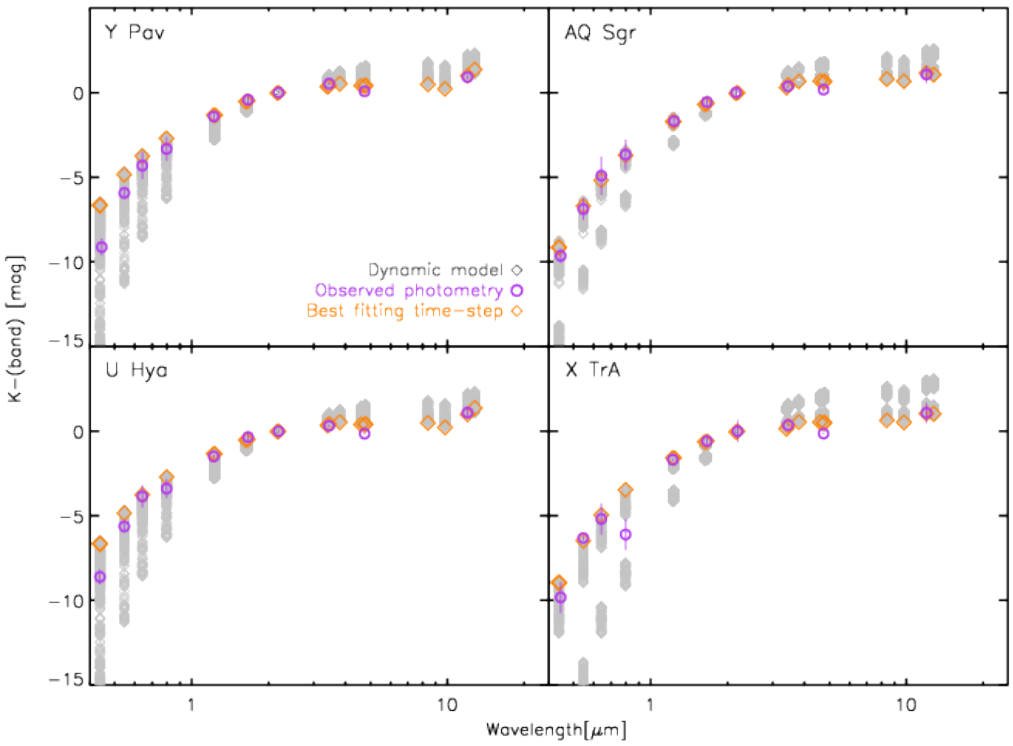

Figure 5.2: Photometric observations of **SRb and Lb** stars: Y Pav (upper left) and AQ Sgr (upper right), U Hya (lower left) and X TrA (lower right). Observations (violet circles), compared to the DARWIN models synthetic photometry (grey diamonds). Orange diamonds show the best fitting time-steps of the four stars.

Two MIDI data points are available for R Vol (uv-coverage shown in Fig. A.3, left side). The angular diameters derived from the fit are: $\theta_8 = 26.38 \pm 0.17$ mas and $\theta_{12} = 33.45 \pm 0.36$ mas for a circular UD fit, and $\theta_8 = 17.88 \pm 0.36$ mas and $\theta_{12} = 24.48 \pm 0.60$ mas for a fit with a circular Gaussian model.

U Hya has only one visibility spectrum available (see uv-coverage in Fig. A.3, right side) therefore only Uniform Disc (UD) and Gaussian models can be applied. By fitting the data we derived a UD-equivalent diameter at 8 and 12 μm, of respectively $\theta_8 = 23.89 \pm 2.54$ mas and $\theta_{12} = 39.26 \pm 2.64$ mas. The Gaussian full width half maximum (FWHM) at 8 and 12 μm of 14.60 ± 1.68 mas and 24.48 ± 1.87 mas respectively.

Geometric modelling for the other stars of our sample are presented in Paladini et al. (submitted). For the discussion and interpretation we refer the reader to the values published in their Table 4.

5.4 Dynamic Models Atmospheres

5.4.1 Overview on the dynamic models

Our observational data are compared with synthetic observables obtained from the grid of DARWIN models presented in Mattsson et al. (2010) and Eriksson et al. (2014), and model spectra. A detailed description of the modelling approach can be found in Höfner and Dorfi (1997), Höfner (1999), Höfner et al. (2003) and Höfner et al. (2016). Applications to observations are described in Loidl et al. (1999), Gautschy-Loidl et al. (2004), Nowotny et al. (2010), Nowotny et al. (2011), Sacuto et al. (2011a) and Rau et al. (2015c).

Those models result from solving the system of equations for hydrodynamics, and spherically symmetric frequency-dependent radiative transfer, plus equations describing the time-dependent dust formation, growth, and evaporation. The initial structure of the dynamic model is hydrostatic. A “piston” simulates the stellar pulsation, i.e. a variable inner boundary below the stellar photosphere. The "method of moments” (Gauger et al., 1990; Gail and Sedlmayr, 1988) calculates the dust formation of amorphous carbon.

The main parameters characterizing the DARWIN models are: effective temperature $T_{\rm eff}$, luminosity L, mass M, carbon-to-oxygen ratio C/O, piston velocity amplitude $\Delta_{\rm u}$, and the parameter f_L used in the calculations to adjust the luminosity amplitude of the model. The emerging proprieties of the hydrodynamic calculations are: the mean degree of condensation, the wind velocit, and the mass-loss rate. A set of “time-steps” describe each model, corresponding to the several phases of the stellar pulsation.

The synthetic photometry, synthetic spectra and synthetic visibilities are computed using the COMA code and the subsequent radiative transfer (Aringer, 2000; Aringer et al., 2009). The synthetic photometry is derived integrating the synthetic spectra over the selected filters mentioned in Sect. 5.2.2. Starting from the radial temperature-density structure at a certain time-step taken from the dynamical calculation, and considering the equilibrium for ionization and molecule formation, all the abundances of the relevant atomic, molecular, and dust species

were computed. The continuous gas opacity and the strengths of atomic and molecular spectral lines are subsequently determined assuming local thermal equilibrium (LTE). The corresponding data, listed in Cristallo et al. (2007) and Aringer et al. (2009) are consistent with the data used for constructing the models.

The amount of carbon condensed into amorphous carbon (amC), in g/cm^3, as a direct output of the calculations, is taken from the models. amC dust opacity is treated consistently (Rouleau and Martin, 1991, in SPL), and further details on the dust treatment are given in Eriksson et al. (2014). SiC is added, artificially, a posteriori with COMA.

We assume that the percentage of condensed material is distributed in this way: 90 % amorphous carbon and 10 % silicon carbide, based on Pegourie (1988). Some experiments that change this configurations are presented in Sect. 5.6.

All grain opacities are calculated for the small particle limit (SPL), in order to be consistent[1] with the model spectra from Eriksson et al. (2014). The assumed temperature of the SiC particles equals the one of amC; this is justified, since the overall distribution of the absorption is quite similar for both species, except for the SiC feature around 11.3 μm. As a consequence, the addition of SiC would also not cause significant changes in the thermal structure of the models. Since the SPL is adopted, the effects of scattering are not included, as they are negligible in the infrared.

5.4.2 The fitting procedure

Generating one synthetic visibility profile for each of the approximately 140 000 time-steps of the models grid, and for each baseline configuration of our observations, would be extremely time-consuming from a computational point of view. Therefore a simultaneous fitting of the three types of observables was excluded a priori, instead implementing the procedure described as follows.

First, the photometric observations were compared to the synthetic models photometry. A χ^2 minimization was performed over the available literature photometric data, for each of the 540 models of the grid, with a total of approximately 140 000 time steps. The best-fitting photometry model, with a corresponding best-fitting-photometry time-step is listed in Table 5.3.

Second, we produced the synthetic visibilities, following the approach of Davis et al. (2000) and Tango and Davis (2002). They are calculated as the Fourier transformation of the intensity distribution I, which results from the radiative transfer. We then compared them to the interferometric MIDI data of each star. For the time-computational reasons mentioned before, we produced the synthetic visibilities only for the best-fitting photometric model, i.e. for all the time-steps belonging to that model.

In the following paragraphs we present the results of the comparison of the DARWIN models with the spectro-photometric and interferometric data for each single star. One example of the confrontation of the intensity profile and visibility vs. baseline at two different wavelengths,

[1] An inconsistent treatment of grain opacities causes larger errors in the results than does using the small particle limits approximation.

namely 8.5 μm for the molecular contribution and 11.3 μm for the SiC feature, is shown in Fig. 5.6 (see Appendix for the other stars).

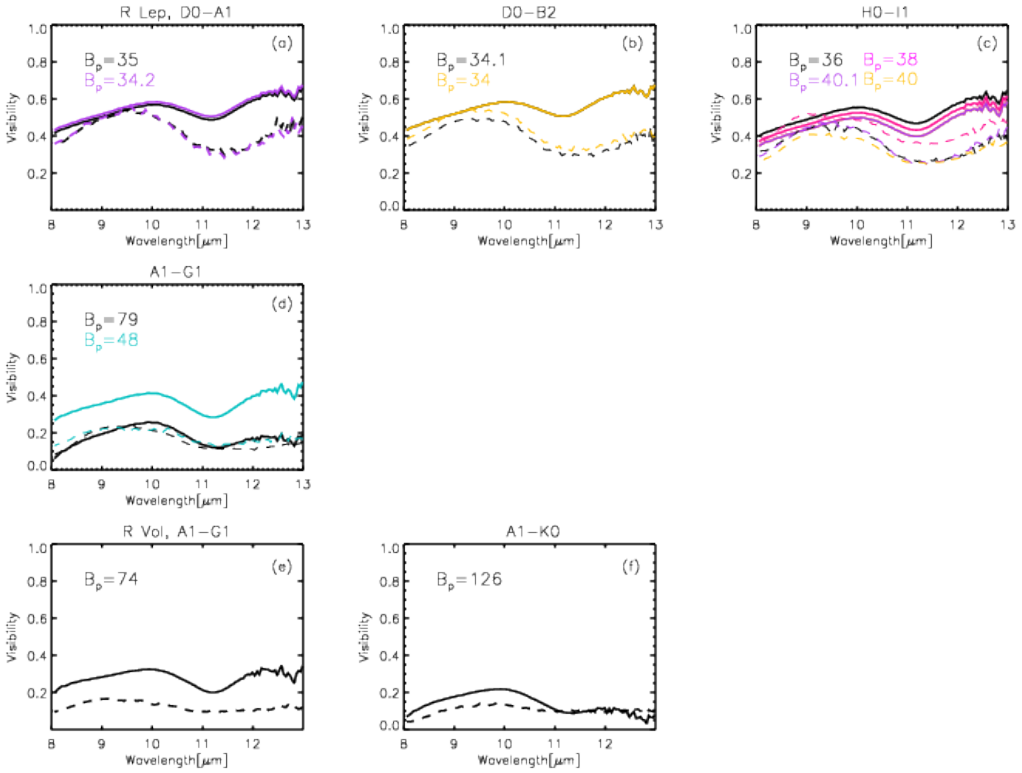

Figure 5.3: Visibility dispersed over wavelengths of R Lep and R Vol. Models are plotted in full line, observations in dashed lines, at the different projected baselines (see color legend). The stars are identified in the title. The six panels show R Lep dispersed visibilities at the baseline configuration D0-A1 (a), D0-B2 (b), H0-I1 (c) and A1-G1 (d), as also marked in the plot titles. R Vol dispersed visibilities are at the baseline configuration A1-G1 (e) and A1-K0 (f). Error bars are of the order of 10%.

5.5 Results

The DARWIN models fits with our three different types of observations, lead to results which are described in this section, for Mira, Semiregular and Irregular stars. Please refer to Sect. 5.6 for a detailed discussion on our results.

The results of the fit, namely the χ^2, are shown in Table 5.3. The main parameters that characterize the models, as described in Sect. 5.4, are listed together with the resulting properties of the DARWIN models, such as the mean mass-loss rate $\dot{M}$. The table also contains the model phases of the single time-steps that best fit the interferometric observations, and the observational MIDI phases for the Mira stars. No assignment of MIDI phases can be done for the Semi-regular

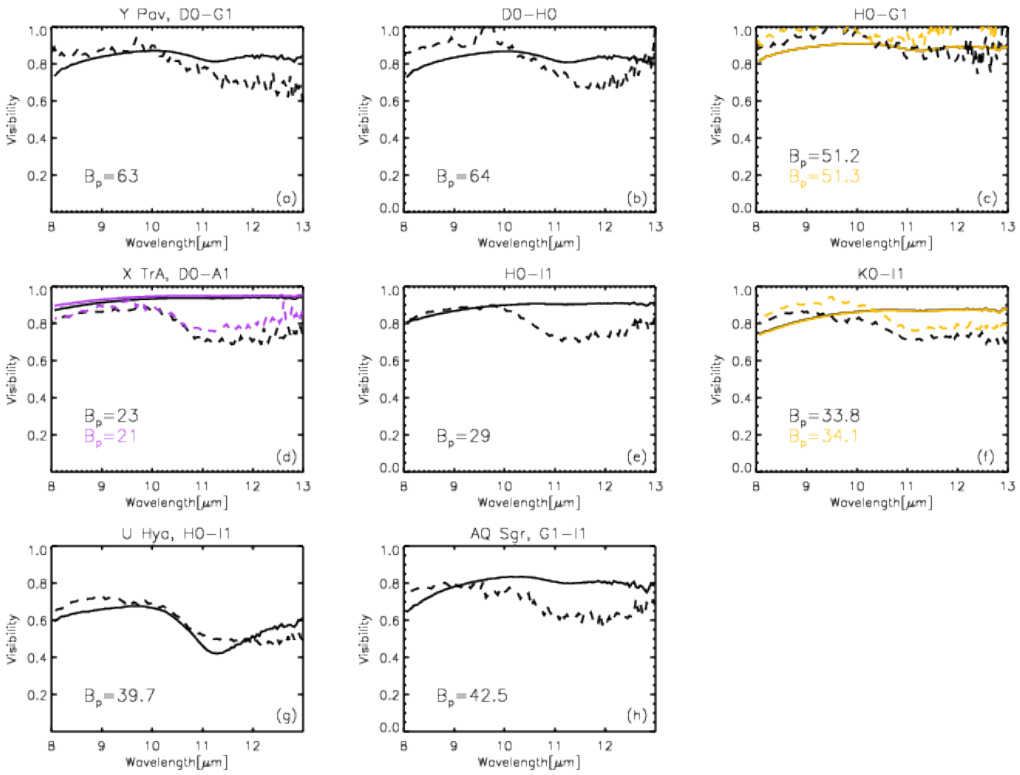

Figure 5.4: Same as Fig. 5.3, for the Semiregular and Irregular stars of our sample: Y Pav in panels (a), (b), (c); X TrA in panels (d), (e), (f); U Hya in panel (g) and AQ Sgr in panel (f). Error bars are of the order of 10%.

and Irregular variables, due to the irregular nature of their light curves and also the sometimes poor phase coverage of the light curves. For the Miras, the MIDI observations were combined for the fit and therefore a comparison between observed and model phases is not appropriate for any of our targets.

The best fitting models of Y Pav, AQ Sgr, U Hya and X TrA resulted, at first, in models without mass-loss. Since those stars are instead highly pulsating and show presence of mass-loss in the literature (see Table 5.1), we decided to perform a selection a priori, choosing from the whole grid of 560 models, only the ones allowing for wind formation, i.e. having a condensation factor $f_c > 0.2$. This results in a sub-grid of 168 models, among which we performed our analysis for the Semiregular and Irregular stars.

Based on our findings, some general statements can be made: overall, the χ^2 from SED fitting of non-Miras is higher than the one obtained for Mira variables (Table 5.3). We also found that the Miras interferometric observations show the SiC feature shallower than the one produced by the models. Also, the visual phase of the models does not match the one of the interferometric observations.

5.5.1 Mira stars

In summary, the Mira stars exhibit a visibility vs. wavelength profile always flatter than the models, which agrees better at wavelengths shorter than 10 μm. A similar finding was reported by Sacuto et al. (2011a) for R Scl.

R Lep

The spectroscopic and photometric data of R Lep agree well with the model predictions, as can be seen in Fig. 5.5 (in which the IRAS spectrum has been over-plotted for qualitative comparison reasons) and Fig. 5.1, left panel. The small differences at wavelength shorter than 1 μm are discussed later in Sect. 5.6.1. The good fit is confirmed by a χ^2 of 0.99 and 1.01 for photometry and interferometry respectively (Table 5.3). R Lep interferometric data (see Fig. 5.3, upper panels) show the typical SiC shape around 11.3 μm. This shape is reproduced by the models, and their difference in level at wavelength longwards of 10 μm is discussed in Sect. 5.6.1.

R Vol

R Vol photometric data show good agreement at all wavelength ranges, well within the error bars (see Fig. 5.1, right panel). The interferometric data of R Vol are taken with long baselines (B_p = 74 m and B_p = 126 m), and cover visibility values between 0.05 and 0.15. Overall, the observations taken with the 126 m baseline (Fig. 5.3) are reproduced good by the model in the wavelength range between 11 and 13 μm. However the model predicts higher visibilities for the 74 m baseline.

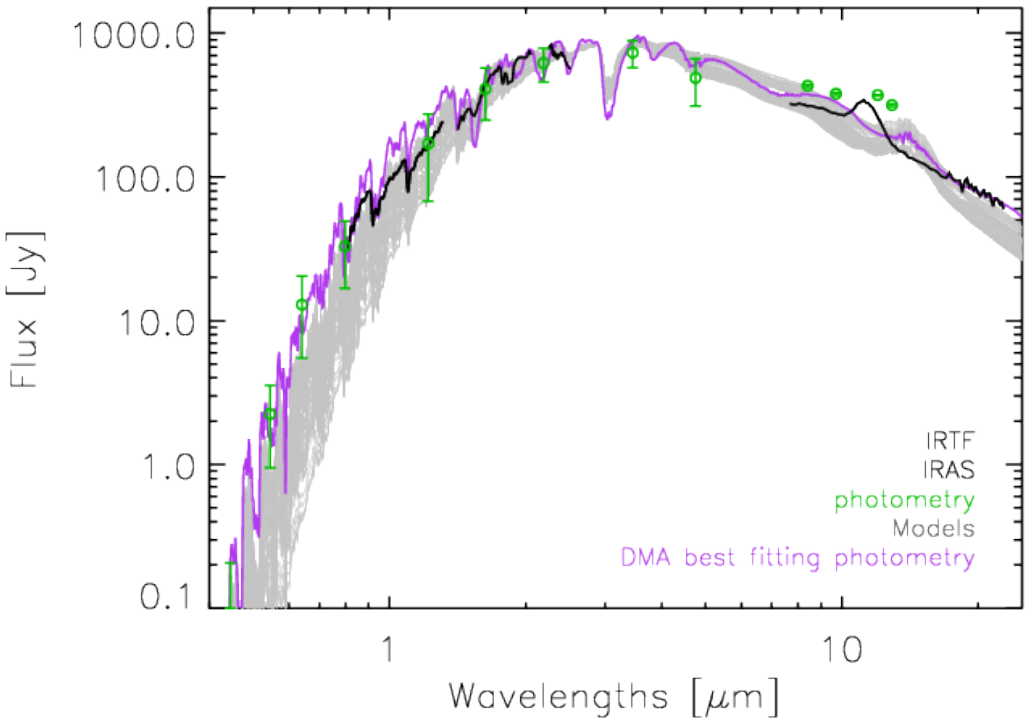

Figure 5.5: Observational spectro-photometric data of **R Lep**, compared with the synthetic spectrum of the best-fitting time-step (violet). Photometry is plotted in green circles, while IRAS (Olnon et al., 1986) and NASA/IRTF (Rayner et al., 2009) spectra are plotted in black lines, to the purpose to check qualitatively the photometric fit. The spectrum of the model for which the synthetic photometry fits best the corresponding observational data is shown, in violet.

Interferometric variability

The data of Y Pav, U Hya and AQ Sgr, have been taken at single epochs, therefore no interferometric variability can be assessed for those stars. The observations of R Vol are one year apart, but very different in projected baseline (B_p) and projected angles (PA), a configuration that makes the variability check impossible to perform. The X TrA observations are numerous and taken at the same time, but they are different in PA, thus the time-variability can not be evaluated.

The only target for which a variability check could be performed is the Mira star R Lep. R Lep observations show a cycle-to-cycle variation, observed in the level of the visibility spectrum (Paladini et al., subm), which is more pronounced in the molecular dominated region between 9 μm and 10 μm, while no variation between 11 and 12 μm is observed.

This variation in the visibility level among the two datasets at $B_p = 40$ m, is noticeable between 9 μm and 10 μm (see Fig. 5.3, panel (c)). The highest visibility difference in level is found at 9.7 μm, where the variation of visibility is $\delta V = 0.072$: the visibility level decreases, moving from pre-minimum ($\phi = 1.43$ at $B_p = 40$, PA = 147) to post-minimum ($\phi = 0.66$ at $B_p = 40$, PA = 142). This result goes in the same direction as the studies of the Mira star V Oph by Ohnaka et al. (2007), who observed the star to be smaller in the proximity of the visual phase minimum, but with a stronger variation of the visibility level: $\delta V = 0.25$ between dataset #3 (phase $\phi = 0.49$) and #6 ($\phi = 0.69$) at 8.3, 10.0 and 12.5 μm - see Fig 2 in (Ohnaka et al., 2007).

Also, there are two R Lep observations which belong to two different cycles, i.e. are taken one year apart, but have the same projected baseline and similar projected angles. An independent fit of those two observations to our models has been performed, leading to the same best fitting time-step. This could indicate that the models do not differ (enough) in the observed quantities from phase to phase, i.e. the comparison between models and observations is not sensitive enough to study the temporal variation.

Moreover, we notice that the long baselines observations of R Lep (namely $B_p = 48$ corresponding to phase $\phi = 0.23$, and $B_p = 79$ corresponding to phase $\phi = 0.22$, see also Fig. 5.6), are very low in visibility with respect to the other points. A comparison with the baselines of Ohnaka et al. (2007) datasets #1 (phase $\phi = 0.18$) and #5 (phase $\phi = 0.61$), which show variability, could be in principle discussed. Indeed, those baselines are roughly comparable with our long baselines datasets. But the distance of the Mira star V Oph is $d = 237$ pc (van Leeuwen, 2007), i.e. about half the distance of R Lep. Thus our long baselines point would not increase much their visibility level in Fig. 5.6.

5.5.2 Semi-regular and Irregular Variables

In general, the χ^2 of the photometry of the Semi-regular and Irregular stars is higher than for the Miras (see Table 5.3).

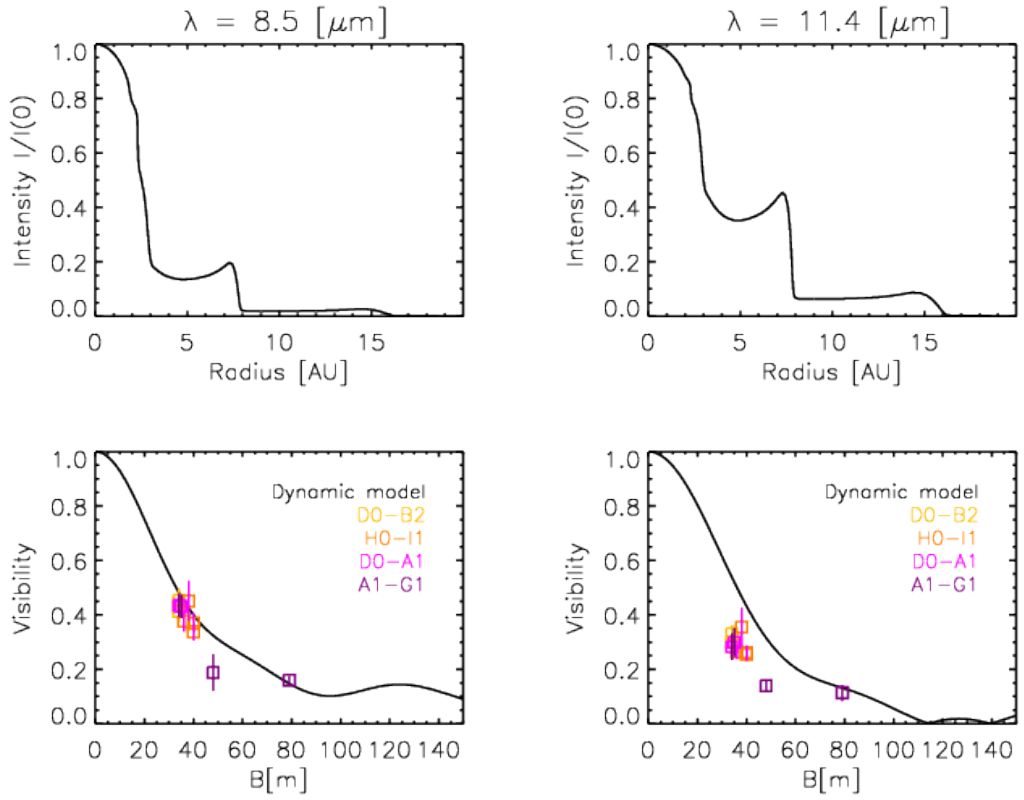

Figure 5.6: Interferometric observational MIDI data of R Lep, compared with the synthetic visibilities based on the DARWIN models. **Up**: intensity profile at two different wavelengths: 8.5 μm and 11.4 μm. **Down**: visibility vs. baseline; the black line shows the dynamic model, the colored symbols illustrate the MIDI measurements at different baselines configurations.

Y Pav

The problem of having the B filter photometric data off the fit, also appearing for some of the other targets, manifests itself also in the SED of Y Pav, and a likely reason of this is discussed in Sect. 5.6. The interferometric data show high visibility level at all three Y Pav baseline configurations. The models agree in level with the MIDI observations, and their difference in shape is discussed in Sect. 5.6.

AQ Sgr

The synthetic photometry of AQ Sgr fits the data well within the error bars. The models are in good agreement with the MIDI data in level, but the SiC feature shape is not as pronounced in the models as in the observations.

U Hya

The synthetic model SED of U Hya is in good agreement with the observations. The small discrepancy shorter than 1 μm is discussed in Sect. 5.6. The synthetic visibilities seems to reproduce well, within the error bars, the shape and level of the MIDI U Hya observations.

X TrA

Since at first the photometry of X TrA (in Fig. 5.2 lower right panel), had the value in the filter I particularly offset compared to the overall fit, we performed a new fit excluding those values. The results are shown in Table 5.3 and Fig. 5.2. There is a good agreement between models and MIDI observations, and the discrepancy in shape is examined in Sect. 5.6.

5.6 Discussion

5.6.1 The SEDs and visibilities

Our attempts to reproduce the SED (photometry + IRTF spectrum in the R Lep case) and interferometric MIDI data with DARWIN models show a strong improvement with respect to our previous study of RU Vir. The models can fit the SEDs of all stars longward of 1 μm quite well and also the visibilities between 8 μm and 10 μm. The observed faster decline and leveling off of the Miras visibility profiles, compared to the non-Miras, is also predicted by the models which are significantly more extended for the Miras and have a more pronounced shell-like structure. This can be best seen by comparing R Lep and Y Pav (Fig. 5.6, Fig. 5.7 which have similar distances. It is also supported by the fact that the best fitting models (with wind) for the non-Miras have a lower average mass loss rate and show only episodic mass loss. We remind the reader that actually the best fitting models for the non-Miras were those without a wind, but we excluded those because of the known mass loss for these stars (Sect. 5.4). Both

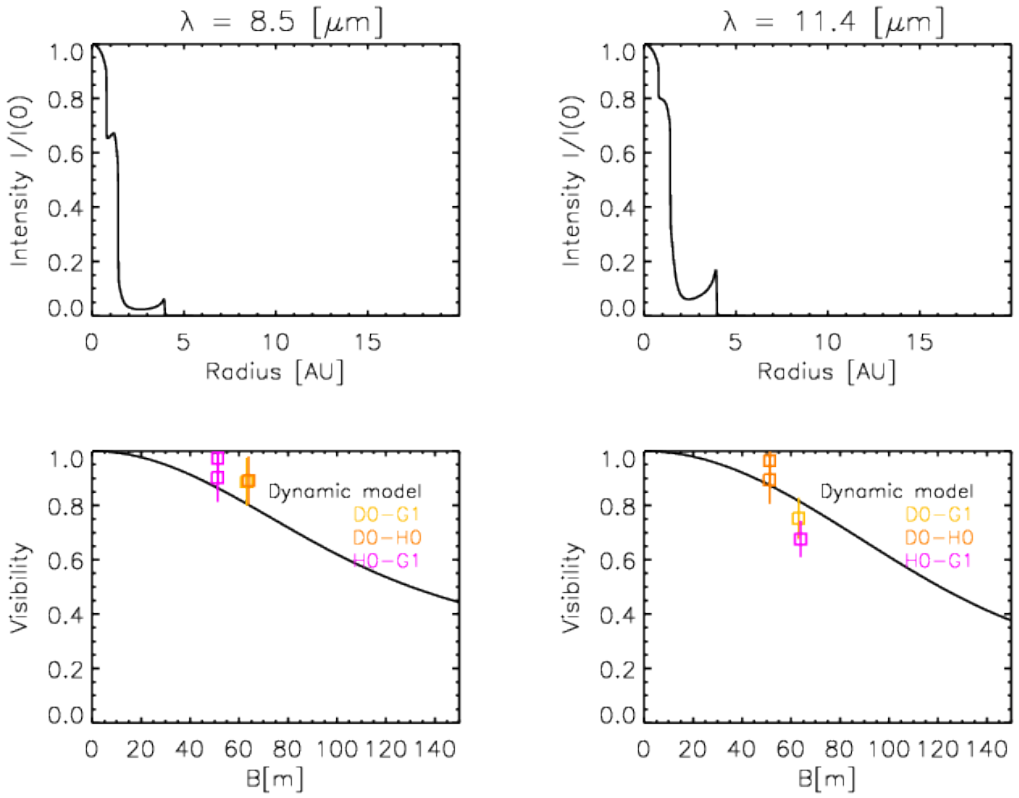

Figure 5.7: Interferometric observational MIDI data of Y Pav, compared with the synthetic visibilities based on the DARWIN models. **Up**: intensity profile at two different wavelengths: 8.5 μm and 11.4 μm. **Down**: visibility vs. baseline; the black line shows the dynamic model, the colored symbols illustrate the MIDI measurements at different baselines configurations.

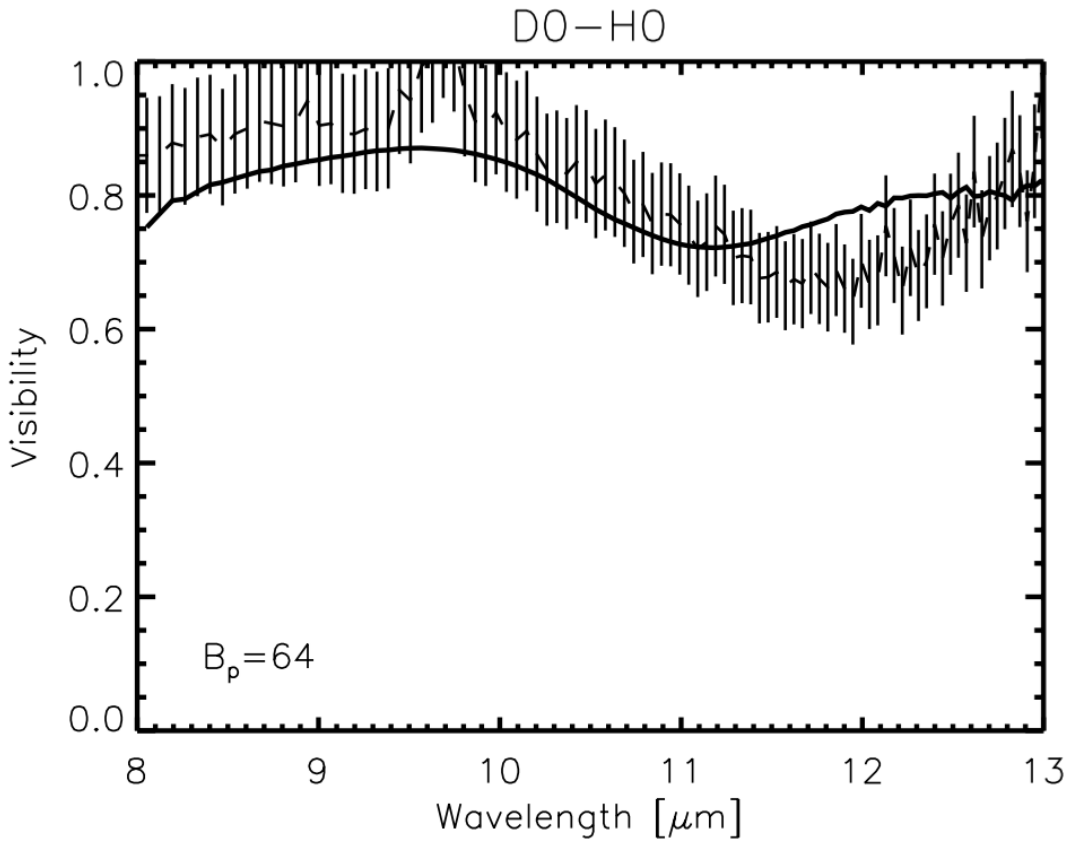

Figure 5.8: Y Pav wavelength dependent visibilities in the MIDI range, for the only baseline configuration D0-H0, in the case of the amount of SiC increased to 50% in the models.

Table 5.3: Summary of the best fitting model for each type of observation: photometry, spectroscopy and interferometry. Listed are the corresponding values of the χ^2, the parameters of the models, and the phase of the best fitting time-step and of the interferometric observations.

	$T_{\rm eff}$ $[K]$	log $L_\star$ $[L_\odot]$	M $[M_\odot]$	P [d]	log g	C/O	$\Delta u_{\rm p}$	$f_{\rm L}$	$\dot{M}$ $10^{-6}[M_\odot/yr]$	$\lambda_{\rm fit\ range}$ [μm]	$\chi^2{}_{\rm red}$
R Lep											
Spectr	3000	3.85	1.0	390	-0.57	1.69	6	2	2.45	[0.805-5.06]	0.99
Photom	2800	3.85	1.00	390	-0.69	1.69	6	1	2.24	[0.4-25.0]	1.03
Interf	2800	3.85	1.00	390	-0.69	1.69	6	1	2.24	[8.0-13.0]	1.01
R Vol											
Spectr	...	...	...	...	...	...	...	...	...		
Photom	2800	3.85	0.75	390	-0.81	1.69	6	2	1.89	[0.4-25.0]	1.08
Interf	2800	3.85	0.75	390	-0.81	1.69	6	2	1.89	[8.0-13.0]	23.40
Y Pav											
Spectr	...	...	...	...	...	...	...	...	...		
Photom	3200	3.55	0.75	221	-0.28	2.38	6	2	0.36	[0.4-25.0]	11.15
Interf	3200	3.55	0.75	221	-0.28	2.38	6	2	0.36	[8.0-13.0]	1.02
AQ Sgr											
Spectr	...	...	...	...	...	...	...	...	...		
Photom	2600	3.70	0.75	294	-0.79	1.35	6	2	1.69	[0.4-25.0]	1.41
Interf	2600	3.70	0.75	294	-0.79	1.35	6	2	1.69	[8.0-13.0]	4.60
U Hya											
Spectr	...	...	...	...	...	...	...	...	...		
Photom	3200	3.55	0.75	221	-0.28	2.38	6	2	0.36	[0.4-25.0]	13.58
Interf	3200	3.55	0.75	221	-0.28	2.38	6	2	0.36	[8.0-13.0]	1.53
X TrA											
Spectr	...	...	...	...	...	...	...	...	...		
Photom	2600	4.00	1.5	525	-0.79	1.35	6	1	2.51	[0.4-25.0]	14.70
NOR,I	2600	3.85	2.0	390	-0.51	1.35	6	1	...	[0.4-25.0]	6.20
Interf	2600	4.00	1.5	525	-0.79	1.35	6	1	2.51	[8.0-13.0]	1.04
dist-20%	2600	4.00	1.5	525	-0.79	1.35	6	1	2.51	[8.0-13.0]	1.00

the windless and episodic models are characterized by rather compact atmospheres and weakly pronounced gas and dust shells.

In spite of these encouraging results in reproducing the observations, some notable (and partly systematic) differences remain. Therefore, our discussion will focus on three major parts: (1) differences at wavelengths shorter than 1 μm; (2) differences in the visibilities longward of 10 μm and (3) differences related to SiC dust.

Differences at wavelength shorter than 1 μm

The difference in the R Lep SED fit at the short wavelengths, appearing in Fig. 5.1 left panel and Fig. 5.5, could be caused by a possible combination of data related and model related effects. The data related ones are due to the stars variability, i.e. lack of light curves, especially in B, R and I and partly in the IR. As mentioned above, the best fitting models for the Semiregular and Irregular stars are episodic models and thus show no regular light curve behavior. These two effects in combination introduce a larger uncertainty in the determination of mean magnitudes for the observations and models and are also responsible for the higher χ^2 of the SED fits for non-Miras in comparison with the Miras. Deviations may also be due to the assumption of SPL in the models or uncertainties of the used data set for amC (Nanni et al., 2016).

Differences in the visibilities longward of 10 μm

Comparing the wavelength dependence of the visibilities for the Miras and the non-Miras with the models, and ignoring for the moment the differences in the SiC feature which will be discussed in the next section, one notices that at shorter baselines the Mira-models show an increase of visibility with wavelength which is not observed. A similar difference was also noticed by us for RU Vir. In Rau et al. (2015c) two explanations for this were discussed: (i) a smoother density distribution than in the models and (ii) a clumpy environment. A smoother density distribution with less pronounced dust shells seems possible as the models for the non-Miras do not show this slope in the wavelength-dependent visibilities, and these models generally have weakly pronounced shells (see Fig. 5.7). A clumpy environment is not excludable, but from our data we do not have any evidence of deviations from spherical symmetry. Furthermore, the slopes agree quite well for the long baselines, where clumps should be more prominent.

In this work we extended our search for other possible origins of the slope in the models. Using different opacity laws for amC (Zubko et al., 1996 and Jager et al., 1998) did not change the slope. Also changing the distance within the expected uncertainties did not lead to a better agreement.

The models are known to poorly reproduce the SED around the 14 μm feature of C_2H_2 and HCN, mostly due to uncertain opacity and chemistry data (Gautschy-Loidl et al., 2004). Spectra should be more affected than interferometry since they contain contributions from the whole stellar disk. Nevertheless we have checked the possible influence on the visibilities, by artificially removing the C_2H_2 and HCN contributions from the opacity, in the outer parts of the

model. But also this experiment did not affect the slope. Thus, a smoother density distribution than the one produced by the models is the most likely explanation for the slope difference in the Mira models.

Except for U Hya, all the non-Miras show high visibility levels but no increase with wavelength. The differences to the models are partly related to SiC (see below). For Y Pav they could be also due to calibration problems at the longest wavelengths (Paladini et al., subm.). The high visibility levels also reduce the sensitivity to the differences in the models parameters.

Differences related to SiC dust

Lacking a consistent description of SiC formation in the models, the spectra and visibilities were calculated from the DARWIN models with the assumption that SiC condenses together with amorphous carbon (see Sect. 5.4). This means that the amount of SiC is proportional to the amount of amC grains and assumed SPL is adopted. This assumption did not lead to major inconsistencies with the observations. However, SiC is likely to condense before amC (e.g. Ferrarotti and Gail, 2006) but a verification of this hypothesis would require modifications in the models in a similar way as currently done for M-type stars (Höfner et al., 2016). This will be subject of future work.

In this context, we would like to underline that the visibilities level, lower *in* the SiC feature than around this feature, has not to be interpreted as a larger extension of SiC with respect to amC and the molecular gas. This conclusion is only true for simple intensity profiles, while our stars have rather complex profiles and the contrast between the different shells containing dust and gas contributes to the influence on the level of visibility. This is illustrated in the comparison of the synthetic intensity and visibility profiles at 8.5 μm and 11.4 μm in Fig. 5.6. The lower visibility level around 11.3 μm is solely due to the higher SiC opacity with respect to the one of amC.

Whenever the MIDI observations show a clear SiC dust feature, the feature in the models is more peaked and narrower. A similar effect was noted for RU Vir, both for the spectra and the visibilities. For RU Vir the spectral fit with hydrostatic models and More Of Dusty (MOD) could be improved by using the distribution of hollow spheres (Groenewegen, 2012; Rau et al., 2015c). However, this distribution is not yet available for the dynamic model atmospheres used in the present work, and thus it could not be tested.

Another free parameter for the fits is the fraction of Si condensed onto SiC. As explained in Sect. 5.4, we generally adopted a fraction of 10 %. Increasing this fraction to up to 50 % slightly improves the agreement for R Lep and possibly also Y Pav (see Fig.5.8). Although for the latter star, the shape of the observed wavelength dependent visibilities is quite different and might not be due to SiC at all. A complete test of the SiC fraction for our stars has to await the above mentioned full implementation of SiC in the DARWIN models.

X TrA is the only star for which no satisfactory fit of the wavelength dependent visibilities could be found. The shape of the model visibility vs. wavelength shows almost no SiC, while this is quite prominent in the data. Scaling the distance and increasing the SiC fraction did not

remove this discrepancy. Also, we checked the two models closest in χ^2 to the best fitting model (i.e. within 68 % of confidence level), and for those ones, the predicted SiC feature improves slightly, but the increase with wavelength is too steep, as in the case of Miras. The star is thus compact but apparently has a significant mass-loss. This combination cannot be reproduced by any of the models, and probably this is caused by the fact that the star is located in the parameter region of the models with episodic mass loss.

5.6.2 Fundamental stellar parameters compared to literature, and evolutionary tracks

The best fitting DARWIN models yield a number of parameters as listed in Table 5.3.

For a comparison of temperature and luminosity with the literature values, we did not use the values given in Table 5.3 as these refer to the hydrostatic initial model and thus not to the dynamic structure of the model at the time-step (i.e. phase) best fitting the interferometric data (see also Nowotny et al., 2005b). Instead, we calculated for these time-steps a Rosseland diameter ($\theta_{\rm Ross}$). The temperature of the time-step at this radius ($\rm T_{Ross}$) is the corresponding effective temperature, i.e. the temperature at the Rosseland radius, defined by the distance from the center of the star to the layer at which the Rosseland optical depth equals 2/3. From this and $\theta_{\rm Ross}$ the luminosity $\rm L_{Ross}$ is calculated. From the photometry of our stars we also derive the bolometric luminosity $\rm L_{bol}$, a diameter $\theta_{\rm (V\text{-}K)}$ and an effective temperature $\rm T(\theta_{(V\text{-}K)})$ using the diameter/(V-K) relation of van Belle et al. (2013). The error on the luminosity is assumed to be about 40 %, on the basis of the distance uncertainty. The errors of the temperature are estimated through the standard propagation of error.

The above various resulting stellar parameters are listed in Tab. 5.4 together with diameters at 8 μm and 12 μm from geometrical models (see Sect. 5.3). In Fig. 5.9 the temperatures and luminosities are compared to thermally-pulsing (TP) AGB evolutionary tracks from Marigo et al. (2013). Starting from the first thermal pulse, extracted from the PARSEC database of stellar tracks (Bressan et al., 2012), the TP-AGB phase is computed until all the envelope is removed by stellar winds. The TP-AGB sequences are selected with an initial scaled-solar chemical composition: the mass fraction of metals Z is 0.014, and the one of helium Y is 0.273. In order to guarantee the full consistency of the envelope structure with the surface chemical abundances, that may significantly vary due to the third dredge-up episodes and hot-bottom burning, the TP-AGB tracks are based on numerical integrations of complete envelope models in which, for the first time, molecular chemistry and gas opacities are computed on-the-fly with the ÆSOPUS code (Marigo and Aringer, 2009). The results are shown in Fig. 5.9, where the TP-AGB tracks for two choices of the initial mass on the TP-AGB, $M = 1.0\,M_{\odot}$, and $M = 2\,M_{\odot}$, are compared with the stars considered in this work.

We note the the TP-AGB model for $M = 1.0\,M_{\odot}$ does not experience the third dredge-up, hence remains with C/O<1 until the end of its evolution. Conversely, the model with $M = 2\,M_{\odot}$ suffers a few third dredge-up episodes which lead to reach C/O > 1, thus causing the transition to the C-star domain. The location of the observed C-stars in the H-R diagram, as well as their

C/O ratios, appear to be nicely consistent with the part of the TP-AGB track that corresponds to the C-rich evolution. It is worth remarking that the current mass along the TP-AGB track is reduced during the last thermal pulses, which supports (within the uncertainties) the relatively low values of the mass ($\sim 0.75 - 1.0\,M_{\odot}$) assigned to some stars through the best-fitting search on the DARWIN models dataset.

Except for Y Pav, the model luminosities and temperatures place the stars in the C-rich domain of the tracks. The model masses are all 1 $M_{\odot}$ or less except for X TrA. Such low current masses are in agreement with the tracks if the stars are in an advanced stage of the TP-AGB (when $log(L) > 3.8$). This seems plausible for the Miras but not really the non-Miras. We note, that Hinkle et al. (2016) also found C-star masses of the order of 1 $M_{\odot}$ from 1.5 $M_{\odot}$. One should however keep in mind the uncertainties in the masses derived from the DARWIN models, and the ones predicted by the tracks.

The differences between the luminosity and temperature estimations derived from the models (L_{Ross}, T_{Ross}) and the observations (L_{bol}, $T(\theta_{(V\text{-}K)})$ are well within the error bars. Only for AQ Sgr the difference in luminosity exceeds the error. This may be related to the above mentioned episodic mass-loss of the best fitting model. Literature values of luminosities can be found for three stars in McDonald et al. (2012) and they all agree within the uncertainties and considering the differences in the used data sets and the methods used. We underline the surprisingly good agreement between T_{Ross} and the purely empirically determined $T(\theta_{(V\text{-}K)})$.

Temperature estimates in the literature are all based on fitting photometry with a combination of black bodies or spectra from hydrostatic model atmospheres and a dust envelope around it (Lorenz-Martins et al., 2001, Bergeat and Chevallier, 2005, McDonald et al., 2012). For each star different estimates typically differ by several hundred degrees and our values always are within the range of literature values. For R Vol only one determination is found in the literature (Lorenz-Martins et al., 2001) which gives a temperature 900 K lower than our estimated T_{Ross}. This apparently large difference can be understood by the method used in Lorenz-Martins et al. (2001) which cannot take into account the very non-static character of a Mira variable and the strong radial overlap of photosphere and dusty envelope in C-rich atmospheres (for a detailed discussion on the concept of an effective temperature for these stars, see also Sect. 3 of Nowotny et al., 2005b).

The diameters, θ_{Ross} and $\theta_{(V\text{-}K)}$ agree very well for the Miras, while the differences are larger for the non-Miras. This is probably again caused by the structure of models with episodic mass loss. Only R Lep, U Hya and AQ Sgr have available observed K-diameters (see Table 5.4). The values agree only roughly and there is no clear systematics in the differences between the three types of parameters. This can be understood by the fact that the K-diameter is not a purely photospheric diameter but also influenced by dust opacity (Paladini et al., 2009) and the non-static structure of the atmosphere.

The mass-loss values of the best-fitting DARWIN models of the Miras are in reasonable agreement with the literature (see Table 5.1), while for the non-Miras we find large differences for AQ Sgr and X TrA. Again, the episodic mass loss of the models is the probable cause.

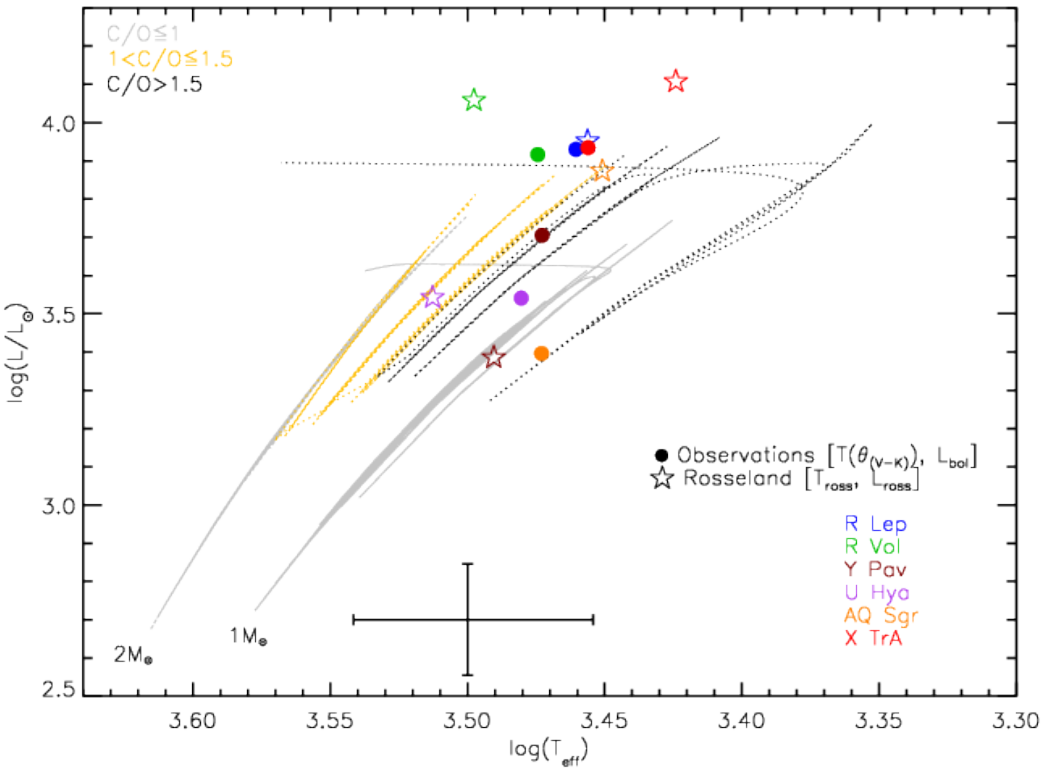

Figure 5.9: AGB region of the H-R diagram. The lines display solar metallicity evolutionary tracks from Marigo et al. (2013): grey lines mark the regions of Oxygen-rich stars with C/O $<$ 1.0; yellow lines denote the region of C-rich stars with 1.0 $<$ C/O $\leqslant$ 1.5, while black lines with C/O $>$ 1.5. The numbers indicate the mass values at the beginning of the thermal pulsing (TP)-AGB. For better visibility, the track with 2 $M_{\odot}$ is plotted with a dotted line. Different symbols and colors refer to the luminosity and effective temperature, estimated through the comparison in this work of the the models with spectro-photometric-interferometric-observations. A typical error-size bar is shown in the lower side of the figure.

Table 5.4: Observed and calculated temperatures and diameters.

Target	$\theta_{(V-K)}$ [a] [mas]	θ_K [mas]	$\theta_8/FWHM_8$ [mas]	$\theta_{12}/FWHM_{12}$ [mas]	θ_{Ross} [e] [mas]	T_{Ross} [K]	$T_{\theta_{(V-K)}}$ [K]	T_{θ_K} [K]
R Lep	7.30	12.0 ± 1.92 [b]	15/30.13±0.93	15/44.53±2.16	7.64	2860	2890 ± 350	2250
R Vol	3.60	...	32.01 ± 0.32	36.77 ± 0.48	3.80	3140	2980 ± 360	...
Y Pav	6.26	...	.../5.29±1.08	.../12.06±1.07	4.00	3090	2970 ± 360	...
U Hya	9.62	10.87 ± 3.16 [c]	23.89 ± 2.54	$101.87 \pm ...$	8.30	3260	3020 ± 370	2840
AQ Sgr	5.31	6.13 ± 0.52 [d]	16.58±2.7	32.92±2.82	10.18	2824	2970 ± 360	2770
X TrA	9.78	...	21.89±2.46	38.76±3.04	13.82	2650	2860 ± 350	...

Notes. (a) Relation from van Belle et al. (2013). (b) van Belle et al. (1997). (c) VINCI unpublished data. (d) Richichi et al. (2005). (e) θ_{Ross} is the Rosseland diameter of the best fitting time-step of the corresponding best-fitting model. (f) paper in prep. based on AMBER and PIONIER data; see also Paladini (2011), PhD thesis.

5.7 Conclusions

In this work we presented a study on the atmospheres of six C-rich AGB stars, combining photometric and interferometric observations, comparing them consistently with a grid of dynamic model atmospheres.

Overall, we found that the fit of DARWIN models SEDs with the photometric and interferometric observations presented in this work show a strong improvement with respect of the one of RU Vir. The best agreement is found for Mira stars, while for non-Miras the DARWIN models have more difficulties to reproduce the photometric observations at wavelengths shorter than 1 μm.

This could be related to the stars variability, since the photometric data in that wavelength region come from various studies, therefore a difference in phase is likely. There is a slight improvement in the agreement of the interferometric data with the models in level, but the difference in shape still remains and is probably due to the amount of condensed dust included in the models, as the experiments mentioned in Sect. 5.6 prove. Also, the observations show a consistency with the model assumption that SiC and amC condense together.

From our interferometric analysis, it resulted that models for Miras appear to have steeper slope, and a larger extension, than the models for Semi-regular and Irregular stars. The models for the non-Miras don't show this slope in the wavelength-dependent visibilities, and these models generally have weakly pronounced shells.

We derived stellar parameters through the comparison of photometric and interferometric observations with dynamic models atmospheres and geometric models. Those parameters are summarized in Table 5.4 and Table 5.3. In the latter, errors on the temperatures are of the order of ±400 K and on the luminosity of the order of 2000 $L_\odot$.

Models without the small particle limit assumption have lower condensation degrees, which probably implies less dust extinction in the visual region. Those models will represent a good test to verify the visual excess shown by some of the stars analyzed in this study. Indeed, ex-

clusion of the SPL assumption in a dust-shell changes the mid-IR interferometric shape and the temperature-structure. Thus, models without the SPL assumption, compared with our observations, will be tested in a follow-up of this work (Rau et al. in prep).

The second generation VLTI instrument MATISSE (Lopez et al., 2006), will allow imaging at the highest angular resolution. It will therefore be a perfect tool to better reconstruct the intensity profiles of the objects in this study, and to investigate the small scale asymmetries, in order to confirm or deny the asymmetric nature of the objects studied in this work. MATISSE will also help to improve the variability study of those stars and the global distribution of molecules and dust.

Additional interferometric observations of those targets will help us also to constrain the models better, e.g. VLTI/PIONIER (H-band, Le Bouquin et al., 2011), GRAVITY (K-band, Eisenhauer et al., 2008) or Millimeter/sub-millimeter interferometric e.g. ALMA measurements and VISIR observations could provide further constraints to solve the open questions.

Chapter 6

The VLTI/MIDI large program (Paper III)

My contribution to the study presented in this chapter focused on the data reduction, analysis, and quality check of the MIDI interferometric data of all the carbon-rich AGB stars of this publication.
The work described in this chapter is part of the submitted paper:

Title: *The VLTI/MIDI view on the inner mass loss of evolved stars from the Herschel MESS sample*
Authors: C. Paladini, D. Klotz, S. Sacuto, E. Lagadec, M. Wittkowski, J. Hron, A. Jorissen, A. Richichi, M. A. T. Groenewegen, F. Kerschbaum, T. Verhoelst, **G. Rau**, H. Olofsson, R. Zhao-Geisler
Year: 2016
Journal: Astronomy and Astrophysics, submitted on the 19$^{\text{th}}$ of August 2015.

The mass-loss process from evolved stars is a key ingredient for our understanding of many fields of astrophysics, including stellar evolution and the chemical enrichment of the interstellar medium (ISM) via stellar yields. Nevertheless, many questions are still unsolved, one among them being the geometry of the mass-loss process. Taking advantage of the results from the Herschel mass-loss of Evolved StarS (MESS) program, we initiated a coordinated effort to characterise the geometry of mass loss from evolved red giants at various spatial scales. For this purpose we used the MID-infrared interferometric Instrument (MIDI) to resolve the inner envelope of 14 asymptotic giant branch stars (AGBs) in the MESS sample. In this contribution we present an overview of the interferometric data collected within the frame of our Large Program, and we also add archive data for completeness. The geometry of the inner atmosphere is studied by comparing the observations with predictions from different geometric models.

Asymmetries are detected for 5 stars: R Leo, RT Vir, π^1 Gruis, omi Ori, and R Crt. All the objects are O-rich or S-type, suggesting that asymmetries in the $N-$band are more common among stars with such chemistry. We speculate that this fact is related to the characteristics of the dust grains. Except for one star, no interferometric variability is detected, i.e. the changes in size of the shells of non-Mira stars correspond to changes of the visibility of less than 10%. The observed spectral variability confirms previous findings from the literature. The detection of dust in our sample follows the location of the AGBs in the IRAS color-color diagram: more dust is detected around oxygen-rich stars in region II, and in the carbon stars in region VII. The SiC dust feature does not appear in the visibility spectrum of the U Ant and S Sct, two carbon stars with a detached shell. This finding will have implication on the theory of SiC dust formation.

6.1 Introduction

Most of the material processed during the lifetime of low- to intermediate-mass stars is returned to the interstellar medium (ISM) during the asymptotic giant branch (AGB) stage. This material is crucial for the chemical evolution of galaxies (perhaps even at high redshift; Valiante et al., 2009), and it contributes to build new generations of stars and planets.

The general picture which explains the mass-loss process assumes that stellar pulsation triggers shock waves in the atmosphere. These shocks lift the gas above the stellar surface, creating dense cool layers where dust may form. Depending on the chemistry of the star, theory predicts that the radiation pressure on dust, or the scattering on micron-size dust grains drive the stellar material away (Höfner and Dorfi, 1997; Woitke, 2006; Höfner, 2008). An important aspect of the mass loss process which is poorly understood is its geometry, i.e., the deviation of the density distribution from spherical symmetry on different spatial scales. The assumption on the geometry of the circumstellar environment affects calculations of mass-loss rates and other fundamental parameters (Ohnaka et al., 2008b). Over the last years several observing campaigns were carried out with the purpose of investigating the geometry of the envelope of AGB stars (references below). Observations suggest that the wind mechanism may depend on the initial mass of the objects, and on the evolution along the AGB (Habing and Olofsson, 2003). Despite first evidences in favor of overall spherical symmetry, some observations (Knapp et al., 1997, e.g. V Hya) show very complicated geometry at various spatial scales, and no consensus on its origin has been reached so far (Habing and Olofsson, 2003). Understanding how the mass loss shapes the envelope of AGB stars is crucial also for the progeny. Although a binary companion is currently the most accepted explanation, other mechanisms such as rotation velocity and magnetic fields might still play a role (De Marco, 2009). Investigating the morphology of the atmosphere of AGB stars at different spatial scales and evolutionary stages (early-AGB and Thermal-Pulse AGB) will help to clarify the picture on the follow-up stages.

By scanning the envelope of an AGB star from the inside to the outside one can distinguish the following:

Inner Circumstellar Envelope (CSE). At milliarcsecond scales (1-2.5 stellar radii), close to the

photosphere of the stars, asymmetries are frequently detected with lunar occultation (Richichi et al., 1995; Meyer et al., 1995) and optical interferometry (Ragland et al., 2006; Le Bouquin et al., 2009; Pluzhnik et al., 2009; Chiavassa et al., 2010; Wittkowski et al., 2011b; Cruzalèbes et al., 2013b; van Belle et al., 2013; Mayer et al., 2014; van Belle et al., 2013; Cruzalèbes et al., 2015). The asymmetric structures are often ascribed to convective patterns, but other interpretations are also invoked (mainly the effect of stellar rotation and binarity). It is observed that asymmetries in the brightness distribution are more frequent for Miras (Cruzalèbes et al., 2015, i.e., towards the end of the AGB life), and Irregular variables (Ragland et al., 2006), asymmetries are more frequent in C-rich stars than in the O-rich ones.

Intermediate CSE. Between 2 and 10 stellar radii, asymmetries and clumpiness are also observed for several objects (Weigelt et al., 1998; Tuthill et al., 2000; Weigelt et al., 2002; Leão et al., 2006; Tatebe et al., 2006; Chandler et al., 2007; Paladini et al., 2012; Sacuto et al., 2013). In a very few cases the asymmetries have a clear pattern resembling a spiral or a disc. These cases are usually related to the presence of a hidden binary companion (Mauron and Huggins, 2006; Deroo et al., 2007; Ohnaka et al., 2008a; Maercker et al., 2012; Mayer et al., 2013; Decin et al., 2015; Kervella et al., 2014; Ramstedt et al., 2014; Lykou et al., 2015; Kervella et al., 2015). On the other hand many other authors detect time variability but no clear signatures of asymmetries (Danchi et al., 1994; Ohnaka et al., 2005; Wittkowski et al., 2007; Karovicova et al., 2011; Sacuto et al., 2011b; Zhao-Geisler et al., 2011, 2012; Karovicova et al., 2013). To confuse even more the picture, SiO maser observations show evidences for clumpy isotropic mass loss in the atmosphere of O-rich AGB stars, while H_2O and OH masers (at R $>$ 10 $R_\star$) probing the intermediate-outer part of AGB stars are less conclusive about the geometry.

Outer CSE. Submillimiter observations of CO line profiles obtained toward M stars may deviate significantly from those expected from a spherical envelope (Knapp et al., 1998; Winters et al., 2003; Klotz et al., 012a). Imaging in the CO radio emission lines of carbon stars revealed spherically-symmetric thin "detached" shells (Olofsson et al., 2000), probably originating during the thermal pulses known to occur during the AGB phase. Images provided by the Herschel/PACS instrument within the frame of the Herschel Mass loss of Evolved StarS guaranteed time key program (MESS; Groenewegen et al., 2011) showed that the morphology of the outer atmosphere (R $>$ 1000 $R_\star$) of AGBs differs depending on various factors (for example interaction between wind and the interstellar medium, or wind-wind interaction, Cox et al., 2012).

Altogether it is clear that one has to probe all spatial scales to understand the physics of these complex outflows. While previous studies with the aim of detecting asymmetries suffered from a lack of (u, v)-coverage (cfr. optical/infrared interferometry) and/or instruments with sufficient sensitivities, the advent of new facilities with improved resolution and sensitivity like Herschel, ALMA, and VLTI offers the unique chance to understand the mass loss and dust-formation processes, and generally speaking, the life cycle of dust and gas in the Universe.

In September 2010, we proposed a Large Program (LP) to the European Southern Observatory (ESO) to complement the Herschel observations with observations using the mid-infrared instruments MIDI on the Very Large Telescope Interferometer (VLTI) and VISIR on the Very

Large Telescope (VLT). The aims of the study are i) to establish whether asymmetries of the outer CSE originate in the dust-forming region, or whether they are only due to interaction with the ISM; ii) to evaluate at which height, the mass-loss process becomes manifestly non-spherical; iii) to understand how the geometry of the atmosphere changes at the different evolutionary stages (M-S-C stars, and from almost dust-free to very dusty objects) within the AGB sequence.

In this paper, we present the program and the data of the interferometric (MIDI) campaign interpreted with geometric models. All the ESO archive data available for the targets are incorporated in the analysis to give a complete overview. This first work will be followed by a paper including a detailed interpretation of the MIDI data in terms of model atmospheres. The VISIR observing campaign was severely affected by bad weather conditions, a new observing proposal was recently accepted.

The selection of the targets is described in Sect. 6.2.1, while the strategy for observations in Sect. 6.2.2. The data reduction is reported in Sect. 6.2.3. We also used archive data that are introduced in Sect.6.2.4. The program used for the interpretation of the interferometric data is described in Sect. 6.3. Results are presented in Sect. 6.4. The discussion, conclusions and outlooks are given in Sects. 6.5 and 6.6, respectively. The detailed description of every single target can be found in Sect. 6.7, and the journal of the observations in Appendix A.3.

6.2 Target selection and data

6.2.1 Target selection

A sub-sample of the AGB stars observed within the Herschel key program MESS (Groenewegen et al., 2011; Cox et al., 2012) was selected on the basis of the following criteria: declination accessible from the Southern hemisphere where the ESO telescopes are located, brightness within the limits of the instruments, and to have different chemistries and variability types. The IRAS two-colour diagram (van der Veen and Habing, 1988) was used as a reference, with the purpose of sampling AGBs with different shell properties (Fig. 6.1). Every region includes targets with well-defined infrared characteristics: variability, and IRAS Low Resolution Spectrometer (LRS) classification.

The mildly variable O-rich AGB stars without extended circumstellar shells are expected to populate region I. In region II the objects are surrounded by young O-rich shells, while in region IIIa the shells are more evolved and mass-loss rates are higher. In region VIa most of the C-rich objects with relatively cold dust are located (so called detached-shell objects), while the objects located in region VIb have hot oxygen-rich dust close to the star, and cold dust at larger distances. The variable stars with evolved C-rich shells as well as infrared carbon stars are in region VII. The panels not covered within the observing sample are populated by objects with optically thick envelopes having no visual counterparts, and by Planetary Nebulae. The list of targets is presented in Table 6.1 together with the location in the IRAS color-color diagram, the morphological class identified by Cox et al. (2012) from the Herschel/PACS images, and general characteristics such as spectral type, variability class, IRAS 12 μm flux, period, distance, and

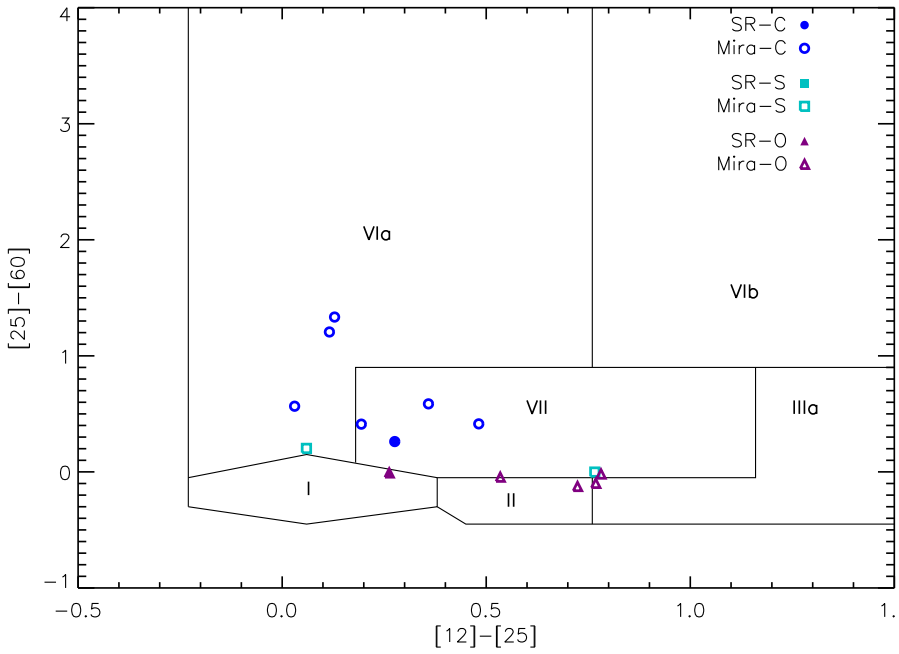

Figure 6.1: The targets of our sample shown in the IRAS two-colour diagram of van der Veen and Habing (1988).

mass-loss rate.

6.2.2 Observing strategy

In this work we concentrate on possible asymmetries developing in the dust forming region. Danchi et al. (1994) and more recently Norris et al. (2012) observed that dust is forming between 3 and 5 stellar radii, and even closer to the star in the case of Mira variables, as Draine (1981) already predicted. As a consequence, to observe the *locus* of dust formation for AGBs within 1 kpc, one needs to have an angular resolution of ~ 20 mas. For this reason, the MIDI instrument (Leinert et al., 2003a) installed at the ESO Very Large Telescope Interferometer (VLTI) on Cerro Paranal (Chile) until March 2015 was chosen. MIDI is a 2-beam combiner interferometer observing in the $N-$band (8-13 μm). For every observation, the instrument delivers one visibility spectrum (sometime shortened to "visibility" in the text), one total flux spectrum, and one differential phase spectrum (phase difference between different spectral channels, Sect. 6.4.2). Depending on the correlated magnitude of the target, either the HIGH-SENS (where the correlated and the total flux are measured one after the other) or SCI-PHOT (where the correlated and the total flux are measured simultaneously) mode was chosen. All the LP data have spectral resolution $R = \lambda/\Delta\lambda \sim 30$.

To optimise the observations for studying the geometry the following strategy was used. The choice for the baseline configurations was split in two different categories, based on the Herschel

Table 6.1: Target list.

Target	IRAS color-color region	Herschel/PACS[(a)] morphology	Spectral Type	Variability	F_{12} [Jy]	Period [d]	Distance[(b)] [pc]	Mass-Loss rate $[M_\odot yr^{-1}]$
θ Aps	II (O-rich shells)	Fermata	M6.5III	SRb	734.30	119[(c)]	113^{+7}_{-6}	0.4×10^{-7} [(d)]
R Crt	II (O-rich shells)	Eye	M7III	SRb	637.90	160[(c)]	261^{+86}_{-52}	8×10^{-7} [(d)]
R Leo	I	Fermata	M8IIIe	M	2161.00	310[(e)]	110^{+17}_{-11}	9.4×10^{-8} [(f)]
T Mic	II (O-rich shells)	Fermata	M7III	SRb	493.80	347[(c)]	200^{+57}_{-37}	8×10^{-8} [(d)]
RT Vir	IIIa	Fermata	M8III	SR	462.20	375[(g)]	136^{+17}_{-14}	5×10^{-7} [(d)]
π^1 Gru	II/IIIa/VII	Irregular	S5+G0V	SRb	908.50	198[(h)]	153^{+23}_{-18}	4.6×10^{-7} [(i)]
omi Ori	VIa/I	Irregular	S+WD	SR	85.35	...	200^{+33}_{-25}	$< 0.4 \times 10^{-7}$ [(j)]
U Ant	VIa	Ring	N:var	Lb	167.50	...	270^{+45}_{-34}	2×10^{-8} [(k)]
R Lep	VII	Point Source	CIIe	M	379.50	427[(c)]	470^{+301}_{-122}	1.6×10^{-6} [(k)]
Y Pav	VII	Point Source	CII	SRb	72.38	233[(c)]	400^{+126}_{-77}	4×10^{-7} [(l)]
TX Psc	VIa	Fermata	CII	Lb	162.90	...	275^{+33}_{-27}	3.2×10^{-7} [(k)]
S Sct	VIa	Ring	CII	SR	65.31	148[(c)]	386^{+109}_{-70}	5.6×10^{-6} [(k)]
AQ Sgr	VII	Fermata	CII	SR	56.64	199[(c)]	333^{+96}_{-61}	7.7×10^{-7} [(k)]
X TrA	VII	Ring	C	Lb	201.00	...	360^{+68}_{-49}	1.8×10^{-7} [(k)]

Notes. (a) Cox et al. (2012); (b) van Leeuwen (2007); (c) Samus et al. (2009a); (d) Olofsson et al. (2002a); (e) Whitelock and Feast (2000); (f) Knapp et al. (1998); (g) Imai et al. (1997); (h) Tabur et al. (2009); (i) Jorissen and Knapp (1998); (j) Groenewegen and de Jong (1998); (k) Bergeat and Chevallier (2005); (l) Winters et al. (2003).

data available: configurations for non-spherical (like the bow shock in the case of TX Psc, Jorissen et al., 2011), and for spherical objects (like the detached-shell object U Ant, Kerschbaum et al., 2010). For the non-spherical cases we selected one baseline oriented in the direction of the asymmetry, and one perpendicular to the latter. A third baseline with orientation in between the two, was selected to put constraints on the possible elongation. Baselines with random orientation were selected for the symmetric stars, as well as in the cases where PACS images were not yet available. Thus, we are able to constrain any possible deviation from sphericity. We also tried to sample the same spatial frequencies by choosing the same baseline lengths for all points. The baseline length also has to be selected carefully for resolving the dust formation zone. Given the fact that not all the targets of the sample had a measured photospheric diameter, the latter was estimated through the $(V-K)$ relation of van Belle et al. (1999). Following the results of Danchi et al. (1994), we thus assumed that the diameter in the $N-$band is approximately three times the photospheric one, and the baseline was selected accordingly.

For planning the observations, we used ASPRO and ASPRO2 developed by the Jean-Marie Mariotti Center `Aspro` service [1]. The observations were carried out between 2011 April 23 and 2012 July 01 on the 1.8 m Auxiliary Telescopes (ATs). We used the recommended observation sequence CAL-SCI-CAL. The following selection criteria for calibrator stars were applied: brightness (difference between calibrator and science target of ± 1 mag), position (RA and Dec as close as possible to the science target), size (the calibrator should be as small as possible), spectral type (if possible the calibrator should have a spectral type earlier than M0). The list of calibrators and their main characteristics are presented in Table 6.2. The journal of the MIDI observations is available as online material (Appendix A.3).

6.2.3 Observations and data reduction

MIDI data were reduced using the data reduction pipeline MIA+EWS[2] (Jaffe, 2004; Ratzka, 2005; Leinert et al., 2004). A detailed description of the data quality tests that were applied during the data reduction can be found in Klotz et al. (2012b). Data are reduced with all calibrators observed in the same night (if possible within ± 2 hours) and with the same baseline configuration as the science target. The final calibrated visibilities are then the mean of all the visibilities, differential phases and fluxes reduced with suitable calibrators. The error is derived from the standard deviation of that series. If the former error is lower than $\pm 10\%$ or only one calibrator was available during the night, a multiplicative error of $\pm 10\%$ was used (Chesneau, 2007).

The extraction of the differential phase is done following the standard procedure of EWS (Jaffe, 2004). The differential phase is corrected for the changing index of refraction of air by subtracting a linear slope, so that the mean phase over the N-band is zero. We did not correct for higher order effects due to water vapor content (PWV). Instead, we employ a very simplistic approach, by calibrating the differential phases using several calibrators taken over the night and

[1] Available at `http://www.jmmc.fr/aspro`

[2] `http://www.strw.leidenuniv.nl/~jaffe/ews/MIA+EWS-Manual/index.html`

Table 6.2: Calibrator list.

HD	Spectral type [a]	F_{12} [(a)] [Jy]	θ [(b)] [mas]	used for
18884	M1.5IIIa	234.7	12.28 ± 0.05	omi Ori, R Lep
20720	M3/M4III	162.70	10.14 ± 0.04	R Lep
25025	M1IIIb	109.6	8.74 ± 0.09	R Leo
29139	K5III	699.7	20.398 ± 0.087	R Leo, U Ant
32887	K4III	56.82	5.90 ± 0.06	R Lep
39425	K1IIICN+1	28.0	3.752 ± 0.017	omi Ori
48915	A1V	143.1	6.08 ± 0.03	R Leo, R Lep, U Ant
50778	K4III	24.6	3.904 ± 0.015	omi Ori
61421	F5IV-V	79.1	5.25 ± 0.21	R Leo
81797	K3II-III	157.6	9.142 ± 0.045	θ Aps, R Crt, RT Vir, R Leo
112142	M3III	47.0	5.90 ± 0.7	R Crt, RT Vir, AQ Sgr
120323	M4.5III	255.4	13.25 ± 0.06	R Crt, RT Vir, R Leo, U Ant, AQ Sgr
123139	K0III	56.9	5.33 ± 0.057	R Crt, RT Vir, R Leo, AQ Sgr
129456	K5III	21.4	3.37 ± 0.014	T Mic
133216	M3/M4III	200.7	11.154 ± 0.046	RT Vir
150798	K2II-III	144.0	8.76 ± 0.12	θ Aps, R Crt R Leo, Y Pav, X TrA
151249	K5III	52.18	5.515 ± 0.179	Y Pav
152786	K3III	82.1	8.02 ± 3.23	θ Aps, R Crt R Leo, AQ Sgr
165135	K1III	23.4	3.47 ± 0.015	T Mic
167618	M3.5III	213.7	11.665 ± 0.043	θ Aps, T Mic
168454	K3III	62.17	5.874 ± 0.026	S Sct, AQ Sgr
169916	K0IV	31.2	3.995 ± 0.019	T Mic, Y Pav, S Sct, AQ Sgr
177716	K1III	26.0	3.78 ± 0.21	T Mic
206778	K2Ib	103.9	7.59 ± 0.046	θ Aps, R Leo, π^1 Gru
211416	K3III	59.3	5.92 ± 0.28	AQ Sgr
224935	M3III	86.90	7.25 ± 0.03	π^1 Gru

Notes: (a)`http://simbad.u-strasbg.fr/simbad/`;
(b)`http://www.eso.org/observing/dfo/quality/MIDI/qc/calibrators_obs.html`

deriving our error estimate on the phase from the scatter of these multiple calibrations. The instrumental phase measured for the calibrators during the different nights is usually stable and of the order of $\pm 5°$. Any uncertainty on the differential phase caused by the lack of correction for the dispersion effects due to PWV is therefore transferred to the errors on our phases.

A word of caution must be issued concerning the MIDI spectra. The water vapor content in the Earth atmosphere can change conspicuously on a time scale of half an hour without any changes in seeing or coherence time. So, it is possible that the water vapor content and thus the transmission of the Earth atmosphere changes between science and calibrator. Whereas the calibration of the interferometric visibility is not affected, the fluxes (i.e. the MIDI spectra) will be affected. To limit such effects, fluxes were only derived if the airmass difference to the science target is smaller than 0.2 and the calibrator was observed within $\pm$ 2 hours from the science target. Only calibrators of spectral type earlier than M0 were selected for the flux calibration. Henceforth the possibility that the science spectra is contaminated by possible dust around the calibrator is minimized (Chesneau, 2007). Adding the LP to the archive data (Sect. 6.2.4), we collected a total of 201 visibility points; 60% of these data were of good quality and are used in this work.

6.2.4 Additional observations and variability check

Archive MIDI observations were available for TX Psc, AQ Sgr, U Ant, T Mic, R Crt, R Leo, RT Vir, π^1 Gru, omi Ori, and R Lep. Some of these data were observed in `GRISM` mode (spectral resolution $R = 230$). These high resolution archive observations were convolved to a spectral resolution $R = 30$ before any comparison with the LP data. We also noticed that most of these observations were done with different baselines but at the same position angle. Such datasets allow to probe the atmosphere at different spatial scales, i.e. they are optimal for tomography studies. Moreover these observations carry information about intra-cycle and cycle-to-cycle interferometric and spectroscopic variability. When possible we assigned to every MIDI observation a variability phase calculated from the visual light curve. For this purpose light curves were collected from: the American Association of Variable Star Observers (AAVSO), the All Sky Automated Survey (ASAS), and the Association Française des Observateurs d'Étoiles Variables (AFOEV). The phase is determined from the light curve using the following relation:

$$\phi = \frac{(t - \mathrm{T}_0)}{P} - int\left(\frac{(t - \mathrm{T}_0)}{P}\right),$$

where t stands for the date of the MIDI observation(s) expressed in Julian date. T_0 is the phase-zero point which was selected as the maximum light closest in time to the first MIDI observation. P is the period of variability already listed in Table 6.1. Visual phases are assigned to the stars θ Aps, R Crt, R Leo, T Mic, RT Vir, R Lep, Y Pav, S Sct, and AQ Sgr. The values are listed in Appendix A.3, and errors are assumed to be of the order of 10% of the period.

The analysis of spectroscopic variability is performed by comparing MIDI spectra obtained at different visual phase, and also by comparing the MIDI spectra to available ISO and/or

IRAS spectra. The interferometric variability was studied by comparing (when available) sets of visibilities at similar baseline lengths and position angles, observed at different dates. If no interferometric variability is detected, one can assume that the data can be combined for the geometric fit. The (u, v)-coverages obtained for all the data of the LP, including the archive data is shown in Fig. 6.2.

6.3 Geometric fitting

A model-independent way to identify departure from spherical symmetry of the CSE is by comparing visibilities taken at similar baseline and different position angle. We performed this check where the dataset allowed it. As a second approach we employ the software GEM-FIND (GEometrical Model Fitting for INterferometric Data, Klotz et al., 2012b) to interpret our observations. This software fits geometrical models to interferometric visibility data, where different spherically-symmetric, centro-symmetric and asymmetric models are available. The different parameters of the models can be either wavelength-dependent (e.g. diameter, flux ratio of two components) or wavelength-independent (e.g., inclination or axis ratio of a disk) as GEM-FIND will fit each wavelength-point separately. This gives us the possibility to study the dependence of the model parameters on e.g. molecular and dust features. The output of GEM-FIND is a $\chi^2_{\rm red}$, the best-fitting parameters, and wavelength-dispersed visibilities and differential phases. The errors of the best-fitting parameters given by GEM-FIND are the 1σ statistical errors derived from the covariance matrix (calculated within the MPFIT[3] IDL routines implemented in GEM-FIND). It is known that the models in the Fourier space are not linear, therefore the errors are not Gaussian distributed. We tested the validity of the approach with Monte-Carlo simulations (Klotz et al., 2012b). We find that 1σ errors from the Monte-Carlo simulations are comparable to the ones derived from the covariance matrix. Therefore, in the following, errors will be computed from the covariance matrix.

For the study of the geometry of the circumstellar environment, the following models were used to fit the data: circular uniform disk (UD, representing an approximation of the stellar disk), circular Gaussian distribution (Gauss, approximation to an object with a molecular or dusty environment and limb darkening), elliptical uniform disk (Ell. UD, like the UD case with non central symmetric brightness distribution), elliptical Gaussian distribution (Ell. Gauss, like in the Gauss case with non central symmetric brightness distribution). The latter two models were applied only for the objects with more than 2 position angles available. In the case where a sufficient number of observations sampling different spatial frequencies was available, a spherical two-component model (circular UD plus circular Gaussian, where the two components represent typically the photosphere and a optically thin dust and/or molecular component) was used additionally. In this latter case the diameter of the UD was fixed to a value corresponding to the $\theta_{(V-K)}$ diameter (van Belle et al., 1999), to simulate the central star (or to the observed $K-$band value, when available). Only the Gaussian envelope was fitted. The fit with GEM-

[3] `http://purl.com/net/mpfit`

Table 6.3: Reduced $\chi^2_{\rm red}$ from GEM-FIND fitting.

Target	Baseline [m]	Year	N_{OB}	UD	Gauss	Ell. UD	Ell.Gauss.	UD+Gauss
θ Aps	10–17	2011/12	6	**0.78**	0.69	0.41	0.38	...
R Crt	10–16	2012	5	10.17	2.53	1.18	**1.04**	...
	10–64	2009/11/12	8	46.27	28.31	18.18	17.74	**0.66**
R Leo	11–16	2012	4	**0.93**	0.78	0.09	0.11	...
	11–64	2006/07	18	38.55	14.73	8.03	10.84	**6.45**
T Mic	11–16	2011	4	**0.28**	0.27	0.09	0.11	...
	11–46	2004/11	7	1.16	**0.96**	0.49	0.46	0.24
RT Vir	13–15	2012	2	1.31	**1.13**	...	...	...
	12–128	2008/09/11/12	14	49.10	25.13	22.80	20.51	**3.04**
π^1 Gru	10-15	2011	3	4.83	3.44	**0.57**	0.42	...
	10-62	2006/11	11	23.23	23.56	21.59	21.49	**0.85**
o^1 Ori	32–46	2011	7	1.30	1.30	**0.79**	0.78	...
	32-129	2005/11	14	2.04	2.01	1.90	1.85	**1.42**
U Ant	30	2012	1	...	...	...	...	...
	30-95	2008-2012	3	**1.20**	1.23	0.65	0.63	...
R Lep	34-40	2012	6	1.59	**0.93**	1.32	0.90	...
	34-79	2011/12	10	2.38	3.65	1.39	3.55	**1.00**
Y Pav	50-63	2011	4	0.77	**0.78**	0.44	0.44	
TX Psc	60-140	2011	6	**0.99**	1.19	0.90	1.09	...
	11-140	2004-2011	15	**1.28**	1.32	1.29	1.32	1.34
S Sct	40-45	2011	2	2.63	**2.61**	...	...	...
X TrA	21-34	2011	5	**0.95**	0.89	0.31	0.30	...
AQ Sgr	37-42	2011	2	**1.59**	1.67	...	...	...

Notes. The range in baseline length is given as 'Baseline'. The number of observations used for the fitting is given as N_{OB}. The first row corresponds to the data of the LP. The second row corresponds to fits were the LP and archive data were merged. If only data points with similar position angles were available, the elliptical models were not fitted. The $\chi^2_{\rm red}$ of the model best fitting the data is highlighted in bold-face. The resulting best fitting parameters are given in Table 6.4, whereas the dates of the observations are given in Appendix A.3.

FIND was performed in two stages: first only the LP data are fitted, afterwards the LP data are merged with the archive ones and a new fit is performed. The reasoning behind this strategy is that the LP data are chosen to sample the same spatial frequencies and different position angles, therefore they are more suitable for detecting possible elongations due to a non central symmetric distribution. The fit with all data (LP + archive) is done for completeness, and it allows us to study the stratification of the stars.

6.4 Results

This section summarises the general findings of the LP. Detailed discussion for the single targets are given in Sect 6.7.

6.4.1 Visibility vs. wavelength

A visual inspection of the visibility spectrum reveals certain spectral features characterising the chemical composition of the CSE. For this study, we inspect the visibilities in the range between $0.1 \leq V \leq 0.9$. In the case of $V \geq 0.9$, it is not possible to distinguish details of the spectral signature, or even distinguish the visibilities from that of a point source due to the typical errors. At $V \leq 0.1$ the relation between visibility and spatial frequency may not be univocal (as the visibility function may consist of several lobes). Fig. 6.3 shows the spectrally dispersed visibility curves for stars with different chemistry.

M-type and S-type stars. The most prominent molecular feature of oxygen-rich stars in the $N-$band is SiO around 8 μm. In some cases, this is followed by silicates and Al_2O_3 dust. For stars not showing a pronounced silicate feature like R Leo (upper left panel of Fig. 6.3), T Mic, and the S-type stars omi Ori and π^1 Gru (upper right panel of Fig. 6.3), the visibility is rather flat with a small bump at short wavelengths. The diameter increases slightly at longer wavelengths. For stars showing the dust and molecular features (R Crt shown in the central upper panel of Fig. 6.3; RT Vir, and θ Aps) the visibility has a peak in the 8-9 μm region, a decrease between 9-11 μm, and a subsequent increase.

C-type stars. The molecules contributing to the carbon stars opacity in the N-band are mainly C_2H_2 and HCN. Concerning the dust, evolved carbon-rich objects show SiC dust at 11.3 μm and amorphous carbon dust (featureless). Examples of visibilities of stars with SiC dust were shown by e.g. Ohnaka et al. (2007), Sacuto et al. (2011b), Paladini et al. (2012), and Rau et al. (2015c). The lower left panel of Fig. 6.3 shows the visibility of the C-rich Mira R Lep with the typical drop at 11.3 μm due to SiC. Y Pav, X Tra, and AQ Sgr show similar visibility curves. The visibilities of carbon rich stars *without* SiC have a typical bow shape. The visibility gets lower (i.e. the star is larger) between 8-9 μm and after 12.5 μm where the molecular opacity is higher. Fig. 6.3 shows an example of such kind of stars: TX Psc (also presented in Klotz et al., 2013b).

Other stars. The IRAS and the MIDI spectra of U Ant show the signature of SiC dust feature, while there is no trace of such feature in the (spatially resolved) interferometric observations

(lower right panel of Fig. 6.3). This could be the result of resolving-out part of the total emission, revealing only the emission of the spatial scale the interferometer is sensitive too (at the employed baselines).

The case of S Sct is slightly different. There is no trace of SiC in the (spatially resolved) interferometric observations nor in the MIDI spectrum. The dust feature is observed in the ISO spectrum recorded 14 years before the LP observations. The IRAS spectrum of S Sct obtained $\sim$ 30 years before is very noisy but seems to agree with the MIDI one (Fig. 6.28). The latter was derived by averaging data taken on two different days, therefore one should be able to rule out a problem with the calibration. The S Sct observations suggest a temporal variability in the stratification of SiC.

To our knowledge it is the first time that such findings are reported for AGB stars. We refer the reader to Sect. 6.5 for a detailed discussion.

6.4.2 Differential Phase

Except for the cases where the differential phase is equal to 180°, and/or it is accompanied by a null value in the visibility, a non-zero differential phase measured by MIDI implies an asymmetric brightness distribution. The latter can be explained by two effects (Tristram et al., 2014): (i) the object is composed of two sources (for example the photosphere and the resolved dust component) with different spectral distribution through the $N-$band ; (ii) the object is composed of two objects with a spatial distribution more resolved at a certain wavelength than at another across the $N-$band. In nature we usually observe a mixture of these two effects, which are very difficult to distinguish, unless one has enough information for detailed modelling or to attempt an image reconstruction. Non-zero differential phase was observed in a few AGB stars. Usually this is interpreted as a typical signature of a disk (Kervella et al., 2014; Ohnaka et al., 2008a; Deroo et al., 2007) or the signature of a clump (Sacuto et al., 2013; Paladini et al., 2012). Since modelling very few differential phases gives highly non unique solutions, no attempt to interpret the differential phase will be done here.

We report non-zero differential phase only for two objects: R Leo and RT Vir (Figs. 6.4 and 6.5). The morphology of the differential phases of R Leo can be classified in two groups, according to the projected baseline used for the observations. The three upper panels of Fig. 6.4 show a jump of the differential phase around 9 μm. These data are acquired at different time (see Sect. 6.4.3), at the same position angle and very similar projected baseline. The lower panels show a much more complex behaviour with features at $\sim$ 10 and $\sim$ 11.8 μm.

The differential phase of RT Vir shown in Fig. 6.5 is characterised by a jump between 8 and 9 μm, followed by a monotonic increase. For an interpretation of the RT Vir differential phase with a geometric model, we refer to Sacuto et al. (2013).

All the non-zero differential phases occur at visibility spectra below 10%.

6.4.3 Spectroscopic and interferometric variability

As already mentioned in Sect. 6.2.4, we used archive spectroscopic and interferometric observations to study the N-band variability.

The spectroscopic variability typically corresponds to the variation in the color (temperature) or a specific variation in certain line strength. On the other hand, the interferometric variability is usually connected with a change in the morphology of the object, in particular the spatial scale of the N-band emission region. Of course the real picture is more complex, and interferometric variability might also be due to brightness variation: when the stellar atmosphere is spatially resolved, and in the FOV of the interferometer there are multiple components (i.e. photosphere plus extended molecular/dust layer, or photosphere plus clumpy structures) it is possible to observe variation in the visibility (at the same spatial frequency) because of a change in the flux ratio between the two components.

In Fig. 6.6 we compared the level of the MIDI spectra with ISO and IRAS spectra (when the ISO observations were not available). The ISO and IRAS observations are taken approximately 30 years apart from the MIDI ones. Such kind of comparison can in principle provide information around long-time variability due to dust formation and/or mass-loss variation. On the other hand this can be caused by the FOV difference between the various telescopes. The FOV of the MIDI observations is $\sim$ 2.3 " $\times$ 1.6 " , and it is smaller than the FOV of IRAS and ISO, 45 " $\times$ 45 ", and 33 " $\times$ 20 " respectively). Only a detailed modelling will be able to distinguish between these effects. Such kind of modelling is beyond our scope, we simply report cases of suspected variability leaving the modelling to future investigation Rau et al. (2016b).

We observe that 3 stars out of 13 have a mid-infrared flux very similar to the IRAS one (U Ant, omi Ori and R Crt). AQ Sgr, Y Pav, RT Vir and T Mic have a flux level below the one observed by ISO/IRAS. The "shape" of the spectrum is usually consistent, exception made for Y Pav where a calibration problem cannot be excluded. This hypothesis is also supported by the fact that in the Y Pav spectrum, one can still see the telluric ozone feature at 9.7 μm.

For R Crt, R Leo, R Lep, and RT Vir, we had several MIDI spectra observed at different visual phases. By plotting the flux a various wavelengths (8, 10, and 12 μm) vs. visual phase, we study the intra-cycle and cycle-to-cycle variability of the star (Figs. 6.10, 6.12, 6.16, 6.22). R Crt shows no significant variability (Fig. 6.10). R Lep and R Leo show variations. RT Vir is by far the star with the best coverage in phase. The variation of the flux over the pulsation period resembles a sinusoid (Fig. 6.16). The flux variation within the cycle corresponds to an amplitude of variability of 0.48 mag at 8 μm, and 0.75 mag at 10 and 12 μm.

The interferometric variability of the visibility spectrum was studied only for θ Aps, R Leo, RT Vir and R Lep. The intra-cycle observations of the carbon-rich Mira R Lep are taken at very similar visual phase (0.01 difference), therefore it is not a surprise if no interferometric variability is detected (Fig. 6.23, left panel). However, a cycle-to-cycle variation is observed in the level of the visibility spectrum (Fig. 6.23, right panel). The variation is more pronounced in the molecular dominated region between 9 and 10 μm. We do not observe variation between 11 and 12 μm, where SiC is located. The visibility level is higher before the visual phase minimum

($\phi_V = 1.43$), corresponding to a smaller diameter.

Both θ Aps and RT Vir do not show any evidence of variability in the visibility spectrum. Two sets of data are available to check the interferometric variability for R Leo. The first set includes three observations taken with the short baseline configurations. The visibility level is ~ 0.6, the observations are taken at similar visual phase, but one of them was observed 6 cycles before. No variability is observed for this set of data (Fig. 6.13, left panel). The second set of data also includes three data point, but the first two were averaged because taken within two consecutive days (with very similar PA and projected baseline). The observations are shown in the right panel of Fig. 6.13, and the difference between the visual phases is 0.13. It is obvious that in this case we do observe a variation in the visibility level from one visual phase to the other. However, these observations are associated to a differential phase signature (Fig. 6.4, upper row). The differential phase is also changing from one set of observations to the other.

6.4.4 The geometric fitting results

Large Program data only. As a first step, the geometric models are fitted solely to the LP data. As described in Sect. 6.2.2, the LP observations sample very similar spatial frequencies (i.e. the same part of the star) at different position angles. In Table 6.3, for each star, we present in the first row the results of the fit on the large-program data only. The model with the χ^2_{red} closest to 1 is considered as the one best fitting the data, and it is highlighted in bold in Table 6.3. The elliptical models have been tested for 10 objects out of 14, because in some cases not enough data points were available. One oxygen-rich star (θ Aps) out of the 4 tested with elliptical models is asymmetric. Two S-type objects (π^1 Gru and omi Ori) also show indication of ellipticity from the GEM-FIND fit. Out of the sample of 4 carbon-rich objects that were tested, none turned out to be asymmetric. This means that by analysing only the visibilities, approximately 30 % of the stars shows a signature of non spherically-symmetric brightness distribution. All these "asymmetric" stars have O-rich chemistry and are located in the lower part of the IRAS color-color diagram, as shown in panel (a) of Fig. 6.7. It has to be underlined that an elliptical solution does not necessarily imply that the environment has a truly elliptical shape. It only means that the CSE is non central symmetric. More complex geometries than ellipses cannot be excluded.

Large Program & archive data. After excluding interferometric variability, we combined the data of the LP with the ones obtained from the archive. Nine stars of our sample have archive data, and two of these stars have non zero differential phase. For the latter objects we performed a GEM-FIND fit with the only purpose of deriving a size, and/or to detect the presence of molecular/dust multiple components. Despite the resulting χ^2_{red}, these stars are marked as asymmetric in panels (b) and (d) of Fig. 6.7.

Beside R Lep and TX Psc, all the other stars have archive data that sample mostly the same position angle but at different spatial scales. As already stated in Sect. 6.2.4, these kind of data are optimal for studying the stratification of the star, but they are obviously less sensitive to asymmetries. Exception made to TX Psc, every time archive data are added to the fit, the composite (UD plus Gaussian) model turns out to be the best fitting one. This implies that the

stars have an extended environment due to molecular and/or dust opacities. We note that the additional archive data *wash away* the elliptical solution for all the 3 objects mentioned at the beginning of this section. This is a consequence of the fact that the additional data have always the same position angle. Being more numerous than the LP data, they drive the fit towards symmetric solutions, but this result certainly does not imply that the asymmetry detected by the dedicated LP data must be considered spurious. The panel (b) of Fig. 6.7 shows the result of the GEM-FIND fit of the LP+archive data including all the asymmetric results. It is shown that asymmetric brightness distributions are mainly located in the lower part of the IRAS color-color diagram, where O-rich stars are located.
Ignoring the asymmetric results, and by looking at the LP+archive fitting results of Table 6.3, one notes the following. Six stars are best-fitted by the composite model UD+Gauss, i.e. six stars have an extended, optically thin, component. However, it is possible that by adding more visibility points, other objects will also increase in complexity and they will be best fitted with a composite geometric model. This is very likely for X Tra, AQ Sgr, θ Aps, and Y Pav where the coverage of the visibility spectrum does not extend below 0.6. Given the fact that no dust feature is detected around S Sct, we expect that the visibility spectrum will be reproduced only with one component, even by adding other visibility points. So far, in our sample, only TX Psc has a visibility that goes down to V$\sim$ 0.2 without showing departure from uniform disc: no dust envelope is detected. A summary of these results is shown in panel (c) of Fig. 6.7. Exception made for the Mira R Leo that can be fit with two components model in region I, the presence of multiple components (i.e. dust) increases from left to right. This is in agreement with what is observed with spectroscopy. The carbon stars in region VIa, following the loop for the carbon stars, can be fit with single component models and are supposed to be younger than the ones located in region VII. The only carbon Mira of the sample is fitted with the composite model in region VII. All the objects in region VIa do not show SiC in the visibility (i.e. within the FOV of the interferometer).

Diameters. In Sect. 6.2.2 the strategy for choosing the baseline that allows to resolve the dust forming region was explained. One of the output of the GEM-FIND fitting is the diameter (or the full-width-half-maximum for the Gaussian profile) of the object in the fitted wavelength. It is known that geometric models are not the best tool for determining diameters, but as the diameters come "for free" from the fit, we compare them with the photospheric ones. In Table 6.4 we report the photospheric angular and linear diameters (see Sect. 6.2.2) calculated from the $V-K$ relationship (van Belle et al., 1999), the name of the GEM-FIND best-fitting model for the archive + LP data (as a reminder), the angular diameters (or full width half maximum, FWHM) at different wavelengths resulting from the geometric fitting, the linear diameter (FWHM) at 8 μm, and finally the ratio between the photospheric and the 8 μm diameter. The comparison between the diameters is not easy because of the mix of UD sizes and FWHM, but overall most of the diameters at 8 μm are of the order of 2 times the photospheric diameter. The exceptions are the two S-type stars and the carbon Mira R Lep, which have a much larger environment ($> 3\ D_{V-K}$). Diameters at longer wavelength are even larger with some extreme cases for the

more dusty stars as R Crt, RT Vir. The values of the D_8/D_{V-K} obtained for the carbon stars are in general agreement with the ratio between the photospheric and 8-9 μm diameters predicted by dynamic model atmospheres (Paladini et al., 2009, Fig. 6).

6.5 Discussion

6.5.1 Silicon carbide dust

As a matter of fact, up to now, all the carbon stars observed with MIDI that were showing SiC in the spectrum, always had a signature of such dust component in the visibility (Ohnaka et al., 2007; Sacuto et al., 2011b; Paladini et al., 2012; Zhao-Geisler et al., 2012; Rau et al., 2015c).

van Boekel et al. (2004) showed the case of protoplanetary discs where the (normalized) correlated flux spectrum (or visibility spectrum) reveals certain chemical features that are not detected in the total flux spectrum. The MIDI observations of U Ant show a similar behaviour, although in this specific case the chemical feature (SiC) is present in the total flux and not in the correlated one. The diameter measured with GEM-FIND (Table 6.4) at 8 and 12 μm is 10 mas, hence very similar to the one obtained via the $(V-K)$ relation (van Belle et al., 1999). This implies that the interferometer does not see any significant molecular or dusty environment, but rather the "naked" star. SiC is very likely outside the FOV of MIDI, which at the projected baselines of 30 m corresponds to $\sim$ 130 mas (i.e. $\geq$10 stellar radii). Spectrally resolved imaging observations with VISIR should be able to detect, or at least further constrain, the location of the SiC dust shell.

The MIDI observations (correlated and uncorrelated flux) of S Sct point to variability in the SiC abundance. We searched in the literature for possible variation in the mass-loss rate values, to test if a recent strong stellar wind event might have pushed away or dissolved the SiC dust. No such event was reported within the last decades. A spectrum with VISIR is needed to confirm the lack of SiC in the uncorrelated MIDI flux, and to eventually monitor the changes in abundance. The FOV of the interferometer for the S Sct observations is $\sim$ 100 mas (i.e. $\sim$10 times the $N-$band UD diameter).

6.5.2 The variability

Flux changes of up to 30% with less flux observed at the minimum visual phase are reported by Karovicova et al. (2011); Wittkowski et al. (2007); Tevousjan et al. (2004). Monnier et al. (1998) studied multi-epoch mid-infrared spectra of 30 late-type stars and found that stars with a strong silicate feature exhibit spectral shape fluctuations, where a narrowing of the feature is detected near maximum light. They report that R Leo shows unusually large spectral shape variations that may be attributed to a dynamic dust condensation zone. Although based only on 4 targets, our findings on the $N-$band spectroscopic variability largely confirms previous literature results. The flux variation of RT Vir, the star in our sample with the best temporal coverage, is comparable to the amplitude of $\sim 0.8-1$ mag found by Le Bertre (1993) for O-rich

Table 6.4: Predicted, observed diameters, and geometric characteristics.

Target	θ_{V-K} [mas]	D_{V-K} [AU]	GEM-FIND	$\theta_8/FWHM_8$ [mas]	$\theta_{10}/FWHM_{10}$ [mas]	$\theta_{12}/FWHM_{12}$ [mas]	$D_8/FWHM$ [AU]	D_8/D_{V-K}
θ Aps	24	$2.71^{+0.16}_{-0.14}$	UD	40.46±4.82	85.40±3.12	85.49±4.75	$4.58^{+0.81}_{-0.79}$	1.69
R Crt	19	$4.96^{+1.64}_{-0.99}$	UD+Gauss	20/41.95±10.63	20/169.32±34.90	20/91.03±7.36	$/10.95^{+6.39}_{-4.95}$	2.21
R Leo	25	$1.78^{+0.41}_{-0.28}$	UD+Gauss	25/41.73±0.62	25/47.68±0.88	25/55.26±0.93	$/2.97^{+0.74}_{-0.52}$	1.67
T Mic	25	$5.26^{+1.42}_{-0.92}$	UD	32.64±1.29	33.60±1.83	41.52±1.96	$6.87^{+2.13}_{-1.48}$	1.31
RT Vir	15	$2.03^{+0.26}_{-0.21}$	UD+Gauss	15/27.62±4.68	15/115.06±15.02	15/52±2.53	$/3.74^{+1.11}_{-1.02}$	1.84
π^1 Gru	28	$4.57^{+0.65}_{-0.50}$	UD+Gauss	20/121.56±38.58	20/159.71±34.07	20/167.69±32	$/19.83^{+9.10}_{-8.48}$	4.34
omi Ori	11	$2.20^{+0.36}_{-0.27}$	UD+Gauss	11/110.03±11.	11/213.69±21	11/221±22	$/21.97^{+5.82}_{-4.92}$	10.01
U Ant	10	$2.68^{+0.45}_{-0.34}$	Gauss	.../10.26±0.40	.../7.56±0.84	.../10.69±0.86	$/2.75^{+0.57}_{-0.46}$	1.03
R Lep	9	$3.72^{+2.71}_{-1.10}$	UD+Gauss	15/30.13±0.93	15/34.76±2.70	15/44.53±2.16	$/12.45^{+9.46}_{-4.08}$	3.35
Y Pav	7	$2.82^{+0.88}_{-0.54}$	Gauss	.../5.29±1.08	.../4.75±1.84	.../12.06±1.07	$/2.13^{+1.10}_{-0.85}$	$\sim$ 1
TX Psc	11	$3.03^{+0.36}_{-0.29}$	UD	12.41±0.13	9.70 ± 0.47	12.11 ± 0.56	$3.42^{+0.45}_{-0.37}$	1.13
S Sct	7	$2.70^{+0.76}_{-0.49}$	Gauss	.../11.77±1.29	.../10.53±2.19	.../12.78±2.65	$/4.54^{+1.78}_{-1.32}$	1.68
AQ Sgr	6	$2.00^{+0.58}_{-0.37}$	UD	16.58±2.7	19.55±3.54	32.92±2.82	$5.53^{+2.49}_{-1.92}$	2.76
X Tra	11	$3.96^{+0.74}_{-0.54}$	UD	21.89±2.46	22.69±3.70	38.76±3.04	$7.87^{+2.37}_{-1.96}$	1.99

Notes. The diameter of carbon stars showing SiC at 11.3 μm is usually comparable to the one measured at 8 μm or 12 μm, depending on the visibility level (see Appendix 6.7).

Mira stars.

Interferometric variability was so far observed in the carbon-rich Miras V Oph (Ohnaka et al., 2007) and R For (Paladini et al., 2012). The latter case, however, might be related to the presence of an asymmetric structure. The variability we observe in the case of R Lep is at the limit of the error bars, however it goes in the same direction of the literature findings. The visibility level suggests that R Lep is smaller close to the minimum visual phases, similarly to V Oph (Ohnaka et al., 2007), and model predictions at 10 μm showed in Fig. 7 of Paladini et al. (2009). Model predictions for O-rich Mira stars presented in Karovicova et al. (2011) show that the expected visibility changes with visual phase are wavelength dependent, and in the range of $5-20\%$. The largest difference is predicted at around 10 μm. Karovicova et al. (2011) argue that these limited variations are because the sizes of the molecular and dust layers do not change significantly with visual phase. According to the authors, the changes are within their measurement uncertainties. The star observed by Karovicova et al. (2011) is a Mira variable. As these objects are known to exhibit larger variability with visual phase, the size changes for our Semiregular stars (all except R Leo) are expected to be even smaller. In fact, the RT Vir and R Crt data suggest that interferometric variability for Semiregular O-rich stars should be less than 10%. The interferometric variability of R Leo reported here is associated to a non-zero differential phase, as in the case of R For (Paladini et al., 2012), and therefore very likely caused by (variable) asymmetries. Since low visibilities are more constraining for the size-changes, future interferometric snap-shot campaignes on temporal variability should concentrate on those projected baselines able to probe V$\leq$ 0.2.

6.5.3 The geometry

One may wonder why only two objects out of 14 show a non-zero differential phase. Both objects are O-rich M8III giants, the coolest objects of the sample. The fact that the two stars appear in a completely different part of the IRAS color-color diagram could be due to different masses, hence mass loss. What these stars have also in common are the spatial frequencies probed. In both cases the differential phase is detected while sampling visibilities below 0.2. Looking at our whole sample, these spatial scales are also probed in two observations of the carbon Mira R Lep. The differential phase is $< 10^\circ$, hence we conclude that R Lep is spherical (at least at PA = 48° and 248°). There have been only a few cases of non-zero differential phase in the literature detected with MIDI: R For (Paladini et al., 2012), BM Gem (Ohnaka et al., 2008a), IRAS+18006-3213 (Deroo et al., 2007), and L_2 Pup (Kervella et al., 2014). All these observations had also in common the fact of probing visibilities < 0.2. Thereupon we can assume that the lack of detection of non-zero differential phase does not necessarily exclude the existence of asymmetries in the brightness distribution in the other targets of our sample. Very likely asymmetric structures show up in the differential phase when probing high spatial frequencies, similarly to what is reported in the near-IR (Ragland et al., 2006; Cruzalèbes et al., 2013a).

If we include the objects with differential phase $\sim 57\%$ of the stars with O-rich chemistry (O-type plus S-type stars) are asymmetric. These results suggest that asymmetries in the dusty

environment are more common among the oxygen-rich objects. Near-infrared investigations of AGBs (Ragland et al., 2006; Cruzalèbes et al., 2015), on the other hand, indicate that asymmetries are more common among the carbon stars. This result can be explained with the large-grains scenario for O-rich stars (Höfner, 2008). Oxygen-rich dust grains are nearly transparent in the near-infrared, therefore not many brightness-asymmetries are expected at those wavelengths. The dusty region of O-rich stars probed in the mid-IR should be more "blobby" than for C-rich stars because there are stronger non-linear effects in radiative acceleration. This is valid *if* the scattering on transparent grains scenario is correct, in fact scattering depends much more steeply on grain size (S. Höfner, private communications). It is interesting also to note that bipolar objects on the post-AGB are mainly O-rich (Lagadec et al., 2011). The latter well agrees with our results on the AGB.

The result obtained by fitting only the LP data, plus the results of the differential phase study, indicate that asymmetries in the dust-forming region are concentrate in the lower part of the IRAS color-color diagram. No object located in region VII showed so far asymmetries. More observations covering long baselines (high spatial frequencies), or (ideally) N-band images obtained with the next generation VLTI/MATISSE instrument (Lopez et al., 2006) are needed to confirm this finding.

6.5.4 Comparison with the MESS results

The aim of our program is to observe the evolution of asymmetric structures through the atmosphere of a representative sample of AGBs. For this purpose we selected stars imaged with the Herschel/PACS instrument and we complemented these observations of the large-scales of the atmospheres with interferometric VLTI/MIDI observations of the inner spatial scales. Panel d) of Fig. 6.7 shows the stars of our sample in the IRAS color-color diagram. The objects are color coded to highlight their MESS classification. The symbols are the same as in panel b) and indicate the presence of non spherically-symmetric environment. Three objects out of the LP sample are classified by Cox et al. (2012) as Rings, 6 are Fermata type, 2 Irregulars, 1 Eye, and 2 unresolved.

All the stars from the Ring class are fitted with the one-component geometric model, no asymmetry is detected in the dust-forming region. For two of them (S Sct and U Ant) no SiC dust component is spatially resolved. The dust observed in their spectra might have been pushed away by episodic wind, or it forms further than ten stellar radii. As already mentioned in the previous section, for X TrA we have only a few data points and we cannot exclude that by adding more visibilities the picture will become more complex.

The carbon-rich stars TX Psc and AQ Sgr, plus most of the Herschel images of our oxygen-rich sample, are of Fermata-type, i.e. show an interaction with the ISM. R Crt is classified as an Eye-morphology by Cox et al. (2012). However, the fact that R Crt is the only oxygen-rich AGB star in the MESS sample being of Eye-shape and the fact that the Eye-shape is not very pronounced may indicate that also R Crt could also be of Fermata-type (Cox et al., 2012). If we consider R Crt among the possible Fermata, 3 out of 7 of the stars in this class show a direct

detection of an asymmetry (via differential phase) or at least a hint of non spherically-symmetric environment (detected by fitting only the LP data). This fact translate in saying that 42% of the stars classified as fermata have an asymmetric dust-forming region, and they all have O-rich chemistry.

The Irregular class contains objects with diffuse irregular extended emission. Both the stars classified as Irregular are S-type stars, and they can be fitted with two-components model, and show non central-symmetric CSE in the LP data.

6.6 Conclusions and outlook

In this paper, we present mid-IR interferometric and spectroscopic data observed with VLTI/MIDI for a sample of 14 AGB stars. The sample is based on the list of objects observed within the frame of the MESS program with Herschel PACS (Groenewegen et al., 2011). The aim of our study is to investigate the morphology of the dusty environment of these objects at different spatial scales and to answer the questions: i) are the asymmetries of the outer CSE intrinsic to the mass loss process, are they only due to interaction with the ISM? ii) At which height, the mass-loss process becomes manifestly non-spherical? iii) How the geometry of the atmosphere changes at the different evolutionary stages (M-S-C stars, and from almost dust-free to very dusty objects) within the AGB sequence?

The first question cannot be addressed using only the mid-infrared interferometric data here presented. These data in fact scan the stellar atmosphere between 1-2 and 10 stellar radii, and the intermediate spatial scales probed by VISIR are needed to have a connection with the Herschel/PACS images. Nevertheless, we report that all the objects in our sample classified as "symmetric" Rings by Cox et al. (2012) have so far a symmetric dust forming region. All the objects classified as Irregular need a composite model (i.e. they have an extended environment), and the fit of the LP data indicates some asymmetric behaviour. Approximately 42% of the objects classified as Fermata (i.e. show interaction with the ISM) have also an asymmetric dust-forming region.

To answer the second question, it is obvious that asymmetries in the brightness distribution appears already in the dust forming region of AGB stars. We directly detected asymmetries via differential phase measurement in two cases: RT Vir (already reported by Sacuto et al., 2013), and R Leo. However, the fact that the other objects are found symmetric does not preclude the presence of clumps, small or very faint asymmetric structures. GEM-FIND fitting of the LP data shows that beside these two stars, three more show a hint of non central-symmetric morphology. Concerning the third question, all the stars with asymmetric behaviour have O-rich chemistry. Therefore asymmetric structures in the mid-infrared are more common among O-rich and S-type stars. On the contrary literature suggest that C-rich stars are more asymmetric in the near-IR. We speculate that this result supports the large grains scenario for O-rich stars.

Another major finding of our program is that silicon carbide dust is not detected within 10 stellar radii of the detached shell objects S Sct and U Ant. U Ant shows SiC in the spectrum,

therefore this material is simply outside the FOV of the interferometer. The case of S Sct might be related to variability in the stratification of this material.

Finally, by analysing archive data, we studied the spectroscopic and interferometric variability. Spectroscopic variability is reported in a few cases, and the flux variations are in agreement with what was already observed in the literature (Le Bertre, 1993). Exception made for the carbon-rich Mira R Lep, case which nevertheless needs a confirmation through monitoring campaigns, interferometric variability (i.e. change in the shell-size) is observed in the O-rich Mira R Leo. In the latter case the variability is associated to an asymmetry in the brightness profile of the star. The lack of detection for the other stars suggest that interferometric variability in non-Mira stars is less that $\sim 10\%$ of the visibility.

The next step of this study will be, as already mentioned, to bridge the gap between MIDI and Herschel with additional single-dish images in the mid-infrared. These observations will be crucial for completing the picture of the morphology of the dusty environment. Finally, MIDI was recently decommissioned, but a second generation instrument VLTI/MATISSE will be available at VLTI in 2018. This interferometer will combine the light from 4 telescopes, and it will observe in the L, M, and $N-$band. While MIDI with only two telescopes gave us a rough idea of how stars look like, MATISSE will provide images allowing not only to detect the asymmetric structures, but also to unveil their nature (disk-like or clumps). Because of the complex nature of the targets here studied, a complete coverage of the visibility curve is mandatory. This will require in certain cases baselines longer than the 150 m (for stars like omi Ori and TX Psc), but also very short baselines. In this frame, an aperture masking experiment on the VISIR instrument matching the spectral resolution of MATISSE is required.

6.7 MIDI results on individual stars

6.7.1 θ Aps

θ Aps is a Semiregular variable star located at a distance of 113 pc (van Leeuwen, 2007). In its ISO spectrum the star shows silicate emission that is typical for an oxygen-rich AGB star (e.g. Fabian et al., 2001) with features at 10, 13, 19.5 and 32 μm. The mass-loss rate of the star was determined to be $0.4 \times 10^{-7}\,\mathrm{M}_{\odot}\,\mathrm{yr}^{-1}$ by Olofsson et al. (2002b). The Herschel image is of 'Fermata'-type with indications for a companion (Cox et al., 2012). Mayer et al. (2013) find indications for a jet that is interfering with the wind-ISM bow shock.

θ Aps was observed in 2011 and 2012. Six out of 7 data sets are of good quality. There are no archive data.

Variability

The variability period for θ Aps is given as P=119 d (Samus et al., 2009a). We calculated visual phases of the observations adopting phase-zero point $T_0 = 2\,454\,622$ JD.

The MIDI spectra have similar visual phases. Thus, a check for intra-cycle variability is not possible. However, a check for cycle-to-cycle spectroscopic variations can be performed by comparing the MIDI with ISO and IRAS data (Fig. 6.6). The flux level of the ISO and MIDI spectra is the same at least in the range $\sim$ 9.8 – 12.5 μm, i.e. no spectroscopic cycle-to-cycle variations are found. However, below $\sim$ 9.8 μm, a clear change in flux level is observed.

To check for interferometric variability, a set with similar baseline lengths and position angles observed at different visual phases is shown in Fig. 6.8. No interferometric variability is detected.

Morphology

Calibrated visibilities are shown in Fig. 6.9. No differential phase signature is detected, i.e. no asymmetries are observed in the brightness distribution.

The $\chi^2_{\rm red}$ of the GEM-FIND fitting for the different models are given in Table 6.3. The increase of the UD-diameter from 8 – 10 μm is particularly strong for θ Aps, indicating that the star shows a strong silicate feature. This is in agreement with the ISO spectrum. The difference between the K-band (18.1 mas, Dumm and Schild, 1998) and N-band diameter ($\sim$40–90 mas), is evidence for dusty material in the circumstellar surrounding of the star. As θ Aps has a low mass-loss rate, the circumstellar environment can be assumed to be optically thin, therefore one cannot exclude that observations at larger baselines would point to a two-component structure of the CSE of θ Aps, as it is the case for RT Vir and R Crt.

6.7.2 R Crt

R Crt is a Semiregular variable star. Its distance is given as 261 pc (van Leeuwen, 2007). The star was part of many maser and CO-line studies. The CO-envelope seems to be consistent with a uniformly expanding envelope (Kahane and Jura, 1994). The Herschel image was interpreted to be of 'eye'-shape (Cox et al., 2012). This shape, however, is not well constrained (A. Mayer, private communication). The strength of the silicate feature is quite large (Begemann et al., 1997). R Crt also has a higher mass-loss rate ($8 \times 10^{-7}\,{\rm M}_\odot\,{\rm yr}^{-1}$) than the other O-rich sources.

R Crt was observed in 2009, 2011 and 2012, and out of 12 data sets 8 are of good quality.

Variability

The variability period of R Crt is given as $P = 160$ d (Samus et al., 2009a). We calculated the visual phase of our observations assuming a phase-zero point $T_0 = 2\,454\,225$ JD. The observations were carried out at different visual phases within different cycles. This makes a check for cycle-to-cycle and intra-cycle variability necessary.

Possible variability effects can be checked in Fig. 6.10 which gives the visual phase versus flux at 8, 10 and 12 μm. Fluxes agree within the errors for 8 and 10 μm. At 12 μm there seems to be a variation in the flux level when comparing MIDI and IRAS.

No sets with similar baseline lengths and position angles observed at different epochs are available. Therefore, no statement can be made on the interferometric variability.

Morphology

Calibrated visibilities are shown in Fig. 6.11; the differential phase is always zero.

As for θ Aps, the strong silicate feature can be seen in the visibility profile at $\sim 9.8\,\mu$m for short baselines. On the other hand, for R Crt we also have at our disposal long baseline observations. The shape of the visibility for the longer baselines may still show some silicate feature, but much less pronounced than for the short ones. Contributions from other molecular and dust species may shape the visibility profile (e.g. SiO, H_2O, Al_2O_3).

The LP observations of R Crt are best described by an elliptical Gaussian profile with an axis ratio of 0.7 and an inclination angle of $\phi_{\rm incl} = 157°$.

As can be seen in the second row of Table 6.3, all one-component models fail to fit the observations of the LP combined with the archive data. The best-fitting model is a two-component model (CircUD+CircGauss, Fig. 6.11). This suggests that the environment of R Crt is optically thin, with the outer environment being dominated by silicate-rich dust.

6.7.3 R Leo

R Leo is a well-studied O-rich AGB star of Mira type. Its distance is 110 pc (van Leeuwen, 2007). Its magnitude in the V-band ranges from 11.3 to 4.4 (Kholopov et al., 1998). Knapp et al. (1998) determined a mass-loss rate of $9.4 \times 10^{-8} M_\odot$ yr^{-1}. The Herschel image suggests that R Leo is of 'Fermata' type (Cox et al., 2012).

Asymmetries. Evidences for asymmetries were found by Ireland et al. (2004b) and Burns et al. (1998) from the closure phases obtained with optical interferometry (650 – 1000 nm). Non-zero closure phases are also reported in the mid-infrared by Tatebe et al. (2008). They suggest that the closure phase signal of the star comes from an asymmetry that is located in the southern hemisphere of the star. Wiesemeyer et al. (2009) claim that they detect a planet at a separation of 24 mas in their SiO maser data. They do not mention whether such a planet could be responsible for the closure phase signals observed in the other wavelength ranges. Perrin et al. (1999) used near-infrared interferometry and show that their observations at low spatial frequency ($< 40\,\mathrm{arcsec}^{-1}$) are well represented by a UD-model. On the other hand, data at high spatial frequencies ($40 - 80\,\mathrm{arcsec}^{-1}$) cannot be explained by a UD or Gaussian intensity distribution, which may point to the presence of one or more extra structures. This is confirmed by the observations of Mennesson et al. (2002). Perrin et al. (1999) mention that the low spatial frequency observations within the first null cannot resolve small structures like spots and this may be the reason why a UD-model fits those data well. Monnier et al. (2004), however, report that both the low and high frequency data ($1 - 50\,\mathrm{arcsec}^{-1}$) in the near-infrared can be perfectly fitted with a UD model. This may depend on the visual phase and is further discussed below under heading "Visual phase-dependent diameter". The CO line-profile of R Leo shows an asym-

metric shape with the red side being stronger (Knapp et al., 1998; Teyssier et al., 2006).
Ellipticity. Reports of an elliptical shape of the CSE of R Leo are reported in the optical (Lattanzi et al., 1997) and in the mid-infrared (Tatebe et al., 2008). On the other hand, several other studies do not find any signs of ellipticity (e.g. Burns et al., 1998; Monnier et al., 2004).
Wavelength-dependent diameter. A dependence of the diameter on wavelength is reported in the optical by Hofmann et al. (2001), where the size is twice as large in the TiO band-head as in the continuum. A size increase from the K-band to the L-band of 20 – 30% was reported by Mennesson et al. (2002) and Schuller et al. (2004). The multi-wavelength study of Woodruff et al. (2009) in the near-infrared showed that there is a clear anti-correlation between the angular diameter and the features seen in the spectrum.
Visual phase-dependent diameter. Chagnon et al. (2002) interferometrically observed the star in the near-IR at two different visual phases and find that one set can be modeled with a UD, the other not. This is confirmed by Fedele et al. (2005) who find that their pre-maximum data can be explained by a UD, the post-maximum data however cannot. Such a variability in the size of R Leo is detected by several authors in the near-IR (Perrin et al., 1999; Chagnon et al., 2002; Mennesson et al., 2002; Fedele et al., 2005; Woodruff et al., 2008, 2009), with the star being largest at visual minimum as already predicted by pulsation models, although none of such models can reproduce the pulsation amplitude of R Leo (Ireland et al., 2004a). Such variability was also detected in the optical (Burns et al., 1998) and mid-infrared (Tatebe et al., 2006, 2008). Mennesson et al. (2002) mention that such changes may be caused by variations in the spatial extent and/or in the opacity of the outer atmospheric layers.

R Leo was observed in 2006, 2007, and 2012. Out of 26 data sets, 17 are of good quality.

Variability

The variability period of R Leo is $P = 310$ d (Whitelock and Feast, 2000) and we adopted phase-zero point $T_0 = 2\,453\,540$ JD to calculate the corresponding visual phase. The observations were carried out at different visual phases within different cycles. This makes a check for cycle-to-cycle and intra-cycle variability possible.

The variation of the flux with visual phase was detected in the mid-infrared by Monnier et al. (1999) and Tatebe et al. (2006), with the flux being 30% lower at visual minimum. We confirm the trend of lower fluxes towards the minimum in Fig. 6.12, which shows visual phase versus flux at 8, 10 and 12 μm.

The interferometric observations with similar baselines and position angle shown in green in the left panel of Fig 6.13 are taken at very similar visual phase, therefore it does not come as a surprise that no intra-cycle variability is detected. A third observation (black line in the left panel of Fig. 6.13) is taken six cycles apart. Even in this case no cycle-to-cycle interferometric variability is observed. Changes in the visibility with visual phase are shown in the right panel, Fig 6.13. The black line here is the result of the average of two observations taken at the same baseline and position angle, and one day apart. The variability in the visibility is accompanied with a

non-zero differential phase. Such kind of variation were found in the mid-infrared by Tatebe et al. (2006) and Tatebe et al. (2008). This may be an indication that for R Leo observations at different visual phase should not be combined.

Morphology

Calibrated visibilities are shown in Fig. 6.14.

The $\chi^2_{\rm red}$ of the GEM-FIND fitting for the LP data is given in the first row of Table 6.3. The morphology of R Leo seems to be quite complex. When performing a GEM-FIND fit on the whole LP data sets, the best model is a UD with a diameter ranging from 63 to 95 mas (as a function of wavelengths). However, combining the LP and the archive data, none of the GEM-FIND models was able to provide a good fit (confirmed by the high value of $\chi^2_{\rm red}$ for the best fitting model). One explanation could be that the environment of R Leo is made of more than two components, i.e. multiple shells are observed with MIDI. Another possible explanation could be variability in the N-band that was already reported by Tatebe et al. (2006, 2008) and confirmed in this work. Therefore, considering that there may be intra-cycle variability, we combined all data at similar visual phases to do the fitting. Also in this case the UD model does not provide a good fit to the data. As all the observations in the archive were observed at approximately the same position angle, they do not provide supplementary constraints to fit more complex asymmetric models.

There is a differential phase signature present for observations with baselines ∼40 and ∼60 m (Fig. 6.4).

6.7.4 T Mic

T Mic is a Semiregular variable star located at a distance of 200 pc (Loup et al., 1993). This star was part of different photometric, spectroscopic and CO-line-profile studies. Its mass-loss rate is estimated to be $8 \times 10^{-8}\,{\rm M}_\odot\,{\rm yr}^{-1}$ (Olofsson et al., 2002b). The Herschel image is interpreted as of 'Fermata'-type (Cox et al., 2012), i.e. shows signs of interaction with the ISM. T Mic was observed in 2004, 2010 and 2011. Out of 10 data sets, 7 are of good quality.

Variability

We derived visual phases for the observations, however the values need to be considered with caution. In fact light curves available from AAVSO, ASAS, DIRBE and HIPPARCOS, do not cover the epoch of the ISO or MIDI data. The adopted origin for the visual phase determination is $T_0 = 2\,452\,832$ JD. The observations were carried out at different visual phases within different cycles. The two spectra obtained on 2004 July 30 and 31 were averaged. The flux level of the ISO and MIDI spectra in Fig. 6.6 is not the same, i.e. the level of N-band emission may have changed. No data set with similar baseline lengths and position angles observed at different epochs is available. Therefore, no statement can be made on the interferometric variability.

Morphology

Calibrated visibilities are shown in Fig. 6.15.

T Mic does not show a strong silicate feature. However, the slight drop that is observed in the visibility of baselines shorter than 16 m at $\sim 9.8\,\mu$m can be attributed to silicate dust. No differential phase signature is detected in T Mic, i.e. no asymmetries are detected with MIDI.

The fitting of the LP data of 2011 with GEM-FIND reveals that T Mic can be well described with a circular UD model. The $\chi^2_{\rm red}$ of the GEM-FIND fitting for the different models is given in the first row in Table 6.3.

If the LP data are combined with the archive data, the best-fitting model is a circular Gaussian model. The fit has problems, however, to describe the short-baseline and the 46 m baseline data. This could mean that the close environment of T Mic is more complex and cannot be described with a one-component or two-component geometric models. The other possibility is that the short-baseline data (observed in 2011) cannot be combined with the longer-baseline data (2004 and 2010) because of a variability effect.

6.7.5 RT Vir

RT Vir is a Semiregular variable star that is located at a distance $d = 136\,$pc (van Leeuwen, 2007). RT Vir is a well-studied and one of the brightest water maser sources (Richards et al., 2011). Several mass-loss estimates are given, lying between $1.1 \times 10^{-7}\,M_\odot\,{\rm yr}^{-1}$ (Knapp et al., 1998) and $5 \times 10^{-7}\,M_\odot\,{\rm yr}^{-1}$ (Olofsson et al., 2002b). Sacuto et al. (2013) recently reported an asymmetry revealed through the MIDI differential phase at 9 stellar radii (12 AU), and also spectroscopic cycle-to-cycle variability. The Herschel image is interpreted as being of 'Fermata' type (Cox et al., 2012).

RT Vir was observed in 2008, 2009, 2011 and 2012. For our program, we obtained 6 data sets, but only 2 turned out to be of good quality. The archive data, on the other hand, are of good quality. Twelve out of 13 data sets can be used.

Variability

The visual phase of the MIDI observations is derived using the light curve from ASAS (Pojmanski, 2002). The variability period for RT Vir is given as P=375 d (Imai et al., 1997) and the phase-zero point is $T_0 = 2\,454\,854$ JD (adopted from Sacuto et al., 2013). The observations were carried out at different visual phases within different cycles.

The flux level of the ISO and MIDI spectra is not the same, i.e. the level of N-band emission has changed. From Fig. 6.16, one can see that the flux is lowest at visual minimum. At glance, it also seems that the flux follows a sinusoid with maximum flux shifted from the visual maximum. This kind of behaviour was already predicted by model atmosphere simulations (Ireland et al., 2004a, for near infrared wavelengths), and observed by Zhao-Geisler et al. (2012). Since

these observations are carried at different cycles, the effect of cycle-to-cycle variation cannot be completely ruled out (Sacuto et al., 2013).

To check for interferometric variability, data sets with similar baseline lengths and position angles observed at different visual phases are shown in Fig. 6.17. Although photometric variability is present, we do not report any interferometric variability, confirming the results of Sacuto et al. (2013). It would be interesting to monitor the atmosphere with long baselines in order to check whether interferometric variability can be detected at high spatial frequencies, where the object presents also an asymmetry (see following section). As no interferometric variability is so far observed, all data-sets can be combined in the further analysis.

Morphology

Calibrated visibilities are shown in Fig. 6.18. The drop that is observed in the visibility can be attributed to amorphous silicate. For RT Vir, a non-zero differential phase is detected for the longest baselines (89 and 128 m) by Sacuto et al. (2013). This is the signature of an asymmetry. Sacuto et al. (2013) used GEM-FIND to fit different geometric models to a subset of the data. Not only one-component but also two- and three-component models are used in their work. The best-fitting model is a three-component model: a UD that describes the central star, a spherical Gaussian that represents the optically-thin dust environment and a Dirac function that represents the unresolved asymmetry (which could be a companion or a dust clump). This model is also able to reproduce the observed differential phase.

Although Sacuto et al. (2013) find the environment of RT Vir to be asymmetric, we start by fitting spherically-symmetric models to the LP data that do not show any asymmetry. The LP data can be fitted best with a circular Gaussian profile with a FWHM of $\sim$60 mas at 10 μm (see first row in Table 6.3). As only two observations with the same position angle are available, no attempt to fit elliptical models was made. If we combine the LP data with the archive data, a one-component model is no longer able to describe the observations (see second row in Table 6.3). Therefore, we fit a spherical model, composed of a circular UD and a circular Gaussian, to the data. The best-fitting diameter of the circular UD is 16 mas. The diameter derived by Richichi et al. (2005) in the K-band is θ_K=12.4 mas. Our model does not fit well enough the short-baseline data. The model of Sacuto et al. (2013), on the other hand, fits all the visibility and differential phase observations (as the model is asymmetric). The diameter of their UD is wavelength-dependent and larger than the K-band diameter determined by Richichi et al. (2005), which suggests that the environment is composed of more than one silicate-rich layer (Sacuto et al., 2013).

6.7.6 π^1 Gru

π^1 Gru is a well-studied S-type star close to the tip of the AGB (Jorissen et al., 1993; Van Eck et al., 2000). The star is known to have a G0V companion located $\approx$ 2.7" ($\approx$ 450 AU) away from the primary, and possibly a third component much closer as suggested by Makarov

and Kaplan (2005); Frankowski et al. (2007) and more recently, Mayer et al. (2014). CO line observations (Sahai, 1992; Knapp et al., 1999; Chiu et al., 2006) reveal an asymmetric, double-peaked structure and extended emission wings which are interpreted as an expanding disk and a fast bipolar outflow oriented perpendicular to the disk. The Herschel/PACS image shows an elliptical emission and a hook east of the star at a distance of 38" (Fig. 5, Mayer et al., 2014). This kind of hooks or arcs is most probably part of an Archimedean spiral formed by the interaction with a companion (like for *o* Cet, Mayer et al., 2011). Therefore the presence of the companion(s) affects the geometry of the atmosphere at different spatial scales. The star was observed with MIDI in 2008 and 2011. We have a total of 11 data sets to fit, 4 from the LP.

Variability

π^1 Gru is a SRb variable with period 198 d. However, as already stated in Sect. 2.2 of Sacuto et al. (2008), because of the Semiregular nature of the object, it is very difficult to assign a visual phase to a given observation. Sacuto et al. (2008) give two explanations for the discrepancy between the level of the ISO and the 2006 MIDI spectra: (i) MIDI is missing some of the flux that is seen by the larger ISO beam; (ii) a difference in the emission due to pulsation. The difference we observe between the 2011 LP data, ISO and the 2006 could be a cycle-to-cycle variability.

Morphology

Concerning the shape of the visibility vs. wavelength, we observe the typical shape of silicate dust with a bump between 8 and 9 μm. A drop is also observed in the visibilities at wavelengths longer than 12 μm. The lower left panel of Fig. 6.19 shows a slightly different shape in the visibility with respect to the other panels. This may be a residual of a non perfect calibration (Sacuto et al., 2008). A fit including only the LP data points to an elliptical UD morphology with axis ratio 0.2 and inclination 140°. The visibilities observed for π^1 Gru can be well fitted with a composite model UD+Gaussian, as shown in Fig. 6.19. The best-fitting model has a UD diameter of 20 mas, a flux ratio ranging between 1.97 ± 0.22 and 1.01 ± 0.09 with the UD being always brighter than the Gaussian envelope, but it becomes fainter at longer wavelengths. The Gaussian envelope is larger at longer wavelengths and varies between 120 ± 38 and 167 ± 25 mas, values in agreement with those found by Sacuto et al. (2008).

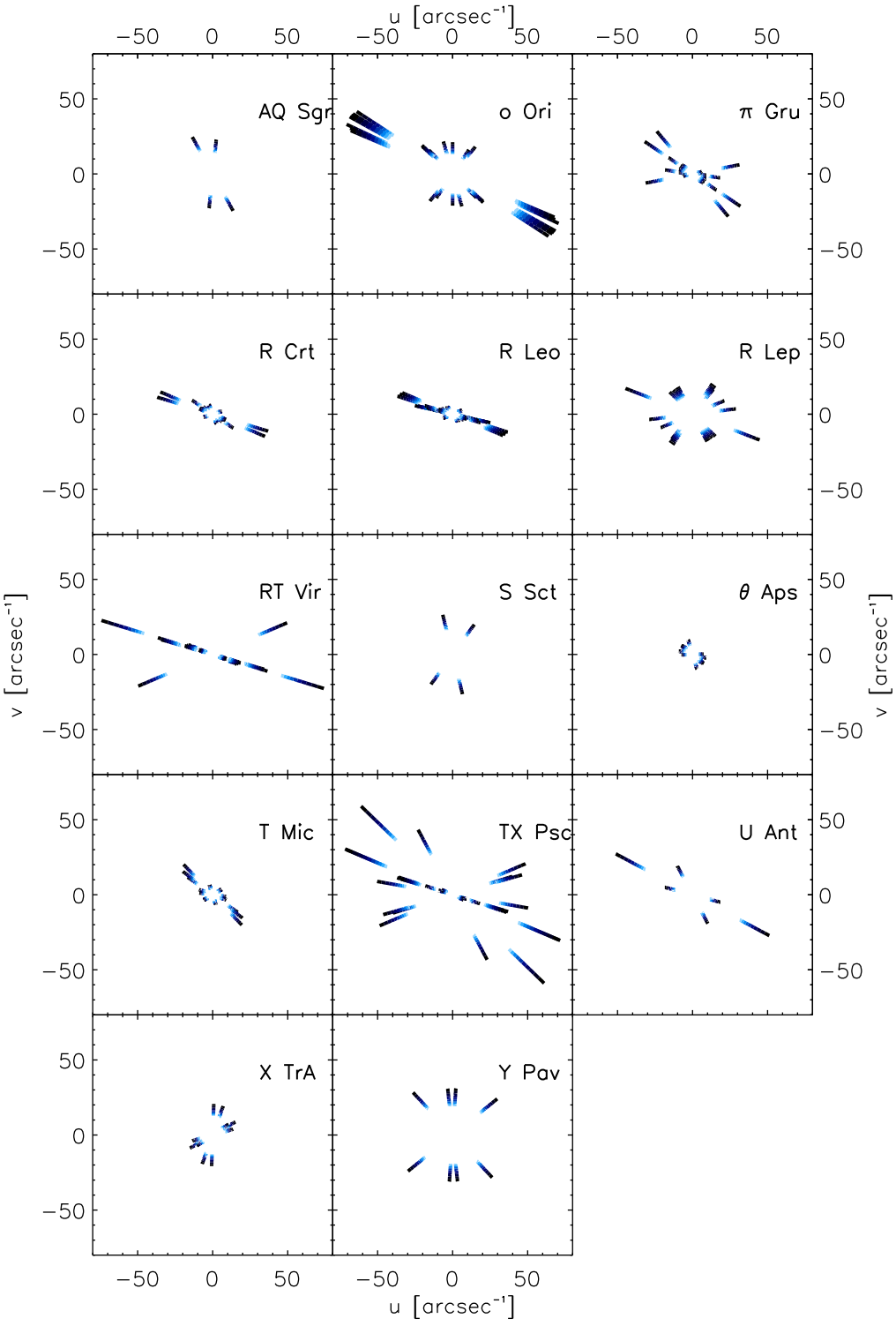

Figure 6.2: (u, v)-coverages obtained for all the targets. The different wavelengths from 8 – 13 μm are colour-coded (dark to light, respectively).

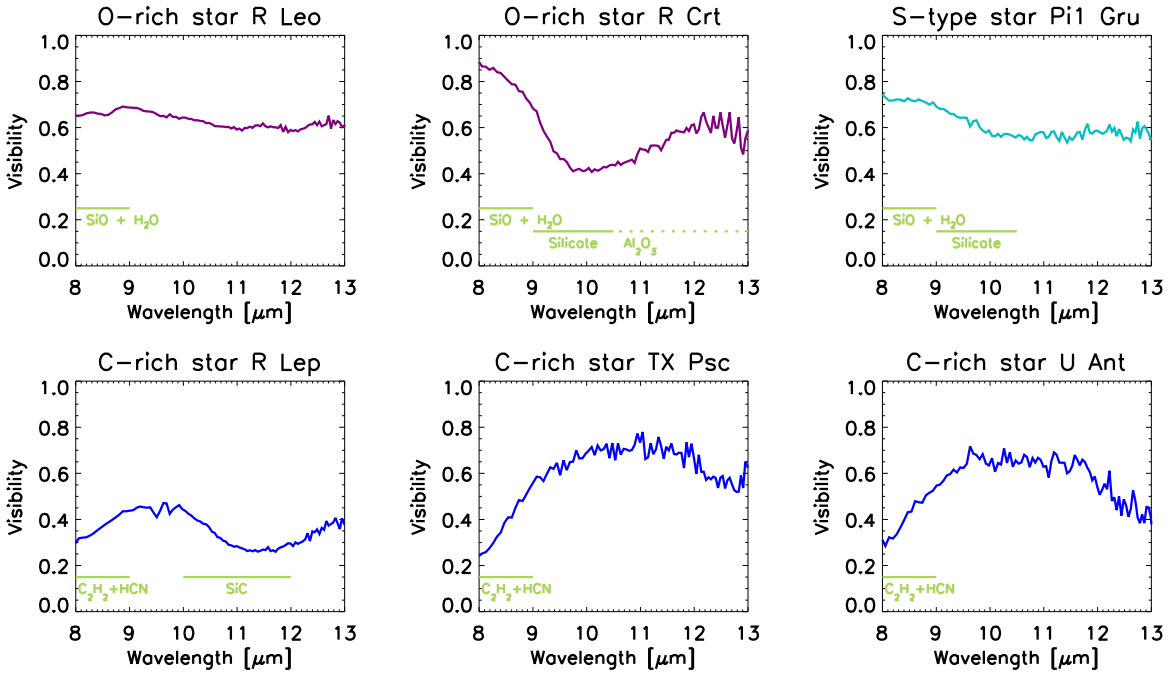

Figure 6.3: Some examples of visibility spectra for given baselines. The complete sample can be found in Appendix 6.7. Molecular and dust features are highlighted for stars with different chemistry: R Leo and R Crt are M-type stars, π^1 Gru is an S-type object, while R Lep and TX Psc are C-type stars. The lower right panel shows an example of the visibility spectra of the carbon star U Ant (cf. Sect. 6.4.1). The typical error bars are of the order of 10%.

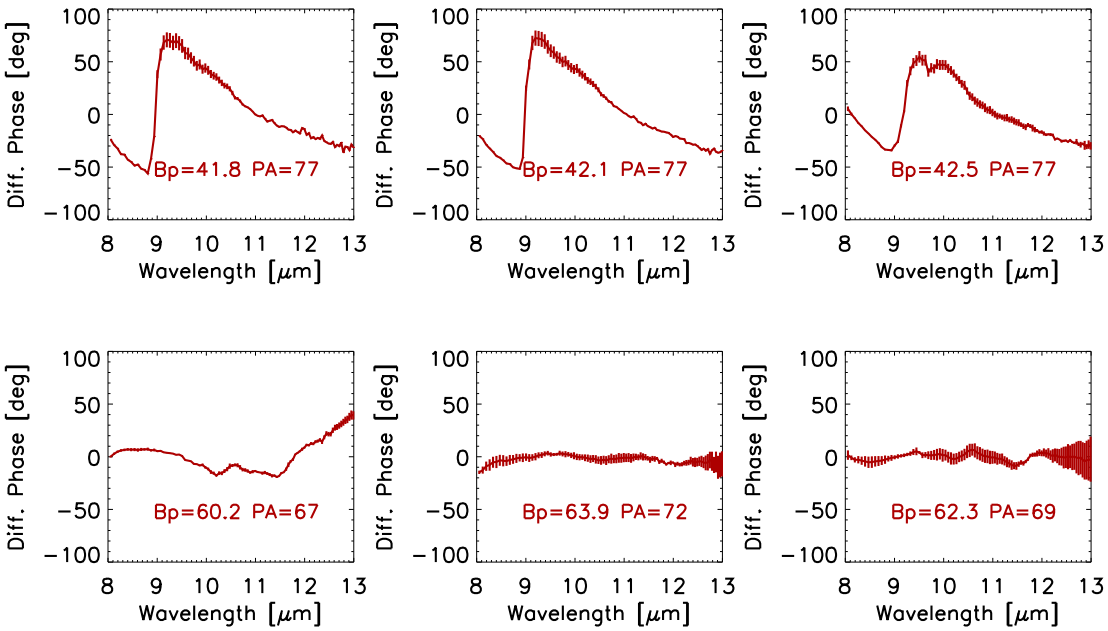

Figure 6.4: The non-zero differential phases measured by MIDI for R Leo ordered in increasing projected baseline (B_p).

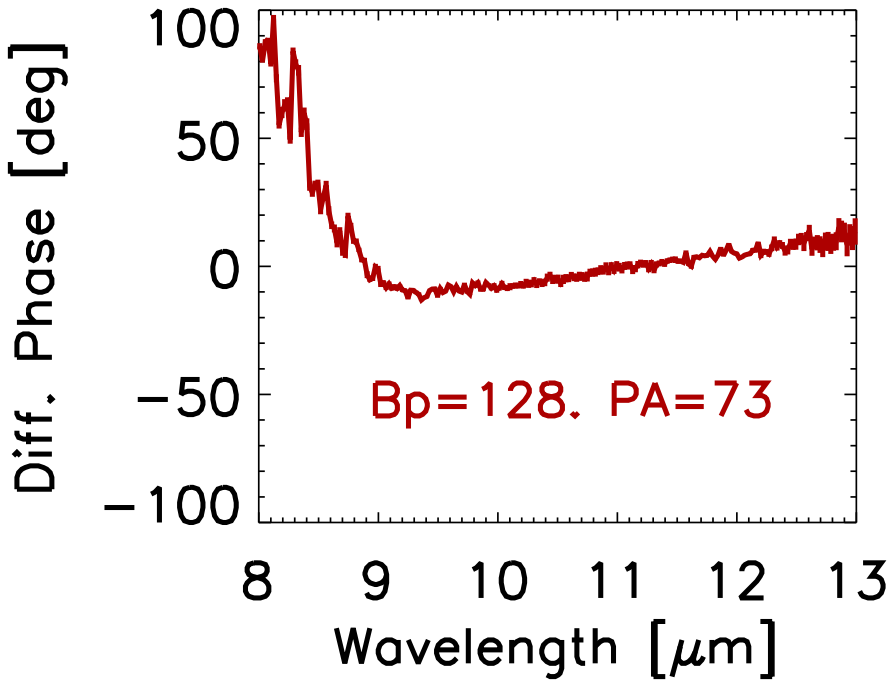

Figure 6.5: Same as Fig. 6.4 for RT Vir.

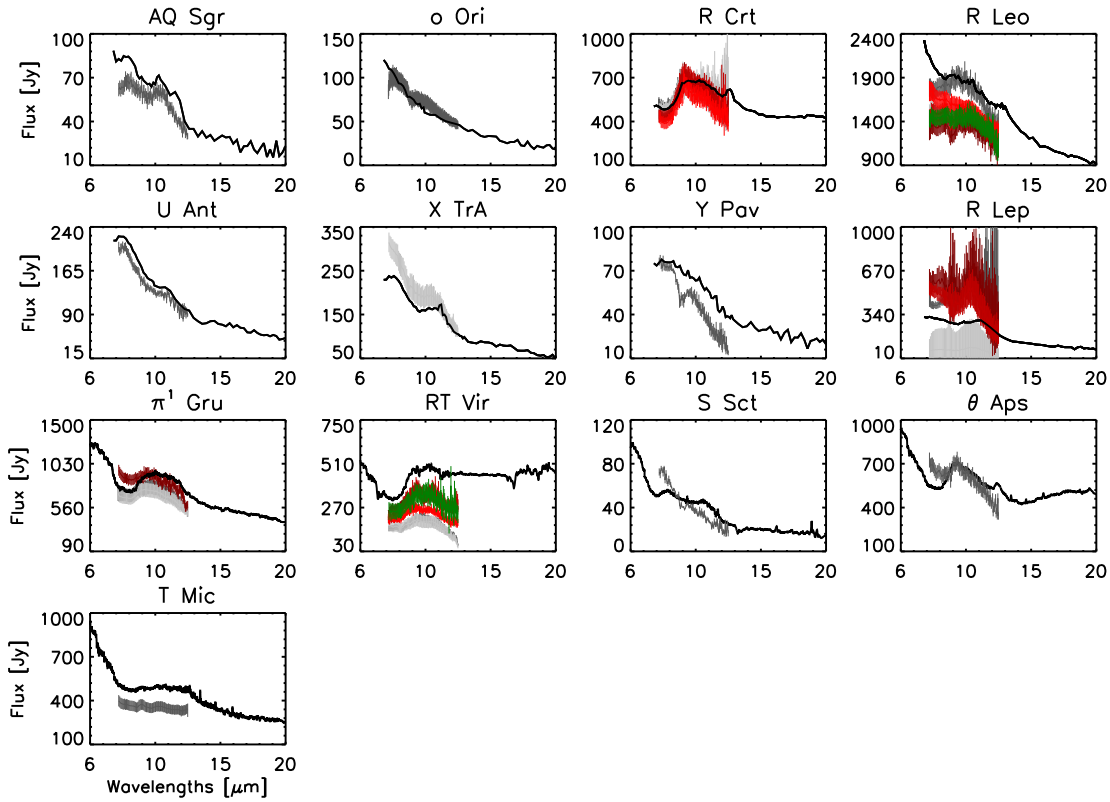

Figure 6.6: IRAS or ISO spectra (black lines) compared with the MIDI spectroscopic observations (shaded areas).

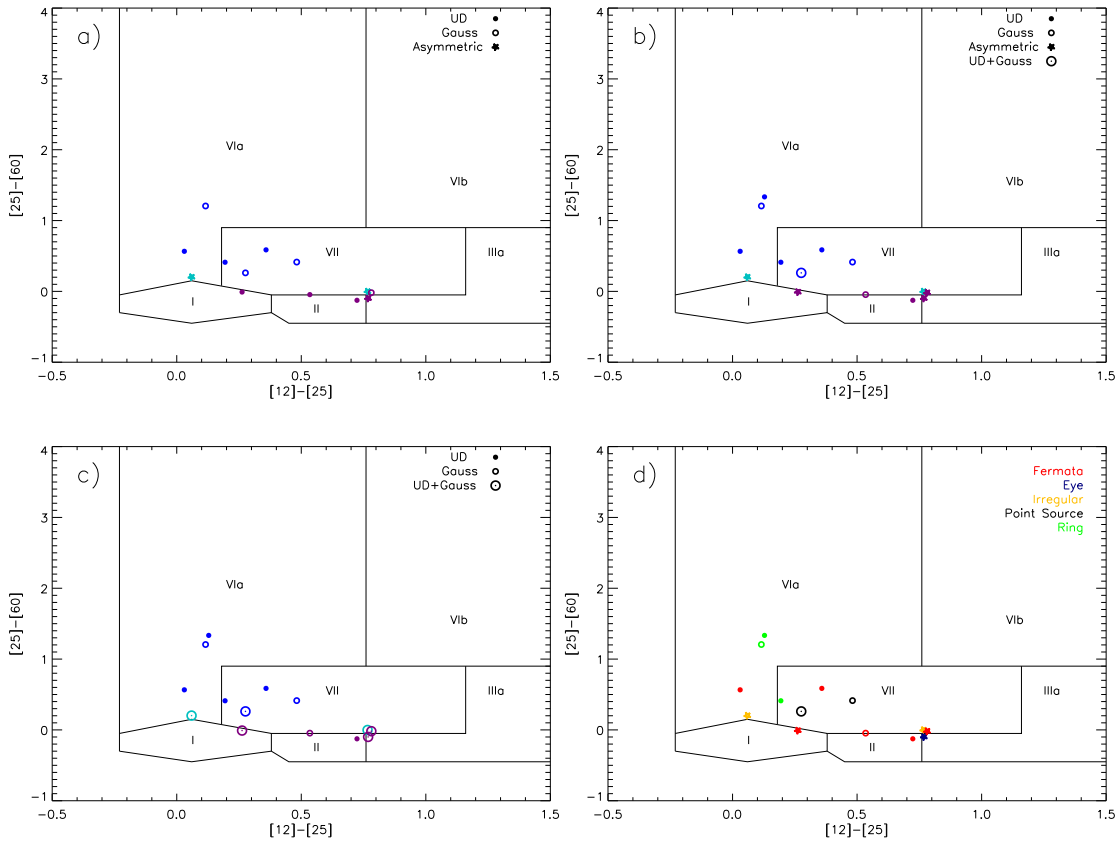

Figure 6.7: *Panel (a):* our sample of stars in the IRAS color-color diagram. The symbols show the results of the GEM-FIND fit using only LP data. The color code is the same as in Fig. 6.1. *Panel (b):* same as Panel (a), the symbols refer to the fit of LP+archive data. Asymmetric solution from previous fit and from non-zero differential phase are marked. *Panel (c):* same as Panel (a), no asymmetric solutions shown. This panel highlights the presence of multiple components (shells). *Panel (d):* same as Panel (b) color coded to highlight the Herschel/PACS morphology observed in Cox et al. (2012).

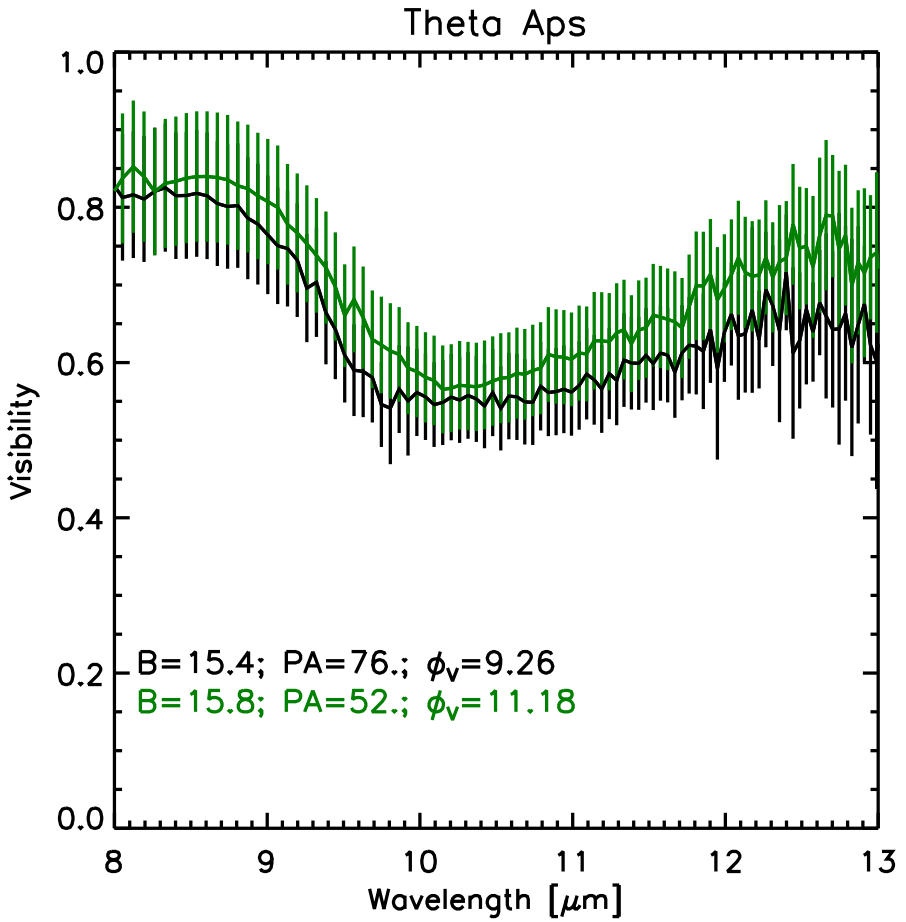

Figure 6.8: Interferometric variability check for θ Aps. B is the projected baseline, PA the position angle, and ϕ_V is the visual phase.

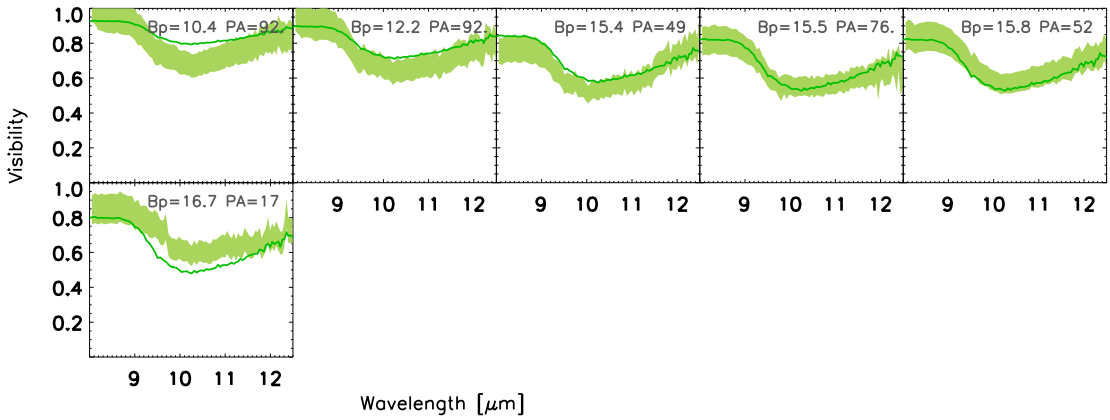

Figure 6.9: Best-fitting GEM-FIND model (solid line) for the MIDI visibilities of θ Aps.

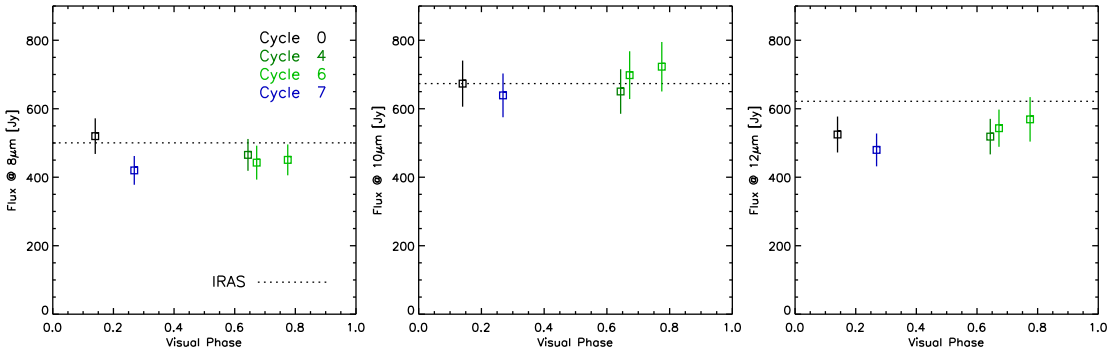

Figure 6.10: The MIDI fluxes at 8, 10, and 12 μm observed for R Crt at various visual phases, are compared with the IRAS flux.

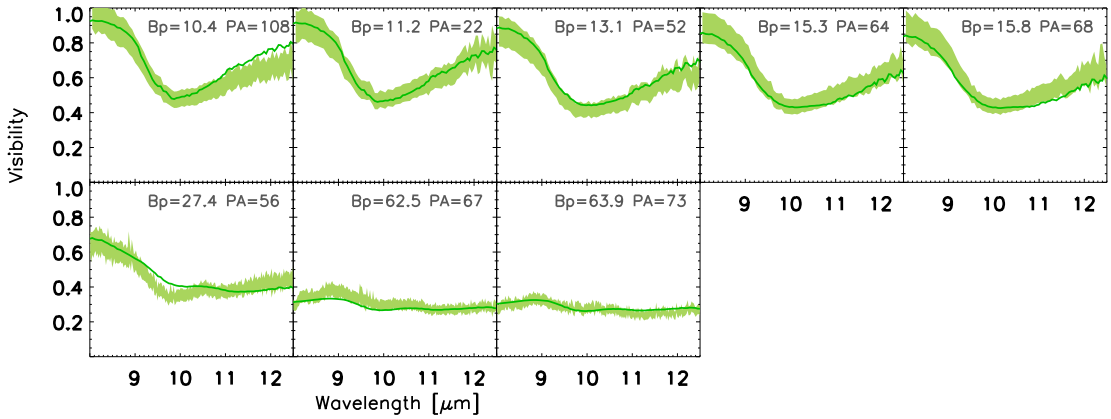

Figure 6.11: Best-fitting GEM-FIND model (solid line) for the MIDI visibilities of R Crt.

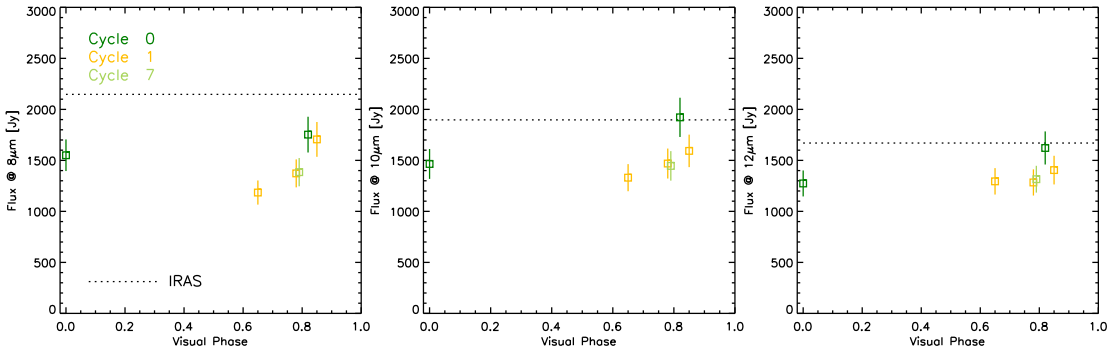

Figure 6.12: Visual phase vs MIDI flux at 8, 10, and 12 μm for R Leo.

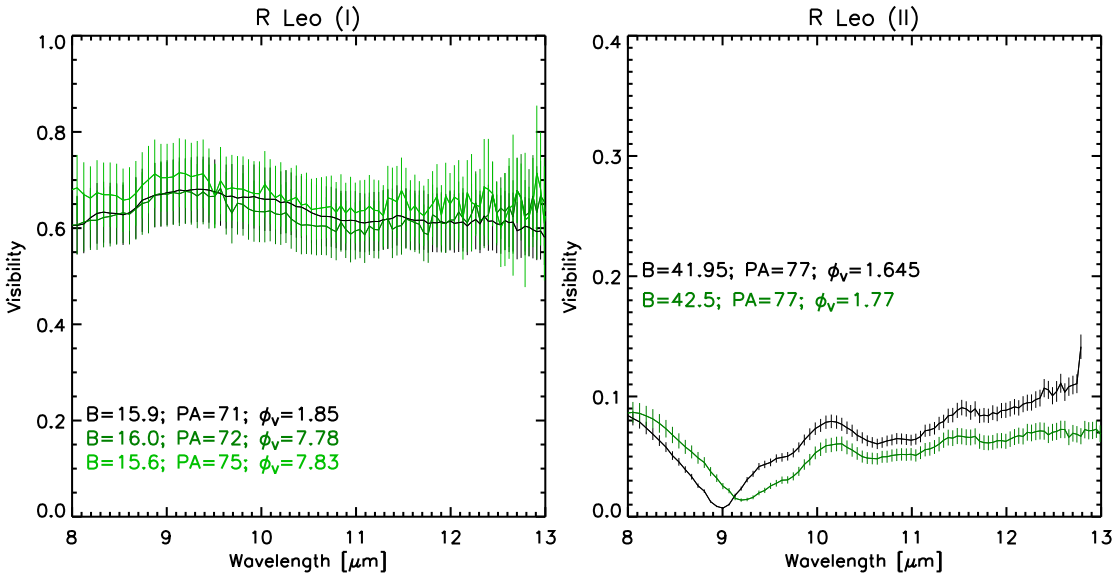

Figure 6.13: Interferometric variability check for R Leo. The black line shown in the right panel is the result of the average of two observations. The latter were observed one day apart with similar projected baseline and PA.

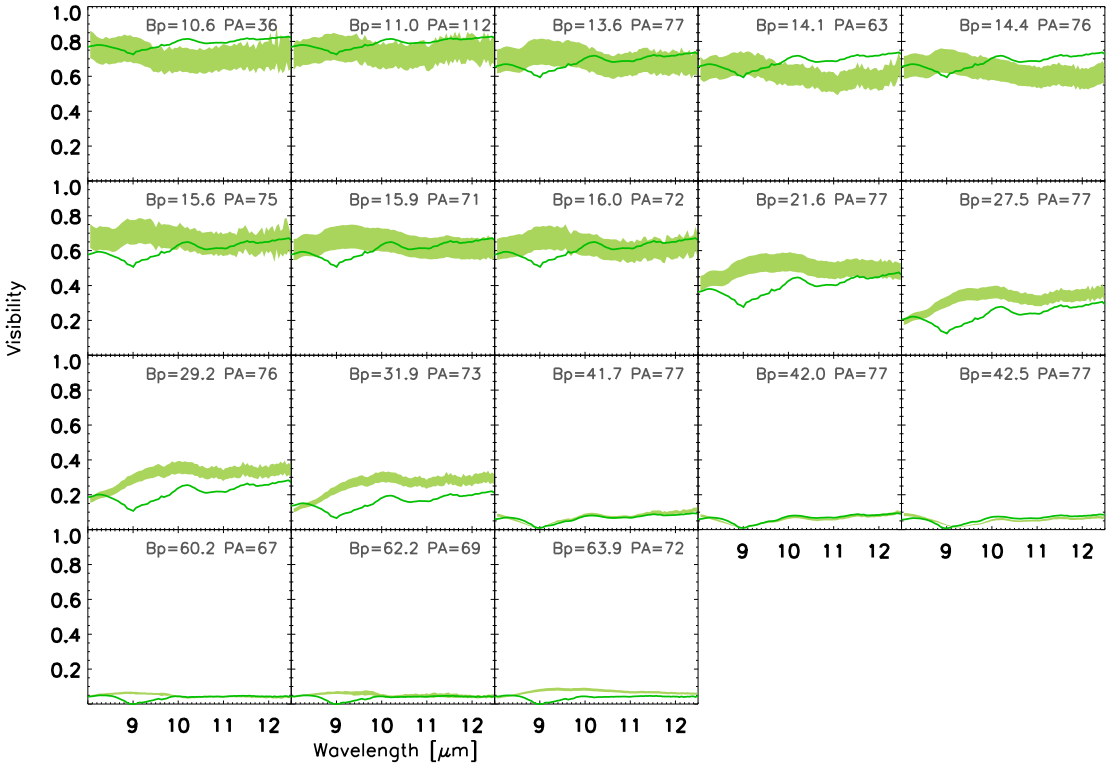

Figure 6.14: Best-fitting GEM-FIND model (solid line) for the MIDI visibilities of R Leo.

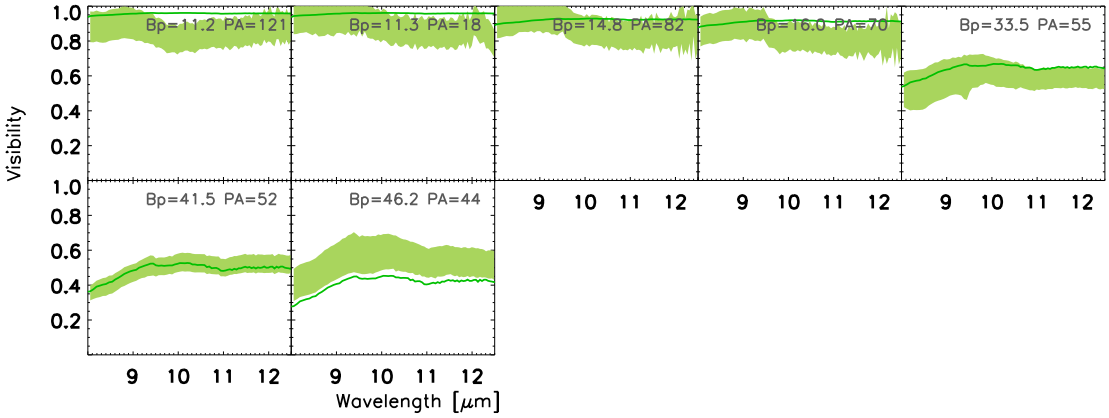

Figure 6.15: Best-fitting GEM-FIND model for the MIDI visibilities of T Mic.

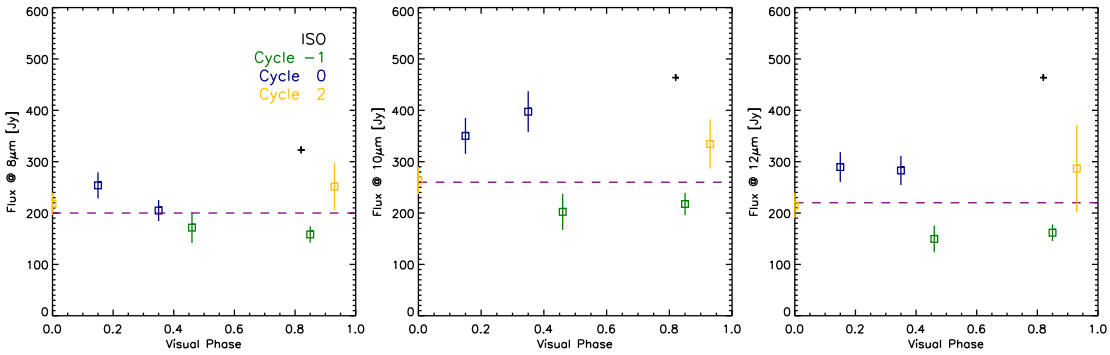

Figure 6.16: Visual phase versus 8 (left), 10 (center), and 12 μm (right) flux for RT Vir. The colours refer to the cycles, while the cross marks the ISO flux. A cyan horizontal line has been drawn to guide the eye and to make the sinusoidal-like variations clearer.

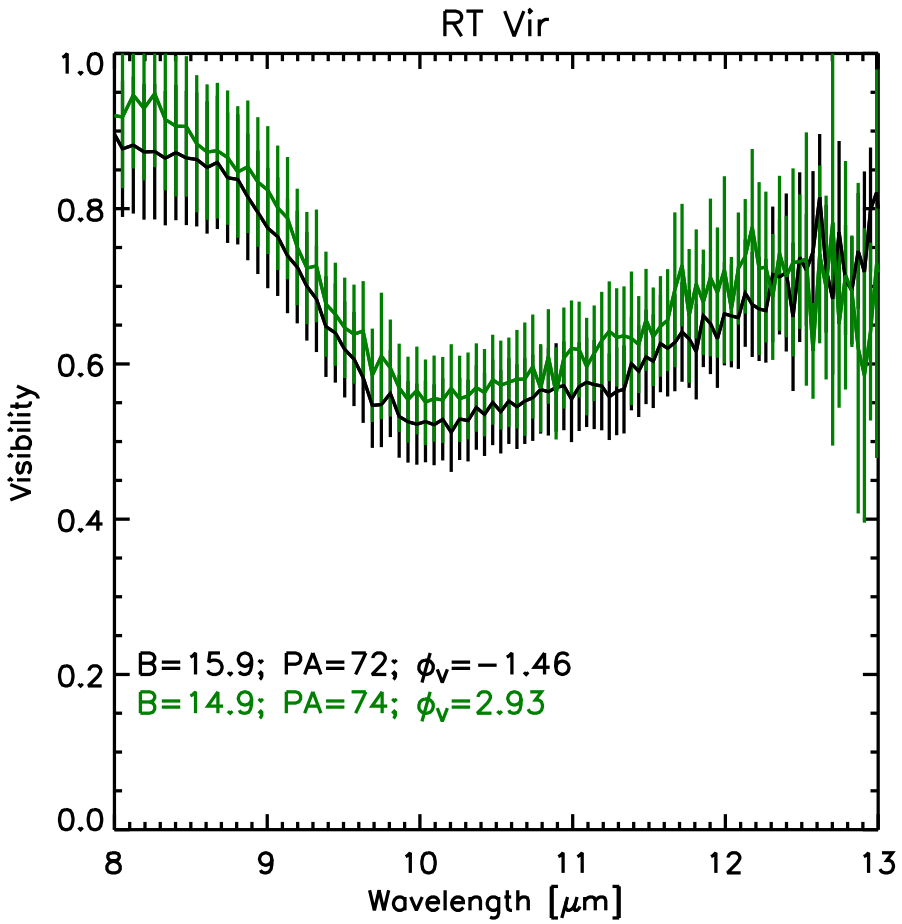

Figure 6.17: Interferometric variability check for RT Vir.

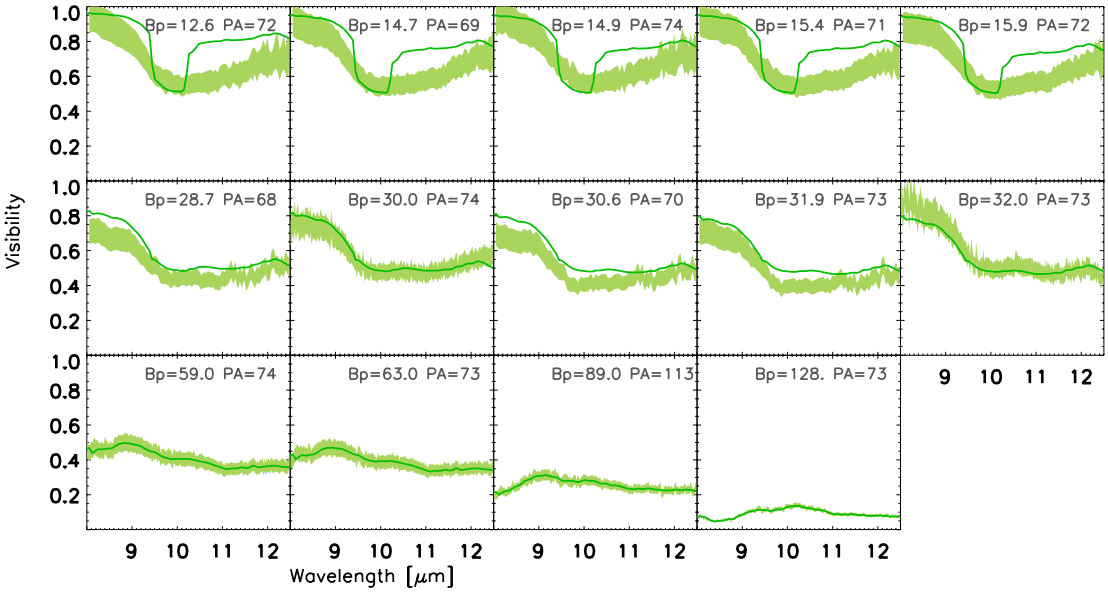

Figure 6.18: Best-fitting GEM-FIND model (solid line) for the MIDI visibilities of RT Vir.

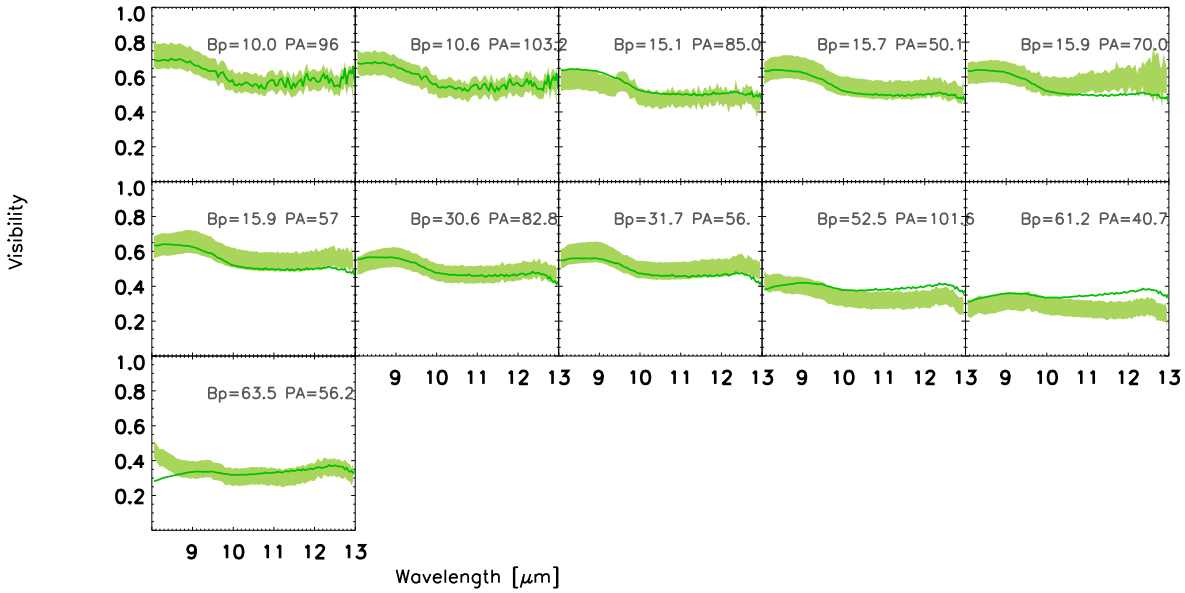

Figure 6.19: Best-fitting GEM-FIND model (solid line) for the MIDI visibilities of π^1 Gru.

6.7.7 omi Ori

omi Ori is one of the two S-type stars of our sample. According to the recent parameter determination by Cruzalèbes et al. (2013b), the star has a $K-$band angular diameter of 9.78 mas. Cruzalèbes et al. (2013a) reports asymmetric structures detected (via a closure-phase signature) in the near-infrared. The star is known to have a white dwarf companion (Ake and Johnson, 1988), but the separation between the two stars, and more generally the orbit of the system, are not known. The star was classified among the irregular morphologies in the Herschel/PACS images (Cox et al., 2012). omi Ori was observed by MIDI in 2005 and 2011, and we collected a total of 14 data sets, 7 of which are archive data.

Variability

Classified as SRb, omi Ori has a period of 30 days. We collected a light curve from ASAS, but the data are limited to 2010, therefore we could not estimate the visual phase for the MIDI data of the LP. A comparison of the IRAS spectrum with the MIDI spectrum from 2005 shows no evidence of variability. The data of the LP were collected within a few days, therefore we do not need to worry about interferometric intra-cycle variability. As there is no overlap between the baselines and position angles of the archive data and the ones from the LP, it is not possible to issue any statement concerning cycle-to-cycle interferometric variability. As a consequence, one should consider the results from the $\chi^2_{\rm red}$ combining all the data only as indicative.

Morphology

The visibility curve of omi Ori does not show any sign of dust when plotted vs. wavelength. The feature observed around 9.58 μm is due to telluric ozone. The LP data sample the upper part of the visibility curve. Therefore a fit on these data cannot really distinguish between Gaussian and UD profiles. As a confirmation, the $\chi^2_{\rm red}$ of the two models are very close to each other. GEM-FIND fit of the LP data point to an elliptical UD model with inclination 55° and axis ratio 0.4. The $\chi^2_{\rm red}$ obtained by fitting all the data (archive+LP) points towards a composite model (UD+Gauss) with a very extended Gaussian (FWHM $>$ 150 mas) enshrouding the UD (see also Fig. 6.20). The flux ratio is > 50, meaning that the central source is the dominant contributor.

6.7.8 U Ant

U Ant is a nearby N-type carbon star. Knapp et al. (2003) reported a distance of 260 pc. Bergeat and Chevallier (2005) estimated its parameters as follows: $T_{\rm eff} = 2810K$, the $C/O = 1.44$, $\dot{M} = 2.0 \times 10^{-6} M_{\odot}$ yr^{-1}. More recently, McDonald et al. (2012) estimated a much hotter temperature (3317 K) through Spectral Energy Distribution (SED) fitting. Five "spherical" detached shells were detected at long wavelength and large scales $\sim 25", 37", 43", 50", 3'$ (Izumiura et al., 1996; Olofsson et al., 1996; González Delgado et al., 2001, 2003; Maercker et al., 2010). Herschel-PACS imaged in the FIR a shell with a distance from the star of 42" (Kerschbaum et al., 2010).

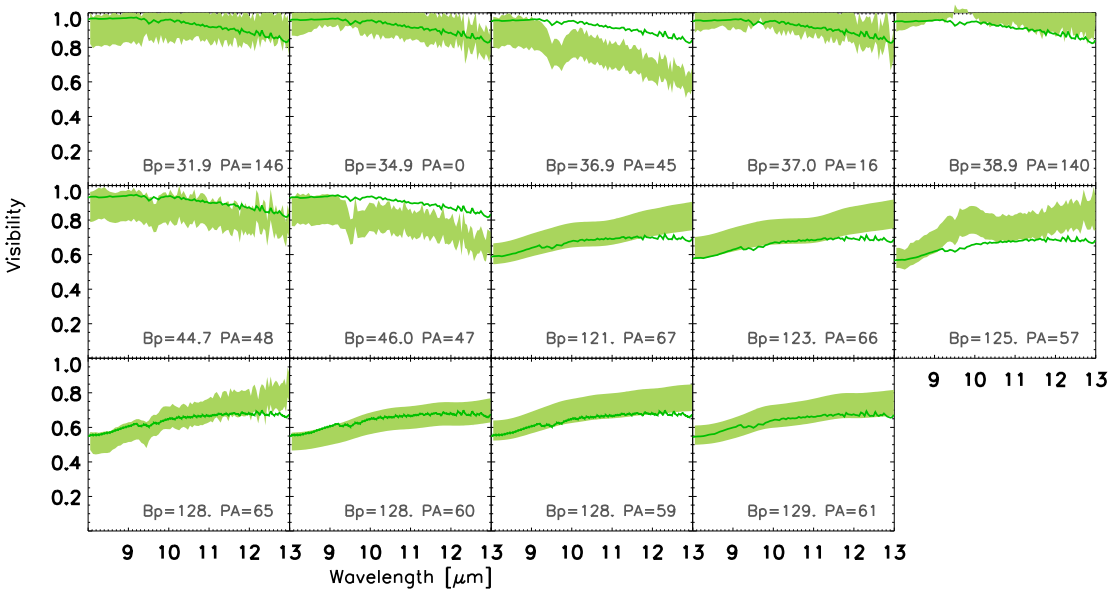

Figure 6.20: Best-fitting GEM-FIND model for the MIDI visibilities of omi Ori.

The star was observed with MIDI in 2008 and 2012. For our program, we obtained 5 observations, but only one of them turned out to be of any use. The reason for this is mostly poor seeing conditions during the nights of observation. Most of the archive data are also of mediocre quality. Only 2 points out of 5 from archive will be hereafter used.

Variability

Since U Ant is an irregular variable of type Lb, it is not possible to determine at which visual phase the observations were taken. Moreover, there are no V-band measurements available at the time of the MIDI observations. Therefore, a study of the interferometric variability is not possible for this star. We retrieved the IRAS spectrum from the archive and compared it with the MIDI spectrum in Fig.6.6. The star is classified as SiC+ by Sloan et al. (1998). This class of objects is characterised by a spectrum with a weak 8.5-9 μm feature, a weak dust continuum, and a weak SiC feature which is observed in our spectra. The MIDI spectrum is within the error bars of the the IRAS spectrum.

Morphology

Three visibility points (Fig. 6.21) are definitely too few to have an idea about the morphology of the star, especially if one considers that the data are taken 4 years apart. Therefore, for this star, we can only derive sizes and study the molecular and dust components. The diameter of the best fitting FWHM varies between 7 and 10 mas as a function of wavelength.

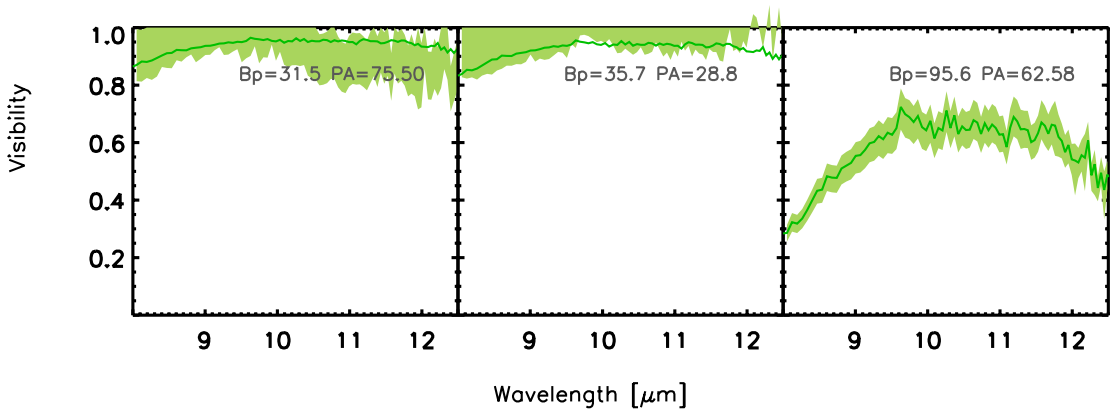

Figure 6.21: Best-fitting Gaussian profile (solid-line) for the MIDI visibilities of U Ant.

It is interesting to note that even though both MIDI and IRAS spectra exhibit a weak SiC feature, the visibilities are typical of the carbon stars without SiC (Fig. 6.3). Indeed the typical visibility drop around 11.3 μm is not observed here. A small decrease of the visibility is observed only for one of the observations with the 30 m baseline. On the other hand, the high level of visibility, and consequently its large associated uncertainty, do not allow us to infer whether or not that decrease is real and due to SiC. With the baseline range chosen for this star, the FOV of the interferometer is 43 (projected baseline $\sim$ 95 m) and 130 mas (projected baseline $\sim$ 30 m). Assuming that the star has a size of around 10 mas, one can state that there is no signature of SiC within 10 stellar radii.

6.7.9 R Lep

R Lep is one of the closest carbon-rich Miras in the southern hemisphere showing intermediate mass-loss rates and very red colors (Whitelock et al., 2006, $J - K = 2.23$,). van Belle et al. (1997) reported a K-band diameter of 11.50 mas, while Chagnon et al. (2002) measured 37.10 mas in the L'-band. Signatures of asymmetric structures were observed by Ragland et al. (2006) with the IOTA interferometer in the near-IR. The object is classified as "non-detection" by Cox et al. (2012). Nevertheless, the authors predict the presence of a bow shock at a distance < 1 pc from the stellar envelope. The star was observed with MIDI in 2010, 2011, and 2012.

Variability

The MIDI spectra of R Lep, shown in Fig. 6.6, are very noisy. The flux also changes a lot within the MIDI data and between MIDI and IRAS. Excluding the data point from cycle 0 (yellow square in Fig. 6.22) which has an unrealistic low flux, the variations within the MIDI data

are of the order of 0.2 magnitude. This is a reasonable value if compared with the variations[4] $\Delta m_N < 0.48$ mag predicted by Le Bertre (1992). The flux variation between the MIDI data from cycle 2 and the IRAS spectrum is of the order of 0.7 mag. Nevertheless we warn the reader that the MIDI spectra should be considered with caution. Regarding interferometric variability, the left panel of Fig. 6.23 shows data sets too close in time to detect any intra-cycle variability. On the other hand, in the right panel of Fig. 6.23 there is a hint for a cycle-to-cycle variability: the visibility from cycle 0 is systematically lower than the others in the range where molecular opacities are at play ($8-10$ μm). Since the variability effect is small, the data are still combined together for the GEM-FIND fit.

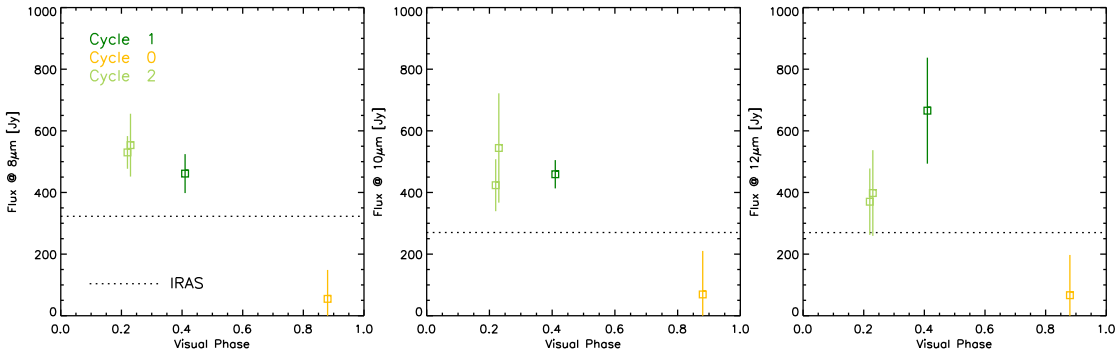

Figure 6.22: MIDI fluxes at 8, 10, and 12 μm for R Lep. The dotted line represent the IRAS flux.

Morphology

The visibility curve of R Lep (Fig. 6.24) is typical for a carbon Mira with a SiC feature, and it is described in Sect. 6.4. By using only the LP data, we obtain a better $\chi^2_{\rm red}$ for the Gaussian model, whereas adding all the observations together we have a good fit of the data with a two-component model (UD+Gaussian, see Fig. 6.24). The UD diameter is 15 mas, the resulting Gaussian envelope has a size ranging between 30 and 44 mas, while the flux ratio varies between 0.20 and 0.10. We do not observe any asymmetric structure that might be related to the asymmetries observed at other spatial scales and wavelengths (i.e. near-infrared by Ragland et al., 2006). The SiC depression is always present in the visibility curve, but we note that at long baselines and long wavelengths the visibility increases again. This might be explained by the fact that at those spatial frequencies, there is some extra molecular opacity appearing making the object smaller. SiC is clearly present in the IRAS spectrum of the star, and since we are sampling the spatial

[4]Le Bertre (1992) observed a decrease in the amplitude of variability of Mira stars towards the long wavelengths. There are no $N-$band measurements reported for R Lep, but the variability in the $M-$band is 0.48 mag, i.e. the variability in the $N-$band must be smaller than this value.

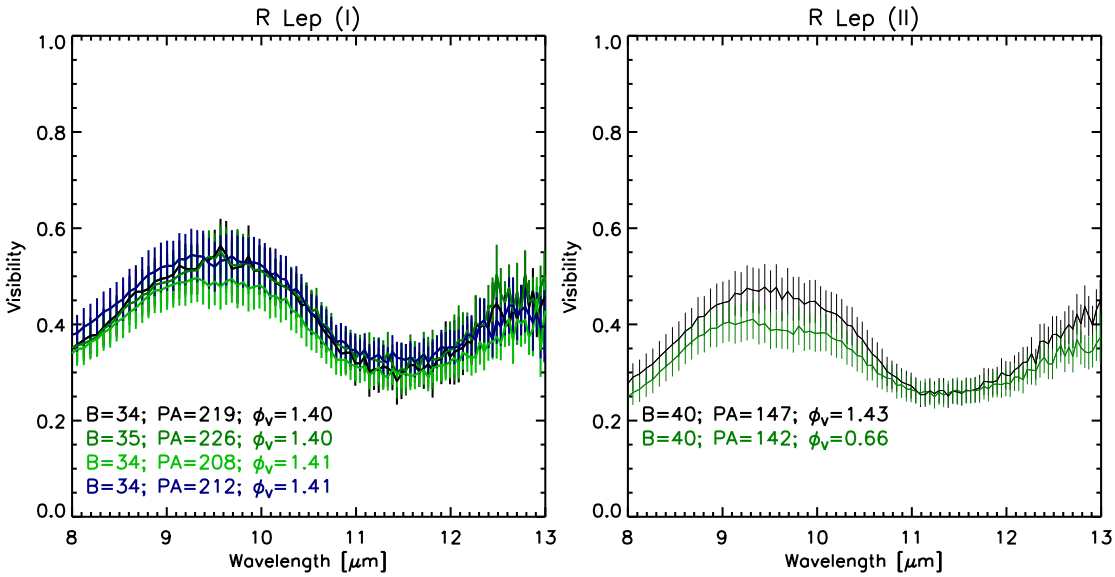

Figure 6.23: Interferometric variability for R Lep.

frequencies at 2 stellar radii (using as a reference the photospheric diameter given by van Belle et al., 1997), we can say that already at 2 stellar radii SiC is observed.

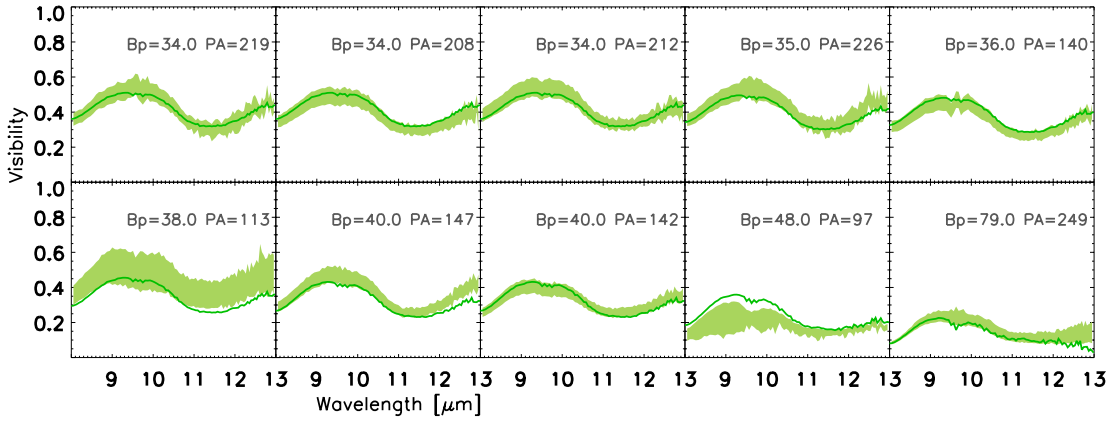

Figure 6.24: Best-fitting UD+Gaussian profile (solid line) for the MIDI visibilities of R Lep.

6.7.10 Y Pav

Y Pav is a Semiregular C-rich variable with period 232 days and distance 400 pc (van Leeuwen, 2007). The object is classified class "X" by Cox et al. (2012); no bow-shock nor detached shell were identified. Sloan et al. (1998) classified the spectrum of this object as Br1 (Broad 1). This class

includes stars showing broad emission features extending from 8-9 μm to 12 μm. The authors are not able to identify the opacities contributing to these extended features, and suggest that the Br1 class of objects is physically different from the other classes which are. It is observed that the Br1 stars have similar colour distribution as the SiC class, but the central object is cooler. According to the IRAS color-color diagram, this object is evolving toward a carbon Mira. Y Pav was observed only in the framework of our program in 2011, and we will use 4 out of 7 observations for the modelling (u, v-coverage shown in Fig. 6.2). The data discarded suffered from poor weather conditions.

Variability

No interferometric variability can be assessed, as the data were taken at a single epoch. The difference between the IRAS and MIDI spectra is very likely due to calibration problems. They will not be mentioned further.

Morphology

The visibility vs. wavelength plotted in Fig. 6.26 shows a minimum in the visibility curve slightly shifted towards shorter wavelength than the SiC feature. The difference is very small, and it can be seen also in Fig. 6.25. It is not clear whether this difference is related to the Br1 spectral classification, mainly because this is the only Br1 of the sample. A detailed modelling of the visibilities and of the ISO spectrum by means of model atmospheres will clarify what kind of opacities are contributing most (Rau et al., 2016b).

The visibility obtained are quite high and can be well fitted by a Gaussian profile (Fig. 6.26). The FWHM of the resulting Gaussian is between 5.29 and 12 mas depending on wavelengths.

6.7.11 TX Psc

A detailed mid-infrared spectro-interferometric study of TX Psc can be found in Klotz et al. (2013b). In this section, we will present the new visibility data from the LP and discuss the morphology of the source. As the spectral type of the calibrators used for the LP data are MI and MIII, the MIDI spectra were not flux calibrated (see details in Sect. 6.2.3), therefore no discussion on spectroscopic variability will be done.

Morphology

The model fitting best both the archive and LP data is a UD with size between 12 and 9 mas. The star is larger in the $8-9$ μm region where C_2H_2 and HCN opacities contribute, following the same wavelength dependency plotted in Fig. 3 (right panel) of Klotz et al. (2013b). We confirm that no asymmetric structures are observed, and that the object can be described by a single component. This result is in line with the finding of Klotz et al. (2013b), however asymmetric structures are detected much further than 10 $R_\star$ by several authors (see Hron et al., 2015b, and

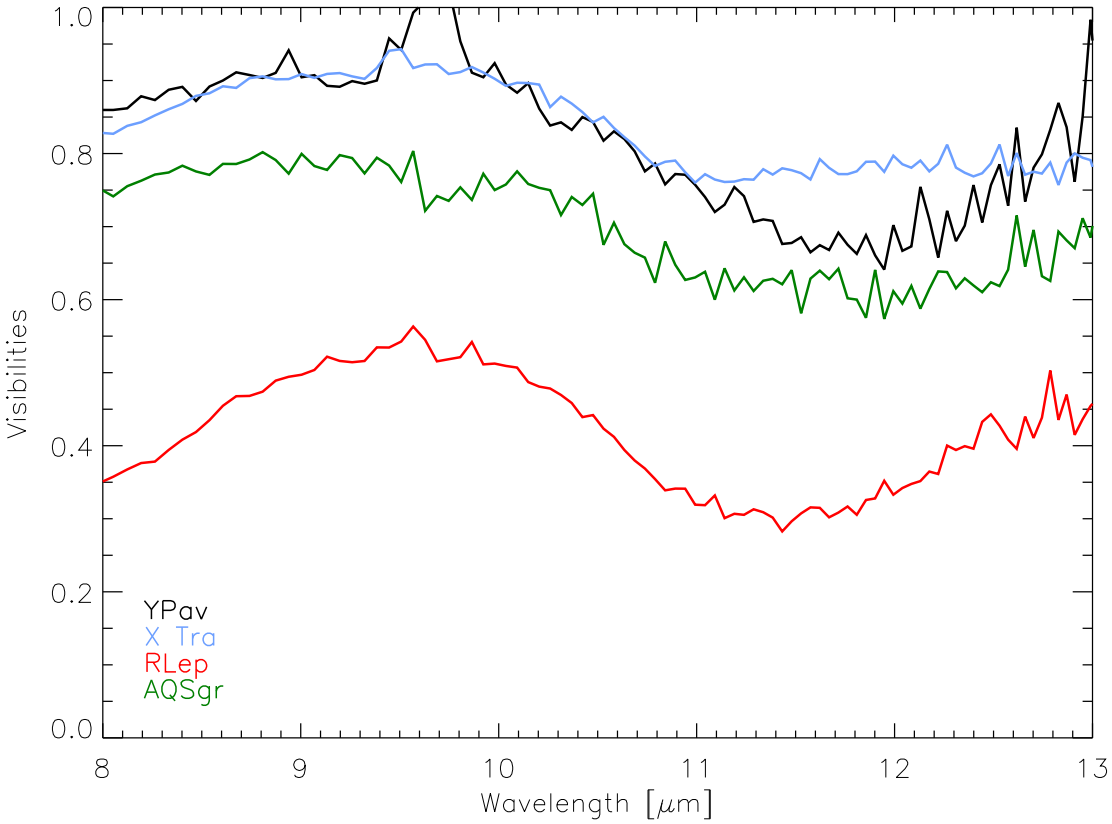

Figure 6.25: Comparison between the shape of the visibility of all the stars showing SiC.

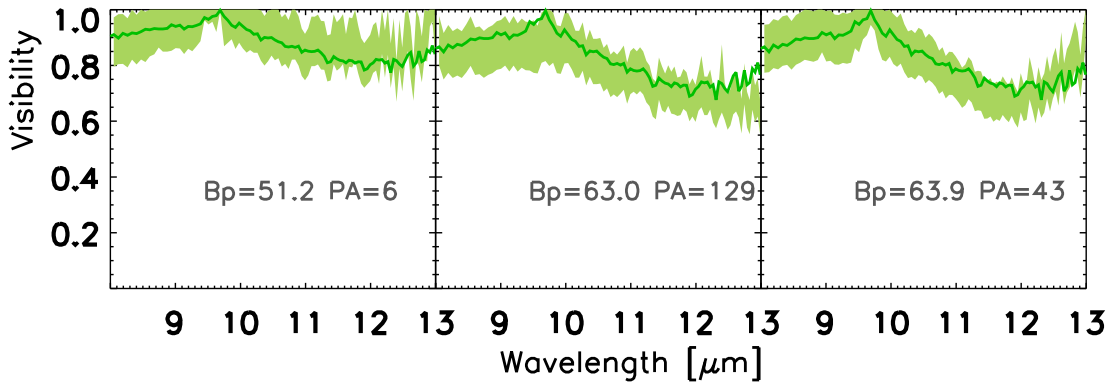

Figure 6.26: Best-fitting Gaussian profile (solid line) for the MIDI visibilities of Y Pav.

references therein). The object is classified in class "N" (naked) by Sloan et al. (1998). This class includes stars that do not exhibit dust excess in the ISO spectrum. We confirm that the visibilities do not show signs of dust (Fig. 6.27).

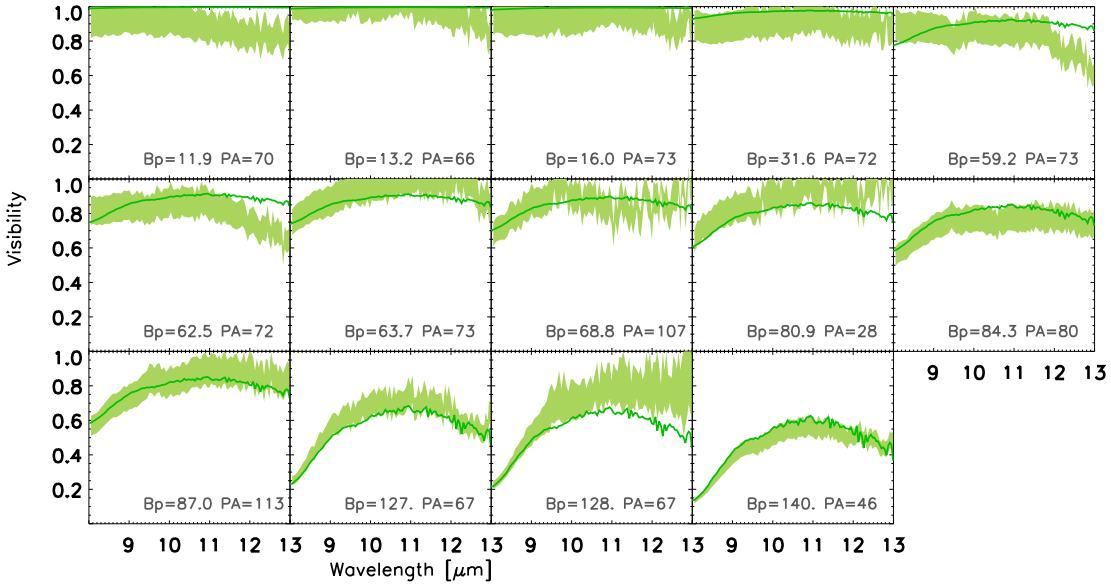

Figure 6.27: Best-fitting GEM-FIND model (solid line) for the MIDI visibilities of TX Psc.

6.7.12 S Sct

S Sct is a carbon-rich Semiregular pulsator, with a variability amplitude of 1.5 mag in the $V-$band and, an uncertain distance (between 367 pc and 580 pc according to van Leeuwen, 2007; Bergeat and Chevallier, 2005, respectively). The temperature of the star is 2755 K according to Bergeat and Chevallier (2005) and 2895 K following Lambert et al. (1986). The mass-loss rate reported in literature is of the order of 10^{-6} $M_{\odot}$ yr^{-1} (see Table 6.1). The star is one of the targets surrounded by a detached shell (Olofsson et al., 1992) that formed $\sim 10^4$ yrs ago because of a super-wind episode with a mass-loss rate of $\sim 10^4$ $M_{\odot}$ yr^{-1}. This shell is also observed in the Herschel/PACS images and was recently modelled by Mečina et al. (2014). The inner spatial scales probed by VLTI/PIONIER ($H-$band 4-beam combiner interferometer; Le Bouquin et al., 2009) can be well fitted by a UD of diameter 6.22 ± 0.3 mas ($\chi^2 = 1.4$). PIONIER did not detect any asymmetric structure (Le Bouquin, private communication).

MIDI observed this object 7 times between the 2011 May 28 and 30. For the modelling and data interpretation, we will use only 2 data sets, keeping in mind that the one of May 30th is very good, while the data of May 28th are very noisy after 11.5 μm. The other 5 observations were affected by poor weather conditions.

Variability

The MIDI spectrum agrees with the flux level of the ISO observations. However, ISO shows a small bump around 11.3 μm attributable to SiC, while nothing similar is seen by MIDI. Although we cannot exclude that the shape of the MIDI spectrum is still affected by calibration problems, it is an interesting coincidence that neither is SiC observed in the visibilities (see following Section), nor that the shape of the MIDI spectrum resembles the one from IRAS (Fig. 6.28). Like TX Psc, also S Sct is classified as N (naked) in the Sloan et al. (1998) classification based on IRAS spectra. This could mean that the amount of SiC was too small at the time of the IRAS observations, and that it increased afterwards. But given the shape of the MIDI spectrum, one presumes that the feature recently disappeared again (Fig. 6.28). A more likely possibility would be a photospheric variation, i.e. no change in the SiC, but rather in the molecular opacity at wavelengths > 10 μm.

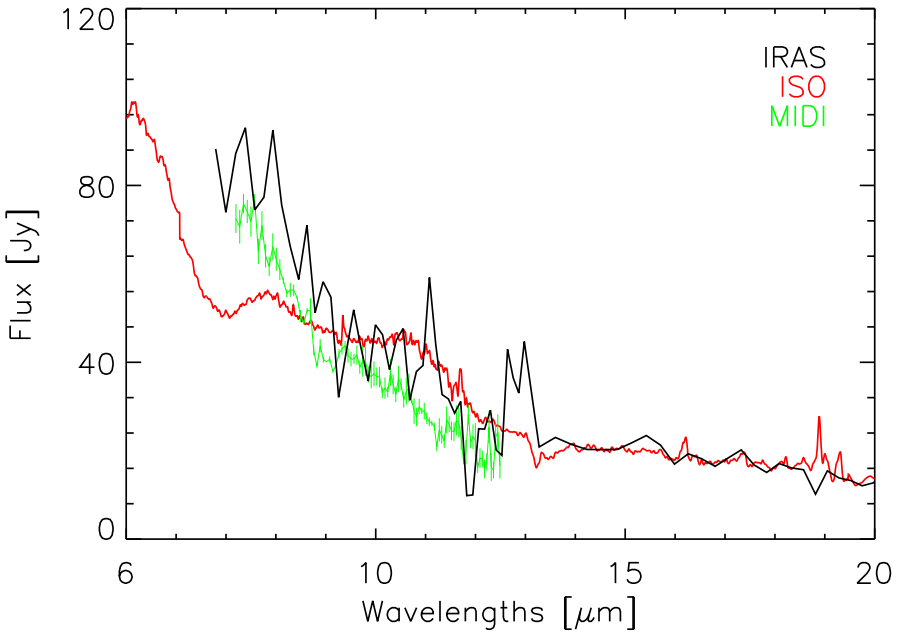

Figure 6.28: The MIDI spectrum of S Sct compared with those from IRAS and ISO. While the flux levels are very similar, the MIDI and the IRAS spectra do not show any signature of SiC, despite being clearly visible in the ISO spectrum.

Morphology

The 2 visibility points shown in Fig. 6.29 are easily fitted with circular models, and the fit shows a slight preference for the Gaussian shape. Nevertheless, the robustness of that conclusion should not be overestimated because of the high visibilities and of the small amount of data available. The FWHM of the Gaussian varies between 11.77 and 12.78 mas ($\sim$ 2 $R_\star$), while the corresponding UD varies between 19 and 21 mas (almost 3 times the H-band diameter).

Like in the case of U Ant, we stress that the visibility of S Sct does not show any signature of SiC. By comparing the N-band UD diameter with the H-band one measured by PIONIER, we conclude that molecular and dust (amorphous carbon) material enshrouds the object in the N-band. No SiC is detected within the FOV of the interferometer, which for this set of observations is ~ 100 mas at 10μm.

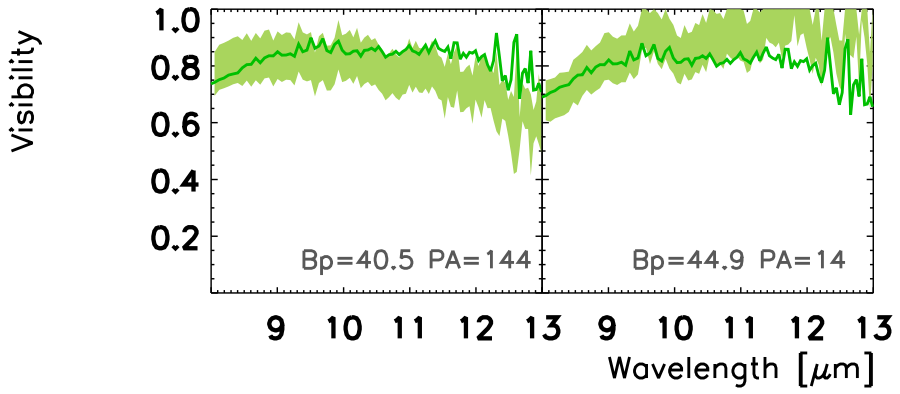

Figure 6.29: Best-fitting GEM-FIND model for the MIDI visibilities of S Sct.

6.7.13 AQ Sgr

AQ Sgr is a carbon-enriched Semiregular variable. The period of variability is 190 d, and the distance 330 pc (van Leeuwen, 2007). The mass-loss estimates vary between 7.7x10^{-7} $M_{\odot}$ yr^{-1} (Bergeat and Chevallier, 2005), and 10^{-7} $M_{\odot}$ yr^{-1} (Ramstedt et al., 2014). The star is classified as Fermata by Cox et al. (2012). Richichi et al. (2005) report a K-band diameter of 6.13 mas. The star was already observed with MIDI in 2008 but those data are very noisy and they were discarded during data reduction. Only two points from the LP were used for the analysis. The archive data are corrupted by weather.

Variability

The MIDI spectrum of AQ Sgr is compared with the one from IRAS in Fig. 6.6, and they fit within the uncertainties of IRAS. The shape of the spectra is rather similar, and we observe a bump around 11.3 μm due to SiC. The star was classified as SiC+ by Sloan et al. (1998) and Gupta et al. (2004). No interferometric variability can be determined from the available dataset.

Morphology

The visibility curve presented in Fig. 6.30 matches the shape of the spectrum, showing the SiC signature. The observations are well fitted by a UD profile with a diameter between 16 and 32 mas (depending on wavelength). The level of visibility at 11.3 μm is comparable to the one at

12 μm were the UD diameter measures 32 mas. By comparing the latter value with the K-band diameter, we can conclude that SiC is being detected at 5 $R_\star$.

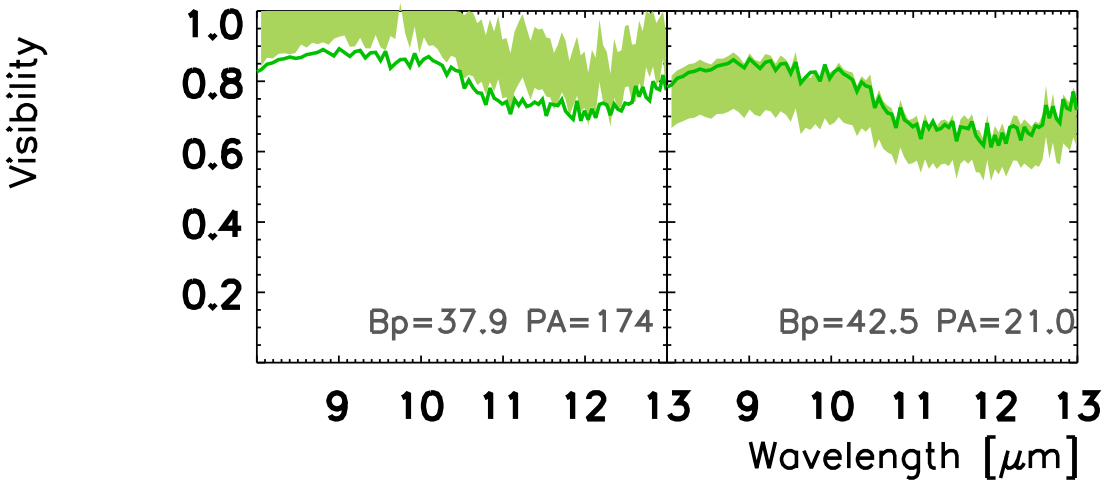

Figure 6.30: Best-fitting GEM-FIND model (solid line) for the MIDI visibilities of AQ Sgr.

6.7.14 X TrA

X TrA is a carbon-rich irregular variable. A detailed near-infrared spectroscopic study with line identification was presented for this object by Lebzelter et al. (2012). The star is a single object, as no indication of binarity was so far reported. Izumiura et al. (1995) detected a detached shell at a distance of 1.3′. In Cox et al. (2012) the star is classified among the rings, but the ring detected by Herschel is faint with only a bright arc to the East. These authors conclude that more observations are needed. X TrA was observed for the first time with MIDI within the frame of our LP. Four points out of 7 will be used for the geometric modelling. The other points were affected by weather conditions.

Variability

Because of the irregular nature of the light curve, time variability cannot be studied in detail for this star. However a comparison between the MIDI and the IRAS spectra (Fig. 6.6) shows that the flux level is unchanged, and SiC is observed. The object is classified as SiC+ in the Sloan et al. (1998) classification. The presence of SiC is already detected in the IRAS spectrum shown in Fig. 6.6 and also in the MIDI ones.

Morphology

The X Tra MIDI data can be reproduced with a UD of size 21.9 - 38.8 mas. The $\chi^2_{\rm red}$ of the Gaussian (Table 6.3) is similar for the already mentioned reason: the data sample the upper

part of the visibility curve where both Gaussian and UD profiles are very similar. The visibility curve vs. wavelength shown in Fig. 6.31 exhibits the shape typical of stars with SiC. The level of visibility at 11.3 μm is comparable to the one at 12μm, and so do the diameters. Therefore we can conclude that for X Tra, SiC is detected at $\sim$4 R$_\star$.

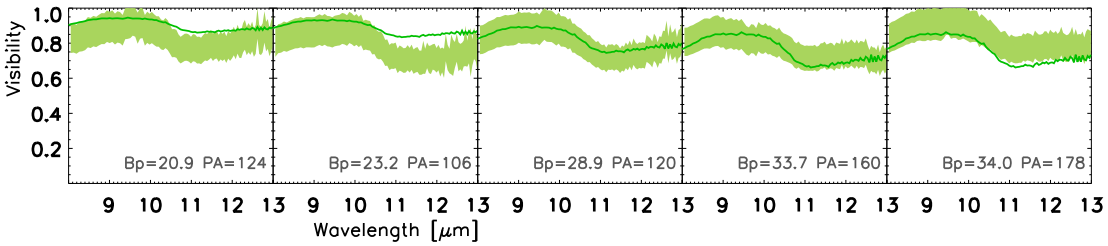

Figure 6.31: Best-fitting GEM-FIND model (solid line) for the MIDI visibilities of X Tra.

Chapter 7

Dynamic model atmospheres *without* the SPL approximation, compared with observations - The observational test case of R Lep (Paper IV)

This chapter will be part of a publication in preparation (Rau et al., 2016a)

Preliminary title: *Comparison of spectro- photometric and interferometric observations with dynamic model atmospheres, with and without the small particle limit approximation - The observational test case of R Lep*
Authors: G. Rau, K. Eriksson, B. Aringer, J. Hron, C. Paladini
Year: 2016
Journal: Astronomy and Astrophysics

When comparing the dynamic model atmospheres grid from Eriksson et al. (2014) with multi-technique observations, some differences are noticeable (see Rau et al., 2015c, 2016b). Removing the SPL assumption in the models could provide a potential solution to those discrepancies, especially for the short wavelengths.

In this small chapter, which will be part of a forthcoming publication, the comparison of one non-SPL model with a test-case star, R Lep, is presented. The whole grid of non-SPL models will be computed by our collaborators of the Uppsala group, and a comparison of the observations

with this complete grid will allow a much more complete view on the improvements that non-SPL models could produce.

7.1 Introduction

In the recent years, several attempts have been made to model the atmospheres of C-rich AGB stars. While hydrostatic models (e.g. Aringer et al., 2009) have been able to reproduce observations (e.g. Ohnaka et al., 2007; Paladini et al., 2011; Cruzalèbes et al., 2013a; Klotz et al., 2013a; van Belle et al., 2013), objects characterized by strong atmospherical dynamics can not be modelled by hydrostatic atmospheres.

On the AGB, the stars cool, expand and increase in brightness. During its life on the AGB, the star could eventually start to pulsate, generating shocks waves that go through the star's atmosphere, which could create conditions of high enough pressure, at low enough temperature to generate the environment suitable for dust formation. Radiation pressure acting on high opacity amorphous carbon (amC) grains, can transfer enough momentum to the grains, accelerating them, and inducing a wind outflowing the object (e.g. Fleischer et al., 1992; Höfner and Dorfi, 1997).

A new generation of dynmic model atmospheres (Dynamic Atmosphere and Radiation-driven Wind models based on Implicit Numerics, DARWIN from now on, Höfner et al., 2016) depicts this scenario with the inclusion of a time-dependent treatment of grain growth and evaporation of amC dust. Radiative transfer which is frequency-dependent, including gas and dust opacities, is combined with time-dependent hydrodynamics and non-equilibrium dust formation.

The models initial structures are hydrostatic. The varying inner boundary conditions below the stellar photosphere are simulated by a "piston". This is described in detail in Höfner et al. (2003) and Mattsson et al. (2010). The shock waves induced by the pulsating structure, and the variation of the luminosity with period, are considered. In order to reduce the complexity in the treatment of dust opacities, the radiative cross sections are generally calculated assuming that the dust grains are small in comparison to the wavelengths around the maximum of the stellar flux, and this assumption is called the small particle limit assumption (from now on SPL, Mattsson and Höfner, 2011).

Several studies compared these models with interferometric observations (Rau et al., 2015c, Rau et al., 2016b, hereafter Paper I and Paper II, respectively, or e.g. Sacuto et al., 2011a), which compared observations with a grid of dynamic model atmospheres from Eriksson et al. (2014) and Mattsson et al. (2010). While they were rather successful in reproducing the data, some discrepancies between models and observations still remain. Those show up in the photometric and spectroscopic fits at wavelengths shortwards of 1 μm and in the N-band interferometric fits e.g. (Paper I; Paper II)). In the current work we aim to investigate if and how those differences could be related to the SPL assumption.

Already Mattsson and Höfner (2011) studied how, for certain critical cases, the effect of grain-size dependent opacities can be quite important, especially when strong dust-driven winds

do not form in the SPL case. They note that indeed, if the restriction to the SPL is dropped, the wind speed could increase by an order of magnitude and the mass-loss rate by a factor of up to two. Also, a model without the SPL assumption, which results in having a wind, seems to have a lower dust condensation degree with respect to SPL models. Therefore the dust-loss rates could get lower when removing the assumption of SPL (from now on: non-SPL case). In particular, Mattsson and Höfner (2011) underline that models near the limit of windless solutions could be the most affected by removing this assumption. This might be of special relevance for the semiregular variables (see Chap. 5).

In this work we therefore study the effect of dropping the SPL assumption for one specific set of model parameters described in Table 7.1. This is done performing a grain-size dependent radiative transfer, to produce the model described in Sect. 7.2. One star is used as a test-case, which is portrayed in Sect. 7.3. Following our previous works (Paper I; Paper II), we have compared the models with the spectroscopic, photometric and interferometric observations, and the findings are shown in Sect. 7.4, together with their discussion. Concluding remarks are given in Sect. 7.5.

7.2 Model description

In the present study we introduce one specific model which does not include the SPL approximation, and whose parameters are shown in Table 7.1. For the model calculation the parameters were chosen in order to represent a "typical" carbon-star.

This model is built according to the principles given in Höfner et al. (2016) (DARWIN models) except for the dust opacity which was treated as in Mattsson and Höfner (2011). The K_3 moment, representing the total amount of material condensed into dust, was used to compute the grain radii. New gas opacities data (Aringer et al., 2016) were adopted, together with new starting (hydrostatic) models structures, which have the same opacity data in order to preserve the consistency. Also the RHD code has been updated in minor ways. The frequency-dependent molecular and dust opacities radiative transfer, and non-equilibrium dust formation, were calculated following the method described in Höfner et al. (2003). This single model will be part of a forthcoming wide grid of dynamic model atmospheres without the SPL assumption (Eriksson et al. in prep).

A previous grid of models without the SPL assumption was presented in the work of Mattsson and Höfner (2011). There one can find a description of dust opacities that could be applied to any size of the grains, and not only for particles much smaller[1] than the wavelengths (Mie approximation). This affects the computation of the radiative cross section, which could in turn influence the radiative energy transfer, the radiative pressure on the dust grains, and consequently the wind acceleration. For details on the dust opacity treatment, please refer to Mattsson and Höfner (2011).

[1] A grain size with an average radius smaller than $4 \cdot 10^{-6}$ cm is considered to be "small", concerning radiative cross-sections.

Table 7.1: Summary of the results or the modeling & model parameters.

	$T_{\rm eff}$ [K]	$lg\ L_\star$ [$L_\odot$]	M [$M_\odot$]	P [d]	C/O	f_L	$\dot{M}$ $10^{-6}[M_\odot/\rm yr]$	Cond. Fraction	Outflow Vel. [km/s]
SPL	2600	3.85	1.00	390	1.69	2	2.1	0.25	17
NO SPL	2600	3.85	1.00	390	1.69	2	1.9	0.12	22
NO SPL*	2800	3.85	1.00	390	1.69	1	2.24	...	...

Notes. (*): best-fitting model resulting from the fit presented in Chap. 5.

7.3 The test case of R Lep

For our comparison we chose one Mira star whose best-fitting SPL-model from the Eriksson et al. (2014) grid, which agreed rather well with the observations (see Paper II and Table 7.2).

The particular model without the SPL assumption produced, is described by the parameters listed in Table 7.1. The same table shows also the resulting dynamic properties, i.e. mass-loss rates, outflow velocities and dust condensation fraction.

This model has been compared with the observations of R Lep in the same way as done for the SPL-case in Chap. 5. This is done in order to perform a consistent confrontation of models described by the same parameters, even if the SPL-model, described in Table 7.1, is not the one best fitting the observations (Paper II). The parameters of the original best-fitting photometric SPL-model are added for completeness in Table 7.1 −− see also Table 3 of (Paper II).

7.4 Results and discussion

The output of the fit, namely the χ^2, the phases of the best fitting models for the two cases (SPL and non-SPL) and the wavelengths at which the fit was performed, are shown in Table 7.2). From our comparison, some overall conclusions can be drawn. We want to remark how this specific set of model parameters is only a "test-case-model", by meaning of a model described by a set of parameters which are "exemplary" for a carbon star. A fit with a whole grid of models having different parameters will be necessary in order to progress with our analysis and give better insights on the comparison of the non-SPL models with the observations.

In the spectroscopic fit the improvement from the SPL to the non-SPL model at wavelengths shortwards of 3 μm is substantial. This can be seen confronting the left and right panel of Fig. 7.1. Looking at these plots it is noticeable how the 3 μm feature becomes weaker in the new model, and the 14 μm feature emission disappears for many phases, while it is always present in the SPL models. A discussion on the nature of the 14 μm feature and its comparison with observations can be found in Loidl (2001) (see also Paper I; Paper II).

The R Lep photometric fit (Fig. 7.2) shows an improvement in the ability of the non-SPL models to reproduce the photometry in V, R, I, and also in the N-band. Conversely, the fit at the other photometric filters does not change significantly then removing the SPL assumption.

We do not notice any improvement in the quality of the fit to the interferometric observations,

in both cases of SPL or not. This is probably due to the specific set of the test-case model parameters. Nevertheless, we underline one specific slight improvement. That is, while the SPL model shows synthetic visibilities that increase towards longer wavelengths (Fig 7.3, lower left panel; see also Paper II), this behaviour is less obvious when dropping the SPL assumption. The non-SPL model produces synthetic visibilities which are flatter as a function of wavelengths (Fig 7.3, upper left panel). But we notice that the small gradient in the visibility vs. wavelengths and the visibility-decrease from 8 to 10 μm in the observations, which was well reproduced in the SPL model, is not present anymore.

The synthetic visibilities level of the non-SPL model is much higher than for SPL one. The corresponding intensity profiles show a much more compact atmosphere (Fig 7.3, upper right panel) compared to the one produced by the SPL model (Fig 7.3, lower right panel). An explanation of that could reside in the fact that the removal of the SPL assumption lowers the condensation fractions of the non-SPL model, and reduces its grains sizes. This plausibly leads to a smaller size of the circumstellar envelope, which implies higher visibility level (considering that the other parameters stay the same).

We therefore conclude that, in order to obtain a good fit to our interferometry data, we would require a non-SPL model with a higher mass-loss rate. In this way we would achieve a more extended envelope, and thus lower visibilities. Whether this leads to a disagreement in the spectrum and photometry remains to be seen. This will be tested in our next work (Rau et al. in prep) which will include the whole grid of non-SPL models by Eriksson et al. (in prep).

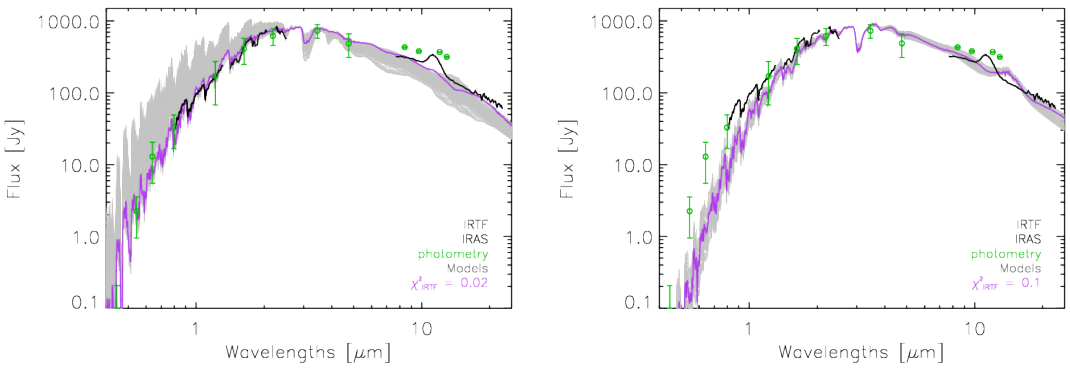

Figure 7.1: Observational spectro-photometric data of **R Lep** (IRTF spectrum in black thick line and photometry in green circles) compared with the synthetic spectrum of the best-fitting time-step (violet). The IRAS spectrum is also plotted (black thin line), only to the purpose to check qualitatively the fit at longer wavelengths. **Left**: new models *without* the SPL assumption. **Right**: models with SPL.

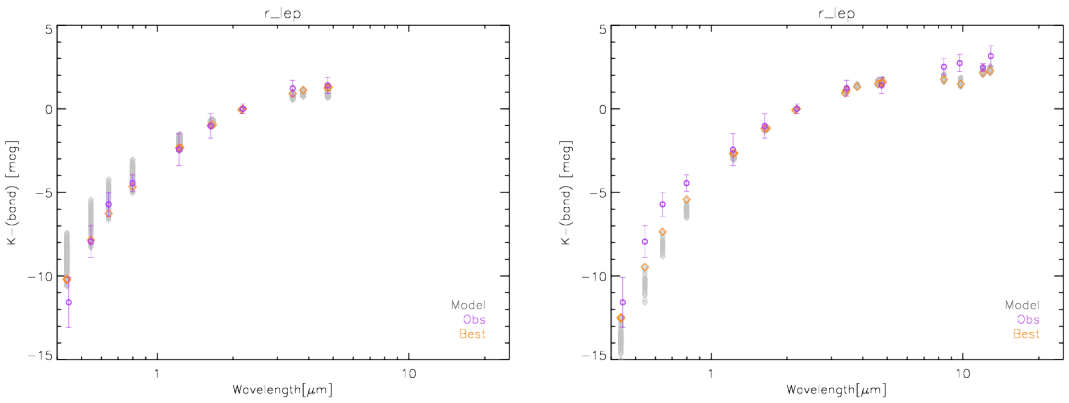

Figure 7.2: Photometric observations of the R Lep (violet circles), compared to the models synthetic photometry (grey diamonds). Marked in orange is the best fitting time-step. **Left**: new models *without* the SPL assumption. **Right**: models with SPL.

Table 7.2: Summary of R Lep corresponding values of the χ^2 and the phase of the best fitting time-step and of the interferometric MIDI observations.

	${\chi^2}_{\text{no SPL}}$	${\chi^2}_{\text{SPL}}$	$\phi_{\text{no SPL}}$	ϕ_{SPL}	$\lambda_{\text{fit range}}$ [μm]
R Lep					
Spect	0.02	0.15	0.64	0.45	[0.805-5.06]
Phot	0.22	1.55	0.50	0.40	[0.4-25.0]
Interf	250	10.03	0.86	0.90	[8.0-13.0]

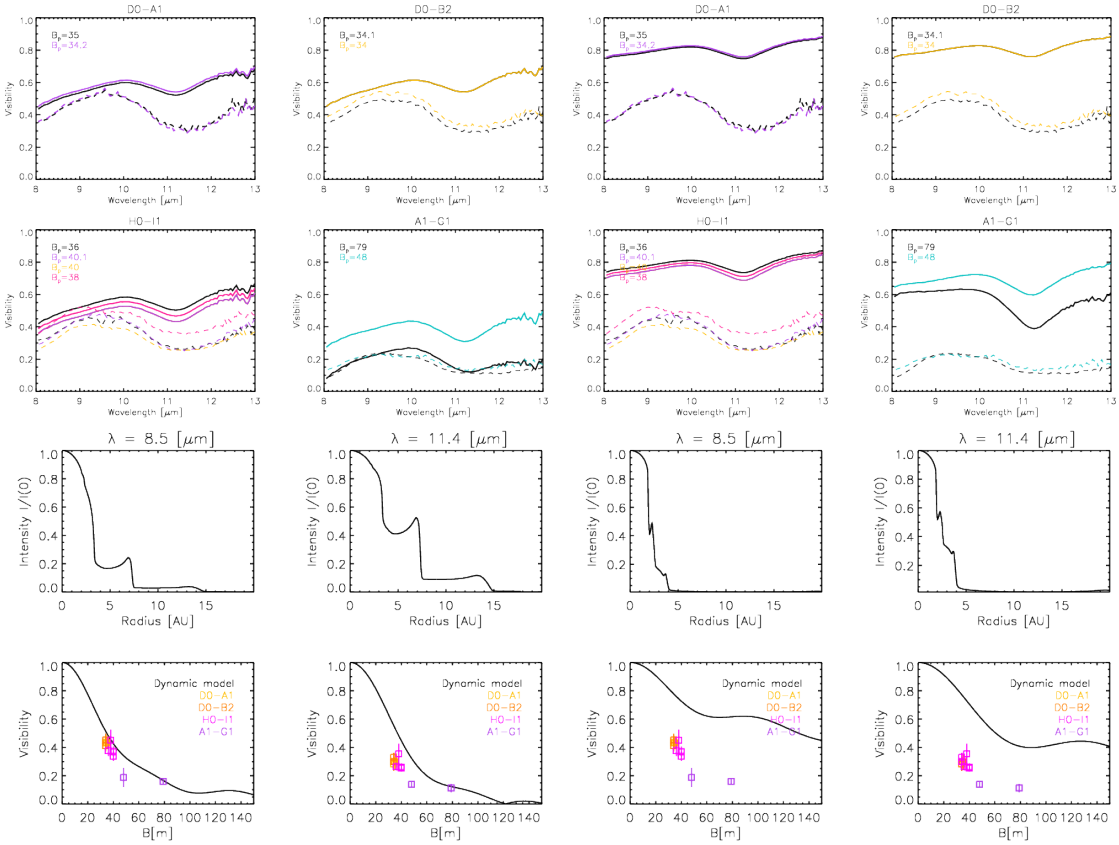

Figure 7.3: Upper two rows: Wavelength dependent visibilities of R Lep in the MIDI range, compared with the synthetic visibilities based on the DMA. Models are plotted in full line, observation in dashed lines, at the three different projected baselines (see color legend). **Lower two rows**: intensity profiles at two different wavelengths: 8.5 μm and 11.4 μm (third row), and visibility vs. baseline (fourth row); the black line shows the dynamic model, the colored symbols illustrate the MIDI measurements at different baselines configurations. **Left**: models with SPL. **Right**: new models *without* the SPL assumption.

7.5 Conclusions

Overall we notice in our tests some improvements using the non-SPL model. The slope in the visibility vs. wavelengths of the SPL model disappears when using the non-SPL models. In addition, the spectroscopy and photometry of the non-SPL model show in general better agreement with the R Lep data.

We suspect that the new grid of models without the small particle limit assumption (Eriksson et al., in prep), will somehow improve the fit. The broader parameter space of the models will allow us to perform the fit to our multi-technique observations through a wider range of models, in order to get a better fit.

Chapter 8

Preliminary comparison of the VLTI/MIDI observations of the carbon-rich Mira R For, with dynamic model atmospheres (Paper V)

This chapter will be part of a forthcoming publication:

Tentative title: *Comparison of the VLTI/MIDI observations of the carbon-rich Mira R For with dynamic models atmospheres*
Authors: C. Paladini, **G. Rau** et al.
Year: 2016
Journal: Astronomy and Astrophysics, in prep.

The comparison of the R For VLTI/MIDI observations with the dynamic model atmospheres from Eriksson et al. (2014) is not published yet. This small Chapter presents the results of the preliminary analysis performed until now, which will be part of a work in preparation to be published in the next months.

We want to remark that this is only a preliminary analysis on R For MIDI data, and that only a separate fit for the different MIDI phases (see Table 1 in Paladini et al., 2012) could give us better information on the model parameters which could better fit the star, and consequently provide insights on its structure (Paper V, in prep.). The comparison here is presented for

completeness and as a starting point for further analysis.

8.1 R For

R For is a C-rich Mira widely studied by several authors (e.g. Feast et al., 1984; Le Bertre, 1988; Winters et al., 1994; Paladini et al., 2012). Its literature parameters are shown in Table 8.1.

Table 8.1: Main parameters of R For, adopted from the literature.

Name	Variab. Type [a]	P [a] [d]	d [b] [pc]	L_{bol} $[L_\odot]$	$\dot{M}$ [c] $10^{-6}[M_\odot/\mathrm{yr}]$	$\dot{M}$ [d] $10^{-6}[M_\odot/\mathrm{yr}]$	$\dot{M}$ [e] $10^{-6}[M_\odot/\mathrm{yr}]$	ΔV [a]
R For	M	389	690^{+270}_{-130}	5985	2.2 ± 0.22	1.3 ± 0.6	1.35 ± 0.27	5.5

Notes. (a): Samus et al. (2009b) (b): van Leeuwen (2007). (c): Loup et al. (1993) (d) Schöier and Olofsson (2001) (e) Whitelock et al. (2006).

Interferometric variability was detected, using MIDI observations carried out in 2007 and 2009, by Paladini et al. (2012), who asserts that this variability could be caused by the appearance of a non-symmetric structure.

In the following, we present the comparison of spectroscopic, photometric and interferometric data with the dynamic model atmospheres grid from Eriksson et al. (2014). For a detailed description of the models used, please refer to Chap. 4, Chap. 5 and Mattsson et al. (2010).

8.2 Observations

R For was observed with the Short Wavelength Spectrometer (SWS, de Graauw et al., 1996) on board of ISO (Sloan et al., 2003) on 13 February 1998. The ISO spectrum covers the wavelengths range: $[2.36 - 45.35]$ μm, and has a spectral resolution R $\sim$ 200. To the purpose of the current study, an error of $\pm$ 10% is assumed until 4.05 μm, and $\pm$ 5% afterwards (Sloan et al., 2003).

Photometric observations are summarized in Table 8.2.

Table 8.2: R For photometric data adopted from the literature. Different filters and different sources are given in units of mag. The consideration of the errors is described in Chapter 5.

Star	B	V	R	I	J	H	K	L'	$N1$	$N2$	$N3$	$IRAS12$
R For	13.06	9.97	9.20	8.53	4.08	2.41	1.21	-0.07	-1.72	-1.87	-2.02	-1.92

Notes. The values are given in magnitudes.

For the aim of this thesis, only the 2009 R For VLTI/MIDI data are used for the comparison with the dynamic model atmospheres. Details on the journal of the MIDI observations, calibrators used and uv-coverage are given in Paladini et al. (2012).

8.3 Preliminary results

The fitting procedure described in Chapter 5 is used in the present study on R For as well. That is, first we fit independently the spectroscopy to the ISO spectrum, and the photometry to the data as in Table 8.2. Results of those fits are shown in Fig. 8.1 and Fig. 8.2 which illustrate the SED fit to the ISO spectrum and to the photometric data respectively. The ISO spectrum can be reasonably well reproduced by the DMA, but the model fit to the ISO spectrum deviates strongly from the photometry shortward of 1 μm,. The agreement of the DMA with the observed photometry is good in the whole spectral range, but the B and V model photometry is not fitting the data. As for the other objects, we think that the reasons of both discrepancies in the spectroscopic and photometric fits could reside in a combination of data- and model-related reasons.

The results of the χ^2 analysis are listed in Table 8.3, together with the parameters of the models best fitting the different types of observations.

Table 8.3: Summary of the best fitting model for each type of observation: photometry, spectroscopy and interferometry. Listed are the corresponding values of the χ^2, the parameters of the models and the phase of the best fitting time-step.

	$T_{\rm eff}$	log $L_\star$	M	P	log g	C/O	$\Delta u_{\rm p}$	$f_{\rm L}$	$\dot{M}^{\rm a}$	$\lambda_{\rm fit\ range}$	${\chi^2}_{\rm red}$
	$[K]$	$[L_\odot]$	$[M_\odot]$	[d]						[μm]	
R For											
Spectr	2800	4.00	1.5	525	-0.66	2.38	6	2	3.54	[2.36-25.0]	6.02
Photom	3000	3.85	0.75	390	-0.79	2.38	6	2	5.62	[0.4-25.0]	1.01
Interf	3000	3.85	0.75	390	-0.79	2.38	6	2	5.62	[8.0-13.0]	1.00

Notes. (a): in $10^{-6}[M_\odot/{\rm yr}]$

As in the previous chapters, synthetic visibilities and intensity profiles were computed for all the phases of the best-fitting photometric model. The results of the comparison with the MIDI data are shown in Fig. 8.3 and Fig. 8.4.

For R For the short baselines observations do not agree well with the models, beeing too low in level of visibility. Moreover, the visibility spectra show a more prominent SiC feature (drop in level around 11.4 μm) with respect to the models. This could be probably due to an underestimation of the amount of carbon being condensed in SiC. Another explanation may relate to the asymmetry detected in the dusty envelope by Paladini et al. (2012), but further investigations are necessary.

Following the approach of Chapter 5, we placed the star in the evolutionary context, as shown in Fig. 8.5, together with the other stars presented in Chap. 5 for comparison. The location of the star in the diagram, its C/O ratio and mass as predicted from the fit, seems consistent with the C-rich part of the evolutionary tracks.

The angular diameter was calculated from the empirical diameter/(V-K) relation of van Belle et al. (2013), and the corresponding temperature was derived. Those are shown in Table 8.4,

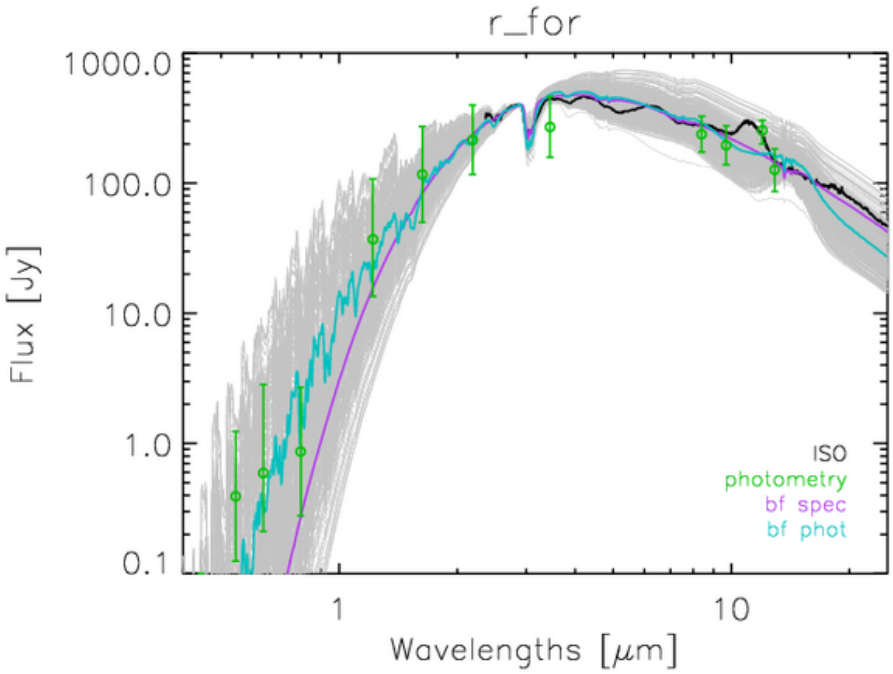

Figure 8.1: Observational spectro-photometric data of R For. The synthetic spectrum of the time-step best fitting the ISO spectrum is shown in violet. The time-step at which the synthetic photometry fits best the corresponding observational data is shown in cyan for a qualitative comparison. Photometry is plotted in green circles, while the ISO spectrum as a black line. The grey shadow represents all the time-steps spectra belonging to the best-fitting spectroscopic model.

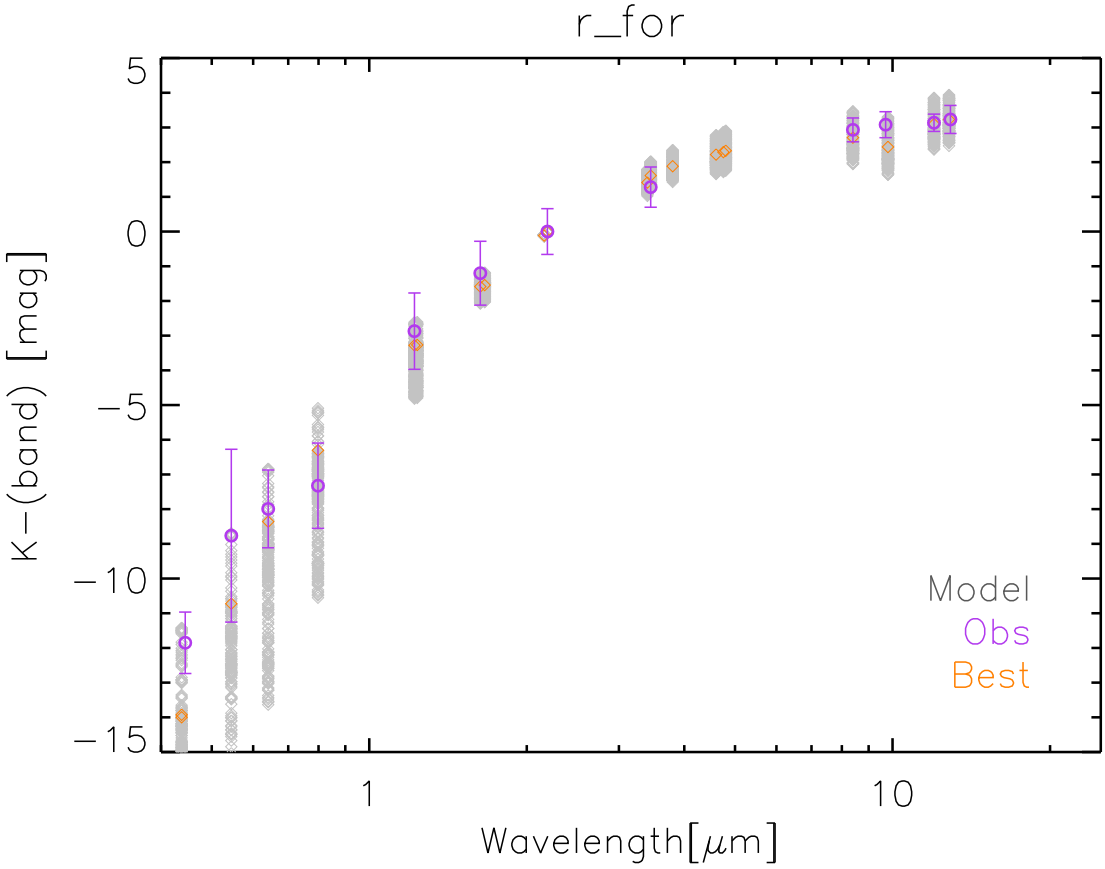

Figure 8.2: Photometric observations of the Mira star R For. Observations (violet circles), compared to the models synthetic photometry (grey diamonds). Orange diamonds show the best fitting time-step for the star.

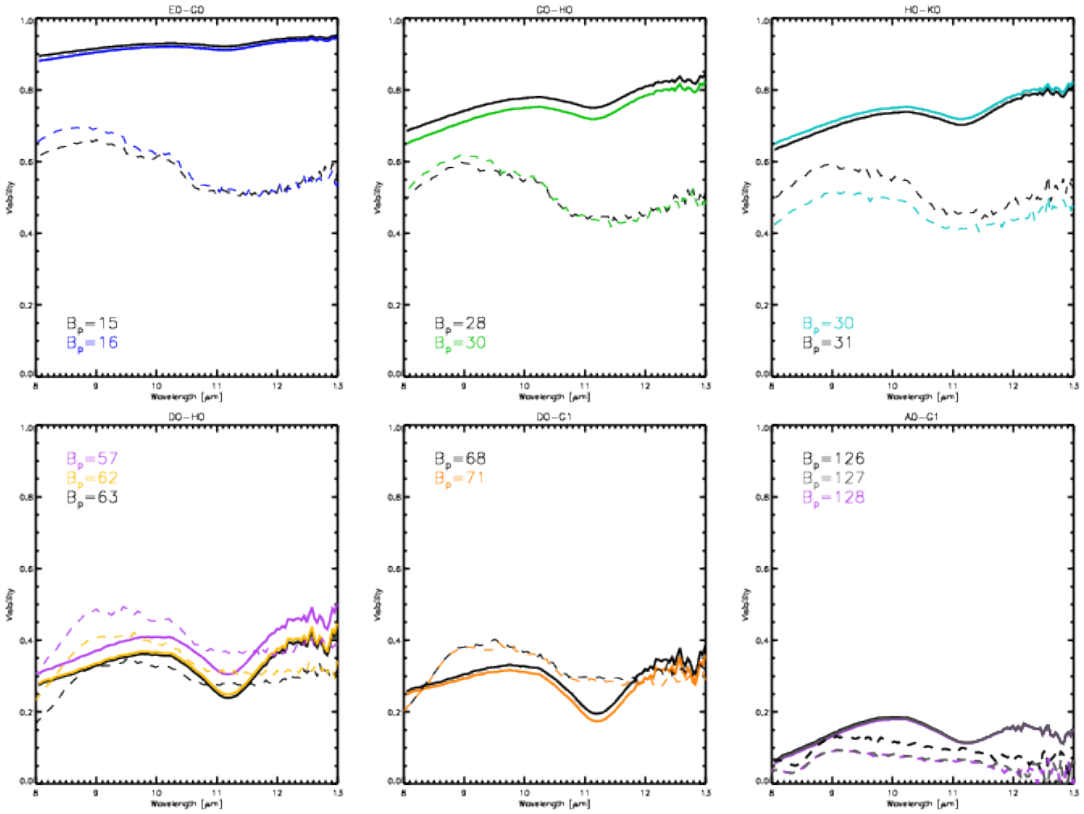

Figure 8.3: Visibility dispersed over wavelength of R For. The different panels show the various baselines. Different colors underline different projected baselines.

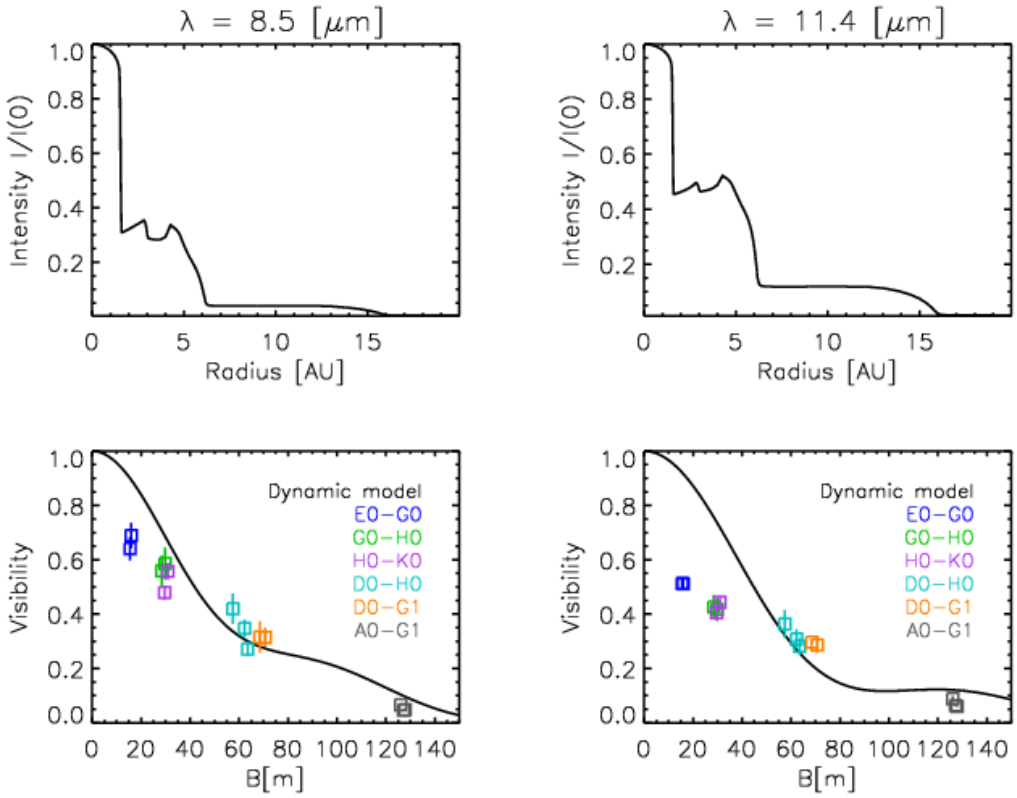

Figure 8.4: R For interferometric observational MIDI data from 2009, compared with the synthetic visibilities based on the dynamic models. **Upper**: intensity profiles at two different wavelengths: 8.5 μm and 11.4 μm. **Lower**: visibility vs. baseline; the black line shows the dynamic model, the colored symbols illustrate the MIDI measurements for different baselines.

together with literature K-band diameter and the corresponding temperature. As for the other Miras studied in this thesis, we stress the reasonable agreement, within the errors, between T_{Ross} and $T_{\theta_{(V-K)}}$. Contrary to the other Mira stars of Chap. 5, θ_{Ross} does not agree well with $\theta_{(V-K)}$, and this could be probably due to the structure of the models. The star has also available a θ_K diameter and $T_{\theta_{(K)}}$ can be derived. The values agree only roughly, without any clear systematics in the differences between the three types of parameters. This is probably related to the the non-static structure of the atmosphere, and to the nature of the K-diameter, which is not a purely photospheric diameter, but influenced by dust opacity.

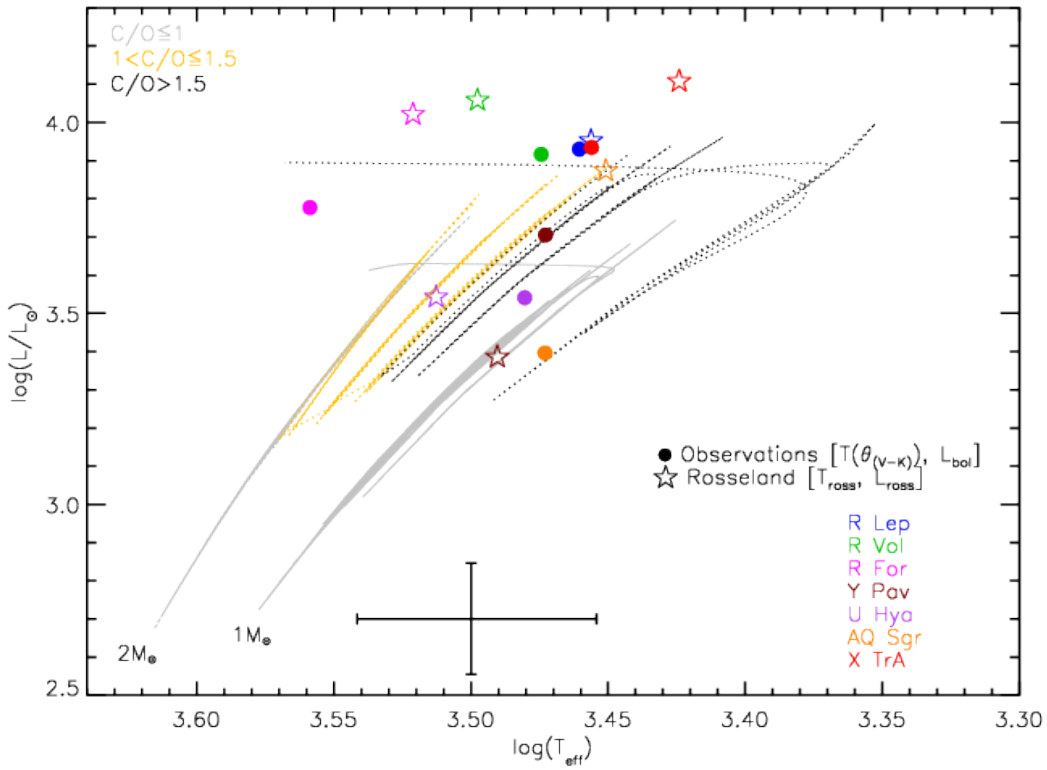

Figure 8.5: AGB region of the H-R diagram and the location of our targets, including R For. The lines display solar metallicity evolutionary tracks from Marigo et al. (2013): grey lines mark the regions of Oxygen-rich stars with C/O $<$ 1.0; yellow lines denote the region of C-rich stars with 1.0 $<$ C/O $\leqslant$ 1.5, while black lines with C/O $>$ 1.5. The numbers indicate the mass values at the beginning of the thermal pulsing (TP)-AGB. For better visibility, the track with 2 $M_\odot$ is plotted with a dotted line. Different symbols and colors refer to the luminosity and effective temperature, estimated through the comparison in this work of the the models with spectro-photometric-interferometric-observations. A typical error-size bar is shown in the lower part of the figure.

The authors would like to remind the reader that the study presented in this Chapter is

Table 8.4: Observed and calculated temperatures and diameters.

Target	$\theta_{\text{(V-K)}}$ [a] [mas]	θ_{K} [mas]	θ_{Ross} [b] [mas]	T_{Ross} [K]	$\text{T}_{\theta_{\text{(V-K)}}}$ [K]	$\text{T}_{\theta_{\text{K}}}$ [K]
R For	4.56	8.0 [c]	2.1	3320	3620 ± 440	2730

Notes. (a) Relation from van Belle et al. (2013). (b) θ_{Ross} is the Rosseland diameter of the best fitting time-step of the corresponding best-fitting model. (c) paper in prep. based on AMBER and PIONIER data; see also Paladini (2011), PhD thesis.

merely a preliminary work, to have a first overview of the behaviour of R For when compared to dynamic model atmospheres. To be consistent with the detected variability, separate fits for the different MIDI phases need to be performed. This will be presented in a forthcoming publication.

Chapter 9

Conclusions and outlook

This thesis is devoted to the investigation of C-rich AGB stars atmospheres, from an observational point of view.

Dynamic models atmospheres, as well as hydrostatic and geometric models, were used to interpret multi-technique data. Mid-infrared interferometry was used to compare models with observations, together with spectroscopic and photometric literature data. The thesis focuses on eight carbon-enriched targets, namely: RU Vir, R Lep, R Vol, Y Pav, AQ Sgr, U Hya, X TrA, and R For as a preliminary work.

This chapter summarizes the most important results obtained, and introduces perspectives for further studies.

9.1 Results

9.1.1 Fits

For all the stars mentioned above, the best agreement in the SEDs fits is found at wavelengths longer than 1 μm, and in the interferometric fits in the region $[8-10]$ μm. The models in best agreement with the observations of Semi-regular and Irregular stars were all episodic and periodic models (according to the description of Eriksson et al., 2014). In the SEDs fits some discrepancies persist at wavelengths shorter than 1 μm and beyond 10 μm for all the stars. Probably those differences are both driven by a combination of model- and data-related effects.

In the case of RU Vir (Chap. 4), we found that the agreement is lost already at wavelengths shorter than 2 μm, and this is likely due to a combination of inter- & intra-cycles effects. Also, at wavelengths longer than 10 μm and for short baselines, all the Mira stars display an increase of visibility with wavelength in the models. This shape is not observed in the data. Chap. 4 gives as possible reasons the smother density distribution than in the models, and/or a clumpy environment. In Chap. 5 the investigation on the visibility shape was carried out by performing some experiments, such as changing the opacity laws and checking the eventual influence of the

14 μm feature on the visibility. Both resulted in no significant effect for the visibility slope.

9.1.2 DMA Extension: Mira stars vs. Semi-regular and Irregular stars

Dynamic model atmospheres appear to be more extended in radius for Mira stars than for Semi-regular and Irregular stars, with a more marked shell-like structure (see Chap. 5). Conversely, the non-Miras best-fitting models appear less extended in radius, with an average lower rate of mass loss, and rather weak gas and dust shells.

9.1.3 Multi-technique observations

This thesis demonstrated how the joint use of multi-technique observations, such as photometry, spectroscopy and interferometry, is crucial to constrain better the models (see Chap. 4 and 5). To constrain the advanced dynamic model atmospheres developed by the Uppsala Group, we used VLTI/MIDI interferometric data collected by our group during several observational campaigns. Literature SEDs, spectroscopic and photometric data were collected for all the targets and compared with the models as well. In Chap. 4 we used also the MOD routine, which allowed us to perform a more flexible fit of the stellar parameters. This fit leads to similar conclusions as for the DMA.

9.1.4 Dust

C-rich AGB stars are characterized by amC dust, featureless in the SED, and SiC dust. Molecular contributions in the N-band are mainly due to C_2H_2 and HCN opacities. The SiC dust feature manifests its presence in the visibility spectra of evolved C-rich stars, with its typical drop in the level of visibility at around 11.4 μm. The same feature appears in emission in the SEDs. From the comparison presented in this study, we observed that the SiC feature is sharper and narrower in the models. In Chap. 4 the SiC shape fit improved with the MOD fit using the distribution of hollow spheres, which is not available for the DARWIN models. In the latter, the generally used 10% of SiC dust was included, and several experiments have been performed changing (increasing) this percentage. This leads to improvements in the R Lep and possibly also Y Pav fit, but both to a very small extent.

Reasonably good fits of the wavelength-dependent visibilities were found for all the targets, showing a well shaped SiC feature, but not for X TrA. Experiments of scaling the distance and enlarging the amount of SiC dust of the models did not produce any significant improvement in X TrA. This star seems undergoing a high period of mass loss, with a compact environment, and none of the dynamic models seems able to reproduce this combination of factors.

9.1.5 The geometry of the objects environment

The geometry of some targets was explored in the present work, namely RU Vir, R Vol, U Hya. For the first one, a general agreement with the size of the dynamic models in the N-band was

found. The best fit to the data resulted in a two-component model: circular UD + Gaussian distribution of the dusty envelope.

In general, angular diameters at 8 and 12 μm were derived, and Chap. 4, 5, 6 with the *uv*-coverage and visibility points available for those three targets, no major asymmetry was detected. Also, no signature of differential phase was detected for any of the objects previously mentioned.

In Chap. 5 and 6 we investigated the interferometric variability of R Lep, θ Aps, R Leo and RT Vir. For the first target, the variability is at the limit of the errors, while for the other stars no interferometric variability was detected. In R Leo a signature of differential phase is present.

9.1.6 Stellar parameters

By the comparison of the dynamic models and the geometric models with the observations, it was possible to collect stellar parameters, outlined in Table 5.3 and 5.4. To include the object in an evolutionary scenario, Chap. 5 shows a comparison of the derived stellar parameters with the evolutionary tracks from the Padova group (Marigo et al., 2013). The C/O ratio of the targets and their placement on the evolutionary tracks agrees well with the C-rich evolutionary phase of the TP-AGB track, except for Y Pav. Temperature and luminosities estimations from the models are in good agreement with the ones derived from the observations, within the error bars, but not in the case of AQ Sgr luminosity. Literature temperature values are in good agreement with our findings. The angular diameters derived from the Rosseland definition and the ones calculated from the empirical van Belle et al. (2013) diameter vs. (V-K) relation agree within each other, better for the Miras than for the non-Miras.

9.1.7 Removing the SPL approximation

The observations of R Lep were compared to the model without the SPL approximation, produced by the Uppsala group, and to the model from the Eriksson et al. (2014) grid characterized by the same parameters. Overall, Chap. 7 shows that only limited improvement was found in the non-SPL case for R Lep.

9.2 Outlook

It might be interesting to perform a similar study as in this thesis, for a sample of oxygen-rich Mira, Semi-regular and Irregular, comparing their observations with the O-rich grid from Bladh et al. (in prep.), based on the DARWIN models of Höfner et al. (2016). This would allow to investigatate the stellar atmospheres' estension in the O-rich case, and compare it to the results derived in the present thesis for the C-rich stars.

In order to check the validity of the 10 % SiC dust fraction, and of the simultaneous condensation of amC and SiC dust, tests will be performed as soon as the consistent implementation of SiC in the DARWIN models is available.

It would be straight forward to enlarge the sample of stars to be placed in the evolutionary scenario. E.g. taking the targets listed in van Belle et al. (2013) and locate them in the H-R diagram. It would also be interesting to compare, in the evolutionary context, O-rich objects with C-rich ones. Also, observations of our C-rich objects in H and K (with AMBER, PIONIER, GRAVITY) will help in resolving the small-scale, and pulsation-related physics.

An extensive comparison with the whole grid of non-SPL models by the Uppsala group (Eriksson et al., in prep.), will be a natural continuation of this study. In fact, the exploration of a larger parameter space may facilitate the research for a better agreement with the data. In this way the discrepancies denoted in Sect. 9.1.1 that still remain in the comparison between models and observations, might be settled.

To improve the current constraints on the models, additional spectro-interferometric observations could be performed with VLTI instruments such as PIONIER and GRAVITY, or with millimeter/sub-millimeter instruments such as ALMA.

MATISSE will be the next second generation instrument at VLTI, with its first observation starting supposedly in 2019. Allowing imaging in the L-, M- and N- band, MATISSE will be an excellent tool for a better reconstruction of the targets' intensity profiles, the detection of any (a)symmetries and for the variability study of those stars.

Appendix A

Appendix

A.1 Appendix of Paper I

A.1.1 On the intra/inter-cycle variations

As already mentioned, the synthetic visibilities were produced for all the time-steps, i.e. phases, of the best-fitting spectroscopic model. In general, each model of the grid contains different "epochs", and each of them several "cycles"[1] of the stellar pulsation. RU Vir best fitting model holds 2 epochs, with respectively 6 and 11 cycles.

For the epoch to which RU Vir's best-fitting interferometric time-step belongs, Fig. A.1 shows the visibility curves dispersed in wavelength. The visibilities spectra are plotted for the first and last cycle, at the four baselines $B_p = 40.0$, $B_p = 47.9$, $B_p = 60.6$ and $B_p = 69.4$ that best sample the available MIDI observational baseline range. Both inter- and intra-cycle variations are detectable in Fig. A.1, and this supports the idea that the discrepancies in the interferometric fit are due to those variations.

The χ^2 of the best-fitting visibility time-step is 12.7. Its baseline is $B_p = 67.6$ and phase $\phi = 0.25$, which does not lie in the phase range of MIDI observations (see Table A.2 and A.1).

[1] We refer to "cycle" to denote a complete variation of the phase from one maximum to the subsequent one.

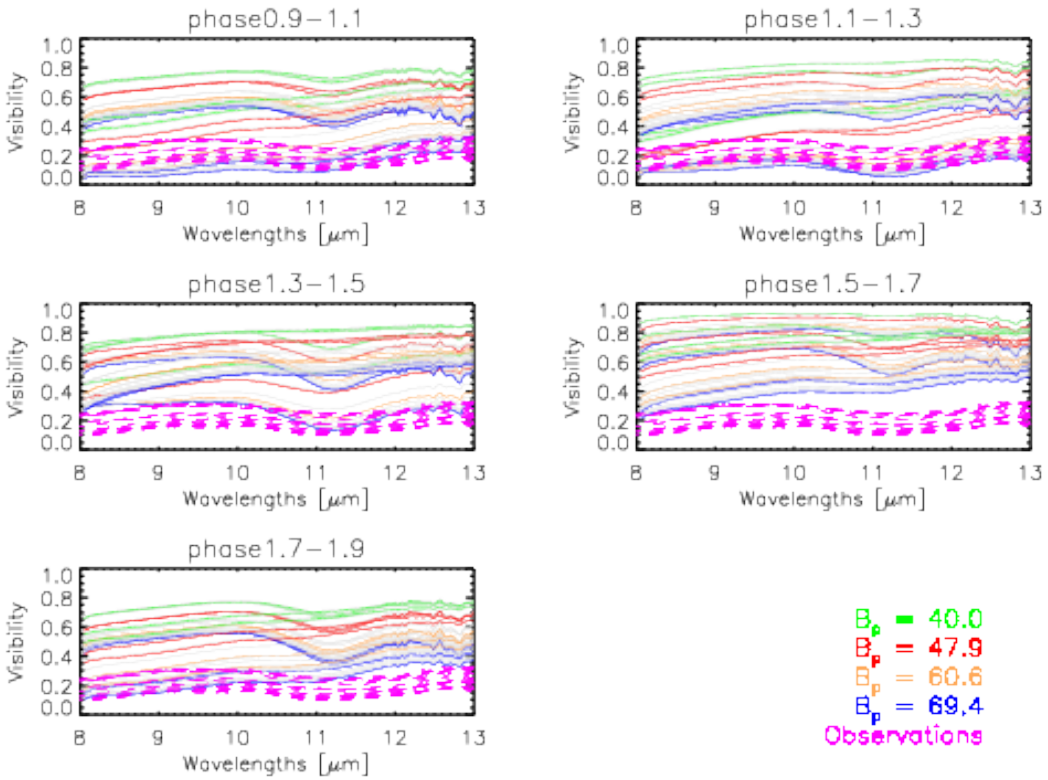

Figure A.1: Synthetic visibilities dispersed in wavelength (in colored lines at different projected baselines) compared to the MIDI observations (in violet). The model visibilities belong to the epoch of the best-fitting interferometric time-step. The different panels depict several pulsational phases, grouped by step of 0.2 in phase.

A.1.2 Journal of observations

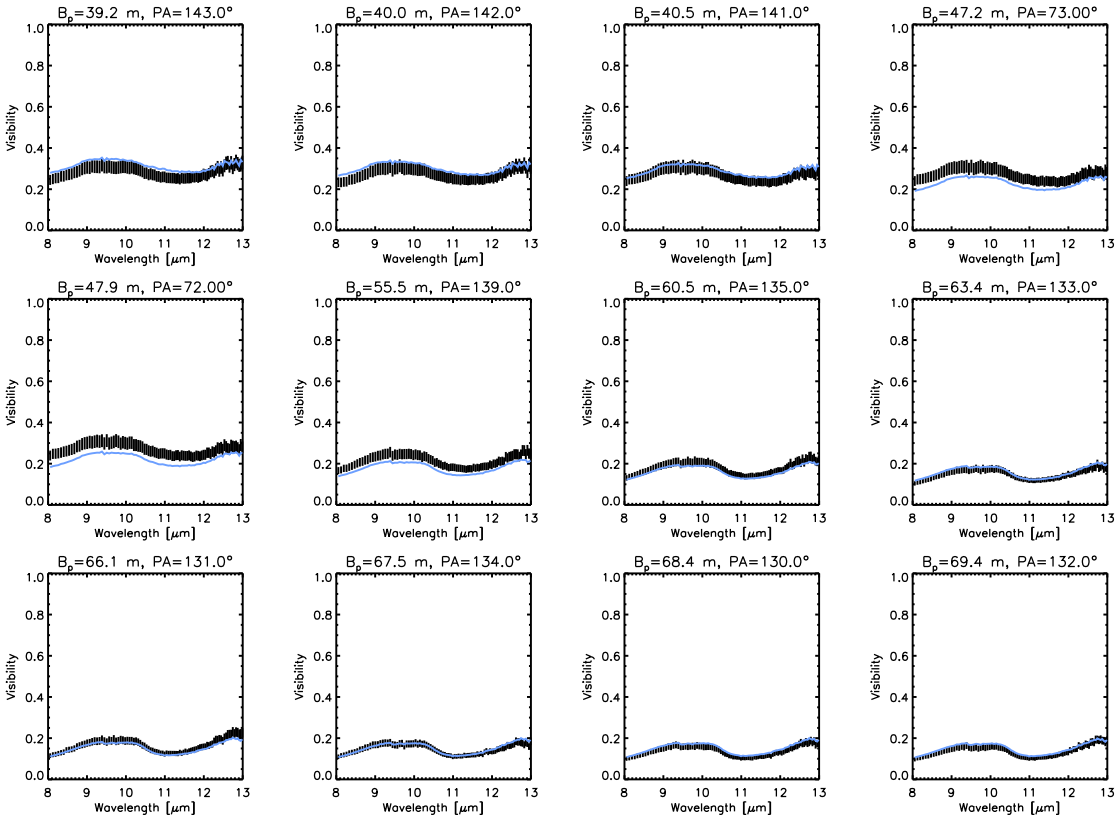

Figure A.2: Comparison of the observational MIDI data with the best-fitting geometrical model (See Table 4.3). Shown are visibilities vs. wavelength at different position angles and baseline lengths (See Fig. 4.3 for the complete set of visibilities). Black lines represent the MIDI observations of RU Vir. Light blue lines represent the fit of the best-fitting UD+Gaussian model.

Table A.1: Journal of the MIDI observations of RU Vir (observations made in 2014 under program number ID: 093.D-0708(A), PI Rau.

RU Vir	2014-04-11 T00:48:17	D0-G1	67.6	134	0.96	1.52	HIGH-SENS	0.37
HD 120323	2014-04-11 T01:03:12	...	45.3	112	0.79	1.70	...	...
...	2014-04-11 T01:28:11	...	49.7	113	0.96	1.52	...	...
RU Vir	2014-04-11 T01:15:18	...	69.4	132	1.00	1.59	...	0.37
HD 120323	2014-04-11 T01:03:12	...	45.3	112	0.79	1.70	...	...
...	2014-04-11 T01:28:11	...	49.7	113	0.96	1.52	...	...
RU Vir	2014-04-11 T02:11:25	H0-I1	40.5	141	1.02	1.32	...	0.37
HD 120323	2014-04-11 T02:25:17	...	35.2	134	0.95	1.26	...	...
HD 81797	2014-04-11 T02:55:16	...	36.5	163	1.03	1.21	...	...
...	2014-04-11 T03:20:45	...	36.0	168	1.13	1.30	...	...
RU Vir	2014-04-11 T02:38:08	H0-I1	40.0	142	0.98	1.24	...	0.37
HD 120323	2014-04-11 T01:58:26	...	33.7	133	0.80	1.36	...	...
...	2014-04-11 T02:25:17	...	35.2	134	0.95	1.26	...	...
HD 81797	2014-04-11 T02:55:16	...	36.5	163	1.03	1.21	...	...
...	2014-04-11 T03:20:45	...	36.0	168	1.13	1.30	...	...
RU Vir	2014-04-11 T03:07:40	H0-I1	39.3	143	1.05	1.18	...	0.37
HD 120323	2014-04-11 T02:25:17	...	35.2	134	0.95	1.26	...	...
HD 81797	2014-04-11 T02:55:16	...	36.5	163	1.03	1.21	...	...
...	2014-04-11 T03:20:45	...	36.0	168	1.13	1.30	...	...
RU Vir	2014-04-11 T03:58:15	D0-G1	68.4	130	1.18	1.14	...	0.37
HD 120323	2014-04-11 T03:45:37	...	66.7	124	1.32	1.07	...	...
...	2014-04-11 T04:11:45	...	68.5	127	1.20	1.04	...	...
...	2014-04-11 T04:39:44	...	69.9	130	1.38	1.02	...	...
...	2014-04-11 T05:47:28	...	71.5	138	1.12	1.03	...	...
RU Vir	2014-04-11 T04:25:14	D0-G1	66.2	131	1.28	1.14	...	0.37
HD 120323	2014-04-11 T03:45:37	...	66.7	124	1.32	1.07	...	...
...	2014-04-11 T04:11:45	...	68.5	127	1.20	1.04	...	...
...	2014-04-11 T04:39:44	...	69.9	130	1.38	1.02	...	...
...	2014-04-11 T05:47:28	...	71.5	138	1.12	1.03	...	...
RU Vir	2014-04-11 T04:53:53	D0-G1	63.4	133	1.26	1.16	...	0.37
HD 120323	2014-04-11 T03:45:37	...	66.7	124	1.32	1.07	...	...
...	2014-04-11 T04:11:45	...	68.5	127	1.20	1.04	...	...
...	2014-04-11 T04:39:44	...	69.9	130	1.38	1.02	...	...
...	2014-04-11 T05:47:28	...	71.5	138	1.12	1.03	...	...
RU Vir	2014-04-11 T05:19:21	D0-G1	60.6	135	1.10	1.20	...	0.37
HD 120323	2014-04-11 T04:11:45	...	68.5	127	1.20	1.04	...	...
...	2014-04-11 T05:47:28	...	71.5	138	1.12	1.03	...	...
RU Vir	2014-04-11 T05:59:56	D0-G1	55.6	139	1.09	1.30	...	0.37
HD 120323	2014-04-11 T04:11:45	...	68.5	127	1.20	1.04	...	...
...	2014-04-11 T05:47:28	...	71.5	138	1.12	1.03	...	...

!hbtp

Table A.2: Journal of the MIDI observations of RU Vir (archive observations).

Target	UT date & time	Config.	B_p [m]	PA [°]	Seeing ["]	Airmass	Mode	ϕ
RU Vir	2010-05-23 T01:23:12	H0-E0	47.2	73	1.14	1.52	SCI-PHOT	0.11
HD 120323	2010-05-23 T00:32:16	...	45.6	53	1.14	1.12	...	...
HD 81797	2010-05-23 T23:05:53	...	47.4	73	0.99	1.06	...	...
...	2010-05-23 T00:00:32	...	44.6	74	0.70	1.18	...	...
HD 133216	2010-05-23 T02:18:36	...	65.0	98	1.14	1.05	...	...
RU Vir	2010-06-04 T01:30:24	H0-E0	47.9	72	1.45	1.17	...	0.14
HD 120323	2010-06-04 T02:06:52	...	43.8	45	1.43	1.21	...	...
...	2010-06-04 T00:50:11	...	47.6	63	1.41	1.03	...	...
...	2010-06-04 T03:03:39	...	45.2	82	1.20	1.07	...	...
...	2010-06-04 T01:12:54	...	47.9	67	1.63	1.02	...	...
...	2010-06-04 T01:50:48	...	47.8	72	1.53	1.02	...	...
HD 133216	2010-06-04 T03:46:05	...	47.0	68	1.43	1.17	...	...

A.2 Appendix of Paper II: observing log, intensity profiles, visibilities vs. baselines

Table A.3: Journal of the MIDI observations of R Vol.

Target	UT date & time	Config.	B_p [m]	PA [°]	Seeing ["]	Airmass	Mode
R Vol	2012-10-05 T08:42:06	G1-A1	74.2	-37	0.58	1.59	SCI-PHOT
HD 32887	2012-10-05 T08:11:05	...	79.2	-106	0.49	1.01	...
HD 82668	2012-10-05 T08:28:26	...	127.4	-85	0.66	1.94	...
R Vol	2013-01-18 T02:09:01	A1-K0	126.0	-32	0.58	1.57	SCI-PHOT
HD 82668	2013-01-18 T01:54:03	...	40.7	-134	0.49	1.81	...

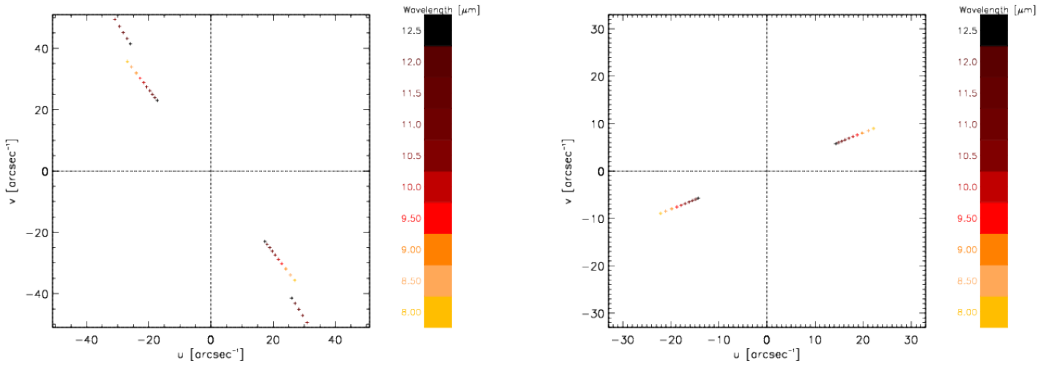

Figure A.3: *uv*-coverage of the MIDI observations of R Vol (left side) and U Hya (right side) listed in Table A.3 and A.4, dispersed in wavelengths.

Table A.4: Journal of the MIDI observations of U Hya.

Target	UT date & time	Config.	B_p [m]	PA [°]	Seeing ["]	Airmass	Mode
U Hya	2011-03-11 T01:24:49	H0-I1	39.70	-112.6	0.85	1.29	SCI-PHOT
HD 81797	2011-03-11 T01:09:56.015	...	40.76	-125.6	0.85	1.42	...
HD 81797	2011-03-11 T01:41:04	...	40.70	-134.2	0.82	1.43	...

Table A.5: Photometric data adopted from the literature. Different filters and different sources are given in units of mag. The consideration of the errors is described in Sect. 5.2.2.

Star	B	V	R	I	J	H	K	L	L'	M	$N1$	$N2$	$N3$	$IRAS12$
	[mag]	[mag]	[mag]	[mag]	[mag]	[mag]	[mag]	[mag]	[mag]	[mag]	[mag]	[mag]	[mag]	[mag]
R Lep	11.71	8.08	5.84	4.58	2.58	1.17	0.14	...	-1.09	-1.26	-2.36	-2.59	-3.01	-2.33
R Vol	14.18	10.68	8.46	6.93	5.08	3.14	1.71	...	0.08	-0.61	...	...	...	-1.70
Y Pav	9.48	6.28	4.67	3.68	1.76	0.77 [a]	0.35	-0.17	...	0.28	...	...	...	-0.56
AQ Sgr	10.40	7.64	5.67	4.43	2.45 [a]	1.31 [a]	0.76 [a]	0.39	...	0.59	...	...	...	-0.29
U Hya	8.00	5.03	3.25	2.79	0.89	-0.25 [a]	-0.59	-0.91	...	-0.45	...	...	...	-1.69
X TrA	9.22	5.71	4.59	5.51	1.09	-0.01 [a]	-0.59	-0.95	...	-0.45	...	...	...	-1.67

Notes. (a): $2MASS$ photometry.

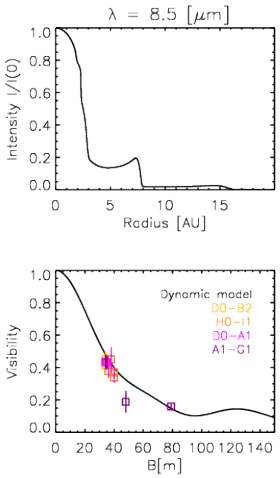

Figure A.4: R Lep

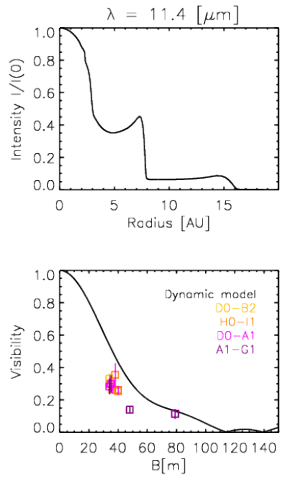

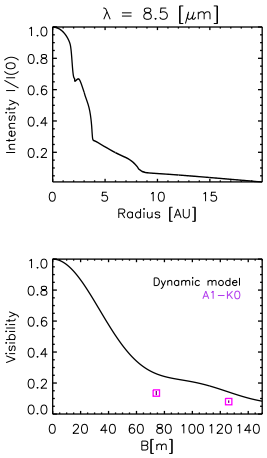

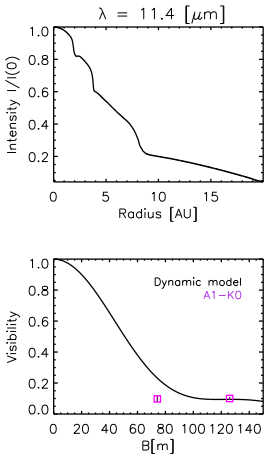

Figure A.5: R Vol

Figure A.6: Interferometric observational MIDI data of the Mira stars of our sample, **R Lep** (upper left), **R Vol** (upper right), compared with the synthetic visibilities based on the DARWIN models. **Up**: intensity profile at two different wavelengths: 8.5 μm and 11.4 μm. **Down**: visibility vs. baseline; the black line shows the dynamic model, the colored symbols illustrate the MIDI measurements at different baseline configurations.

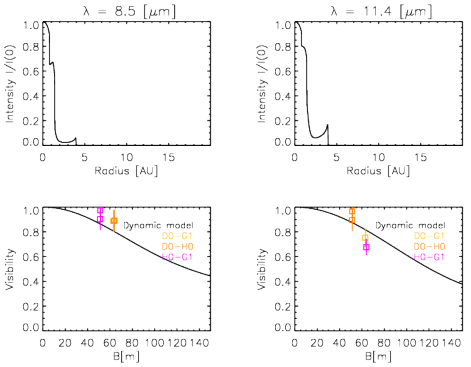

Figure A.7: Y Pav

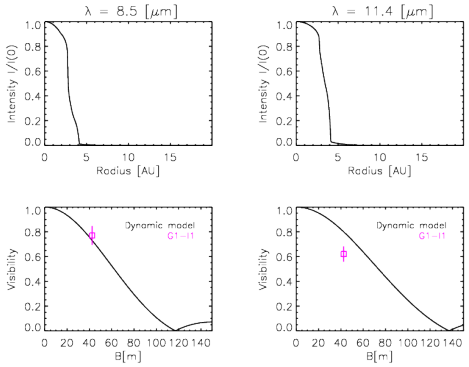

Figure A.8: AQ Sgr

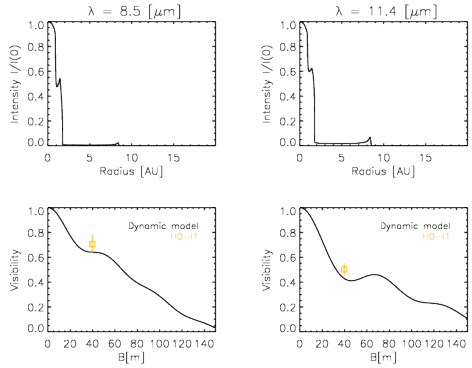

Figure A.9: U Hya

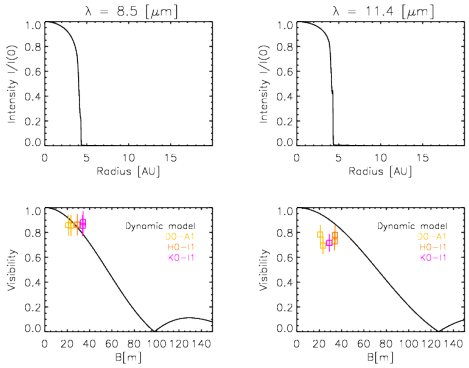

Figure A.10: X TrA

Figure A.11: Interferometric observational MIDI data of the semi-regular and irregular stars of our sample, **Y Pav** (upper left), **AQ Sgr** (upper right), **U Hya** (lower left) and **X TrA** (lower right), compared with the synthetic visibilities based on the DARWIN models. **Upper panels for each star:**: intensity profile at two different wavelengths: 8.5 μm and 11.4 μm. **Lower panels for each star**: visibility vs. baseline; the black line shows the dynamic model, the colored symbols illustrate the MIDI measurements at different baseline configurations.

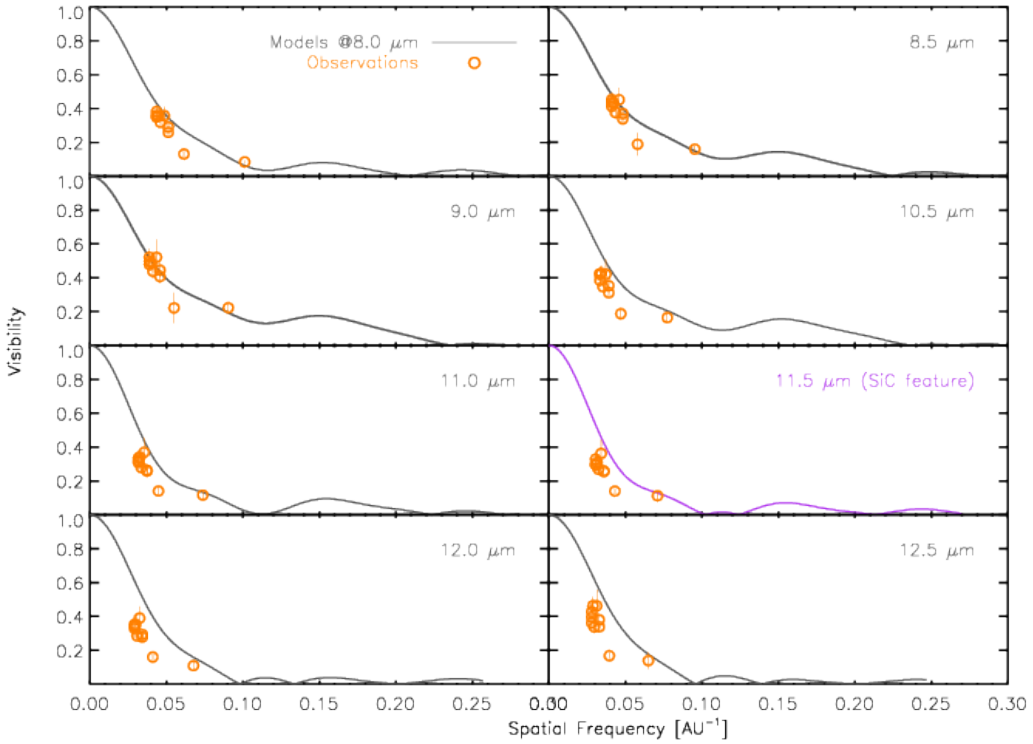

Figure A.12: Visibilities vs. spatial frequencies, at different selected wavelengths in the MIDI range. Observations of R Lep are in orange, models in grey. If the wavelength range is the one in which SiC dust dominates, models are in violet.

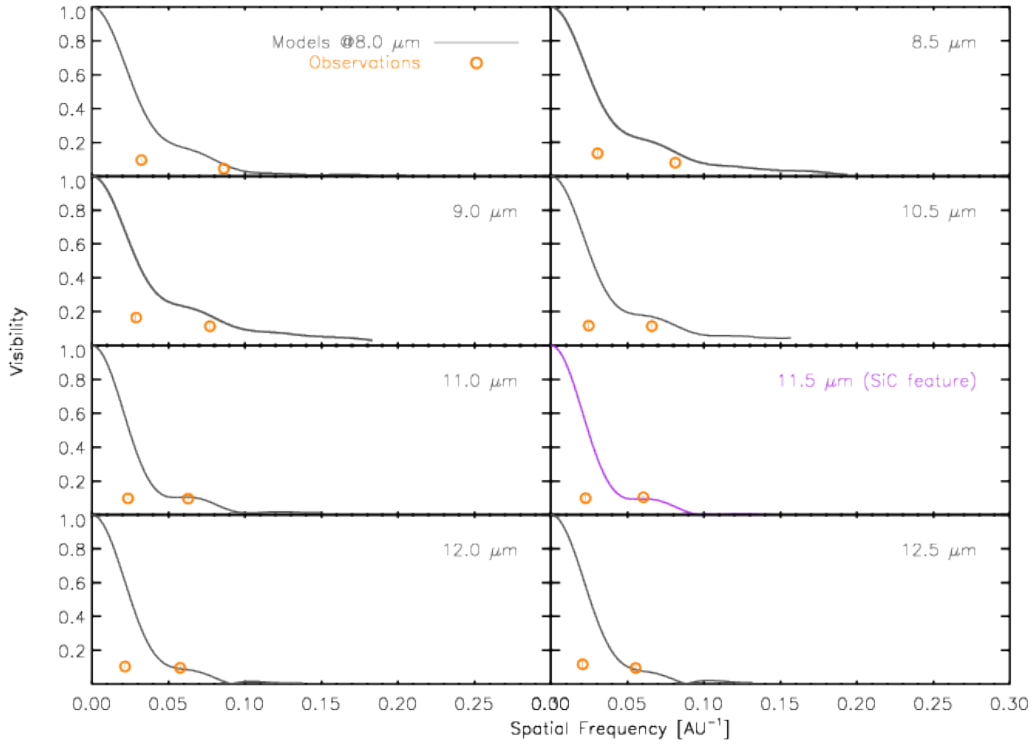

Figure A.13: Visibilities vs. spatial frequencies, at different selected wavelength in the MIDI range. Observations of R Vol are in orange, models in grey. If the wavelength range is the one in which SiC dust dominates, models are in violet.

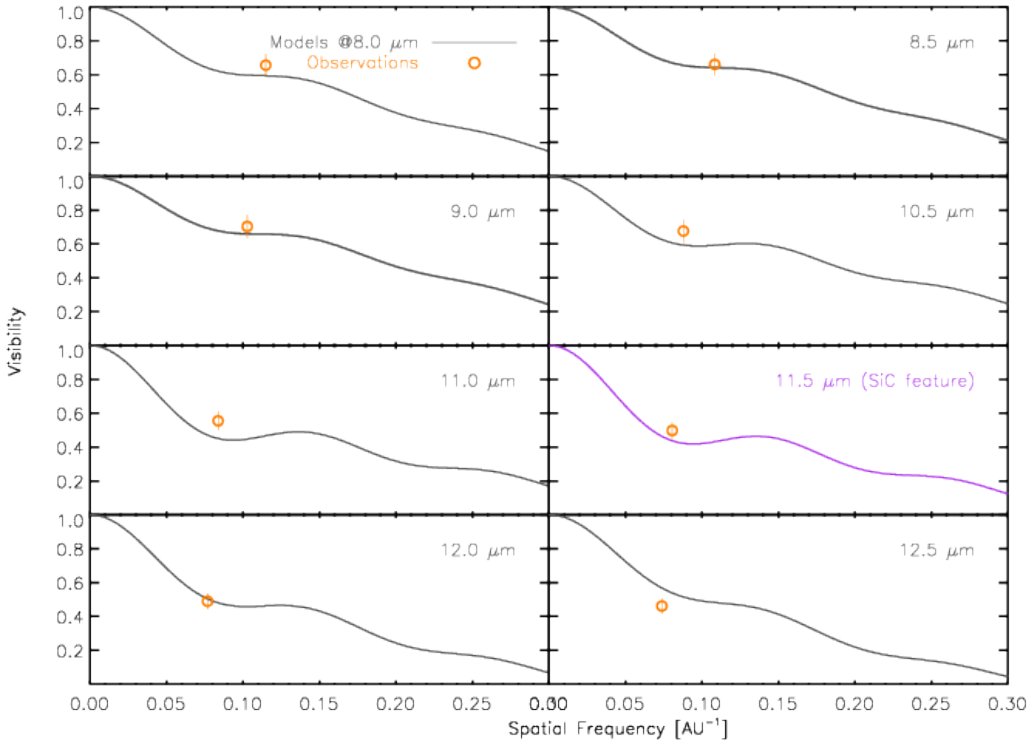

Figure A.14: Visibilities vs. spatial frequencies, at different selected wavelengths in the MIDI range. Observations of U Hya are in orange, models in grey. If the wavelength range is the one in which SiC dust dominates, models are in violet.

Table A.6: Journal of the MIDI Auxiliary Telescopes observations of θ Aps.

Target	UT date & time	ϕ_V	Config.	B_p [m]	PA [°]	Seeing ["]	Airmass	Mode
LP data								
θ Aps	2011-06-11 00:28	9.27	A1-B2	10.4	92	1.01	1.651	SCIPHOT/PRISM
HD167618	2011-06-11 06:24	...	...	...	...	0.69	1.036	SCIPHOT/PRISM
HD167618	2011-06-11 08:20	...	...	...	...	0.63	1.101	SCIPHOT/PRISM
θ Aps	2011-06-11 01:21	9.27	A1-C1	15.5	76	1.66	1.630	SCIPHOT/PRISM
HD167618	2011-06-11 07:23	...	...	...	...	0.67	1.231	SCIPHOT/PRISM
HD206778	2011-06-11 07:54	...	...	...	...	0.64	1.286	SCIPHOT/PRISM
HD167618	2011-06-11 09:14	...	...	...	...	0.46	1.453	SCIPHOT/PRISM
θ Aps	2011-06-12 05:34	9.28	D0-C1	12.2	92	1.01	1.981	SCIPHOT/PRISM
HD150798	2011-06-12 05:18	...	...	...	...	1.01	1.428	SCIPHOT/PRISM
HD152786	2011-06-12 05:48	...	...	...	...	1.02	1.225	SCIPHOT/PRISM
θ Aps	2011-06-22 01:37	9.36	D0-C1	15.4	49	1.87	1.643	SCIPHOT/PRISM
HD150798	2011-06-22 01:19	...	...	...	...	1.46	1.510	SCIPHOT/PRISM
θ Aps$^{\mathrm{F}}$	2012-01-25 08:43	11.18	C1-A1	15.8	52	1.23	1.693	SCIPHOT/PRISM
HD81797	2012-01-25 05:57	...	...	...	...	0.71	1.040	SCIPHOT/PRISM
HD81797	2012-01-25 06:38	...	...	...	...	0.69	1.057	SCIPHOT/PRISM
HD81797	2012-01-25 07:01	...	...	...	...	0.67	1.083	SCIPHOT/PRISM
HD81797	2012-01-25 07:33	...	...	...	...	1.14	1.138	SCIPHOT/PRISM
HD150798	2012-01-25 08:11	...	...	...	...	0.91	2.138	SCIPHOT/PRISM
HD152786	2012-01-25 09:03	...	...	...	...	1.80	1.795	SCIPHOT/PRISM
θ Aps$^{\mathrm{F}}$	2012-01-26 08:41	11.19	D0-C1	16.7	17	1.87	1.691	SCIPHOT/PRISM
HD150798	2012-01-26 08:21	...	...	...	...	1.56	2.055	SCIPHOT/PRISM
θ Aps	2012-01-28 08:56	11.21	B2-A1	10.2	86	0.73	1.668	SCIPHOT/PRISM

A.3 Appendix of Paper III: journal of observations

Where calibrated fluxes are available, points are marked with 'F'. 'AM' gives the airmass at the time of observation. Calibrators used to calibrate the visibilities are given below the science observation. If no calibrator is listed, the science point was not used in the astrophysical interpretation.

Table A.7: Journal of the MIDI Auxiliary Telescopes observations of R Crt.

Target	UT date & time	ϕ_V	Config.	B_p [m]	PA [°]	Seeing ["]	Airmass	Mode
LP data								
R Crt[F]	2012-01-24 04:57	6.66	C1-A1	13.1	52	1.60	1.242	SCIPHOT/PRISM
HD81797	2012-01-24 05:16	...	...	...	...	1.08	1.057	SCIPHOT/PRISM
HD123139	2012-01-24 07:53	...	...	...	...	1.16	1.252	SCIPHOT/PRISM
HD112142	2012-01-24 08:25	...	...	...	...	0.81	1.069	SCIPHOT/PRISM
HD123139	2012-01-24 08:59	...	...	...	...	1.05	1.097	SCIPHOT/PRISM
R Crt[F]	2012-01-25 06:18	6.66	C1-A1	15.3	64	0.73	1.047	SCIPHOT/PRISM
HD81797	2012-01-25 05:57	...	...	...	...	0.71	1.040	SCIPHOT/PRISM
HD81797	2012-01-25 06:38	...	...	...	...	0.69	1.057	SCIPHOT/PRISM
HD81797	2012-01-25 07:01	...	...	...	...	0.67	1.083	SCIPHOT/PRISM
HD81797	2012-01-25 07:33	...	...	...	...	1.14	1.138	SCIPHOT/PRISM
HD150798	2012-01-25 08:11	...	...	...	...	0.91	2.138	SCIPHOT/PRISM
HD152786	2012-01-25 09:03	...	...	...	...	1.80	1.795	SCIPHOT/PRISM
R Crt[F]	2012-02-01 05:05	6.71	B2-A1	10.4	108	1.06	1.126	SCIPHOT/PRISM
HD81797	2012-02-01 04:44	...	...	...	...	0.96	1.057	SCIPHOT/PRISM
HD81797	2012-02-01 07:43	...	...	...	...	1.24	1.238	SCIPHOT/PRISM
HD81797	2012-02-01 08:15	...	...	...	...	1.25	1.366	SCIPHOT/PRISM
R Crt	2012-02-01 06:43	6.71	C1-B2	11.2	24	1.28	1.009	SCIPHOT/PRISM
R Crt	2012-02-01 08:00	6.71	B2-A1	10.9	122	1.38	1.037	SCIPHOT/PRISM
R Crt[F]	2012-02-12 05:47	6.78	C1-A1	15.8	68	0.86	1.014	SCIPHOT/PRISM
HD81797	2012-02-12 04:36	...	...	...	...	0.88	1.041	SCIPHOT/PRISM
HD81797	2012-02-12 05:11	...	...	...	...	1.13	1.047	SCIPHOT/PRISM
HD81797	2012-02-12 05:27	...	...	...	...	0.99	1.058	SCIPHOT/PRISM
HD81797	2012-02-12 06:05	...	...	...	...	0.80	1.104	SCIPHOT/PRISM
R Crt[F]	2012-05-01 00:26	7.27	C1-B2	11.2	22	1.59	1.017	SCIPHOT/PRISM
HD81797	2012-05-01 00:04	...	...	...	...	1.05	1.048	SCIPHOT/PRISM
HD81797	2012-05-01 00:46	...	...	...	...	1.29	1.091	SCIPHOT/PRISM
Archive								
R Crt[F]	2009-03-17 04:30	0.14	H0-D0	63.9	73	0.78	1.010	SCIPHOT/GRISM
HD81797	2009-03-17 04:05	...	...	...	...	1.07	1.130	SCIPHOT/GRISM
R Crt[F]	2009-03-18 03:17	0.14	H0-D0	62.5	67	1.09	1.020	SCIPHOT/GRISM
HD81797	2009-03-18 03:31	...	...	...	...	0.85	1.080	SCIPHOT/GRISM
HD120323	2009-03-18 05:23	...	...	...	...	1.46	1.070	SCIPHOT/GRISM
R Crt	2011-02-08 05:54	4.47	D0-A0	125.9	68	0.85	1.020	SCIPHOT/GRISM
R Crt	2011-02-08 06:06	4.47	K0-A0	126.8	69	0.78	1.010	SCIPHOT/GRISM
R Crt[F]	2011-03-08 02:28	4.64	H0-G0	27.4	56	1.33	1.190	SCIPHOT/GRISM
HD81797	2011-03-08 01:56	...	...	...	...	1.23	1.090	SCIPHOT/GRISM
HD81797	2011-03-08 02:44	...	...	...	...	1.14	1.040	SCIPHOT/GRISM

Table A.8: Journal of the MIDI Auxiliary Telescopes observations of R Leo.

Target	UT date & time	ϕ_V	Config.	B_p [m]	PA [°]	Seeing ["]	Airmass	Mode
LP data								
R Leo	2012-01-24 06:18	7.78	C1-A1	15.7	75	0.77	1.235	SCIPHOT/PRISM
R Leo[F]	2012-01-25 07:18	7.78	C1-A1	16.0	72	0.75	1.289	SCIPHOT/PRISM
HD81797	2012-01-25 05:57	...	...	...	...	0.71	1.040	SCIPHOT/PRISM
HD81797	2012-01-25 06:38	...	...	...	...	0.69	1.057	SCIPHOT/PRISM
HD81797	2012-01-25 07:01	...	...	...	...	0.67	1.083	SCIPHOT/PRISM
HD81797	2012-01-25 07:33	...	...	...	...	1.14	1.138	SCIPHOT/PRISM
HD150798	2012-01-25 08:11	...	...	...	...	0.91	2.138	SCIPHOT/PRISM
HD152786	2012-01-25 09:03	...	...	...	...	1.80	1.795	SCIPHOT/PRISM
R Leo	2012-01-28 03:32	7.79	B2-A1	10.7	120	0.91	1.605	SCIPHOT/PRISM
R Leo	2012-01-28 04:39	7.79	C1-B2	8.5	21	0.89	1.333	SCIPHOT/PRISM
R Leo[F]	2012-01-28 05:55	7.79	B2-A1	11.0	112	1.08	1.236	SCIPHOT/PRISM
HD81797	2012-01-28 03:11	...	...	...	...	0.79	1.297	SCIPHOT/PRISM
HD81797	2012-01-28 03:51	...	...	...	...	0.99	1.169	SCIPHOT/PRISM
HD81797	2012-01-28 05:35	...	...	...	...	1.32	1.041	SCIPHOT/PRISM
HD152786	2012-01-28 09:26	...	...	...	...	0.90	1.605	SCIPHOT/PRISM
R Leo[F]	2012-01-28 07:27	7.79	C1-B2	10.6	36	1.08	1.341	SCIPHOT/PRISM
HD81797	2012-01-28 04:20	...	...	...	...	1.10	1.107	SCIPHOT/PRISM
HD81797	2012-01-28 04:59	...	...	...	...	1.12	1.059	SCIPHOT/PRISM
HD81797	2012-01-28 07:10	...	...	...	...	0.94	1.115	SCIPHOT/PRISM
HD81797	2012-01-28 07:48	...	...	...	...	0.89	1.203	SCIPHOT/PRISM
R Leo[F]	2012-02-12 04:55	7.83	C1-A1	15.6	75	0.86	1.237	SCIPHOT/PRISM
HD81797	2012-02-12 04:36	...	...	...	...	0.88	1.041	SCIPHOT/PRISM
HD81797	2012-02-12 05:11	...	...	...	...	1.13	1.047	SCIPHOT/PRISM
HD81797	2012-02-12 05:27	...	...	...	...	0.99	1.058	SCIPHOT/PRISM
HD81797	2012-02-12 06:05	...	...	...	...	0.80	1.104	SCIPHOT/PRISM
R Leo	2012-02-12 07:34	7.83	C1-A1	14.7	65	0.97	1.601	SCIPHOT/PRISM

Table A.9: Journal of the archive MIDI Auxiliary Telescopes observations of R Leo.

Target	UT date & time	ϕ_V	Config.	B_p [m]	PA [°]	Seeing ["]	Airmass	Mode
Archive								
R Leo	2006-01-02 07:18	0.63	G0-H0	30.6	75	0.94	1.244	HIGHSENS/PRISM
R Leo^{F}	2006-02-25 03:16	0.81	D0-G0	29.2	76	0.70	1.271	HIGHSENS/PRISM
HD48915	2006-02-25 02:48	...	...	...	...	0.90	1.106	HIGHSENS/PRISM
R Leo^{F}	2006-02-25 04:38	0.81	D0-G0	31.9	73	0.57	1.248	HIGHSENS/PRISM
HD48915	2006-02-25 02:48	...	...	...	...	0.90	1.106	HIGHSENS/PRISM
R Leo^{F}	2006-03-03 05:29	0.83	A0-G0	62.2	69	1.06	1.395	HIGHSENS/PRISM
HD25025	2006-03-03 01:23	...	...	...	...	0.68	1.554	HIGHSENS/PRISM
HD25025	2006-03-03 02:10	...	...	...	...	1.99	2.034	HIGHSENS/PRISM
HD61421	2006-03-03 04:14	...	...	...	...	0.86	1.507	HIGHSENS/PRISM
HD123139	2006-03-03 07:22	...	...	...	...	0.76	1.035	HIGHSENS/PRISM
R Leo	2006-03-04 05:55	0.83	A0-G0	60.2	67	0.54	1.514	HIGHSENS/PRISM
HD61421	2006-03-04 01:10	...	...	...	...	0.65	1.159	HIGHSENS/PRISM
HD123139	2006-03-04 06:57	...	...	...	...	0.57	1.050	HIGHSENS/PRISM
R Leo	2006-04-20 02:17	0.98	D0-G0	31.3	69	0.69	1.38	SCIPHOT/PRISM
R Leo	2006-04-22 00:05	0.99	D0-G0	30.6	75	1.35	1.242	SCIPHOT/PRISM
R Leo^{F}	2006-04-23 03:14	1.0	E0-G0	14.1	63	0.86	1.667	SCIPHOT/PRISM
αHya	2006-04-23 03:38	...	...	...	...	...	1.649	SCIPHOT/PRISM
R Leo^{F}	2006-04-24 23:17	1.0	E0-G0	14.4	76	0.87	1.283	SCIPHOT/PRISM
αHya	2006-04-24 23:40	...	...	...	...	0.98	1.043	SCIPHOT/PRISM
αHya	2006-04-24 00:39	...	...	...	...	0.73	1.055	SCIPHOT/PRISM
2Cen	2006-04-24 01:49	...	...	...	...	0.60	1.207	SCIPHOT/PRISM
2Cen	2006-04-24 02:35	...	...	...	...	0.77	1.103	SCIPHOT/PRISM
epsPeg	2006-04-24 09:26	...	...	...	...	1.18	1.682	SCIPHOT/PRISM
R Leo	2006-05-25 23:59	1.1	A0-G0	62.5	69	0.74	1.384	SCIPHOT/PRISM
R Leo	2006-11-11 08:27	1.64	H0-D0	41.7	77	0.77	1.681	SCIPHOT/PRISM
αHya	2006-11-11 08:53	...	...	...	...	1.02	1.172	SCIPHOT/PRISM
R Leo^{F}	2006-11-12 08:25	1.65	H0-D0	42	77	0.71	1.651	SCIPHOT/PRISM
αHya	2006-11-12 09:03	...	...	...	...	0.70	1.138	SCIPHOT/PRISM
R Leo^{F}	2006-12-15 07:27	1.75	E0-G0	13.6	77	0.78	1.338	SCIPHOT/PRISM
αHya	2006-12-15 07:46	...	...	...	...	0.64	1.061	SCIPHOT/PRISM

Table A.10: Journal of R Leo continued.

Target	UT date & time	ϕ	Config.	B_p [m]	PA [°]	Seeing ["]	Airmass	Mode
R Leo^F	2006-12-19 06:01	1.77	K0-G0	42.5	77	0.39	1.63	SCIPHOT/PRISM
αHya	2006-12-19 05:49	...	...	...	...	0.50	1.28	SCIPHOT/PRISM
αHya	2006-12-19 07:09	...	...	...	...	0.65	1.08	SCIPHOT/PRISM
αHya	2006-12-19 07:46	...	...	...	...	0.68	1.049	SCIPHOT/PRISM
R Leo^F	2006-12-21 07:07	1.78	H0-G0	27.5	77	0.91	1.33	SCIPHOT/PRISM
αHya	2006-12-21 07:26	...	...	...	...	1.20	1.057	SCIPHOT/PRISM
R Leo^F	2007-01-13 08:18	1.85	E0-G0	15.9	71	1.03	1.323	SCIPHOT/PRISM
αTau	2007-01-13 01:38	...	...	...	...	1.80	1.223	SCIPHOT/PRISM
αTau	2007-01-13 04:05	...	...	...	...	0.86	1.670	SCIPHOT/PRISM
2Cen	2007-01-13 07:32	...	...	...	...	1.19	1.436	SCIPHOT/PRISM
αHya	2007-01-13 08:04	...	...	...	...	1.00	1.113	SCIPHOT/PRISM
2Cen	2007-01-13 08:36	...	...	...	...	1.35	1.889	SCIPHOT/PRISM
R Leo^F	2007-01-18 04:07	1.86	H0-G0	21.6	77	-1.0	1.612	SCIPHOT/PRISM
αHya	2007-01-18 03:54	...	...	...	...	0.95	1.271	SCIPHOT/PRISM
2Cen	2007-01-18 07:09	...	...	...	...	1.25	1.450	SCIPHOT/PRISM
αHya	2007-01-18 07:41	...	...	...	...	0.97	1.462	SCIPHOT/PRISM
2Cen	2007-01-18 08:15	...	...	...	...	1.53	1.191	SCIPHOT/PRISM
αHya	2007-01-18 08:50	...	...	...	...	1.62	1.296	SCIPHOT/PRISM
R Leo^F	2007-01-21 07:29	1.87	H0-D0	63.9	72	0.70	1.296	SCIPHOT/PRISM
αHya	2007-01-21 07:03	...	...	...	...	0.55	1.071	SCIPHOT/PRISM
2Cen	2007-01-21 07:54	...	...	...	...	0.62	1.491	SCIPHOT/PRISM
αHya	2007-01-21 08:28	...	...	...	...	0.64	1.252	SCIPHOT/PRISM

Table A.11: Journal of the MIDI Auxiliary Telescopes observations of T Mic.

Target	UT date & time	ϕ_V	Config.	B_p [m]	PA [°]	Seeing ["]	Airmass	Mode
LP data								
T Mic	2011-06-06 07:02	0.36	B2-C1	11.3	18	1.33	1.040	SCIPHOT/PRISM
T Mic	2011-06-06 07:57	0.36	B2-C1	11.3	18	1.33	1.004	SCIPHOT/PRISM
HD167618	2011-06-06 07:39	...	...	...	...	1.60	1.096	SCIPHOT/PRISM
T Mic	2011-06-11 06:44	0.37	B2-A1	10.9	109	0.64	1.039	SCIPHOT/PRISM
T Mic	2011-06-11 07:40	0.37	C1-A1	16.0	70	0.73	1.003	SCIPHOT/PRISM
HD167618	2011-06-11 07:23	...	...	...	...	0.63	1.101	SCIPHOT/PRISM
HD167618	2011-06-11 09:14	...	...	...	...	0.46	1.453	SCIPHOT/PRISM
T Mic	2011-06-11 08:35	0.37	B2-A1	11.2	121	0.53	1.01	SCIPHOT/PRISM
HD167618	2011-06-11 08:20	...	...	...	...	0.67	1.231	SCIPHOT/PRISM
HD167618	2011-06-11 06:24	...	...	...	...	0.69	1.036	SCIPHOT/PRISM
T Mic	2011-06-11 09:29	0.37	C1-A1	14.8	82	0.55	1.079	SCIPHOT/PRISM
HD167618	2011-06-11 07:23	...	...	...	...	0.63	1.101	SCIPHOT/PRISM
HD167618	2011-06-11 09:14	...	...	...	...	0.46	1.453	SCIPHOT/PRISM
Archive								
T Mic	2004-07-08 10:09	0.08	U3-U2	33.5	55	0.77	1.735	HIGHSENS/PRISM
HD165135	2004-07-08 03:52	...	...	...	...	0.68	1.006	HIGHSENS/PRISM
HD165135	2004-07-08 04:43	...	...	...	...	0.71	1.036	HIGHSENS/PRISM
HD165135	2004-07-08 05:56	...	...	...	...	0.77	1.162	HIGHSENS/PRISM
HD165135	2004-07-08 07:12	...	...	...	...	0.56	1.458	HIGHSENS/PRISM
HD165135	2004-07-08 08:51	...	...	...	...	0.65	2.637	HIGHSENS/PRISM
T Mic[F]	2004-07-30 07:09	0.14	U3-U2	41.5	52	1.31	1.212	SCIPHOT/PRISM
HD129456	2004-07-30 01:20	...	...	...	...	0.52	1.196	SCIPHOT/PRISM
HD169916	2004-07-30 02:14	...	...	...	...	0.74	1.005	SCIPHOT/PRISM
HD169916	2004-07-30 04:57	...	...	...	...	1.08	1.175	SCIPHOT/PRISM
HD177716	2004-07-30 06:16	...	...	...	...	1.04	1.390	SCIPHOT/PRISM
T Mic[F]	2004-07-31 05:10	0.14	U3-U2	46.2	44	1.08	1.014	HIGHSENS/PRISM
HD169916	2004-07-31 01:32	...	...	...	...	0.59	1.029	HIGHSENS/PRISM
HD169916	2004-07-31 02:50	...	...	...	...	0.67	1.003	HIGHSENS/PRISM
HD165135	2004-07-31 03:31	...	...	...	...	0.65	1.057	HIGHSENS/PRISM
HD169916	2004-07-31 04:47	...	...	...	...	0.71	1.161	HIGHSENS/PRISM
T Mic	2010-10-09 00:51	0.34	D0-H0	62.8	76	0.90	1.021	SCIPHOT/GRISM

Table A.12: Journal of the MIDI Auxiliary Telescopes observations of RT Vir.

Target	UT date & time	ϕ_V	Config.	B_p [m]	PA [°]	Seeing ["]	Airmass	Mode
LP data								
RT Vir[F]	2012-01-24 07:33	0.76	C1-A1	12.6	72	0.86	1.338	SCIPHOT/PRISM
HD81797	2012-01-24 05:16	...	...	...	...	1.08	1.057	SCIPHOT/PRISM
HD112142	2012-01-24 07:17	...	...	...	...	0.86	1.207	SCIPHOT/PRISM
HD123139	2012-01-24 07:53	...	...	...	...	1.16	1.252	SCIPHOT/PRISM
HD112142	2012-01-24 08:25	...	...	...	...	0.81	1.069	SCIPHOT/PRISM
HD123139	2012-01-24 08:59	...	...	...	...	1.05	1.097	SCIPHOT/PRISM
RT Vir[F]	2012-01-24 08:42	0.76	C1-A1	14.9	74	0.81	1.182	SCIPHOT/PRISM
HD81797	2012-01-24 05:16	...	...	...	...	1.08	1.057	SCIPHOT/PRISM
HD112142	2012-01-24 07:17	...	...	...	...	0.86	1.207	SCIPHOT/PRISM
HD123139	2012-01-24 07:53	...	...	...	...	1.16	1.252	SCIPHOT/PRISM
HD112142	2012-01-24 08:25	...	...	...	...	0.81	1.069	SCIPHOT/PRISM
HD123139	2012-01-24 08:59	...	...	...	...	1.05	1.097	SCIPHOT/PRISM
RT Vir	2012-05-01 02:44	0.02	B2-A1	11.2	113	0.77	1.158	SCIPHOT/PRISM
RT Vir	2012-05-01 03:50	0.02	B2-A1	10.5	113	0.67	1.172	SCIPHOT/PRISM
RT Vir	2012-05-02 00:19	0.02	C1-B2	8.70	6	0.79	1.554	SCIPHOT/PRISM
RT Vir	2012-05-02 01:18	0.02	C1-B2	9.00	16	0.60	1.294	SCIPHOT/PRISM
Archive								
RT Vir*	2011-02-08 08:29	0.82	A0-G1	89.0	113	0.90	1.151	SCIPHOT/GRISM
HD120323	2011-02-08 08:06	...	...	...	...	0.90	1.053	SCIPHOT/GRISM
HD120323	2011-02-08 08:55	...	...	...	...	1.00	1.019	SCIPHOT/GRISM
RT Vir*	2011-03-06 06:10	0.89	G0-H0	30.0	74	1.20	1.169	SCIPHOT/GRISM
HD120323	2011-03-06 05:42	...	...	...	...	1.20	1.118	SCIPHOT/GRISM
HD120323	2011-03-06 06:35	...	...	...	...	1.20	1.043	SCIPHOT/GRISM
RT Vir*	2011-03-13 07:06	0.91	A0-K0	128.0	73	1.40	1.176	SCIPHOT/GRISM
HD120323	2011-03-13 06:46	...	...	...	...	1.30	1.018	SCIPHOT/GRISM
HD120323	2011-03-13 07:26	...	...	...	...	1.20	1.018	SCIPHOT/GRISM
RT Vir*	2009-03-18 05:03	0.98	D0-H0	59.0	74	1.70	1.189	SCIPHOT/GRISM
HD120323	2009-03-18 05:23	...	...	...	...	1.50	1.068	SCIPHOT/GRISM
RT Vir*	2009-03-18 06:03	0.98	D0-H0	63.0	73	1.00	1.152	SCIPHOT/GRISM
HD120323	2009-03-18 06:26	...	...	...	...	0.80	1.018	SCIPHOT/GRISM
RT Vir*	2009-06-03 01:33	0.18	G0-H0	32.0	73	1.00	1.166	SCIPHOT/GRISM
HD120323	2009-06-03 02:00	...	...	...	...	1.10	1.017	SCIPHOT/GRISM
RT Vir*	2009-07-01 00:26	0.26	A0-K0	126.0	72	2.40	1.017	SCIPHOT/GRISM
RT Vir[F]	2008-06-29 23:40	0.28	H0-G0	31.9	73	1.02	1.159	SCIPHOT/PRISM
HD133216	2008-06-29 01:59	...	...	...	...	1.10	1.016	SCIPHOT/PRISM
RT Vir	2008-06-29 01:09	0.28	H0-G0	30.6	70	0.90	1.317	SCIPHOT/PRISM
HD133216	2008-06-29 01:59	...	...	...	...	1.10	1.016	SCIPHOT/PRISM
RT Vir	2008-06-29 01:45	0.28	H0-G0	28.7	68	1.15	1.464	SCIPHOT/PRISM
HD133216	2008-06-29 01:59	...	...	...	...	1.10	1.016	SCIPHOT/PRISM
RT Vir[F]	2008-07-03 00:08	0.29	E0-G0	15.9	72	0.70	1.206	SCIPHOT/PRISM
HD120323	2008-07-03 01:49	...	...	...	...	1.01	1.141	SCIPHOT/PRISM
HD120323	2008-07-03 02:19	...	...	...	...	1.41	1.220	SCIPHOT/PRISM
RT Vir[F]	2008-07-03 00:45	0.29	E0-G0	15.4	71	0.85	1.291	SCIPHOT/PRISM
HD120323	2008-07-03 01:49	...	...	...	...	1.01	1.141	SCIPHOT/PRISM
HD120323	2008-07-03 02:19	...	...	...	...	1.41	1.220	SCIPHOT/PRISM
RT Vir[F]	2008-07-03 01:19	0.29	E0-G0	14.7	69	1.06	1.416	SCIPHOT/PRISM
HD120323	2008-07-03 01:49	...	...	...	...	1.01	1.141	SCIPHOT/PRISM
HD120323	2008-07-03 02:19	...	...	...	...	1.41	1.220	SCIPHOT/PRISM

Notes. * These observations have been published in Sacuto et al. (2013).

Table A.13: Journal of the MIDI Auxiliary Telescopes observations of π^1 Gru.

Target	UT date & time	ϕ_V	Config.	B_p [m]	PA [°]	Seeing ["]	Airmass	Mode
LP data								
π^1 Gru	2011-05-09 09:03	...	B2-C1	11.1	4	0.80	1.30	SCI-PHOT
π^1 Gru	2011-05-09 09:34	...	B2-C1	11.1	8	0.80	1.22	SCI-PHOT
π^1 Gru	2011-06-12 07:52	...	A1-B2	10.0	96	1.45	1.16	SCI-PHOT
HD206778	2011-06-12 07:36	...	...	...	...	1.08	1.32	SCI-PHOT
HD206778	2011-06-12 08:50	...	...	...	...	0.62	1.22	SCI-PHOT
π^1 Gru	2011-06-12 08:35	...	A1-B2	10.6	103	0.62	1.10	SCI-PHOT
HD206778	2011-06-12 07:36	...	...	...	...	1.08	1.32	SCI-PHOT
HD206778	2011-06-12 08:50	...	...	...	...	0.62	1.22	SCI-PHOT
π^1 Gru	2011-06-12 09:30	...	A1-C1	15.9	70	0.74	1.10	SCI-PHOT
HD206778	2011-06-12 09:14	...	...	...	...	0.62	1.22	SCI-PHOT
HD206778	2011-06-12 09:44	...	...	...	...	0.70	1.24	SCI-PHOT
π^1 Gru	2011-08-11 07:01	...	A1-C1	15.1	85	1.20	1.11	SCI-PHOT
HD206778	2011-08-11 06:41	...	...	...	...	1.20	1.33	SCI-PHOT
HD224935	2011-08-11 07:38	...	...	...	...	1.35	1.45	SCI-PHOT
Archive								
π^1 Gru*	2006-05-21 09:09	...	E0-G0	15.7	50	1.26	1.18	SCI-PHOT
HD214952	2006-05-21 09:28	...	...	...	...	1.57	1.85	SCI-PHOT
π^1 Gru*	2006-05-23 09:32	...	A0-G0	63.5	56	0.76	1.28	SCI-PHOT
HD214952	2006-05-23 10:06	...	...	...	...	0.71	1.12	SCI-PHOT
π^1 Gru*	2006-05-24 09:27	...	D0-G0	31.8	56	0.72	1.30	SCI-PHOT
HD214952	2006-05-24 09:44	...	...	...	...	0.65	1.40	SCI-PHOT
π^1 Gru*	2006-05-25 08:09	...	A0-G0	61.2	41	-1	1.29	SCI-PHOT
HD214952	2006-05-25 07:51	...	...	...	...	0.66	1.42	SCI-PHOT
π^1 Gru*	2006-05-27 09:20	...	E0-G0	15.9	57	1.51	1.23	SCI-PHOT
HD214952	2006-05-27 09:37	...	...	...	...	1.30	1.13	SCI-PHOT
π^1 Gru*	2006-06-19 10:16	...	D0-G0	30.6	83	0.62	1.10	SCI-PHOT
HD214952	2006-06-19 09:50	...	...	...	...	0.72	1.082	SCI-PHOT
π^1 Gru*	2006-08-08 08:40	...	A0-G0	52.6	102	0.88	1.28	SCI-PHOT
HD214952	2006-08-08 08:13	...	...	...	...	1.27	1.18	SCI-PHOT

Notes. * These observations have been published in Sacuto et al. (2008).

Table A.14: Journal of observations of omi Ori.

Target	UT date & time	ϕ_V	Config.	B_p [m]	PA [°]	Seeing ["]	Airmass	Mode
LP data								
o Ori	2011-11-01 04:08	...	G1-I1	26.8	27	1.42	1.794	HIGHSENS/PRISM
o Ori	2011-11-01 05:04	...	K0-I1	34.9	0	0.77	1.474	HIGHSENS/PRISM
HD18884	2011-11-01 04:50	...	...	...	...	0.83	1.143	HIGHSENS/PRISM
HD18884	2011-11-01 06:50	...	...	...	...	1.45	1.277	HIGHSENS/PRISM
o Ori	2011-11-01 06:04	...	G1-I1	36.9	45	1.04	1.321	HIGHSENS/PRISM
HD18884	2011-11-01 03:55	...	...	...	...	1.12	1.198	HIGHSENS/PRISM
HD18884	2011-11-01 07:51	...	...	...	...	1.18	1.547	HIGHSENS/PRISM
HD18884	2011-11-01 08:35	...	...	...	...	0.93	1.924	HIGHSENS/PRISM
o Ori	2011-11-01 07:03	...	K0-I1	37	16	1.38	1.285	HIGHSENS/PRISM
HD18884	2011-11-01 04:50	...	...	...	...	0.83	1.143	HIGHSENS/PRISM
HD18884	2011-11-01 06:50	...	...	...	...	1.45	1.277	HIGHSENS/PRISM
o Ori	2011-11-01 08:04	...	G1-I1	44.7	48	0.88	1.355	HIGHSENS/PRISM
HD18884	2011-11-01 03:55	...	...	...	...	1.12	1.198	HIGHSENS/PRISM
HD18884	2011-11-01 07:51	...	...	...	...	1.18	1.547	HIGHSENS/PRISM
HD18884	2011-11-01 08:35	...	...	...	...	0.93	1.924	HIGHSENS/PRISM
o Ori	2011-11-01 08:47	...	G1-I1	46	47	1.05	1.482	HIGHSENS/PRISM
HD18884	2011-11-01 03:55	...	...	...	...	1.12	1.198	HIGHSENS/PRISM
HD18884	2011-11-01 07:51	...	...	...	...	1.18	1.547	HIGHSENS/PRISM
HD18884	2011-11-01 08:35	...	...	...	...	0.93	1.924	HIGHSENS/PRISM
o Ori	2011-11-04 04:40	...	H0-I1	39.6	141	0.87	1.526	HIGHSENS/PRISM
o Ori	2011-11-04 07:24	...	H0-I1	31.9	146	1.80	1.309	HIGHSENS/PRISM
HD18884	2011-11-04 04:23	...	...	...	...	0.80	1.150	HIGHSENS/PRISM
HD18884	2011-11-04 07:08	...	...	...	...	1.62	1.382	HIGHSENS/PRISM
o Ori	2011-11-05 04:58	...	H0-I1	38.9	140	0.83	1.439	HIGHSENS/PRISM
HD18884	2011-11-05 04:40	...	...	...	...	1.42	1.142	HIGHSENS/PRISM
Archive data								
o Ori	2005-11-12 06:51	...	U1-U4	128	65	0.56	1.314	SCIPHOT/PRISM
HD50778	2005-11-12 08:04	...	...	...	...	0.58	1.025	SCIPHOT/PRISM
HD50778	2005-11-12 09:18	...	...	...	...	0.66	1.068	SCIPHOT/PRISM
o Ori	2005-12-26 05:51	...	U1-U4	125	57	1.78	1.718	SCIPHOT/PRISM
HD39425	2005-12-26 00:25	...	...	...	...	0.73	1.553	SCIPHOT/PRISM
HD50778	2005-12-26 07:13	...	...	...	...	1.23	1.159	SCIPHOT/PRISM
o Ori	2005-12-30 05:10	...	U1-U4	128	59	0.80	1.570	SCIPHOT/GRISM
HD50778	2005-12-30 05:48	...	...	...	...	0.85	1.040	SCIPHOT/GRISM
HD50778	2005-12-30 05:37	...	...	...	...	0.81	1.040	SCIPHOT/GRISM
o Ori	2005-12-30 05:00	...	U1-U4	128	60	0.86	1.510	SCIPHOT/GRISM
HD50778	2005-12-30 05:48	...	...	...	...	0.85	1.040	SCIPHOT/GRISM
HD50778	2005-12-30 05:37	...	...	...	...	0.81	1.040	SCIPHOT/GRISM
o Ori	2005-12-30 04:50	...	U1-U4	129	61	0.77	1.480	SCIPHOT/GRISM
HD50778	2005-12-30 05:48	...	...	...	...	0.85	1.040	SCIPHOT/GRISM
HD50778	2005-12-30 05:37	...	...	...	...	0.81	1.040	SCIPHOT/GRISM
o Ori^{F}	2005-12-31 02:53	0.61	U1-U4	123	66	0.70	1.280	SCIPHOT/GRISM
HD50778	2005-12-31 03:29	...	...	...	...	0.59	1.100	SCIPHOT/GRISM
o Ori	2005-12-31 02:42	...	U1-U4	121	67	0.64	1.290	SCIPHOT/GRISM
HD50778	2005-12-31 03:29	...	...	...	...	0.59	1.100	SCIPHOT/GRISM

Table A.15: Journal of the MIDI Auxiliary Telescopes observations of U Ant.

Target	UT date & time	ϕ_V	Config.	B_p [m]	PA [°]	Seeing ["]	Air-mass	Mode
LP data								
U Ant	2012-01-25 04:03	...	D0-A1	35.7	28	1.26	1.3	HIGHSENS/PRISM
U Ant	2012-01-25 05:10	...	D0-A1	35.7	28.8	1.08	1.1	HIGHSENS/PRISM
HD29139	2012-01-25 02:12	...	...	...	...	1.1	1.40	HIGHSENS/PRISM
U Ant	2012-01-29 04:46	...	B2-D0	33.8	11	1.00	1.1	HIGHSENS/PRISM
U Ant	2011-11-04 08:38	...	H0-I1	30.2	129	1.54	1.5	HIGHSENS/PRISM
U Ant	2011-11-06 05:10	...	H0-I1	28.6	128	1.39	1.6	HIGHSENS/PRISM
Archive data								
U Ant*	2008-01-10 08:25	...	G0-H0	31.5	75.5	1.07	1.0	HIGHSENS/PRISM
HD48915	2008-01-10 06:50	...	...	...	...	1.46	1.0	HIGHSENS/PRISM
HD120323	2008-01-10 09:00	...	...	...	...	0.92	1.1	HIGHSENS/PRISM
U Ant*	2008-01-11 05:47	...	G0-H0	31.5	49	0.74	1.1	HIGHSENS/PRISM
U Ant*	2008-01-11 07:22	...	G0-H0	32.0	66	1.24	1.0	HIGHSENS/PRISM
U Ant*	2008-01-11 09:17	...	E0-H0	15.2	84	0.66	1.1	HIGHSENS/PRISM
U Ant*	2008-02-20 04:22	...	A0-H0	95.6	62.6	0.66	1.0	HIGHSENS/PRISM
HD48915	2008-02-20 05:14	...	...	...	...	0.58	1.2	HIGHSENS/PRISM
U Ant*	2008-03-14 01:42	...	E0-G0	15.3	50	0.67	1.1	HIGHSENS/PRISM
U Ant*	2008-03-14 02:24	...	E0-H0	15.8	58	0.75	1.1	HIGHSENS/PRISM
U Ant*	2007-11-26 08:33		E0-G0	15.1	46	1.68	1.2	HIGHSENS/PRISM

Notes. * These observations have been published in Ladjal (2011), but we performed a new data reduction.

Table A.16: Journal of the MIDI Auxiliary Telescopes observations of R Lep.

Target	UT date & time	ϕ_V	Config.	B_p [m]	PA [°]	Seeing ["]	Airmass	Mode
LP data								
R Lep[F]	2011-10-24 06:36	1.40	D0-A1	34	219	0.82	1.042	SCIPHOT/PRISM
HD20720	2011-10-24 06:16	...	...	...	...	0.69	1.00	SCIPHOT/PRISM
HD48915	2011-10-24 06:54	...	...	...	...	0.56	1.208	SCIPHOT/PRISM
HD20720	2011-10-24 07:25	...	...	...	...	0.41	1.077	SCIPHOT/PRISM
HD48915	2011-10-24 08:02	...	...	...	...	0.62	1.059	SCIPHOT/PRISM
R Lep[F]	2011-10-24 07:44	1.40	D0-A1	35	226	0.60	1.016	SCIPHOT/PRISM
HD20720	2011-10-24 06:16	...	...	...	...	0.67	1.00	SCIPHOT/PRISM
HD48915	2011-10-24 06:54	...	...	...	...	0.62	1.208	SCIPHOT/PRISM
HD20720	2011-10-24 07:25	...	...	...	...	0.41	1.077	SCIPHOT/PRISM
HD48915	2011-10-24 08:02	...	...	...	...	0.69	1.059	SCIPHOT/PRISM
R Lep[F]	2011-10-26 07:44	1.41	D0-B2	34	208	1.03	1.019	SCIPHOT/PRISM
HD48915	2011-10-26 07:28	...	...	...	...	1.53	1.01	SCIPHOT/PRISM
HD20720	2011-10-26 08:03	...	...	...	...	1.65	1.179	SCIPHOT/PRISM
HD20720	2011-10-26 08:20	...	...	...	...	1.39	1.239	SCIPHOT/PRISM
HD48915	2011-10-26 09:04	...	...	...	...	...	1.01	SCIPHOT/PRISM
R Lep[F]	2011-10-26 08:40	1.41	D0-B2	34	212	1.22	1.068	SCIPHOT/PRISM
HD48915	2011-10-26 07:28	...	...	...	...	1.53	1.01	SCIPHOT/PRISM
HD20720	2011-10-26 08:03	...	...	...	...	1.65	1.179	SCIPHOT/PRISM
HD20720	2011-10-26 08:20	...	...	...	...	1.39	1.239	SCIPHOT/PRISM
HD48915	2011-10-26 09:04	...	...	...	...	...	1.01	SCIPHOT/PRISM
R Lep	2011-11-04 02:55	1.43	H0-I1	36	140	1.14	1.77	SCIPHOT/PRISM
HD20720	2011-11-04 02:37	...	...	...	...	1.30	1.22	SCIPHOT/PRISM
HD20720	2011-11-04 03:12	...	...	...	...	1.31	1.12	SCIPHOT/PRISM
R Lep[F]	2011-11-04 06:26	1.43	H0-I1	40	147	1.01	1.22	SCIPHOT/PRISM
HD20720	2011-11-04 06:08	...	...	...	...	0.84	1.03	SCIPHOT/PRISM
HD48915	2011-11-04 06:49	...	...	...	...	1.38	1.11	SCIPHOT/PRISM
Archive								
R Lep	2010-12-08 02:47	0.66	H0-I1	40	142	0.75	1.12	SCIPHOT/PRISM
HD20720	2010-12-08 02:29	...	...	...	...	0.77	1.00	SCIPHOT/PRISM
HD48915	2010-12-08 03:11	...	...	...	...	0.65	1.47	SCIPHOT/PRISM
R Lep	2011-03-11 00:35	0.88	H0-I1	38	113	1.16	1.17	SCIPHOT/PRISM
HD48915	2011-03-11 00:14	...	...	...	...	1.16	1.01	SCIPHOT/PRISM
HD20720	2011-03-11 00:47	...	...	...	...	1.09	1.73	SCIPHOT/PRISM
R Lep[F]	2012-10-05 07:57	2.22	A1-G1	79	249	0.5	1.034	SCIPHOT/PRISM
HD20720	2012-10-05 07:41	...	...	...	...	0.44	1.01	SCIPHOT/PRISM
HD32887	2012-10-05 08:11	...	...	...	...	0.52	1.01	SCIPHOT/PRISM
R Lep[F]	2012-10-12 04:18	2.23	A1-G1	48	97	1.21	1.79	SCIPHOT/PRISM
HD20720	2012-10-12 04:01	...	...	...	...	1.15	1.26	SCIPHOT/PRISM
HD32887	2012-10-12 04:34	...	...	...	...	0.95	1.61	SCIPHOT/PRISM

Table A.17: Journal of the MIDI Auxiliary Telescopes observations of Y Pav

Target	UT date & time	ϕ_V	Config.	B_p [m]	PA [°]	Seeing ["]	Airmass	Mode
LP data								
Y Pav[F]	2011-05-30 07:12:53	0.57	D0-H0	63.9	43	0.63	1.55	HIGH-SENS
HD 150798	2011-05-30 06:55:42	...	...	...	...	0.84	1.48	...
Y Pav	2011-05-30 09:07:32	0.57	H0-G1	51.2	6	0.78	1.42	HIGH-SENS
HD 150798	2011-05-30 08:50:24	...	...	...	...	0.75	1.77	...
HIP 82363	2011-05-30 09:22:51	...	...	...	...	0.82	1.83	...
Y Pav	2011-05-30 09:59:51	0.57	D0-G1	63	129	0.82	1.42	HIGH-SENS
HIP 82363	2011-05-30 09:42:36	...	...	...	...	0.78	2.03	...
HIP 82363	2011-05-30 10:15:22	...	...	...	...	0.87	2.12	...
Y Pav	2011-05-30 08:04:00	0.57	D0-H0	63.6	55	0.95	1.47	HIGH-SENS
Y Pav	2011-05-31 07:54:30	0.57	H0-G1	51.3	-4	0.77	1.47	HIGH-SENS
Y Pav	2011-05-31 08:50:28	0.57	D0-G1	60.1	116	0.63	1.42	HIGH-SENS
Y Pav	2011-07-02 04:26:06	0.71	H0-I1	51.0	85	0.53	1.83	HIGH-SENS

Table A.18: Journal of MIDI observations of TX Psc.

Target	UT date & time	ϕ	Config.	B_p [m]	PA [°]	Seeing ["]	Airmass	Mode
LP data								
TX Psc	2011-10-30 01:42	...	K0-G1	80.9	28	1.26	1.136	HIGH-SENS
HIP 1170	2011-10-30 01:55		...	...	...	1.31	1.012	HIGH-SENS
TX Psc	2011-10-30 02:29	...	K0-A1	128	67	1.44	1.147	HIGH-SENS
HIP 154	2011-10-30 02:16	...	...	...	...	1.29	1.056	HIGH-SENS
HIP 1170	2011-10-30 02:41	...	...	...	...	1.30	1.008	HIGH-SENS
TX Psc	2011-10-30 03:29	...	G1-A1	68.8	107	1.17	1.239	HIGH-SENS
HIP 1170	2011-10-30 03:41	...	...	...	...	1.10	1.058	HIGH-SENS
TX Psc	2011-10-31 00:55	...	K0-G1	77.4	23	1.00	1.170	HIGH-SENS
TX Psc	2011-10-31 01:45	...	G1-A1	79.5	106	0.87	1.135	HIGH-SENS
TX Psc	2011-11-01 00:38	...	K0-G1	76.4	21	0.66	1.190	HIGH-SENS
TX Psc	2011-11-01 01:57	...	K0-A1	127	67	0.75	1.135	HIGH-SENS
HIP 154	2011-11-01 02:08	...	...	...	...	0.77	1.059	HIGH-SENS

Table A.19: Journal of archive MIDI observations of TX Psc.

Archive								
TX Psc	2006-08-28 02:50	...	E0-G0	9.4	81	1.41	1.718	HIGH-SENS
TX Psc *	2006-10-19 00:19	...	E0-G0	11.9	70	...	1.387	HIGH-SENS
HD48915	2006-10-19 08:26	...	...	...	...	0.57	1.325	HIGH-SENS
TX Psc *	2006-10-18 05:46	...	E0-G0	13.2	66	0.89	1.659	HIGH-SENS
HD48915	2006-10-18 06:57	...	...	...	...	0.87	1.278	HIGH-SENS
TX Psc	2005-06-29 08:55	...	E0-G0	13.7	82	0.54	1.238	HIGH-SENS
TX Psc	2010-09-07 04:13	...	E0-G0	14.4	73	0.93	1.194	HIGH-SENS
TX Psc	2006-08-28 05:48	...	E0-G0	15.6	73	1.30	1.136	HIGH-SENS
TX Psc	2009-11-15 02:18	...	E0-G0	15.7	72	1.26	1.225	HIGH-SENS
TX Psc*	2006-10-18 03:18	...	E0-G0	16.0	73	1.00	1.149	HIGH-SENS
HD48915	2006-10-18 06:57	...	...	...	...	0.87	1.278	HIGH-SENS
TX Psc	2006-09-20 02:28	...	D0-G0	25.1	71	1.21	1.327	HIGH-SENS
TX Psc	2006-09-20 03:23	...	D0-G0	29.0	73	1.90	1.189	HIGH-SENS
TX Psc	2006-10-16 02:12	...	H0-G0	30.5	73	0.67	1.150	HIGH-SENS
TX Psc	2009-11-16 02:13	...	H0-G0	31.0	72	0.95	1.219	HIGH-SENS
TX Psc*	2006-09-20 05:47	...	D0-G0	31.6	72	1.64	1.201	HIGH-SENS
HD20720	2006-09-20 09:48	...	...	...	...	0.89	1.095	HIGH-SENS
TX Psc	2009-11-16 01:20	...	H0-G0	32.0	73	1.36	1.146	HIGH-SENS
TX Psc	2006-09-21 01:48	...	K0-G0	44.0	68	1.01	1.489	HIGH-SENS
TX Psc*	2006-09-21 03:32	...	K0-G0	59.2	73	1.02	1.169	HIGH-SENS
HD48915	2006-09-21 08:36	...	...	...	...	1.51	1.309	HIGH-SENS
TX Psc	2006-09-17 04:20	...	A0-G0	62.0	73	1.36	1.140	HIGH-SENS
TX Psc*	2006-09-21 05:55	...	K0-G0	62.5	72	1.39	1.225	HIGH-SENS
HD48915	2006-09-21 08:36	...	...	...	...	1.51	1.309	HIGH-SENS
TX Psc	2008-09-27 04:45	...	G1-D0	63.6	133	1.00	1.155	HIGH-SENS
TX Psc*	2006-08-17 07:00	...	A0-G0	63.7	73	0.39	1.137	HIGH-SENS
HD224935	2006-08-17 07:23	...	...	...	...	0.43	1.060	HIGH-SENS
TX Psc*	2004-10-30 03:28	...	UT2-UT4	84.3	80	0.78	1.244	HIGH-SENS
HD49161	2004-10-30 09:19	...	...	...	...	0.72	1.196	HIGH-SENS
TX Psc*	2006-08-16 07:06	...	A0-G1	87	113	0.85	1.137	HIGH-SENS
HD18884	2006-08-16 07:57	...	...	...	...	0.81	1.353	HIGH-SENS
TX Psc	2006-08-15 06:20	...	A0-G1	90.3	113	0.88	1.145	HIGH-SENS
TX Psc	2011-09-21 05:39	...	I1-A1	104.0	84	1.03	1.186	HIGH-SENS
TX Psc	2011-10-05 04:21	...	K0-A1	129.0	67	0.57	1.158	HIGH-SENS
TX Psc*	2011-10-02 05:44	...	A1-J3	140.0	46	1.02	1.305	HIGH-SENS
HD45348	2011-10-02 06:42	...	...	...	...	0.88	1.512	HIGH-SENS

Notes. * These observations have been published in Klotz et al. (2013a).

Table A.20: Journal of the MIDI Auxiliary Telescopes observations of S Sct

Target	UT date & time	ϕ_V	Config.	B_p [m]	PA [°]	Seeing ["]	Airmass	Mode
LP data								
S Sct	2011-05-02 08:18:31	0.84	H0-I1	40	146	0.37	1.05	HIGH-SENS
S Sct	2011-05-28 05:34:10	0.02	K0-I1	44	1	1.23	1.13	HIGH-SENS
S Sct	2011-05-28 06:34:05	0.02	K0-I1	44.3	8	1.24	1.05	HIGH-SENS
S Sct	2011-05-28 08:28:37	0.02	G1-I1	46.6	45	0.55	1.11	HIGH-SENS
S Sct	2011-05-28 09:18:32	0.02	G1-I1	45.9	46	0.90	1.23	HIGH-SENS
S Sct^{F}	2011-05-28 07:27:11	0.02	K0-I1	44.9	14	0.96	1.05	HIGH-SENS
HIP89931	2011-05-28 06:15:23	...	K0-I1	46.5	9	1.01	1.01	HIGH-SENS
HIP89931	2011-05-28 07:08:03	...	K0-I1	46.3	14	1.41	1.01	HIGH-SENS
S Sct^{F}	2011-05-30 06:06:29	0.03	H0-I1	40.5	144	1.01	1.07	HIGH-SENS
HIP89931	2011-05-30 05:44:39	...	H0-I1	40.1	144	0.94	1.02	HIGH-SENS
HIP90496	2011-05-30 06:23:06	...	H0-I1	40.7	148	0.86	1.00	HIGH-SENS

Table A.21: Journal of the MIDI Auxiliary Telescopes observations of AQ Sgr

Target	UT date & time	ϕ_V	Config.	B_p [m]	PA [°]	Seeing ["]	Airmass	Mode
LP data								
AQ Sgr[F]	2011-05-02 07:14:32	0.86	G1-I1	42.5	21	0.46	1.20	HIGH-SENS
HIP89931	2011-05-02 07:00:03	...	G1-I1	46.3	29	0.47	1.06	HIGH-SENS
HIP89931	2011-05-02 09:01:28	...	H0-I1	40.7	154	0.49	1.02	HIGH-SENS
HIP90496	2011-05-02 07:31:27	...	G1-I1	46.2	33	0.42	1.02	HIGH-SENS
HIP90496	2011-05-02 08:01:01	...	H0-I1	40.6	146	0.37	1.01	HIGH-SENS
AQ Sgr	2011-06-25 09:29:49	0.14	K0-I1	46.0	27	1.14	1.55	HIGH-SENS
AQ Sgr	2011-06-25 10:14:24	0.14	K0-I1	45.1	28	1.54	1.98	HIGH-SENS
AQ Sgr	2011-06-26 08:39:47	0.14	G1-I1	42.5	48	1.40	1.29	HIGH-SENS
AQ Sgr	2011-06-29 08:53:11	0.16	H0-I1	37.9	174	1.51	1.41	HIGH-SENS
HIP89931	2011-06-29 08:35:10	...	H0-I1	37.9	174	1.47	1.70	HIGH-SENS
AQ Sgr	2011-07-26 05:50:55	0.29	K0-I1	46.6	21	0.55	1.13	HIGH-SENS
AQ Sgr	2011-07-26 06:36:13	0.29	G1-I1	43.8	48	0.43	1.27	HIGH-SENS
AQ Sgr	2011-07-29 03:20:37	0.31	H0-I1	40.7	146	0.76	1.02	HIGH-SENS
Archive								
AQ Sgr	2008-06-29 02:18:18	0.65	H0-G1	22.5	42	1.01	1.50	SCIPHOT
AQ Sgr	2008-06-29 03:28:33	0.65	H0-G1	27.0	56	0.99	1.18	SCIPHOT
AQ Sgr	2008-06-29 07:53:17	0.65	H0-G1	28.4	78	2.08	1.18	SCIPHOT
AQ Sgr	2008-07-01 02:50:34	0.66	E0-G0	12.5	51	0.51	1.29	SCIPHOT
AQ Sgr	2008-07-01 04:01:38	0.66	E0-G0	14.6	62	0.45	1.09	SCIPHOT
AQ Sgr	2008-07-01 05:44:36	0.66	E0-G0	16.0	72	064	1.01	SCIPHOT
AQ Sgr	2008-07-02 05:41:29	0.67	E0-G0	16.0	71	0.84	1.01	SCIPHOT
AQ Sgr	2008-07-02 06:50:18	0.67	E0-G0	15.4	76	0.74	1.07	SCIPHOT
AQ Sgr	2008-07-02 08:46:43	0.67	E0-G0	11.7	81	0.91	1.46	SCIPHOT
AQ Sgr	2008-07-03 07:21:32	0.67	H0-G0	29.3	77	1.43	1.14	SCIPHOT
AQ Sgr	2008-07-03 07:56:31	0.67	H0-G0	27.2	79	0.86	1.24	SCIPHOT

Table A.22: Journal of the MIDI Auxiliary Telescopes observations of X TrA

Target	UT date & time	ϕ_V	Config.	B_p [m]	PA [°]	Seeing ["]	Airmass	Mode
LP data								
X TrA^F	2011-04-23 03:47:06	...	K0-I1	34.0	178	0.82	1.52	HIGH-SENS
X TrA^F	2011-04-23 05:11:55	...	...	33.7	160	0.67	1.43	HIGH-SENS
HD 150798	2011-04-23 03:24:38	...	...	...	...	0.85	1.81	HIGH-SENS
HD 150798	2011-04-23 04:02:21	...	...	...	...	0.71	1.68	HIGH-SENS
HD 150798	2011-04-23 04:56:30	...	...	...	...	0.74	1.54	HIGH-SENS
X TrA	2011-06-12 06:26:20	...	D0-A1	23.2	106	1.08	1.81	HIGH-SENS
HD 150798	2011-06-12 06:12:58	...	...	...	...	1.09	1.50	HIGH-SENS
HD 150798	2011-06-12 06:38:46	...	...	...	...	0.95	1.55	HIGH-SENS
X TrA^F	2011-07-01 23:32:31	...	H0-I1	28.9	120	0.50	1.59	HIGH-SENS
HD 150798	2011-07-01 23:17:56	...	...	...	...	0.54	1.71	HIGH-SENS
HD 150798	2011-07-01 23:47:03	...	...	...	...	0.50	1.61	HIGH-SENS
X TrA	2011-07-02 07:40:35	...	H0-I1	33.2	-149	0.51	2.80	HIGH-SENS
X TrA	2011-07-29 02:33:26	...	H0-I1	34.5	173	0.96	1.65	HIGH-SENS
X TrA	2011-08-10 03:36:41	...	D0-A1	20.9	124	1.65	2.10	HIGH-SENS
HD 150798	2011-08-10 03:17:22	...	...	...	...	1.55	1.62	HIGH-SENS
HD 150798	2011-08-10 03:59:46	...	...	...	...	1.32	1.76	HIGH-SENS

Bibliography

Ake, T. B. and Johnson, H. R. (1988). A white dwarf companion to the main-sequence star 4 Omicron(1) Orionis and the binary hypothesis for the origin of peculiar red giants. ApJ, 327:214–221.

Alfonso-Garzón, J., Domingo, A., Mas-Hesse, J. M., and Giménez, A. (2012). The first INTEGRAL-OMC catalogue of optically variable sources. A&A, 548:A79.

Amari, S., Lewis, R. S., and Anders, E. (1994). Interstellar grains in meteorites. I - Isolation of SiC, graphite, and diamond; size distributions of SiC and graphite. II - SiC and its noble gases. Geochim. Cosmochim. Acta, 58:459.

Andersen, A. C. (2007). Dust from AGB Stars. In Kerschbaum, F., Charbonnel, C., and Wing, R. F., editors, *Why Galaxies Care About AGB Stars: Their Importance as Actors and Probes*, volume 378 of *Astronomical Society of the Pacific Conference Series*, page 170.

Aringer, B. (2000). Carbon Stars in Open Clusters. In Wing, R. F., editor, *The Carbon Star Phenomenon*, volume 177 of *IAU Symposium*, page 519.

Aringer, B., Girardi, L., Nowotny, W., Marigo, P., and Bressan, A. (2016). Synthetic photometry for M and K giants and stellar evolution: hydrostatic dust-free model atmospheres and chemical abundances. MNRAS, 457:3611–3628.

Aringer, B., Girardi, L., Nowotny, W., Marigo, P., and Lederer, M. T. (2009). Synthetic photometry for carbon rich giants. I. Hydrostatic dust-free models. A&A, 503:913–928.

Aringer, B., Jorgensen, U. G., and Langhoff, S. R. (1997). SiO rotation-vibration bands in cool giants. I. A grid of model spectra for different stellar parameters. A&A, 323:202–210.

Ávila, J. N., Ireland, T. R., Gyngard, F., Zinner, E., Mallmann, G., Lugaro, M., Holden, P., and Amari, S. (2013). Ba isotopic compositions in stardust SiC grains from the Murchison meteorite: Insights into the stellar origins of large SiC grains. Geochim. Cosmochim. Acta, 120:628–647.

Barnbaum, C. (1992). Radial velocities of carbon stars - CO versus optical measurements. ApJ, 385:694–707.

Begemann, B., Dorschner, J., Henning, T., Mutschke, H., Guertler, J., Koempe, C., and Nass, R. (1997). Aluminum Oxide and the Opacity of Oxygen-rich Circumstellar Dust in the 12–17 Micron Range. ApJ, 476:199.

Bergeat, J. and Chevallier, L. (2005). The mass loss of C-rich giants. A&A, 429:235–246.

Bernatowicz, T., Fraundorf, G., Ming, T., Anders, E., Wopenka, B., Zinner, E., and Fraundorf, P. (1987). Evidence for interstellar SiC in the Murray carbonaceous meteorite. Nature, 330:728–730.

Bernatowicz, T. J., Cowsik, R., Gibbons, P. C., Lodders, K., Fegley, Jr., B., Amari, S., and Lewis, R. S. (1996). Constraints on Stellar Grain Formation from Presolar Graphite in the Murchison Meteorite. ApJ, 472:760.

Bertelli, G., Girardi, L., Marigo, P., and Nasi, E. (2008). Scaled solar tracks and isochrones in a large region of the Z-Y plane. I. From the ZAMS to the TP-AGB end for 0.15-2.5 $M_{\odot}$ stars. A&A, 484:815–830.

Bianchi, L., Conti, A., and Shiao, B. (2014). VizieR Online Data Catalog: GALEX-GR6/7 data release (Bianchi+ 2014). *VizieR Online Data Catalog*, 2335:0.

Bianchi, L., Efremova, B., Herald, J., Girardi, L., Zabot, A., Marigo, P., and Martin, C. (2011). Catalogues of hot white dwarfs in the Milky Way from GALEX's ultraviolet sky surveys: constraining stellar evolution. MNRAS, 411:2770–2791.

Bidelman, W. P. (1956). The carbon stars: an astrophysical enigma. *Vistas in Astronomy*, 2:1428–1437.

Bougoin, M. and Deny, P. (2004). The SiC technology is ready for the next generation of extremely large telescopes. In Atad-Ettedgui, E. and Dierickx, P., editors, *Optical Fabrication, Metrology, and Material Advancements for Telescopes*, volume 5494 of Proc. SPIE, pages 9–18.

Bowen, G. H. (1988). Dynamical modeling of long-period variable star atmospheres. ApJ, 329:299–317.

Bressan, A., Marigo, P., Girardi, L., Salasnich, B., Dal Cero, C., Rubele, S., and Nanni, A. (2012). PARSEC: stellar tracks and isochrones with the PAdova and TRieste Stellar Evolution Code. MNRAS, 427:127–145.

Burns, D., Baldwin, J. E., Boysen, R. C., Haniff, C. A., Lawson, P. R., Mackay, C. D., Rogers, J., Scott, T. R., St.-Jacques, D., Warner, P. J., Wilson, D. M. A., and Young, J. S. (1998). Large-amplitude periodic variations in the angular diameter of R Leonis. MNRAS, 297:462–466.

Chagnon, G., Mennesson, B., Perrin, G., Coudé du Foresto, V., Salomé, P., Bordé, P., Lacasse, M., and Traub, W. (2002). L'-Band Interferometric Observations of Evolved Stars. AJ, 124:2821–2832.

Chandler, A. A., Tatebe, K., Hale, D. D. S., and Townes, C. H. (2007). The Radiative Pattern and Asymmetry of IRC +10216 at 11 μm Measured with Interferometry and Closure Phase. ApJ, 657:1042–1045.

Chesneau, O. (2007). MIDI: Obtaining and analysing interferometric data in the mid-infrared. New A Rev., 51:666–681.

Chiavassa, A., Lacour, S., Millour, F., Driebe, T., Wittkowski, M., Plez, B., Thiébaut, E., Josselin, E., Freytag, B., Scholz, M., and Haubois, X. (2010). VLTI/AMBER spectro-interferometric imaging of VX Sagittarii's inhomogenous outer atmosphere. A&A, 511:A51.

Chiu, P.-J., Hoang, C.-T., Dinh-V-Trung, Lim, J., Kwok, S., Hirano, N., and Muthu, C. (2006). A Slowly Expanding Disk and Fast Bipolar Outflow from the S Star π^1 Gruis. ApJ, 645:605–612.

Cox, N. L. J., Kerschbaum, F., van Marle, A.-J., Decin, L., Ladjal, D., Mayer, A., Groenewegen, M. A. T., van Eck, S., Royer, P., Ottensamer, R., Ueta, T., Jorissen, A., Mecina, M., Meliani, Z., Luntzer, A., Blommaert, J. A. D. L., Posch, T., Vandenbussche, B., and Waelkens, C. (2012). A far-infrared survey of bow shocks and detached shells around AGB stars and red supergiants. A&A, 537:A35.

Cristallo, S., Straniero, O., Lederer, M. T., and Aringer, B. (2007). Molecular Opacities for Low-Mass Metal-poor AGB Stars Undergoing the Third Dredge-up. ApJ, 667:489–496.

Cruzalèbes, P., Jorissen, A., Chiavassa, A., Paladini, C., Rabbia, Y., and Spang, A. (2015). Departure from centrosymmetry of red giants and supergiants measured with VLTI/AMBER. MNRAS, 446:3277–3284.

Cruzalèbes, P., Jorissen, A., Rabbia, Y., Sacuto, S., Chiavassa, A., Pasquato, E., Plez, B., Eriksson, K., Spang, A., and Chesneau, O. (2013a). Fundamental parameters of 16 late-type stars derived from their angular diameter measured with VLTI/AMBER. MNRAS, 434:437–450.

Cruzalèbes, P., Jorissen, A., Rabbia, Y., Sacuto, S., Chiavassa, A., Pasquato, E., Plez, B., Eriksson, K., Spang, A., and Chesneau, O. (2013b). Fundamental parameters of 16 late-type stars derived from their angular diameter measured with VLTI/AMBER. MNRAS, 434:437–450.

Danchi, W. C., Bester, M., Degiacomi, C. G., Greenhill, L. J., and Townes, C. H. (1994). Characteristics of dust shells around 13 late-type stars. AJ, 107:1469–1513.

Davis, J., Tango, W. J., and Booth, A. J. (2000). Limb-darkening corrections for interferometric uniform disc stellar angular diameters. MNRAS, 318:387–392.

de Graauw, T., Haser, L. N., Beintema, D. A., Roelfsema, P. R., van Agthoven, H., Barl, L., Bauer, O. H., Bekenkamp, H. E. G., Boonstra, A.-J., Boxhoorn, D. R., Cote, J., de Groene, P., van Dijkhuizen, C., Drapatz, S., Evers, J., Feuchtgruber, H., Frericks, M.,

Genzel, R., Haerendel, G., Heras, A. M., van der Hucht, K. A., van der Hulst, T., Huygen, R., Jacobs, H., Jakob, G., Kamperman, T., Katterloher, R. O., Kester, D. J. M., Kunze, D., Kussendrager, D., Lahuis, F., Lamers, H. J. G. L. M., Leech, K., van der Lei, S., van der Linden, R., Luinge, W., Lutz, D., Melzner, F., Morris, P. W., van Nguyen, D., Ploeger, G., Price, S., Salama, A., Schaeidt, S. G., Sijm, N., Smoorenburg, C., Spakman, J., Spoon, H., Steinmayer, M., Stoecker, J., Valentijn, E. A., Vandenbussche, B., Visser, H., Waelkens, C., Waters, L. B. F. M., Wensink, J., Wesselius, P. R., Wiezorrek, E., Wieprecht, E., Wijnbergen, J. J., Wildeman, K. J., and Young, E. (1996). Observing with the ISO Short-Wavelength Spectrometer. A&A, 315:L49–L54.

De Marco, O. (2009). The Origin and Shaping of Planetary Nebulae: Putting the Binary Hypothesis to the Test. PASP, 121:316–342.

Decin, L., Richards, A. M. S., Neufeld, D., Steffen, W., Melnick, G., and Lombaert, R. (2015). ALMA data suggest the presence of spiral structure in the inner wind of CW Leonis. A&A, 574:A5.

Deroo, P., van Winckel, H., Verhoelst, T., Min, M., Reyniers, M., and Waters, L. B. F. M. (2007). The circumbinary disc around the J-type C-star <ASTROBJ>IRAS 18006-3213</ASTROBJ>. A&A, 467:1093–1101.

Dorschner, J., Friedemann, C., and Guertler, J. (1977). Silicon carbide and the infrared excess of carbon stars. *Astronomische Nachrichten*, 298:279–283.

Draine, B. T. (1981). Dust formation processes around red giants and supergiants. In Iben, Jr., I. and Renzini, A., editors, *Physical Processes in Red Giants*, volume 88 of *Astrophysics and Space Science Library*, pages 317–333.

Dumm, T. and Schild, H. (1998). Stellar radii of M giants. New A, 3:137–156.

Dyck, H. M., van Belle, G. T., and Benson, J. A. (1996). Angular Diameters and Effective Temperatures of Carbon Stars. AJ, 112:294.

Eggen, O. J. (1975). Observations of Large-Amplitude Red Variables. ApJS, 29:77.

Eisenhauer, F., Perrin, G., Straubmeier, C., Brandner, W., Boehm, A., Cassaing, F., Clenet, Y., Dodds-Eden, K., Eckart, A., Fedou, P., Gendron, E., Genzel, R., Gillessen, S., Graeter, A., Gueriau, C., Hamaus, N., Haubois, X., Haug, M., Henning, T., Hippler, S., Hofmann, R., Hormuth, F., Houairi, K., Kellner, S., Kervella, P., Klein, R., Kolmeder, J., Laun, W., Lena, P., Lenzen, R., Marteaud, M., Meschke, D., Naranjo, V., Neumann, U., Paumard, T., Perger, M., Perret, D., Rabien, S., Ramos, J. R., Reess, J. M., Rohloff, R. R., Rouan, D., Rousset, G., Ruyet, B., Schropp, M., Talureau, B., Thiel, M., Ziegleder, J., and Ziegler, D. (2008). GRAVITY: microarcsecond astrometry and deep interferometric imaging with the VLTI. In Jin, W. J., Platais, I., and Perryman, M. A. C., editors, *A Giant Step: from Milli- to Micro-arcsecond Astrometry*, volume 248 of *IAU Symposium*, pages 100–101.

Eriksson, K., Nowotny, W., Höfner, S., Aringer, B., and Wachter, A. (2014). Synthetic photometry for carbon-rich giants. IV. An extensive grid of dynamic atmosphere and wind models. A&A, 566:A95.

Fabian, D., Posch, T., Mutschke, H., Kerschbaum, F., and Dorschner, J. (2001). Infrared optical properties of spinels. A study of the carrier of the 13, 17 and 32 mu m emission features observed in ISO-SWS spectra of oxygen-rich AGB stars. A&A, 373:1125–1138.

Feast, M. (1999). Pulsation Modes in Mira and Semiregular Variables. In Le Bertre, T., Lebre, A., and Waelkens, C., editors, *Asymptotic Giant Branch Stars*, volume 191 of *IAU Symposium*, page 109.

Feast, M. W., Whitelock, P. A., Catchpole, R. M., Roberts, G., and Overbeek, M. D. (1984). Variable circumstellar obscuration of the carbon star R Fornacis. MNRAS, 211:331–337.

Fedele, D., Wittkowski, M., Paresce, F., Scholz, M., Wood, P. R., and Ciroi, S. (2005). The K-band intensity profile of R Leonis probed by VLTI/VINCI. A&A, 431:1019–1026.

Ferrarotti, A. S. and Gail, H.-P. (2006). Composition and quantities of dust produced by AGB-stars and returned to the interstellar medium. A&A, 447:553–576.

Fleischer, A. J., Gauger, A., and Sedlmayr, E. (1992). Circumstellar dust shells around long-period variables. I - Dynamical models of C-stars including dust formation, growth and evaporation. A&A, 266:321–339.

Frankowski, A., Jancart, S., and Jorissen, A. (2007). Proper-motion binaries in the Hipparcos catalogue. Comparison with radial velocity data. A&A, 464:377–392.

Friedman, C. (1969). *Physica*, 41:189.

Gail, H.-P. and Sedlmayr, E. (1988). Dust formation in stellar winds. IV - Heteromolecular carbon grain formation and growth. A&A, 206:153–168.

Gail, H.-P. and Sedlmayr, E. (2013). *Physics and Chemistry of Circumstellar Dust Shells*. Cambridge, UK: Cambridge University Press, 2013.

Gauger, A., Sedlmayr, E., and Gail, H.-P. (1990). Dust formation, growth and evaporation in a cool pulsating circumstellar shell. A&A, 235:345–361.

Gautschy-Loidl, R., Höfner, S., Jørgensen, U. G., and Hron, J. (2004). Dynamic model atmospheres of AGB stars. IV. A comparison of synthetic carbon star spectra with observations. A&A, 422:289–306.

Gilman, R. C. (1969). On the Composition of Circumstellar Grains. ApJ, 155:L185.

Glindemann, A. (2011). *Principles of Stellar Interferometry*. Astronomy and Astrophysics Library. ISBN 978-3-642-15027-2. Springer-Verlag Berlin Heidelberg.

Goebel, J. H., Bregman, J. D., Goorvitch, D., Strecker, D. W., Puetter, R. C., Russell, R. W., Soifer, B. T., Willner, S. P., Forrest, W. J., Houck, J. R., and McCarthy, J. F. (1980). The infrared spectrum of the carbon star Y Canum Venaticorum between 1.2 and 30 microns. ApJ, 235:104–113.

González Delgado, D., Olofsson, H., Schwarz, H. E., Eriksson, K., and Gustafsson, B. (2001). Imaging of detached shells around the carbon stars R Scl and U Ant through scattered stellar light. A&A, 372:885–898.

González Delgado, D., Olofsson, H., Schwarz, H. E., Eriksson, K., Gustafsson, B., and Gledhill, T. (2003). Imaging polarimetry of stellar light scattered in detached shells around the carbon stars R Scl and U Ant. A&A, 399:1021–1035.

Groenewegen, M. A. T. (2012). An extension of the DUSTY radiative transfer code and an application to OH 26.5 and TT Cygni. A&A, 543:A36.

Groenewegen, M. A. T. and de Jong, T. (1998). CO observations and mass loss of MS- and S-stars. A&A, 337:797–807.

Groenewegen, M. A. T., Sevenster, M., Spoon, H. W. W., and Pérez, I. (2002). Millimetre observations of infrared carbon stars. I. The data. A&A, 390:501–510.

Groenewegen, M. A. T., Waelkens, C., Barlow, M. J., Kerschbaum, F., Garcia-Lario, P., Cernicharo, J., Blommaert, J. A. D. L., Bouwman, J., Cohen, M., Cox, N., Decin, L., Exter, K., Gear, W. K., Gomez, H. L., Hargrave, P. C., Henning, T., Hutsemékers, D., Ivison, R. J., Jorissen, A., Krause, O., Ladjal, D., Leeks, S. J., Lim, T. L., Matsuura, M., Nazé, Y., Olofsson, G., Ottensamer, R., Polehampton, E., Posch, T., Rauw, G., Royer, P., Sibthorpe, B., Swinyard, B. M., Ueta, T., Vamvatira-Nakou, C., Vandenbussche, B., van de Steene, G. C., van Eck, S., van Hoof, P. A. M., van Winckel, H., Verdugo, E., and Wesson, R. (2011). MESS (Mass-loss of Evolved StarS), a Herschel key program. A&A, 526:A162.

Gupta, R., Singh, H. P., Volk, K., and Kwok, S. (2004). Automated Classification of 2000 Bright IRAS Sources. ApJS, 152:201–209.

Gustafsson, B., Bell, R. A., Eriksson, K., and Nordlund, A. (1975). A grid of model atmospheres for metal-deficient giant stars. I. A&A, 42:407–432.

Gustafsson, B., Edvardsson, B., Eriksson, K., Jørgensen, U. G., Nordlund, Å., and Plez, B. (2008). A grid of MARCS model atmospheres for late-type stars. I. Methods and general properties. A&A, 486:951–970.

Habing, H. J. and Olofsson, H., editors (2003). *Asymptotic giant branch stars, by Harm J. Habing and Hans Olofsson. Astronomy and astrophysics library, New York, Berlin: Springer, 2003.*

Hackwell, J. A. (1972). Long wavelength spectrometry and photometry of M, S and C-stars. A&A, 21:239–248.

Hedrosa, R. P., Abia, C., Busso, M., Cristallo, S., Domínguez, I., Palmerini, S., Plez, B., and Straniero, O. (2013). Nitrogen Isotopes in Asymptotic Giant Branch Carbon Stars and Presolar SiC Grains: A Challenge for Stellar Nucleosynthesis. ApJ, 768:L11.

Henden, A. A., Templeton, M., Terrell, D., Smith, T. C., Levine, S., and Welch, D. (2016). VizieR Online Data Catalog: AAVSO Photometric All Sky Survey (APASS) DR9 (Henden+, 2016). *VizieR Online Data Catalog*, 2336.

Hinkle, K. H., Lebzelter, T., and Straniero, O. (2016). Carbon and Oxygen Isotopic Ratios for Nearby Miras. ApJ, 825:38.

Hofmann, K.-H., Balega, Y., Blöcker, T., and Weigelt, G. (2001). A multi-wavelength study of the oxygen-rich AGB star <ASTROBJ>CIT 3</ASTROBJ>: Bispectrum speckle interferometry and dust-shell modelling. A&A, 379:529–539.

Höfner, S. (1999). A new generation of dynamic model atmospheres for AGB stars: first results. A&A, 346:L9–L12.

Höfner, S. (2007). Headwind: Modelling Mass Loss of AGB Stars, Against All Odds. In Kerschbaum, F., Charbonnel, C., and Wing, R. F., editors, *Why Galaxies Care About AGB Stars: Their Importance as Actors and Probes*, volume 378 of *Astronomical Society of the Pacific Conference Series*, page 145.

Höfner, S. (2008). Winds of M-type AGB stars driven by micron-sized grains. A&A, 491:L1–L4.

Höfner, S., Bladh, S., Aringer, B., and Ahuja, R. (2016). Dynamic atmospheres and winds of cool luminous giants, I. Al_2O_3 and silicate dust in the close vicinity of M-type AGB stars. *ArXiv e-prints*.

Höfner, S. and Dorfi, E. A. (1997). Dust formation in winds of long-period variables. IV. Atmospheric dynamics and mass loss. A&A, 319:648–654.

Höfner, S., Gautschy-Loidl, R., Aringer, B., and Jørgensen, U. G. (2003). Dynamic model atmospheres of AGB stars. III. Effects of frequency-dependent radiative transfer. A&A, 399:589–601.

Hoppe, P., Amari, S., Zinner, E., Ireland, T., and Lewis, R. S. (1994). Carbon, nitrogen, magnesium, silicon, and titanium isotopic compositions of single interstellar silicon carbide grains from the Murchison carbonaceous chondrite. ApJ, 430:870–890.

Hoppe, P., Leitner, J., Gröner, E., Marhas, K. K., Meyer, B. S., and Amari, S. (2010). NanoSIMS Studies of Small Presolar SiC Grains: New Insights into Supernova Nucleosynthesis, Chemistry, and Dust Formation. ApJ, 719:1370–1384.

Hron, J., Blommaert, J., Decin, L., Lebzelter, T., Paladini, C., van Winckel, H., Metis, and Matisse Teams (2015a). E-ELT METIS and MATISSE: Prospects for AGB Stars. In Kerschbaum, F., Wing, R. F., and Hron, J., editors, *Why Galaxies Care about AGB Stars III: A Closer Look in Space and Time*, volume 497 of *Astronomical Society of the Pacific Conference Series*, page 529.

Hron, J., Loidl, R., and Kerschbaum, F. (1997). Dust Features of Visually Bright AGB Variables as Seen by ISO and IRAS. Ap&SS, 251:211–214.

Hron, J., Uttenthaler, S., Aringer, B., Klotz, D., Lebzelter, T., Paladini, C., and Wiedemann, G. (2015b). The complex environment of the bright carbon star TX Piscium as probed by spectro-astrometry. A&A, 584:A27.

Iben, Jr., I. (1975). Thermal pulses; p-capture, alpha-capture, s-process nucleosynthesis; and convective mixing in a star of intermediate mass. ApJ, 196:525–547.

Iben, Jr., I. and Renzini, A., editors (1981). *Physical processes in red giants; Proceedings of the Second Workshop, Advanced School of Astronomy, Erice, Italy, September 3-13, 1980*, volume 88 of *Astrophysics and Space Science Library*.

Iben, Jr., I. and Renzini, A. (1983). Asymptotic giant branch evolution and beyond. ARA&A, 21:271–342.

Imai, H., Shibata, K. M., Sasao, T., Miyoshi, M., Kameya, O., Omodaka, T., Morimoto, M., Iwata, T., Suzuyama, T., Mochizuki, N., Miyaji, T., and Takeuti, M. (1997). Measurement of shifts in line-of-sight velocities of stellar water masers using VLBI. A&A, 319:L1–L4.

Ireland, M. J., Scholz, M., Tuthill, P. G., and Wood, P. R. (2004a). Pulsation of M-type Mira variables with moderately different mass: search for observable mass effects. MNRAS, 355:444–450.

Ireland, M. J., Tuthill, P. G., Bedding, T. R., Robertson, J. G., and Jacob, A. P. (2004b). Multiwavelength diameters of nearby Miras and semiregular variables. MNRAS, 350:365–374.

Ivezić, Z. and Elitzur, M. (1995). Infrared emission and dynamics of outlfows in late-type stars. ApJ, 445:415–432.

Ivezic, Z. and Elitzur, M. (1997). Self-similarity and scaling behaviour of infrared emission from radiatively heated dust - I. Theory. MNRAS, 287:799–811.

Ivezić, Z., Groenewegen, M. A. T., Men'shchikov, A., and Szczerba, R. (1997). Benchmark problems for dust radiative transfer. MNRAS, 291:121–124.

Ivezić, Z., Nenkova, M., and Elitzur, M. (1999). User Manual for DUSTY. *ArXiv Astrophysics e-prints*.

Izumiura, H., Hashimoto, O., Kawara, K., Yamamura, I., and Waters, L. B. F. M. (1996). A detached dust shell surrounding the J-type carbon star Y Canum Venaticorum. A&A, 315:L221–L224.

Izumiura, H., Kester, D. J. M., de Jong, T., Loup, C., Waters, L. B. F. M., and Bontekoe, T. R. (1995). Extended Dust Shells around Carbon Stars resolved by "HIRAS". Ap&SS, 224:495–496.

Jaffe, W. J. (2004). Coherent fringe tracking and visibility estimation for MIDI. In Traub, W. A., editor, *New Frontiers in Stellar Interferometry*, volume 5491 of *Society of Photo-Optical Instrumentation Engineers (SPIE) Conference Series*, page 715.

Jager, C., Mutschke, H., and Henning, T. (1998). Optical properties of carbonaceous dust analogues. A&A, 332:291–299.

Jørgensen, U. G. (1992). Sampling Methods. Rev. Mexicana Astron. Astrofis., 23:195.

Jørgensen, U. G., Hron, J., and Loidl, R. (2000). ISO-SWS spectra of the carbon stars TX Psc, V460 Cyg, and TT Cyg. A&A, 356:253–266.

Jorissen, A., Frayer, D. T., Johnson, H. R., Mayor, M., and Smith, V. V. (1993). S stars: infrared colors, technetium, and binarity. A&A, 271:463.

Jorissen, A. and Knapp, G. R. (1998). Circumstellar shells and mass loss rates: Clues to the evolution of S stars. A&AS, 129:363–398.

Jorissen, A., Mayer, A., van Eck, S., Ottensamer, R., Kerschbaum, F., Ueta, T., Bergman, P., Blommaert, J. A. D. L., Decin, L., Groenewegen, M. A. T., Hron, J., Nowotny, W., Olofsson, H., Posch, T., Sjouwerman, L. O., Vandenbussche, B., and Waelkens, C. (2011). X Herculis and TX Piscium: two cases of ISM interaction with stellar winds observed by Herschel. A&A, 532:A135.

Kahane, C. and Jura, M. (1994). Circumstellar CO around bright oxygen-rich semi-regulars. A&A, 290:183–197.

Karakas, A. I., Lattanzio, J. C., and Pols, O. R. (2002). Parameterising the Third Dredge-up in Asymptotic Giant Branch Stars. PASA, 19:515–526.

Karovicova, I., Wittkowski, M., Boboltz, D. A., Fossat, E., Ohnaka, K., and Scholz, M. (2011). Mid-infrared interferometric monitoring of evolved stars. The dust shell around the Mira variable RR Aquilae at 13 epochs. A&A, 532:A134.

Karovicova, I., Wittkowski, M., Ohnaka, K., Boboltz, D. A., Fossat, E., and Scholz, M. (2013). New insights into the dust formation of oxygen-rich AGB stars. A&A, 560:A75.

Kenyon, S. J. (1986). *The symbiotic stars*. Cambridge and New York, Cambridge University Press.

Kerschbaum, F., Ladjal, D., Ottensamer, R., Groenewegen, M. A. T., Mecina, M., Blommaert, J. A. D. L., Baumann, B., Decin, L., Vandenbussche, B., Waelkens, C., Posch, T., Huygen, E., De Meester, W., Regibo, S., Royer, P., Exter, K., and Jean, C. (2010). The detached dust shells of AQ Andromedae, U Antliae, and TT Cygni. A&A, 518:L140.

Kervella, P., Montargès, M., Lagadec, E., Ridgway, S. T., Haubois, X., Girard, J. H., Ohnaka, K., Perrin, G., and Gallenne, A. (2015). The dust disk and companion of the nearby AGB star L_2 Puppis. SPHERE/ZIMPOL polarimetric imaging at visible wavelengths. A&A, 578:A77.

Kervella, P., Montargès, M., Ridgway, S. T., Perrin, G., Chesneau, O., Lacour, S., Chiavassa, A., Haubois, X., and Gallenne, A. (2014). An edge-on translucent dust disk around the nearest AGB star, L_2 Puppis. VLT/NACO spectro-imaging from 1.04 to 4.05 μm and VLTI interferometry. A&A, 564:A88.

Kholopov, P. N., Samus, N. N., Frolov, M. S., Goranskij, V. P., Gorynya, N. A., Karitskaya, E. A., Kazarovets, E. V., Kireeva, N. N., Kukarkina, N. P., Kurochkin, N. E., Medvedeva, G. I., Pastukhova, E. N., Perova, N. B., Rastorguev, A. S., and Shugarov, S. Y. (1998). Combined General Catalogue of Variable Stars. In *Combined General Catalogue of Variable Stars, 4.1 Ed (II/214A). (1998)*, page 0.

Klotz, D. (2013). *Mass loss from AGB stars – from VLT to Herschel and back*. PhD thesis, Institute for Astrophysics, University of Vienna, Austria.

Klotz, D., Paladini, C., Hron, J., Aringer, B., Sacuto, S., Marigo, P., and Verhoelst, T. (2013a). Catching the fish - Constraining stellar parameters for TX Piscium using spectro-interferometric observations. A&A, 550:A86.

Klotz, D., Paladini, C., Hron, J., Aringer, B., Sacuto, S., Marigo, P., and Verhoelst, T. (2013b). Catching the fish - Constraining stellar parameters for TX Piscium using spectro-interferometric observations. A&A, 550:A86.

Klotz, D., Sacuto, S., Kerschbaum, F., Paladini, C., Olofsson, H., and Hron, J. (2012a). The geometry of the close environment of SV Piscium as probed by VLTI/MIDI. A&A, 541:A164.

Klotz, D., Sacuto, S., Kerschbaum, F., Paladini, C., Olofsson, H., and Hron, J. (2012a). The geometry of the close environment of SV Piscium as probed by VLTI/MIDI. A&A, 541:A164.

Klotz, D., Sacuto, S., Paladini, C., Hron, J., and Wachter, G. (2012b). Geometrical model fitting for interferometric data: GEM-FIND. In *Society of Photo-Optical Instrumentation Engineers (SPIE) Conference Series*, volume 8445 of *Society of Photo-Optical Instrumentation Engineers (SPIE) Conference Series*, page 1.

Knapp, G. R., Jorissen, A., and Young, K. (1997). A 200km/s molecular wind in the peculiar carbon star V Hya. A&A, 326:318–328.

Knapp, G. R., Pourbaix, D., Platais, I., and Jorissen, A. (2003). Reprocessing the Hipparcos data of evolved stars. III. Revised Hipparcos period-luminosity relationship for galactic long-period variable stars. A&A, 403:993–1002.

Knapp, G. R., Young, K., and Crosas, M. (1999). The circumstellar envelope of pi (1) Gru. A&A, 346:175–180.

Knapp, G. R., Young, K., Lee, E., and Jorissen, A. (1998). Multiple Molecular Winds in Evolved Stars. I. A Survey of CO(2-1) and CO(3-2) Emission from 45 Nearby Asymptotic Giant Branch Stars. ApJS, 117:209–231.

Kozasa, T., Dorschner, J., Henning, T., and Stognienko, R. (1996). Formation of SiC grains and the 11.3μm feature in circumstellar envelopes of carbon stars. A&A, 307:551–560.

Labeyrie, A., Lipson, S. G., and Nisenson, P. (2006). *An Introduction to Optical Stellar Interferometry*. pp. 360. Cambridge University Press, June 2006. ISBN-10: 0521828724. ISBN-13: 9780521828727. LCCN: QB117 .L334.

Ladjal, D. (2011). *The Herschel - PACS guaranteed time key programme on evolved stars: its preparation, execution and initial data exploitation.* PhD thesis, Institute of Astronomy, Katholieke Universiteit Leuven, Belgium.

Lagadec, E., Verhoelst, T., Mékarnia, D., Suáeez, O., Zijlstra, A. A., Bendjoya, P., Szczerba, R., Chesneau, O., van Winckel, H., Barlow, M. J., Matsuura, M., Bowey, J. E., Lorenz-Martins, S., and Gledhill, T. (2011). A mid-infrared imaging catalogue of post-asymptotic giant branch stars. MNRAS, 417:32–92.

Lambert, D. L., Gustafsson, B., Eriksson, K., and Hinkle, K. H. (1986). The chemical composition of carbon stars. I - Carbon, nitrogen, and oxygen in 30 cool carbon stars in the Galactic disk. ApJS, 62:373–425.

Lançon, A. and Mouhcine, M. (2002). The modelling of intermediate-age stellar populations. II. Average spectra for upper AGB stars, and their use. A&A, 393:167–181.

Lattanzi, M. G., Munari, U., Whitelock, P. A., and Feast, M. W. (1997). Interferometric Angular Diameters of Mira Variables with the Hubble Space Telescope. ApJ, 485:328.

Leão, I. C., de Laverny, P., Mékarnia, D., de Medeiros, J. R., and Vandame, B. (2006). The circumstellar envelope of IRC+10216 from milli-arcsecond to arcmin scales. A&A, 455:187–194.

Le Bertre, T. (1988). Optical and infrared observations of the carbon Mira R Fornacis - Dust shell modelling as a function of phase. A&A, 190:79–86.

Le Bertre, T. (1992). Carbon-star lightcurves in the 1-20 micron range. A&AS, 94:377–398.

Le Bertre, T. (1993). Oxygen-rich late-type star lightcurves in the 1-20 microns range. A&AS, 97:729–753.

Le Bouquin, J.-B., Berger, J.-P., Lazareff, B., Zins, G., Haguenauer, P., Jocou, L., Kern, P., Millan-Gabet, R., Traub, W., Absil, O., Augereau, J.-C., Benisty, M., Blind, N., Bonfils, X., Bourget, P., Delboulbe, A., Feautrier, P., Germain, M., Gitton, P., Gillier, D., Kiekebusch, M., Kluska, J., Knudstrup, J., Labeye, P., Lizon, J.-L., Monin, J.-L., Magnard, Y., Malbet, F., Maurel, D., Ménard, F., Micallef, M., Michaud, L., Montagnier, G., Morel, S., Moulin, T., Perraut, K., Popovic, D., Rabou, P., Rochat, S., Rojas, C., Roussel, F., Roux, A., Stadler, E., Stefl, S., Tatulli, E., and Ventura, N. (2011). PIONIER: a 4-telescope visitor instrument at VLTI. A&A, 535:A67.

Le Bouquin, J.-B., Lacour, S., Renard, S., Thiébaut, E., Merand, A., and Verhoelst, T. (2009). Pre-maximum spectro-imaging of the Mira star T Leporis with AMBER/VLTI. A&A, 496:L1–L4.

Lebzelter, T., Nowotny, W., Höfner, S., Lederer, M. T., Hinkle, K. H., and Aringer, B. (2010). Abundance analysis for long period variables. Velocity effects studied with O-rich dynamic model atmospheres. A&A, 517:A6.

Lebzelter, T., Seifahrt, A., Uttenthaler, S., Ramsay, S., Hartman, H., Nieva, M.-F., Przybilla, N., Smette, A., Wahlgren, G. M., Wolff, B., Hussain, G. A. J., Käufl, H. U., and Seemann, U. (2012). CRIRES-POP. A library of high resolution spectra in the near-infrared. A&A, 539:A109.

Lederer, M. (2009). *Third dredge-up in cluster AGB stars*. PhD thesis, Department of Astronomy, University of Vienna.

Leinert, C., Graser, U., Przygodda, F., Waters, L. B. F. M., Perrin, G., Jaffe, W., Lopez, B., Bakker, E. J., Böhm, A., Chesneau, O., Cotton, W. D., Damstra, S., de Jong, J., Glazenborg-Kluttig, A. W., Grimm, B., Hanenburg, H., Laun, W., Lenzen, R., Ligori, S., Mathar, R. J., Meisner, J., Morel, S., Morr, W., Neumann, U., Pel, J.-W., Schuller, P., Rohloff, R.-R., Stecklum, B., Storz, C., von der Lühe, O., and Wagner, K. (2003a). MIDI - the 10 \mum instrument on the VLTI. Ap&SS, 286:73–83.

Leinert, C., Graser, U., Richichi, A., Schöller, M., Waters, L. F. B. M., Perrin, G., Jaffe, W., Lopez, B., Glazenborg-Kluttig, A., Przygodda, F., Morel, S., Biereichel, P., Haddad, N., Housen, N., and Wallander, A. (2003b). MIDI combines light from the VLTI: the start of 10 μm interferometry at ESO. *The Messenger*, 112:13–18.

Leinert, C., van Boekel, R., Waters, L. B. F. M., Chesneau, O., Malbet, F., Köhler, R., Jaffe, W., Ratzka, T., Dutrey, A., Preibisch, T., Graser, U., Bakker, E., Chagnon, G., Cotton, W. D., Dominik, C., Dullemond, C. P., Glazenborg-Kluttig, A. W., Glindemann, A., Henning, T., Hofmann, K.-H., de Jong, J., Lenzen, R., Ligori, S., Lopez, B., Meisner, J., Morel, S., Paresce, F., Pel, J.-W., Percheron, I., Perrin, G., Przygodda, F., Richichi, A., Schöller, M., Schuller, P., Stecklum, B., van den Ancker, M. E., von der Lühe, O., and Weigelt, G. (2004). Mid-infrared sizes of circumstellar disks around Herbig Ae/Be stars measured with MIDI on the VLTI. A&A, 423:537–548.

Lewis, R. S., Amari, S., and Anders, E. (1994). Interstellar grains in meteorites: II. SiC and its noble gases. Geochim. Cosmochim. Acta, 58:471–494.

Lewis, R. S., Ming, T., Wacker, J. F., Anders, E., and Steel, E. (1987). Interstellar diamonds in meteorites. Nature, 326:160–162.

Lloyd Evans, T. (2010). Carbon stars. *Journal of Astrophysics and Astronomy*, 31:177–211.

Lobel, A., Doyle, J. G., and Bagnulo, S. (1999). Modelling the spectral energy distribution and SED variability of the Carbon Mira R Fornacis. A&A, 343:466–476.

Loidl, R. (2001). *Spectral variability of carbon stars: A comparison between theory and observations*. PhD thesis, University of Vienna, Department of Astronomy.

Loidl, R., Höfner, S., Jørgensen, U. G., and Aringer, B. (1999). Dynamic model atmospheres of AGB stars. II. Synthetic near infrared spectra of carbon stars. A&A, 342:531–541.

Loidl, R., Lançon, A., and Jørgensen, U. G. (2001). Spectra of carbon-rich asymptotic giant branch stars between 0.5 and 2.5 mu m: Theory meets observation. A&A, 371:1065–1077.

Lopez, B., Wolf, S., Lagarde, S., Abraham, P., Antonelli, P., Augereau, J. C., Beckman, U., Behrend, J., Berruyer, N., Bresson, Y., Chesneau, O., Clausse, J. M., Connot, C., Demyk, K., Danchi, W. C., Dugué, M., Flament, S., Glazenborg, A., Graser, U., Henning, T., Hofmann, K. H., Heininger, M., Hugues, Y., Jaffe, W., Jankov, S., Kraus, S., Laun, W., Leinert, C., Linz, H., Mathias, P., Meisenheimer, K., Matter, A., Menut, J. L., Millour, F., Neumann, U., Nussbaum, E., Niedzielski, A., Mosonic, L., Petrov, R., Ratzka, T., Robbe-Dubois, S., Roussel, A., Schertl, D., Schmider, F.-X., Stecklum, B., Thiebaut, E., Vakili, F., Wagner, K., Waters, L. B. F. M., and Weigelt, G. (2006). MATISSE: perspective of imaging in the mid-infrared at the VLTI. In *Society of Photo-Optical Instrumentation Engineers (SPIE) Conference Series*, volume 6268 of Proc. SPIE, page 62680Z.

Lorenz-Martins, S., de Araújo, F. X., Codina Landaberry, S. J., de Almeida, W. G., and de Nader, R. V. (2001). Modeling of C stars with core/mantle grains: Amorphous carbon + SiC. A&A, 367:189–198.

Loup, C., Forveille, T., Omont, A., and Paul, J. F. (1993). CO and HCN observations of circumstellar envelopes. A catalogue - Mass loss rates and distributions. A&AS, 99:291–377.

Lykou, F., Klotz, D., Paladini, C., Hron, J., Zijlstra, A. A., Kluska, J., Norris, B. R. M., Tuthill, P. G., Ramstedt, S., Lagadec, E., Wittkowski, M., Maercker, M., and Mayer, A. (2015). Dissecting the AGB star L_2 Puppis: a torus in the making. A&A, 576:A46.

Maercker, M., Mohamed, S., Vlemmings, W. H. T., Ramstedt, S., Groenewegen, M. A. T., Humphreys, E., Kerschbaum, F., Lindqvist, M., Olofsson, H., Paladini, C., Wittkowski, M., de Gregorio-Monsalvo, I., and Nyman, L.-A. (2012). Unexpectedly large mass loss during the thermal pulse cycle of the red giant star R Sculptoris. Nature, 490:232–234.

Maercker, M., Olofsson, H., Eriksson, K., Gustafsson, B., and Schöier, F. L. (2010). The detached dust and gas shells around the carbon star U Antliae. A&A, 511:A37.

Makarov, V. V. and Kaplan, G. H. (2005). Statistical Constraints for Astrometric Binaries with Nonlinear Motion. AJ, 129:2420–2427.

Marigo, P. and Aringer, B. (2009). Low-temperature gas opacity. ÆSOPUS: a versatile and quick computational tool. A&A, 508:1539–1569.

Marigo, P., Bressan, A., Nanni, A., Girardi, L., and Pumo, M. L. (2013). Evolution of thermally pulsing asymptotic giant branch stars - I. The COLIBRI code. MNRAS, 434:488–526.

Marigo, P. and Girardi, L. (2007). Evolution of asymptotic giant branch stars. I. Updated synthetic TP-AGB models and their basic calibration. A&A, 469:239–263.

Marigo, P., Girardi, L., Bressan, A., Groenewegen, M. A. T., Silva, L., and Granato, G. L. (2008). Evolution of asymptotic giant branch stars. II. Optical to far-infrared isochrones with improved TP-AGB models. A&A, 482:883–905.

Martí-Vidal, I., Marcaide, J. M., Quirrenbach, A., Ohnaka, K., Guirado, J. C., and Wittkowski, M. (2011). AMBER observations of the AGB star RS Capricorni: extended atmosphere and comparison with stellar models. A&A, 529:A115.

Mattsson, L. and Höfner, S. (2011). Dust-driven mass loss from carbon stars as a function of stellar parameters. II. Effects of grain size on wind properties. A&A, 533:A42.

Mattsson, L., Wahlin, R., and Höfner, S. (2010). Dust driven mass loss from carbon stars as a function of stellar parameters . I. A grid of solar-metallicity wind models. A&A, 509:A14.

Mauron, N. and Huggins, P. J. (2006). Imaging the circumstellar envelopes of AGB stars. A&A, 452:257–268.

Mayer, A., Jorissen, A., Kerschbaum, F., Mohamed, S., van Eck, S., Ottensamer, R., Blommaert, J. A. D. L., Decin, L., Groenewegen, M. A. T., Posch, T., Vandenbussche, B., and Waelkens, C. (2011). Herschel's view into Mira's head. A&A, 531:L4.

Mayer, A., Jorissen, A., Kerschbaum, F., Ottensamer, R., Nowotny, W., Cox, N. L. J., Aringer, B., Blommaert, J. A. D. L., Decin, L., van Eck, S., Gail, H.-P., Groenewegen, M. A. T., Kornfeld, K., Mecina, M., Posch, T., Vandenbussche, B., and Waelkens, C. (2013). Large-scale environments of binary AGB stars probed by Herschel. I. Morphology statistics and case studies of R Aquarii and W Aquilae. A&A, 549:A69.

Mayer, A., Jorissen, A., Paladini, C., Kerschbaum, F., Pourbaix, D., Siopis, C., Ottensamer, R., Mečina, M., Cox, N. L. J., Groenewegen, M. A. T., Klotz, D., Sadowski, G., Spang, A., Cruzalèbes, P., and Waelkens, C. (2014). Large-scale environments of binary AGB stars probed by Herschel. II. Two companions interacting with the wind of π^1 Gruis. A&A, 570:A113.

McDonald, I., Zijlstra, A. A., and Boyer, M. L. (2012). Fundamental parameters and infrared excesses of Hipparcos stars. MNRAS, 427:343–357.

McKellar, A. (1940). Intense λ 6708 Resonance Doublet of Li I in the Spectrum of WZ Cassiopeiae. PASP, 52:407.

Mennesson, B., Perrin, G., Chagnon, G., du Coudé Foresto, V., Ridgway, S., Merand, A., Salome, P., Borde, P., Cotton, W., Morel, S., Kervella, P., Traub, W., and Lacasse, M. (2002). Evidence for Very Extended Gaseous Layers around O-rich Mira Variables and M Giants. ApJ, 579:446–454.

Merrill, P. W. (1952). Spectroscopic Observations of Stars of Class. ApJ, 116:21.

Mečina, M., Kerschbaum, F., Groenewegen, M. A. T., Ottensamer, R., Blommaert, J. A. D. L., Mayer, A., Decin, L., Luntzer, A., Vandenbussche, B., Posch, T., and Waelkens, C. (2014). Dusty shells surrounding the carbon variables S Scuti and RT Capricorni. A&A, 566:A69.

Meyer, C., Rabbia, Y., Froeschle, M., Helmer, G., and Amieux, G. (1995). Observations of lunar occultations at Observatoire de la Cote d'Azur. A&AS, 110:107.

Monnier, J. D. (2007). Phases in interferometry. New A Rev., 51:604–616.

Monnier, J. D., Geballe, T. R., and Danchi, W. C. (1998). Temporal Variations of Midinfrared Spectra in Late-Type Stars. ApJ, 502:833–846.

Monnier, J. D., Geballe, T. R., and Danchi, W. C. (1999). Mid-Infrared Spectra of Late-Type Stars: Long-Term Evolution. ApJ, 521:261–270.

Monnier, J. D., Millan-Gabet, R., Tuthill, P. G., Traub, W. A., Carleton, N. P., Coudé du Foresto, V., Danchi, W. C., Lacasse, M. G., Morel, S., Perrin, G., Porro, I. L., Schloerb, F. P., and Townes, C. H. (2004). High-Resolution Imaging of Dust Shells by Using Keck Aperture Masking and the IOTA Interferometer. ApJ, 605:436–461.

Nanni, A., Marigo, P., Groenewegen, M. A. T., Aringer, B., Girardi, L., Pastorelli, G., Bressan, A., and Bladh, S. (2016). Constraining dust properties in Circumstellar Envelopes of C-stars in the Small Magellanic Cloud: optical constants and grain size of Carbon dust. *ArXiv e-prints*.

Neilson, H. R. and Lester, J. B. (2008). Determining parameters of cool giant stars by modeling spectrophotometric and interferometric observations using the SAtlas program. A&A, 490:807–810.

Norris, B. R. M., Tuthill, P. G., Ireland, M. J., Lacour, S., Zijlstra, A. A., Lykou, F., Evans, T. M., Stewart, P., and Bedding, T. R. (2012). A close halo of large transparent grains around extreme red giant stars. Nature, 484:220–222.

Nowotny, W. (2005). *The dynamic atmospheres of red giant stars. Spectral synthesis in high resolution*. PhD thesis, Institut für Astronomie der Universität Wien, Türkenschanzstrasse 17, A-1180 Wien, Austria.

Nowotny, W., Aringer, B., Höfner, S., and Eriksson, K. (2013). Synthetic photometry for carbon-rich giants. III. Tracing the sequence of mass-losing galactic C-type Miras. A&A, 552:A20.

Nowotny, W., Aringer, B., Höfner, S., and Lederer, M. T. (2011). Synthetic photometry for carbon-rich giants. II. The effects of pulsation and circumstellar dust. A&A, 529:A129.

Nowotny, W., Höfner, S., and Aringer, B. (2010). Line formation in AGB atmospheres including velocity effects. Molecular line profile variations of long period variables. A&A, 514:A35.

Nowotny, W., Lebzelter, T., Hron, J., and Höfner, S. (2005a). Atmospheric dynamics in carbon-rich Miras. II. Models meet observations. A&A, 437:285–296.

Nowotny, W., Lebzelter, T., Hron, J., and Höfner, S. (2005b). Atmospheric dynamics in carbon-rich Miras. II. Models meet observations. A&A, 437:285–296.

Ohnaka, K., Bergeat, J., Driebe, T., Graser, U., Hofmann, K.-H., Köhler, R., Leinert, C., Lopez, B., Malbet, F., Morel, S., Paresce, F., Perrin, G., Preibisch, T., Richichi, A., Schertl, D., Schöller, M., Sol, H., Weigelt, G., and Wittkowski, M. (2005). Mid-infrared interferometry of the Mira variable RR Sco with the VLTI MIDI instrument. A&A, 429:1057–1067.

Ohnaka, K., Driebe, T., Hofmann, K.-H., Weigelt, G., and Wittkowski, M. (2008a). Spatially resolved dusty torus toward the red supergiant WOH G64 in the Large Magellanic Cloud. A&A, 484:371–379.

Ohnaka, K., Driebe, T., Weigelt, G., and Wittkowski, M. (2007). Temporal variations of the outer atmosphere and the dust shell of the carbon-rich Mira variable V Ophiuchi probed with VLTI/MIDI. A&A, 466:1099–1110.

Ohnaka, K., Izumiura, H., Leinert, C., Driebe, T., Weigelt, G., and Wittkowski, M. (2008b). Asymmetric silicate dust distribution toward the silicate carbon star BM Geminorum. A&A, 490:173–178.

Olnon, F. M., Raimond, E., Neugebauer, G., van Duinen, R. J., Habing, H. J., Aumann, H. H., Beintema, D. A., Boggess, N., Borgman, J., Clegg, P. E., Gillett, F. C., Hauser, M. G., Houck, J. R., Jennings, R. E., de Jong, T., Low, F. J., Marsden, P. L., Pottasch, S. R., Soifer, B. T., Walker, R. G., Emerson, J. P., Rowan-Robinson, M., Wesselius, P. R., Baud, B., Beichman, C. A., Gautier, T. N., Harris, S., Miley, G. K., and Young, E. (1986). IRAS catalogues and atlases - Atlas of low-resolution spectra. A&AS, 65:607–1065.

Olofsson, H., Bergman, P., Eriksson, K., and Gustafsson, B. (1996). Carbon stars with episodic mass loss: observations and models of molecular emission from detached circumstellar shells. A&A, 311:587–615.

Olofsson, H., Bergman, P., Lucas, R., Eriksson, K., Gustafsson, B., and Bieging, J. H. (2000). A high-resolution study of episodic mass loss from the carbon star TT Cygni. A&A, 353:583–597.

Olofsson, H., Carlstrom, U., Eriksson, K., and Gustafsson, B. (1992). The circumstellar envelope of the carbon star S Scuti. A&A, 253:L17–L20.

Olofsson, H., Eriksson, K., Gustafsson, B., and Carlstroem, U. (1993). A Study of Circumstellar Envelopes around Bright Carbon Stars. II. Molecular Abundances. ApJS, 87:305.

Olofsson, H., González Delgado, D., Kerschbaum, F., and Schöier, F. L. (2002a). Mass loss rates of a sample of irregular and semiregular M-type AGB-variables. A&A, 391:1053–1067.

Olofsson, H., González Delgado, D., Kerschbaum, F., and Schöier, F. L. (2002b). Mass loss rates of a sample of irregular and semiregular M-type AGB-variables. A&A, 391:1053–1067.

Ossenkopf, V., Henning, T., and Mathis, J. S. (1992). Constraints on cosmic silicates. A&A, 261:567–578.

Paladini, C., Aringer, B., Hron, J., Nowotny, W., Sacuto, S., and Höfner, S. (2009). Interferometric properties of pulsating C-rich AGB stars. Intensity profiles and uniform disc diameters of dynamic model atmospheres. A&A, 501:1073–1085.

Paladini, C., Sacuto, S., Klotz, D., Ohnaka, K., Wittkowski, M., Nowotny, W., Jorissen, A., and Hron, J. (2012). Detection of an asymmetry in the envelope of the carbon Mira R Fornacis using VLTI/MIDI. A&A, 544:L5.

Paladini, C., van Belle, G. T., Aringer, B., Hron, J., Reegen, P., Davis, C. J., and Lebzelter, T. (2011). Determination of the stellar parameters of C-rich hydrostatic stars from spectro-interferometric observations. A&A, 533:A27.

Pegourie, B. (1988). Optical properties of alpha silicon carbide. A&A, 194:335–339.

Percy, J. R. and Bagby, D. H. (1999). Long-Term Changes in Mira Stars. III. Multiperiodicity in Mira Stars. PASP, 111:203–209.

Perrin, G., Coudé du Foresto, V., Ridgway, S. T., Mennesson, B., Ruilier, C., Mariotti, J.-M., Traub, W. A., and Lacasse, M. G. (1999). Interferometric observations of R Leonis in the K band. First direct detection of the photospheric pulsation and study of the atmospheric intensity distribution. A&A, 345:221–232.

Perryman, M. A. C., de Boer, K. S., Gilmore, G., Høg, E., Lattanzi, M. G., Lindegren, L., Luri, X., Mignard, F., Pace, O., and de Zeeuw, P. T. (2001). GAIA: Composition, formation and evolution of the Galaxy. A&A, 369:339–363.

Perryman, M. A. C., Lindegren, L., Kovalevsky, J., Hoeg, E., Bastian, U., Bernacca, P. L., Crézé, M., Donati, F., Grenon, M., Grewing, M., van Leeuwen, F., van der Marel, H., Mignard, F., Murray, C. A., Le Poole, R. S., Schrijver, H., Turon, C., Arenou, F., Froeschlé, M., and Petersen, C. S. (1997). The HIPPARCOS Catalogue. A&A, 323:L49–L52.

Pilbratt, G. L., Riedinger, J. R., Passvogel, T., Crone, G., Doyle, D., Gageur, U., Heras, A. M., Jewell, C., Metcalfe, L., Ott, S., and Schmidt, M. (2010). Herschel Space Observatory. An ESA facility for far-infrared and submillimetre astronomy. A&A, 518:L1.

Pitman, K. M., Hofmeister, A. M., Corman, A. B., and Speck, A. K. (2008). Optical properties of silicon carbide for astrophysical applications. I. New laboratory infrared reflectance spectra and optical constants. A&A, 483:661–672.

Pluzhnik, E. A., Ragland, S., LeCoroller, H., Cotton, W. D., Danchi, W. C., Traub, W. A., and Willson, L. A. (2009). The Structure and Kinematics of the Envelope Around U Ori from Iota Observations. ApJ, 700:114–122.

Pojmanski, G. (2002). The All Sky Automated Survey. Catalog of Variable Stars. I. 0 h - 6 hQuarter of the Southern Hemisphere. Acta Astron., 52:397–427.

Ragland, S., Traub, W. A., Berger, J.-P., Danchi, W. C., Monnier, J. D., Willson, L. A., Carleton, N. P., Lacasse, M. G., Millan-Gabet, R., Pedretti, E., Schloerb, F. P., Cotton, W. D., Townes, C. H., Brewer, M., Haguenauer, P., Kern, P., Labeye, P., Malbet, F., Malin, D., Pearlman, M., Perraut, K., Souccar, K., and Wallace, G. (2006). First Surface-resolved Results with the Infrared Optical Telescope Array Imaging Interferometer: Detection of Asymmetries in Asymptotic Giant Branch Stars. ApJ, 652:650–660.

Ramstedt, S., Mohamed, S., Vlemmings, W. H. T., Maercker, M., Montez, R., Baudry, A., De Beck, E., Lindqvist, M., Olofsson, H., Humphreys, E. M. L., Jorissen, A., Kerschbaum, F., Mayer, A., Wittkowski, M., Cox, N. L. J., Lagadec, E., Leal-Ferreira, M. L., Paladini, C., Pérez-Sánchez, A., and Sacuto, S. (2014). The wonderful complexity of the Mira AB system. *ArXiv e-prints*.

Ratzka, T. (2005). *High Spatial Resolution Observations of Young Stellar Binaries*. PhD thesis, Max-Planck-Institute for Astronomy, Königstuhl 17, 69117 Heidelberg, Germany.

Ratzka, T., Leinert, C., Henning, T., Bouwman, J., Dullemond, C. P., and Jaffe, W. (2007). High spatial resolution mid-infrared observations of the low-mass young star TW Hydrae. A&A, 471:173–185.

Rau, G., Erikssonn, K., Aringer, B., Hron, J., and Paladini, C. (2016a). Comparison of spectro-photometric and interferometric observations with DARWIN model, with and without the small particle limit approximation - The observational test case of R Lep. A&A*, in prep.*

Rau, G., Hron, J., Paladini, C., Aringer, B., Erikssonn, K., Marigo, P., Nowotny, W., and Grellmann, R. (2016b). The adventure of carbon stars - Observations and modelling of a set of C-rich AGB stars. A&A*, submitted.*

Rau, G., Paladini, C., Hron, J., Aringer, B., Erikssonn, K., and Groenewegen, M. (2015a). The carbon star adventure: modelling atmospheres of a set of C-rich AGB stars. *IAU General Assembly*, 22:2254798.

Rau, G., Paladini, C., Hron, J., Aringer, B., Groenewegen, M. A. T., and Nowotny, W. (2015b). Modelling a set of C-rich AGB stars: the cases of RU Vir and R Lep. Mem. Soc. Astron. Italiana, 87:260.

Rau, G., Paladini, C., Hron, J., Aringer, B., Groenewegen, M. A. T., and Nowotny, W. (2015c). Modelling the atmosphere of the carbon-rich Mira RU Virginis. A&A, 583:A106.

Rayner, J. T., Cushing, M. C., and Vacca, W. D. (2009). The Infrared Telescope Facility (IRTF) Spectral Library: Cool Stars. ApJS, 185:289–432.

Richards, A. M. S., Elitzur, M., and Yates, J. A. (2011). Observational evidence for the shrinking of bright maser spots. A&A, 525:A56.

Richichi, A., Chandrasekhar, T., Lisi, F., Howell, R. R., Meyer, C., Rabbia, Y., Ragland, S., and Ashok, N. M. (1995). Sub-milliarcsecond resolution observations of two carbon stars: TX PISCIUM and Y Tauri revisited. A&A, 301:439.

Richichi, A., Percheron, I., and Khristoforova, M. (2005). CHARM2: An updated Catalog of High Angular Resolution Measurements. A&A, 431:773–777.

Rouleau, F. and Martin, P. G. (1991). Shape and clustering effects on the optical properties of amorphous carbon. ApJ, 377:526–540.

Rowan-Robinson, M. and Harris, S. (1982). Radiative transfer in dust clouds. II - Circumstellar dust shells around early M giants and supergiants. MNRAS, 200:197–215.

Sacuto, S., Aringer, B., Hron, J., Nowotny, W., Paladini, C., Verhoelst, T., and Höfner, S. (2011a). Observing and modeling the dynamic atmosphere of the low mass-loss C-star R Sculptoris at high angular resolution. A&A, 525:A42.

Sacuto, S., Aringer, B., Hron, J., Nowotny, W., Paladini, C., Verhoelst, T., and Höfner, S. (2011b). Observing and modeling the dynamic atmosphere of the low mass-loss C-star R Sculptoris at high angular resolution. A&A, 525:A42.

Sacuto, S., Jorissen, A., Cruzalèbes, P., Chesneau, O., Ohnaka, K., Quirrenbach, A., and Lopez, B. (2008). The close circumstellar environment of the semi-regular S-type star π ^{1} Gruis. A&A, 482:561–574.

Sacuto, S., Ramstedt, S., Höfner, S., Olofsson, H., Bladh, S., Eriksson, K., Aringer, B., Klotz, D., and Maercker, M. (2013). The wind of the M-type AGB star <ASTROBJ>RT Virginis</ASTROBJ> probed by VLTI/MIDI. A&A, 551:A72.

Sahai, R. (1992). Discovery of a fast, bipolar mass-outflow from the prototype S-star Pi(1) Gru. A&A, 253:L33–L36.

Sahai, R., Findeisen, K., Gil de Paz, A., and Sánchez Contreras, C. (2008). Binarity in Cool Asymptotic Giant Branch Stars: A GALEX Search for Ultraviolet Excesses. ApJ, 689:1274–1278.

Samus, N. N., Durlevich, O. V., and et al. (2009a). General Catalogue of Variable Stars (Samus+ 2007-2013). *VizieR Online Data Catalog*, 1:2025.

Samus, N. N., Kazarovets, E. V., Pastukhova, E. N., Tsvetkova, T. M., and Durlevich, O. V. (2009b). A Catalog of Accurate Equatorial Coordinates for Variable Stars in Globular Clusters. PASP, 121:1378–1385.

Schöier, F. L. and Olofsson, H. (2001). Models of circumstellar molecular radio line emission. Mass loss rates for a sample of bright carbon stars. A&A, 368:969–993.

Scholz, M. (2003). Mira science with interferometry: a review. In Traub, W. A., editor, *Interferometry for Optical Astronomy II*, volume 4838 of *Society of Photo-Optical Instrumentation Engineers (SPIE) Conference Series*, pages 163–171.

Schuller, P., Salomé, P., Perrin, G., Mennesson, B., Niccolini, G., de Laverny, P., Ridgway, S. T., Coudé du Foresto, V., and Traub, W. A. (2004). Are dust shell models well-suited to explain interferometric data of late-type stars in the near-infrared? A&A, 418:151–162.

Sloan, G. C., Kraemer, K. E., and Price, S. D. (2003). Calibration Issues with Data from the ISO-SWS. In Metcalfe, L., Salama, A., Peschke, S. B., and Kessler, M. F., editors, *The Calibration Legacy of the ISO Mission*, volume 481 of *ESA Special Publication*, page 447.

Sloan, G. C., Little-Marenin, I. R., and Price, S. D. (1998). The carbon-rich dust sequence - Infrared spectral classification of carbon stars. AJ, 115:809.

Smith, B. J., Price, S. D., and Baker, R. I. (2004). The COBE DIRBE Point Source Catalog. ApJS, 154:673–704.

Straniero, O., Gallino, R., and Cristallo, S. (2006). s process in low-mass asymptotic giant branch stars. *Nuclear Physics A*, 777:311 – 339. Special Isseu on Nuclear Astrophysics.

Sugimoto, D. and Nomoto, K. (1975). Thermal instability of helium-burning shell in stars evolving toward carbon-detonation supernovae. PASJ, 27:197–213.

Swan, P. S., Walker, R. M., and Yuan, J. (1989). Location of Small SiC Crystals in Meteorites Using a Low-Voltage X-Ray Mapping Technique. In *Lunar and Planetary Science Conference*, volume 20 of *Lunar and Planetary Science Conference*.

Tabur, V., Bedding, T. R., Kiss, L. L., Moon, T. T., Szeidl, B., and Kjeldsen, H. (2009). Long-term photometry and periods for 261 nearby pulsating M giants. MNRAS, 400:1945–1961.

Tango, W. J. and Davis, J. (2002). The accurate determination of stellar angular diameters using broad-band stellar interferometry. MNRAS, 333:642–648.

Tatebe, K., Chandler, A. A., Hale, D. D. S., and Townes, C. H. (2006). Characterization of Dust Shell Dynamics and Asymmetry for Six Mira-Type Stars. ApJ, 652:666–680.

Tatebe, K., Wishnow, E. H., Ryan, C. S., Hale, D. D. S., Griffith, R. L., and Townes, C. H. (2008). The Evolving Shapes of o Ceti and R Leonis. ApJ, 689:1289–1294.

Tevousjan, S., Abdeli, K.-S., Weiner, J., Hale, D. D. S., and Townes, C. H. (2004). Mid-Infrared Interferometry on Dust Shells around Four Late-Type Stars. ApJ, 611:466–475.

Teyssier, D., Hernandez, R., Bujarrabal, V., Yoshida, H., and Phillips, T. G. (2006). CO line emission from circumstellar envelopes. A&A, 450:167–179.

Thompson, G. D., Corman, A. B., Speck, A. K., and Dijkstra, C. (2006). Challenging the Carbon Star Dust Condensation Sequence: Anarchist C Stars. ApJ, 652:1654–1673.

Treffers, R. and Cohen, M. (1974). High-resolution spectra of cool stars in the 10- and 20-micron regions. ApJ, 188:545–552.

Tristram, K. R. W., Burtscher, L., Jaffe, W., Meisenheimer, K., Hönig, S. F., Kishimoto, M., Schartmann, M., and Weigelt, G. (2014). The dusty torus in the Circinus galaxy: a dense disk and the torus funnel. A&A, 563:A82.

Tuthill, P. G., Monnier, J. D., Danchi, W. C., and Lopez, B. (2000). Smoke Signals from IRC +10216. I. Milliarcsecond Proper Motions of the Dust. ApJ, 543:284–290.

Valiante, R., Schneider, R., Bianchi, S., and Andersen, A. C. (2009). Stellar sources of dust in the high-redshift Universe. MNRAS, 397:1661–1671.

van Belle, G. T. (1999). Predicting Stellar Angular Sizes. PASP, 111:1515–1523.

van Belle, G. T., Dyck, H. M., Thompson, R. R., Benson, J. A., and Kannappan, S. J. (1997). Angular Size Measurements of Carbon Miras and S-Type Stars. AJ, 114:2150.

van Belle, G. T., Lane, B. F., Thompson, R. R., Boden, A. F., Colavita, M. M., Dumont, P. J., Mobley, D. W., Palmer, D., Shao, M., Vasisht, G. X., Wallace, J. K., Creech-Eakman, M. J., Koresko, C. D., Kulkarni, S. R., Pan, X. P., and Gubler, J. (1999). Radii and Effective Temperatures for G, K, and M Giants and Supergiants. AJ, 117:521–533.

van Belle, G. T., Paladini, C., Aringer, B., Hron, J., and Ciardi, D. (2013). The PTI Carbon Star Angular Size Survey: Effective Temperatures and Non-sphericity. ApJ, 775:45.

van Boekel, R., Min, M., Leinert, C., Waters, L. B. F. M., Richichi, A., Chesneau, O., Dominik, C., Jaffe, W., Dutrey, A., Graser, U., Henning, T., de Jong, J., Köhler, R., de Koter, A., Lopez, B., Malbet, F., Morel, S., Paresce, F., Perrin, G., Preibisch, T., Przygodda, F., Schöller, M., and Wittkowski, M. (2004). The building blocks of planets within the 'terrestrial' region of protoplanetary disks. Nature, 432:479–482.

van der Veen, W. E. C. J. and Habing, H. J. (1988). The IRAS two-colour diagram as a tool for studying late stages of stellar evolution. A&A, 194:125–134.

Van Eck, S., Jorissen, A., Udry, S., Mayor, M., Burki, G., Burnet, M., and Catchpole, R. (2000). The Henize sample of S stars. II. Data. A&AS, 145:51–65.

van Leeuwen, F. (2007). Validation of the new Hipparcos reduction. A&A, 474:653–664.

Vassiliadis, E. and Wood, P. R. (1993). Evolution of low- and intermediate-mass stars to the end of the asymptotic giant branch with mass loss. ApJ, 413:641–657.

Verhoelst, T. (2005). *Evolved stars: a combined view from interferometry and spectroscopy*. PhD thesis, Institute of Astronomy, K.U.Leuven, Belgium.

Virag, A., Wopenka, B., Amari, S., Zinner, E., Anders, E., and Lewis, R. S. (1992). Isotopic, optical, and trace element properties of large single SiC grains from the Murchison meteorite. Geochim. Cosmochim. Acta, 56:1715–1733.

Wallerstein, G. and Knapp, G. R. (1998). Carbon Stars. ARA&A, 36:369–434.

Weigelt, G., Balega, Y., Bloecker, T., Fleischer, A. J., Osterbart, R., and Winters, J. M. (1998). 76mas speckle-masking interferometry of IRC+10216 with the SAO 6m telescope: Evidence for a clumpy shell structure. A&A, 333:L51–L54.

Weigelt, G., Balega, Y. Y., Blöcker, T., Hofmann, K.-H., Men'shchikov, A. B., and Winters, J. M. (2002). Bispectrum speckle interferometry of <ASTROBJ>IRC +10216</ASTROBJ>: The dynamic evolution of the innermost circumstellar environment from 1995 to 2001. A&A, 392:131–141.

Welty, A. D. and Wade, R. A. (1995). On the nature of 17 Leporis. AJ, 109:326–331.

Whitelock, P. and Feast, M. (2000). Hipparcos parallaxes for Mira-like long-period variables. MNRAS, 319:759–770.

Whitelock, P. A., Feast, M. W., Marang, F., and Groenewegen, M. A. T. (2006). Near-infrared photometry of carbon stars. MNRAS, 369:751–782.

Whitelock, P. A., Feast, M. W., Marang, F., and Overbeek, M. D. (1997). Mass-loss variations among carbon-rich AGB variables. MNRAS, 288:512–532.

Wiesemeyer, H., Thum, C., Baudry, A., and Herpin, F. (2009). Precessing planetary magnetospheres in SiO stars?. First detection of quasi-periodic polarization fluctuations in R Leonis and V Camelopardalis. A&A, 498:801–810.

Winters, J. M., Fleischer, A. J., Gauger, A., and Sedlmayr, E. (1994). Circumstellar dust shells around long-period variables. II. Theoretical lightcurves of C-stars. A&A, 290.

Winters, J. M., Fleischer, A. J., Gauger, A., and Sedlmayr, E. (1995). Circumstellar dust shells around long-period variables. IV. Brightness profiles and spatial spectra of C-stars. A&A, 302:483.

Winters, J. M., Le Bertre, T., Jeong, K. S., Nyman, L.-Å., and Epchtein, N. (2003). Mass-loss from dusty, low outflow-velocity AGB stars. I. Wind structure and mass-loss rates. A&A, 409:715–735.

Wittkowski, M., Boboltz, D. A., Driebe, T., Le Bouquin, J.-B., Millour, F., Ohnaka, K., and Scholz, M. (2008). J, H, K spectro-interferometry of the Mira variable S Orionis. A&A, 479:L21–L24.

Wittkowski, M., Boboltz, D. A., Ireland, M., Karovicova, I., Ohnaka, K., Scholz, M., van Wyk, F., Whitelock, P., Wood, P. R., and Zijlstra, A. A. (2011a). Inhomogeneities in molecular layers of Mira atmospheres. A&A, 532:L7.

Wittkowski, M., Boboltz, D. A., Ireland, M., Karovicova, I., Ohnaka, K., Scholz, M., van Wyk, F., Whitelock, P., Wood, P. R., and Zijlstra, A. A. (2011b). Inhomogeneities in molecular layers of Mira atmospheres. A&A, 532:L7.

Wittkowski, M., Boboltz, D. A., Ohnaka, K., Driebe, T., and Scholz, M. (2007). The Mira variable S Orionis: relationships between the photosphere, molecular layer, dust shell, and SiO maser shell at 4 epochs. A&A, 470:191–210.

Wittkowski, M., Hummel, C. A., Johnston, K. J., Mozurkewich, D., Hajian, A. R., and White, N. M. (2001). Direct multi-wavelength limb-darkening measurements of three late-type giants with the Navy Prototype Optical Interferometer. A&A, 377:981–993.

Woitke, P. (2003). Modelling the Mass Loss of Cool AGB Stars. In Piskunov, N., Weiss, W. W., and Gray, D. F., editors, *Modelling of Stellar Atmospheres*, volume 210 of *IAU Symposium*, page 387.

Woitke, P. (2006). Too little radiation pressure on dust in the winds of oxygen-rich AGB stars. A&A, 460:L9–L12.

Woodruff, H. C., Ireland, M. J., Tuthill, P. G., Monnier, J. D., Bedding, T. R., Danchi, W. C., Scholz, M., Townes, C. H., and Wood, P. R. (2009). The Keck Aperture Masking Experiment: Spectro-Interferometry of Three Mira Variables from 1.1 to 3.8 μm. ApJ, 691:1328–1336.

Woodruff, H. C., Tuthill, P. G., Monnier, J. D., Ireland, M. J., Bedding, T. R., Lacour, S., Danchi, W. C., and Scholz, M. (2008). The Keck Aperture Masking Experiment: Multiwavelength Observations of Six Mira Variables. ApJ, 673:418–433.

Yamamura, I. and de Jong, T. (2000). Warm gas around AGB stars. In Salama, A., Kessler, M. F., Leech, K., and Schulz, B., editors, *ISO Beyond the Peaks: The 2nd ISO Workshop on Analytical Spectroscopy*, volume 456 of *ESA Special Publication*, page 155.

Yasuda, Y. and Kozasa, T. (2012). Formation of SiC Grains in Pulsation-enhanced Dust-driven Wind around Carbon-rich Asymptotic Giant Branch Stars. ApJ, 745:159.

Zhao-Geisler, R., Quirrenbach, A., Köhler, R., and Lopez, B. (2012). Dust and molecular shells in asymptotic giant branch stars. A&A, 545:A56.

Zhao-Geisler, R., Quirrenbach, A., Köhler, R., Lopez, B., and Leinert, C. (2011). The mid-infrared diameter of W Hydrae. A&A, 530:A120.

Zubko, V. G., Mennella, V., Colangeli, L., and Bussoletti, E. (1996). Optical constants of cosmic carbon analogue grains - I. Simulation of clustering by a modified continuous distribution of ellipsoids. MNRAS, 282:1321–1329.

"E quindi uscimmo a riveder le stelle."
Dante Alighieri - Inferno, Canto XXXIV